JUSTUS-LIEBIG-
UNIVERSITÄT
GIESSEN

Top-down approaches to layered transition metal dichalcogenides and oxides green production and to their use in electrochemical energy conversion and storage

Dissertation

In order to obtain an academic doctorate

"Doctor rerum naturalium"

– Dr. rer. nat. –

Archived at the Department 08

Biology and Chemistry

Of the Justus Liebig University

Matteo Crisci

06 December 2024

Selbstständingkeitserkläreung

Ich erkläre: Ich habe die vorgelegte Dissertation selbstständig und ohne unerlaubte fremde Hilfe und nur mit den Hilfen angefertigt, die ich in der Dissertation angegeben habe. Alle Textstellen, die wörtlich oder sinngemäß aus veröffentlichten Schriften entnommen sind, und alle Angaben, die auf mündlichen Auskünften beruhen, sind als solche kenntlich gemacht. Ich stimme einer evtl. Überprüfung meiner Dissertation durch eine Antiplagiat-Software zu. Bei den von mir durchgeführten und in der Dissertation erwähnten Untersuchungen habe ich die Grundsätze guter wissenschaftlicher Praxis, wie sie in der „Satzung der Justus-Liebig-Universität Gießen zur Sicherung guter wissenschaftlicher Praxis“ niedergelegt sind,eingehalten.

_____ _____

Self-declaration of indipendence

I declare that I have completed this dissertation single-handedly without the unauthorized help of a second party and only with the assistance acknowledged therein. I have appropriately acknowledged and cited all text passages that are derived verbatim from or are based on the content of published work of others, and all information relating to verbal communications. I consent to the use of anti-plagiarism software to check my thesis. I have abided by the principles of good scientific conduct laid down in the charter of the Justus Liebig University Giessen „Satzung der Justus-Liebig-Universität Gießen zur Sicherung guter wissenschaftlicher Praxis“ in carrying out the investigations described in the dissertation.

_____ _____

The present work and the following experiments were performed between May 2020 and December 2024 at the Physical Chemistry Institut of the Justus Liebig University in the working group of Prof. Bernd Smarsly.

First supervisor: Prof. Dr. Bernd Smarsly

Second supervisor: Prof. Dr. Teresa Gatti

Abstract

Energy consumption has increased in recent years, and in our current society, it is expected to grow even more. However, concerns about how the energy is produced are also rising, since we can currently observe issues resulting from past reckless policies. To solve the issues, many countries are shifting towards the production of energy through renewable sources, which, while being a promising way to solve the energy crisis, also have significant problems. One of the main ones is their intermittency, meaning they have periods with high energy production and other where it is much lower. To address this issue, energy storage devices are key to store excess energy in peak production periods and releasing it when necessary.

Super-capacitors are quite interesting from this point of view, due to their good energy and power density, allowing for fast charge and discharge, whilst also providing a good amount of energy, making them suitable for quick energy access and backup power sources. Among the material used for such devices, 2D materials are used, providing high surface area and stability, but suffering from restacking and poor capacitance. On the other hand, another interesting class of materials is Conductive Polymers (CPs) which showcases very high specific capacitance, but are always victims of rapid performances degradation. Therefore, the combination of these two materials can lead to a general improvement of their properties and solving their individual issues.

The focus of this thesis' work is to produce and lay the basis for further work on the use of blends using 2D material, specifically MoS_2 and WS_2 and conductive polymers. To do so, the first part of the thesis is aimed at the production of 2D materials using different solvents and techniques and establishing a characterization protocol. While the second focuses on the actual production of the blends using 2D-TMDC and PANI and their structural and electrochemical characterization in both three and two-electrode set up.

Zusammenfassung

In den letzten Jahren ist der Energieverbrauch gestiegen, und in unserer heutigen Gesellschaft wird erwartet, dass er weiter zunimmt. Gleichzeitig wachsen jedoch auch die Bedenken über die Art und Weise, wie Energie erzeugt wird, da die Probleme, die aus früheren Entscheidungen resultieren, zunehmend sichtbar werden. Um diesen Herausforderungen zu begegnen, setzen viele Länder auf die Energieerzeugung aus erneuerbaren Quellen, die zwar eine vielversprechende Lösung der Energiekrise bieten, aber auch erhebliche Probleme mit sich bringen. Eines der Hauptprobleme ist ihre Intermittenz, was bedeutet, dass es Perioden mit hoher Energieproduktion und andere gibt, in denen sie viel geringer ist. Um dieses Problem anzugehen, sind Energiespeichergeräte entscheidend, um überschüssige Energie in Spitzenproduktionszeiten zu speichern und sie bei Bedarf freizusetzen. Superkondensatoren sind in dieser Hinsicht sehr interessant, da sie eine gute Energiedichte und Leistungsdichte aufweisen, was schnelles Laden und Entladen ermöglicht und gleichzeitig eine beträchtliche Menge an Energie liefert. Dies macht sie geeignet für den schnellen Energiezugriff und als Notstromquellen. Unter den Materialien, die für solche Geräte verwendet werden, werden häufig 2D-Materialien eingesetzt, die eine große Oberfläche und Stabilität bieten, jedoch oft unter dem Problem des Stapelns und einer geringen Kapazität leiden. Eine andere interessante Materialklasse sind leitfähige Polymere (CPs), die eine sehr hohe spezifische Kapazität aufweisen, jedoch oft von einem schnellen Leistungsabbau betroffen sind. Daher kann die Kombination dieser beiden Materialien zu einer allgemeinen Verbesserung ihrer Eigenschaften führen und möglicherweise ihre individuellen Probleme lösen.
Der Schwerpunkt dieser Arbeit liegt auf der Herstellung und der Schaffung der Grundlagen für weitere Untersuchungen zur Verwendung von Mischungen, die 2D-Materialien, insbesondere MoS2 und WS2, sowie leitfähige Polymere enthalten. Zu diesem Zweck zielt der erste Teil der Arbeit auf die Herstellung von 2D-Materialien unter Verwendung verschiedener Lösungsmittel und Techniken sowie auf die Etablierung von Charakterisierungsprotokollen ab. Der zweite Teil

konzentriert sich auf die eigentliche Herstellung der Mischungen aus 2D-TMDC und PANI sowie auf deren strukturelle und elektrochemische Charakterisierung in Drei- und Zwei-Elektroden-Aufbauten.

Abbreviation List

Abbreviation	Description	Abbreviation	Description
2D	Bi-dimensional	PEGDA	Polyethylene glycol diacrylate
AFM	Atomic force microscopy	SAED	Selected area electron diffraction
CMC	Critical micellar concentration	SC	Supercapacitor
CP	Conductive polymer	SDS	Sodium dodecyl sulfate
DFT	Density functional theory	SDBS	Sodium dodecyl benzene sulfate
DLS	Dynamic light scattering	SEM	Scanning Electron Microscopy
DMF	Di methyl formamide	SHS	Sodium hexyl sulfate
DMSO	Di methyl sulfoxide	SM	Shear mixer
EXAFS	Edge x-ray absorption fine structure	TEM	Transmission electron microscopy
EIS	Electrochemical impedance spectroscopy	TGA	Thermogravimetric analysis
GCD	Galvanostatic charge discharge	TMDC	Transition metal di chalcogenides
GO	Graphene oxide	TS	Tip sonicator
HER	Hydrogen evolution reaction	UV-Vis	UV visible spectroscopy
HSP	Hansen solubility parameters	USB	Ultrasonic bath
IR	Infrared spectroscopy	XAS	X-ray absorption spectroscopy
LPE	Liquid phase exfoliation	XANES	X-ray absorption near edge structure
NMP	n-methyl pyrrolidone	XPS	X-ray photoelectron spectroscopy
NS	Nano sheet	XRD	X-ray diffraction
PANI	Poly aniline	ZP	Zeta potential

Table of contents

Chapter 1: Introduction

Energy has been and continues to be a key factor in the development of our society. Ever since the Industrial Revolution and the massive increase in energy demands, the energy supply has been a significant concern for various countries. Initially, fossil fuels were an easy and readily available source of energy. However, only a few decades later, their drawbacks became apparent to the scientific community, and their negative impacts are now evident, with significant changes in greenhouse gas levels, an increase in extreme weather events, and rising average temperatures.[1,2] As a result, countries are striving to find more sustainable and long-term alternatives, such as solar, wind, nuclear, and hydroelectric energy.[3,4]

However, the most desired solution, renewable energy, often has the drawback of being inconsistent, with periods of high and low production. Therefore, storing excess energy during high-production periods to redistribute it back at any given time is key to providing a consistent power supply to all facilities. The solutions for this include batteries and electro-storage devices and the production of chemical energy vessels, such as hydrogen. Both allow for the accumulation of excess electricity produced, that can then be used whenever necessary, either by directly connecting the energy storage device to the source requiring power or by consuming the vessel to retrieve the stored energy.

Among energy storage devices, batteries are the most suited for everyday use due to their high energy density and low power output, allowing the operation of low-energy-demanding devices for extended time periods. However, mass production will be a critical issue in the future due to the cascading effects on the supply chain and the final cost of the device, stemming from the use of critical raw materials such as lithium (Li), cobalt (Co), and nickel (Ni) in the best-performing batteries.[5–7] Therefore, finding and using alternatives that can power large systems or serve similar roles is essential. Supercapacitors have the potential to do so with good energy density as well as better power density compared to batteries, making

them capable of powering large devices, especially when used in series.[8–11] Additionally, they provide quick access to stored electricity, making them suitable as backup power sources or for quickly recharging devices in need of energy. Therefore, their application flexibility is a key feature of such devices, which also encompass their use in small devices. In fact, flexible super-capacitors are devices used to store energy to power up small and wearable devices.[12–14] While they usually have lower capacitances in comparison to larger super-capacitors, they are easy to produce, flexible and have no health-related drawback. Super-capacitor flexibility is also evident in the material used for their production, since they possess different fields of application, different materials proved to be more suitable for one or the other specifically. For example, in the aforementioned flexible super-capacitors, conductive polymers mixed with polymeric matrix are very commonly used, while in more conventional applications, the material choice depends on the storage mechanism used, such as carbon-based materials, where graphene and polymers are examples, and their inorganic counterparts, such as oxide and transition metal compounds. Among all these, a class of material found its way into supercapacitor applications, specifically Transition Metal Dichalcogenides (TMDC).[15–17] The shear amount of materials in this class that can be used is astonishing, while also having vastly different storage properties, based on either pseudo-capacitive or EDLC mechanism. Moreover, their flexibility, *i.e* doping possibilities, blending with other materials and nano-structuring, opens to almost infinite research possibilities. In our case, we found interest in the dimensional reduction to obtain 2D structures. They are the easiest to obtain from this class of materials, due to their inherent structure, as described in detail in Chapter 2.1.2.

Therefore, this dissertation provides examples and studies of the use of TMDCs and 2D materials in energy storage and conversion. The thesis is divided into two main sections: the first section focuses on basic knowledge and establishing protocols for the synthesis of 2D materials, while the second one explores the use

of 2D materials in energy conversion and storage applications, focusing on blending with other materials to further improve their properties.

In **publication 1**, MoO_3 exfoliation is thoroughly studied to provide the theoretical basis for solvent selection when performing exfoliation experiments and setting up characterization routines for subsequent publications involving 2D materials in this work. In this publication, several solvents are tested, according to the Hansen Solubility Parameter theory (HSP), utilizing also different characterization techniques and conducting in-depth analysis via XANES/XAS measurements and theoretical calculations to further support our findings.

Following the example of **publication 1**, **publication 2** also focuses on the synthesis of 2D materials using water-based solvents and studies the surfactant concentration's effect, as well as their lateral chain length's one. Characterizations are performed following the procedure established in the previous paper, providing insight into the series of experiments performed.

As for the second section of this dissertation, **publication 3** and **4** focus on demonstrating the use of TMDC in super-capacitors applications. **Publication 3** provides the basis for studying super-capacitor and outlines the procedures that are further refined in **publication 4**, where the procedures are applied to another TMDC, MoS_2, with the addition of surface functionalization as an extra step. This intermediate step is exploited to further increase the properties already displayed in **publication 3**.

Publication 5 is focused on demonstrating the strength of TMDCs as energy converters and providing efficient alternatives to established, but more expensive, catalysts such Pt on C. In this work, MoS_2 is coupled with BiOBr, produced, and tested by a collaborator, to study not only electrochemical performances, but also photo-electrochemical ones, opening up further system improvements. The material was tested in photo- and electrochemical- set ups but also monitored using synchrotron radiation to understand the kinetics of the reaction, further supported by DFT calculations to integrate experimental and theoretical analysis.

Lastly, **publication 6** studies another application of the functionalized MoS_2 mentioned in publication 4, this time in a pressure sensor material proof-of-concept device. Here MoS_2 is used both as a support on which the various polymers are synthesized and anchored, and as the electro-active component, offering a piezo resistive behavior in the final hydrogel and enabling the pressure sensing properties as low as peripheral pressure ranges.

Chapter 2: Theoretical Background

2.1: Chemistry and properties of transition metal dichalcogenides and oxides

During the thesis, extensive work was done to synthesize different materials. Some of them are reported in the works published through the doctorate period, while others were only assessed, but with no additional focus, therefore, only the materials discussed here had the potential to be used and yield relevant work to be shared. In general, they all shared some properties within each other, such as conductivity, production ease, potential in electrochemical devices, but the main one is their structure, which will be discussed in the next chapters, which allows for dimensional reduction. Specifically, most of these materials showed a stacked layered structure, composed of two-dimensional layers on top of each other, held together via Van der Waals forces, which can be overcome to obtain 2D nanomaterials. A plethora of different properties stems from this dimensional reduction, including variation in band gap, surface properties and electronic properties as well and this topic will be discussed as well in more detail in a subsequent chapter (Chapter 2.2). Therefore, in this sub-chapter, we are going to take an in-depth look at each specific material, used in publications in this thesis work. An overview of their general properties, examples of synthesis routes for bulk and nanostructures, as well as applications will be reported.

2.1.1: Properties, synthesis, and applications: an overview on MoO_3

Molybdenum and oxygen combine to form a plethora of different compounds together, depending on the synthesis conditions. One of these classes of compounds is the molybdate anion, MoO_4^{2-}, and its polyoxometallates These compounds, whose basic structure is octahedral, can polymerize to form complex polyanion complexes at specific conditions, whilst also being used as precursor for the synthesis of MoO_3 oxides. These clusters form at an intermediate acidic pH, from 3 to 7 usually, while the molybdate anion is mostly present at basic pH. When the pH reaches very low values (below 1), the molybdate polyanions are protonated and thereafter, the material precipitates as MoO_3. The precipitated oxide is one of the possible phases of MoO_3, which has four main polymorphs obtainable at different conditions.[18–21] These polymorphs have all the same MoO_6^{6-} octahedral building blocks that can arrange in several ways according to the structure (α, β, γ and *h* phases).

α-MoO_3 is the thermodynamically stable phase, with the octahedra sharing the edges in a zig-zag pattern along two dimensions, forming layers that stack in the third dimension. The stacking layer yields a typical Van der Waals structure, where the different layers are held together via weak intermolecular forces. This characteristic is particularly appealing in this work, since it provides suitable material for exfoliation, forming sheets with a thickness down to 0.7 nm for MoO_3, to be used in nanocomposites or in nano inks. Usually, α-MoO_3 is formed via calcination at 500 °C of the other phases, most of the time from *h*-MoO_3. *h*-MoO_3 is the kinetic favored phase, with an hexagonal Bravais lattice, and forms rapidly at room temperature by simple acidification of a molybdate solutions.[22–26] Compared to α-MoO_3, the *h*-MoO3 phase has building block sharing a corner, instead of an edge, and still assembling in a zig-zag structure forming 1D tunnels in the 3D structure of the material. However, it does not have a layered structure that can be exploited to obtain nano-sheets, therefore it is mostly used as a precursor to α-MoO_3.

The monoclinic ε-MoO_3 phase also has a 2D structure, allowing for its exfoliation, but, in comparison to the alpha phase, it is an high temperature and pressure polymorph, therefore quite difficult to obtain and exfoliate without proper set ups.[27–29] Lastly, β-MoO_3 is another relevant polymorph of MoO_3 which has a ReO_3-like structure, formed by MoO_6 octahedra, sharing oxygen corners forming a three dimensional structure, that cannot be exfoliated anymore.[20,30–32] Other oxides, such as MoO_2 and mixed oxide with molybdenum in oxidation states ranging from IV to VI are present, described often as MoO_{3-x}, but due to structural variation, they are not always suitable for exfoliation.[33–36] Therefore from now on, I will focus only on MoO_3 and its preparation methodologies and applications.

Considering the chemistry already discussed, MoO_3, especially in the *h* phase, can be synthesized quite easily via precipitation[26,37] obtaining a material with low crystallinity or even with an amorphous structure. From this precursor, through calcination, crystalline *h*-MoO_3 is obtained or, if the temperature is high enough, α-MoO_3 is produced.[38–40] Sol gel synthesis[41,42] is another methodology applied to produce the h- phase, but a calcination step is still necessary to obtain the layered phase. Therefore, to solve this issue, hydrothermal synthesis is often used, allowing for peculiar and subcritical condition that can yield the direct production of the desired phase. Hydrothermal synthesis is mostly performed in autoclaves for long reaction times, going from few hours to days.[32,43–47] In addition to the classical hydrothermal methodology, there is also a notable improvement to this techniques that uses microwaves to assist in the homogenous heating of the samples.[48–50]

Once the material is obtained, it can be applied in several applications, with energy storage and sensing being the most prevalent for MoO_3. In general, in battery science h-MoO_3 is preferred[22,51,52], due to its channels and easy diffusion of small cations into the structure. However, α-MoO_3 found applications, especially if the layer distance is tuned, in energy storage related devices.[46,53–55] In sensors, instead, α-MoO_3 is a lot more commonly used than the other phases[56–59] with only few examples for *m*-MoO_3[60] and *h*-MoO_3.[61]

2.1.2: Properties, synthesis, and application: an overview of Transition Metal Dichalcogenides (TMDCs)

TMDCs are a vast class of materials of wide scientific interest, aided by the application possibility of such materials in all energy related topics, as shown by Figure 2, where MoS_2 is taken as a reference. The number of publications in the past 4 years has been outstanding considering the range of fields encompassed in the research. Moreover, focusing on energy storage devices, super-capacitors, and batteries (Figure 2b), an increase in publications in those fields can be observed from the early 2010s, period where research on TMDCs and 2D materials started blooming. TMDCs are compelling in these applications, due to their layered structure and high oxidation states. In fact in conventional lithium ion batteries, the lithium ions intercalate between the layers of the electrodes and TMDCs can be used in a similar way in battery science, with the added advantage of undergoing redox reactions easily and being more earth abundant.[62] For supercapacitor, TMDCs are important because of their redox properties, exploiting then a mechanism similar to a battery, but also due their inherent high surface area that allows also for another surface storage mechanism. (Chapter 2.3.)

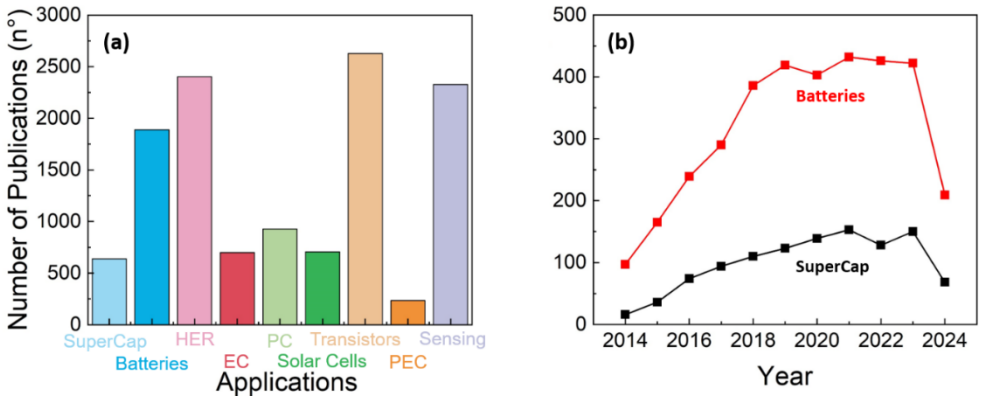

Figure 1. *The number of publications got from Web of Science website, using the words "MoS_2" and the relative application as search keyword. (a) Number of cumulative publications in the year range 2020-2024 for the different applications observed; (b) number of annual publications from 2014 to 2024 for two specific fields: batteries (red) and supercapacitors (black)*

Looking at the basic properties of this class of materials, their stoichiometric formula is MX_2, where M can be any transition metal from the 4^{th} to 7^{th} group and X is an element of the chalcogenide group (usually S, Se, but in some instances also Te). TMDCs formed by 8^{th} and 9^{th} transition metal groups also exist but they exhibit properties which are not pertinent to the current thesis work. Even without these, the number of materials is high, moreover, despite the diversity, they all share with each other some key structural features. The metal ion often has an oxidation state of +4, while the chalcogenide of -2 and the basic structure has either a trigonal prismatic or distorted octahedral coordination, with one of the coordination being the prevalent in any different TMDC.

The unit cell, then, assemble to compose a X-M-X type layer, where the metal atoms are surrounded and sandwiched in between two chalcogenides' layers, forming a Van der Waals structures. The thickness of MX_2 layers is around 7 Å, like graphene's one, and, in a similar way, they are held together by intermolecular forces, enabling their delamination. Moreover, TMDCs show a variety of stacking polymorphs depending on synthesis conditions, resulting in evident structural differences from each other. Three primary polymorphs exist, and they are 1T, 2H and 3R (Fig 1), where the number stands for the amount of X-M-X units present in a unit cell and the letter indicates for the coordination mode, trigonal (T), hexagonal (H) and rhombohedral (R) respectively. The stability of each of these polymorphs depends on the material itself, as well as other properties. Among these, MoS_2 and WS_2 are discussed in more detail in the following chapter, due to their extensive use in this thesis work.

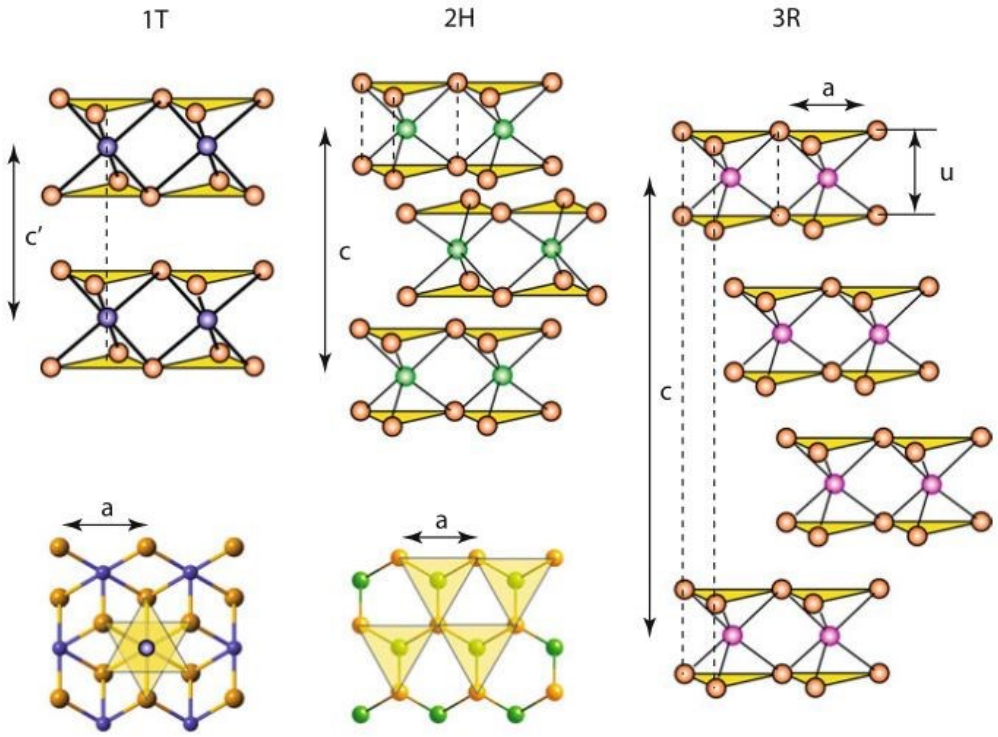

Figure 2. *TMDC polymorphs. From left to right, 1T (tetragonal phase), 2H (hexagonal symmetry) and 3R (rhombohedral symmetry). All of the phases here reported have an octahedral symmetry*[63] *Reprinted from Kolobov A, Tominaga J, Springer Series in Material Science, 2016, 29-77, 239 with permission from Springer Nature. Copyright 2016 Springer Nature.*

MoS_2 and WS_2 exist naturally in the 2H phase, where they both have semi conductive properties, with a band gap of 1.3 eV and 1.8 eV respectively in their bulk form. However, this band gap can be tuned by dimensional reduction, reaching values between 1.8 and 2 eV for MoS_2 and more than 2.1 eV for WS_2. Moreover, dimensional reduction triggers a photoluminescence effect that was not present in the bulk 2H materials. This is a specific feature observed in mono layered MoS_2 and WS_2, where a sharp photoluminescence feature at circa 1.85 eV and 2.0 eV respectively appears, that drastically decrease increasing the amount of layers.[64] Furthermore, an additional optical properties modification can be observed with the transition to the 1T phase. Whenever the two TMDCs' phase change, they lose the before mentioned optical properties in exchange for higher conductivity and catalytic activity.

Therefore, the synthesis methodology and routes are essential to obtain nanostructured TMDCs with all the aforementioned properties. In general, bulk TMDCs are extracted from two minerals, *molybdite* and *tungstite*, but, in a laboratory scale, their synthesis goes through, most of the time, a sulfurization process of metal (VI) oxides or a metallate precursors. Hydrothermal synthesis is also a very common option for the sulfurization reaction, with several sulfur precursors used, such as thioacetamide[65], thiourea[66–68], cysteine[69,70] and other more niche sulfur based compounds.[71] However, a significant difference in condition has been noticed while producing MoS_2 and WS_2. The first one usually needs lower temperatures compared to the latter, varying from 140 and 220 °C[67,72–74], while WS_2 generally needs higher temperature close to 250 °C to ensure the complete sulfurization to the TMDC. However, the material obtained from this synthesis can have one of the two phases mentioned beforehand or a mixture of the two. In general, there is no dividing line between when one is produced and the other. It can be deducted from literature that, using MoS_2 as example, the 1T phase is usually produced at milder conditions, meaning lower temperatures, reaction times and filling factor, gradually giving away in favor of the 2H, when the conditions intensify. For example, very low reaction times[75–77], as well as low filling factors[76,78], usually yield mostly 1T phase. While long reaction times [72,76,79–81]and high filling factors [67,82] usually yield 2H phase rich materials, with a plethora of additional conditions that can provide a mixture of the two in different percentages.[83–85] A short description of how all these conditions changes the reaction media is discussed in Chapter 2.2.1.

However, most of the synthesis found in literature, directly bypasses the production of bulk material to directly produce nanostructured TMDCs, specifically 2D structures, due to their relevance and straightforward production. Both bottom-up and top-down approaches are possible with relative pros and drawbacks. Among the first class, hydrothermal synthesis is the most significant, but it was already discussed beforehand, while also CVD methodologies are also widely used and they allow the production of materials with a precisely defined

number of layers, keeping a tight control on the synthesis procedure.[86–90] However, the parameters to control to obtain specific morphologies are multiple and co-dependent, such as pressure, concentration of precursors, heating of the different sections flowing rate.[91–93] Therefore, CVD is a technique with a steep learning curve, but it rewards the user with its precision and control.

On the opposite end of the spectrum, starting from bulk material is another option to get the nanostructured material. Exfoliation is the preferred method by researchers, and there are several ways to use this technique, ranging from mechanical exfoliations, such as scotch tape methodologies[94–98], first introduced by *Novoselov et al.*[99] in 2004 by exfoliating graphene and further developed in the years,[100–102] and ball milling[103–106] to liquid phase exfoliation[107–110], using different solvents and condition, which is described in more details in the Chapter 2.2.2.

2.2: 2D Materials overview and synthesis methodologies

Nanomaterials constitute a diverse class of materials characterized by at least one dimension in the nanometer scale, typically ranging from few nanometers to hundreds. This defining feature makes them particularly appealing for many research topics and research groups, becoming the base of modern research. As a result, nanomaterials are applied in different and extremely different fields, spanning from sensors to energy storage to bio applications, thanks to their flexibility and the ability to tailor their properties to specific needs. In general, nanotechnology can provide various kinds of materials, classified based on the number of dimensions in the nanoscale range; namely, 0D materials are materials with all dimensions below the nanoscale, 1D materials with two, 2D materials with only one and lastly 3D, or bulk materials, with 0 dimensions in the nanoscale. Each type may have different properties, depending both on the chemistry of the compound and the direct effects of the dimensional reduction on it, but all nanomaterials share some key features common in all nanomaterials. First and foremost, with the size reduction comes an increase in surface to volume ratio, resulting in a larger proportion of surface atoms, which usually improves surface sensitive applications, therefore this geometrical factor is an important variable to tune the desired property. Secondly, with the dimensional reduction, a modification of the band gap will occur in semiconducting and insulating materials. In a bulk material, their discrete energy states will increase in number forming a continuum, or a band. As size decreases, particularly close to the so called *Bohr radius*, this continuum breaks leading to a partial return to a discrete energy level, which have a larger separation compared to the bands of a semiconductor and therefore, provoking blue shift (increase) of the band gap.[111] This phenomenon is referred to as “quantum confinement effect”, first observed in 0D materials[112,113] (quantum dots) and later applied on to 1D and 2D nanocrystals. (Fig 3) Additionally, other physical properties such as magnetism, melting point and mechanical

strength, are modified during the reduction process and can drastically change their applications.[114,115]

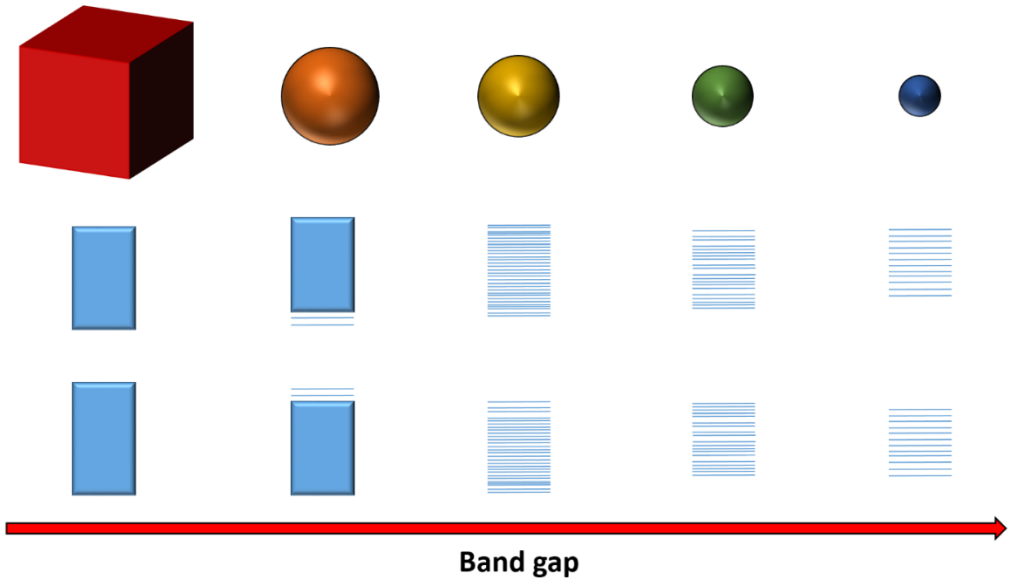

Figure 3. *Schematic of the dimensional reduction effect on the band gap of nanomaterials*

Specifically, 2D materials, or nano-sheets (NSs), are characterized by only one reduced dimension allowing free movements of electrons without restriction in the other two directions. The properties are influenced as described beforehand and they can be produced using both methodologies, from molecular precursors (bottom-up approaches) and from their bulk counterpart (top-down approach). There are plenty of methodologies that can be used from both the two methodologies family: CVDs, scotch tape, hydrothermal, ball milling and colloidal synthesis, but describing all of them would be too lengthy, therefore I will focus only on the used methodologies throughout the doctoral work, mainly LPE technique and hydrothermal methodology. (Fig.4)

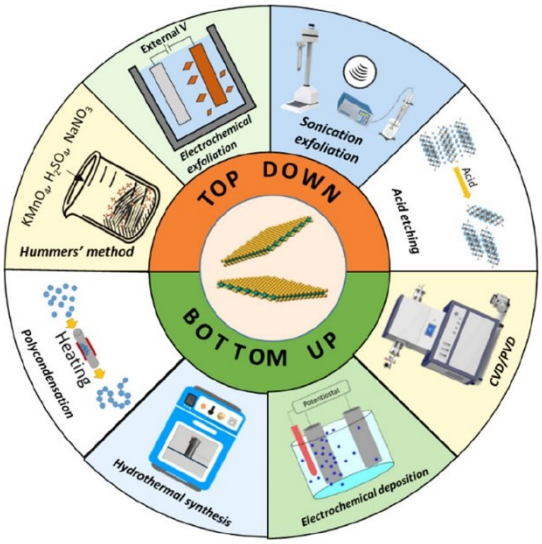

Figure 4. *Scheme of the different synthesis methodologies for nanomaterials and specifically 2D-materials.*[116] *Reprinted with permission from Mengjiao Wang, Michal Langer, Roberto Altieri, Matteo Crisci, Silvio Osella, Teresa Gatti, ACS Nano 2024, 18, 13, 9245-84. Copyright 2024 American Chemical Society.*

2.2.1: Hydrothermal synthesis

Hydrothermal synthesis has always been an easy and efficient methodology to produce nanomaterial in laboratory and larger scales. It is of particular interest because of the wide number of condition that can be used and the possibility of obtain very different morphologies[45,71,117,118] and phases[60,119–121] by simply tuning and refining such parameters.

Briefly, a hydrothermal reaction, or more generally a solvothermal one, is a bottom-up synthesis methodology involving the use of temperature ranging from 80 °C up to 300 °C and high pressures. These conditions are achieved using sealed Teflon liner in iron autoclaves, where pressures going up to hundreds of atmospheres can be reached.[122] Solvothermal reactions usually have a sharp increase in temperature and pressure, large enough to modify the solvent's properties, allowing the solubilization of complex precursors. However, in hydrothermal synthesis, where water is used, the pressure and temperature can reach critical values. The high pressures combined with the high temperature led to a drastic change in the water properties: a supercritical fluid can be reached. (Figure 5a) However, reaching such extreme conditions can be dangerous, so the limits for autoclave reactions are usually set around sub critical conditions. This still translates into sharp changes in dielectric constant, dissociation constant and density of the solvent, thereby altering the reaction condition in the autoclave. (Figure 5b)[123]

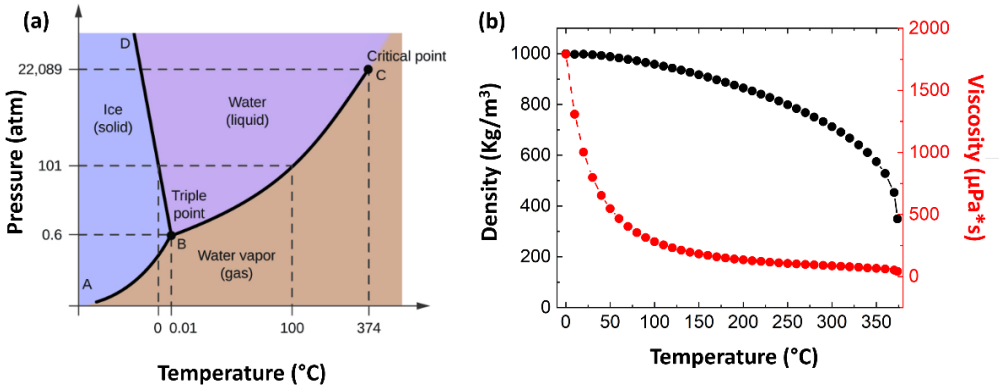

Figure 5. *(a) Water phase diagram Temperature vs Pressure and (b) Water properties change depending on the temperature (b)* [124–126]

Therefore, the choice of solvent and condition can influence the outcome of the reaction. Beyond the obvious parameters, such as temperature and time, another one overlooked and not remarked during these reactions is the Filling Factor (FF), a percentage value that represents how the hydrothermal vessel is the hydrothermal vessel. FF can also greatly enhance the autogenous pressure inside the vessel, as at the same temperature, the volume of solvent would change how quickly this parameter rises. (Fig. 6)

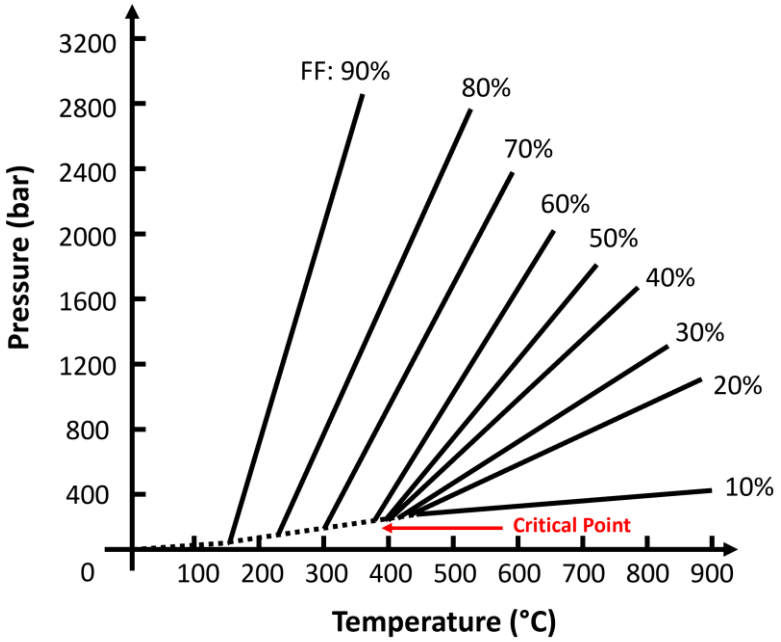

Figure 6. *Filling factor dependency of pressure at different temperatures*[116,122] *Reprinted from Richar I. Walton, Chem Soc Review, 2002, 31, 230-238. Copyright 2002 Royal Chemical Society*[127].

2.2.2: Liquid Phase Exfoliation (LPE)

Dimensional reduction, as stated beforehand, is a highly effective way to tune the properties of specific materials. This process can be achieved thought different ways, which can be categorized in top-down[98,128–132] and bottom-up approaches.[115,133,134] As the names imply, top-down methods start from bulk materials, while bottom-up methods begin with small building blocks.

Specifically, liquid phase exfoliation (LPE) is a straightforward technique among the top-down methodologies and it involves overcoming the Van der Waals forces that keep together the different layers of the 2D materials by using external energy.[135–139] (Chapter 2.1) Although this technique is relatively simple, it requires the optimization of different parameters. In fact, LPE not only depends on time, but also on media and sonication technique.

The first and easiest parameter to consider is time, and it has been proved that longer exfoliation times usually yield higher final material concentration, due to the amount of energy given throughout the whole process to overcome the forces between sheets.[140] However, extended exfoliation times are not ideal, due to concern related to energy consumption, heat control and scalability. Therefore, reducing the duration while optimizing other parameters to maximize yield and minimize the cost is always appealing. To do so, the choice of media is key to improving LPE quality and exfoliation. A lot of research has been done to optimize this parameter, with organic high boiling point solvents leading the way in this sector. (NMP, DMSO, CHP, DMF are examples) They are surely the most performing, but greener and cheaper solutions should be researched as well, however achieving such enormous tasks via trial and error is an impractical solution. For this reason, several theoretical models can be employed for a preliminary screening: one of which is the Hansen Parameter Solubility (HSP) theory. [141–144] It was proposed by Charles Hansen in 1967, and it is based on the Hildebrand parameter theory, already use to predict stability and solubility

between a solvent and a solute. In this theory, one parameter, based on the vaporization energy (*E*) and molar volume of the pure solvent (*V*, Eq.1), was used to ascertain similarities between solute and solvents.

$$\delta = \sqrt[2]{\frac{E}{V}} \qquad \text{(Eq.1)}$$

Matching the as resulting parameters among solute and solvent is a way to predict solubility between substances. In the specific case of LPE and 2D materials, the matching between the solvent's parameters and the exfoliated material's one is an index of the overall final stability of the suspension and indicates also the exfoliation efficiency of the material used. However, these predictions are not always accurate, since Hildebrand theory[145–147] is a rough approximation that does not fully account for the substances' intrinsic properties, considering only the overall cohesive energy density. This is where HSP theory comes into play. It builds from the same concept of the Hildebrand theory, but it expands on it by considering the different interactions between molecules in a solvent. Specifically, the three main contributions are related to dispersive forces, polar interactions, and hydrogen bonds. Inserting these in the overall equation for vaporization or cohesive energy, it will turn out:

$$E_{tot} = E_D + E_P + E_H \qquad \text{(Eq.2)}$$

From this, it is possible to calculate the components to the solubility parameters, applying the Hildebrand parameter theory and dividing the vaporization energy for the volume fraction of the solvent:

$$\delta^2 = \delta_D^2 + \delta_P^2 + \delta_H^2 \qquad \text{(Eq.3)}$$

Most of the parameters for common solvents are already tabulated, and therefore it is possible to compare them with the material's one, using the following equations:

$$(R_a)^2 = 4(\delta_{D2} - \delta_{D1})^2 + (\delta_{P2} - \delta_{P1})^2 + (\delta_{H2} - \delta_{H1})^2 \quad \text{(Eq.4)}$$

$$RED = \frac{R_a}{R_0} \quad \text{(Eq.5)}$$

Where $\delta_{x,y,}$ is one of the parameters (*X= D, P, H*) for one of the components of the mixture (*Y: 1,2*), R_a represents the radius of an imaginary sphere calculated by using the HSP values for solute and solvents, while the interaction radius (R_0) can be calculated by using the parameters of the solute alone. Lastly, *RED* is an index of the affinity between dispersions and represents the matching between the sphere formed using R_a and R_0. The closer this value gets to 0, the higher affinity between the two and the solute will dissolve in the solvent, while for values larger than 1, the system will not dissolve.[141]

Furthermore, the choice of sonication methodology significantly impacts the quality and yield of the exfoliation process. Most commonly used methods comprehend Ultrasonic Bath (USB)[148,149], Tip Sonicator (TS)[150] and Shear Mixers (SM).[151–153] Each technique provides energy to overcome the Van der Waals forces between different layers, each employing a different mechanism:

- **Ultrasonic Bath (USB)** uses indirect vibration through the glassware to transmit the necessary energy to overcome the material's layer-to-layer interaction (Fig 7a);
- **Tip Sonication (TS)**, instead, uses cavitation; a process where bubbles are formed via direct pulses from the tip sonicator in the suspension, until they reach a critical size where they burst, causing high local temperatures and pressures, capable of exfoliating the 2D material[154,155] (Fig 7b);

- **Shear Mixing (SM)** overcomes the Van der Waals interactions between the different layers via direct shear forces, caused by the suspension's movement between a rotor and a stator, slowly reducing the material thickness until the 2D material is obtained (Fig 7c).

There are evident advantages and disadvantages to each of these techniques: Tip Sonication is an aggressive and efficient methodology that allows shorter exfoliation times (20 minutes up to few hours) to obtain high concentration and stable dispersions, while being able to process only smaller amounts of material. Shear Mixing is the opposite: can be used to exfoliate large volumes of material and it is already established as an industrial methodology, while needing longer exfoliation time to obtain the same results as a TS. An Ultra Sonication Bath, on the other hand, is more delicate and therefore produces a smaller amount of surface defect, but also its applicability is often restricted to lab scale experiments.[156]

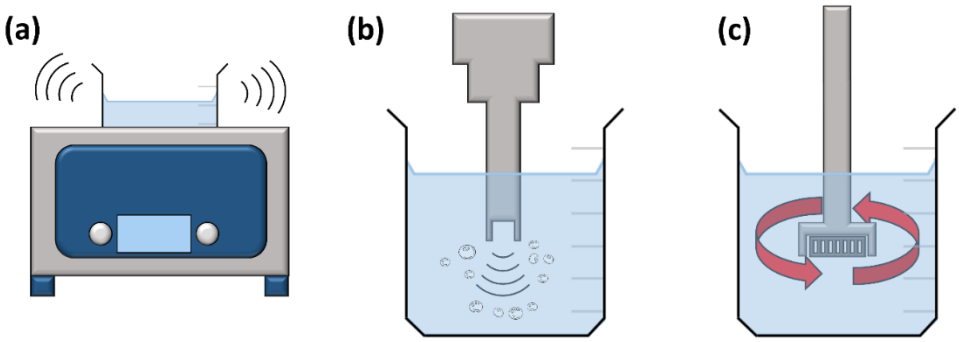

Figure 7. *Scheme of the different sonication instruments possible for Liquid Phase Exfoliation (LPE). (a) Ultrasonic Bath sonication (USB), (b) Tip Sonication (TS) and (c) Shear Mixing (SM)*

The complexity of this simple method does not stop at these parameters, as nowadays researchers are mixing and adding even more pretreatment steps or using different solvent mixtures or surfactants. Some examples include chemical exfoliation: a well-known case is the production of 2D-1T-MoS_2 via lithium ion

intercalation.[107,157,158] The process involves an intercalation step followed by an LPE process in which the energy is mainly provided by the reaction of lithium in water to form hydroxides, which simultaneously expand the 2D structure of the TMDC to obtain high quality, high yield exfoliated material. Another example of chemical exfoliation paired with LPE is the production of MXenes,[159–162] which are generally produced from MAX phases by the removal of an A element via HF etching or a F^- based mixtures and then exfoliated in water with a proper additive. Additives, and more specifically surfactants[163–166], open a new world for exfoliation, as they allow the use of solvents before unsuitable for exfoliation, such as water. However, the evident drawbacks are the additional steps necessary to remove the additives, if possible, at all, and the potential effect of such compounds on the final properties of the device, as these small molecules or polymers can hinder specific applications.

2.3: Characterization of 2D materials

Production of 2D materials was discussed in the previous sections, however, how to characterize them is a key topic, since usually mono-/bi-/few- layered materials are preferred. Therefore, it is of utmost importance to understand the properties and quality of the exfoliated materials. Usually, the techniques employed can be categorized in two main classes: material related, and applications related. In the first class, morphological and structural characterization are included, such as XRD, Raman and microscopies; while in the second class, the characterization may vary depending on the final application. Considering the scope of this dissertation, electrochemical characterization, such as CV, LSV and GCD will be discussed.

2.3.1: Morphological and structural analysis

There are a number of characterizations that can be performed on 2D materials to obtain relevant information on their status, and they can normally be divided into morphological and structural. However, in this dissertation, we will shortly go through these techniques from a production point of view: the material was first obtained as a suspension, characterized and then a powder was obtained from it and then further characterized.

Following this logic, characterization performed on a suspension or starting from a suspension are the first ones performed. They provide information about the size of the nanoparticles (**DLS**), the stability of the suspension (**ZP**), optical (**UV-Vis**), morphological (**electron microscopies**) and structural properties (**Raman**).

Once the characterization on the suspension is performed successfully, the material can be extracted from the media via lyophilization, by evaporation or by centrifugation. These processes yield materials in powder form that can be further

characterized using X Ray Diffraction (**XRD**), **Raman** and Infrared (**IR**) spectroscopy, X-Ray Photoelectron Spectroscopy (**XPS**), Scanning Electron Microscopy (**SEM**) and Thermogravimetric Analysis (**TGA**).

2.3.1.1: Dynamic Light Scattering (DLS) and Zeta Potential (ZP) measurements

Dynamic Light Scattering (DLS) and **Zeta Potential (ZP)** are analyses performed on the same instrument, but they work and give information on different properties of the same suspension. The first (DLS) provides an estimation of the size of the nanoparticles in the liquid, while the second (ZP) gives information about the suspension stability in the form of potential necessary to be able to move the nanoparticles in the media. DLS exploits the Brownian motion of the particles and laser irradiation to obtain the result. Specifically, the measurement monitors the change in laser intensity and scattering when a particle randomly passes through the same path as the laser. The change is then recorded and via a correlation function (Eq. 6, Eq. 7, Eq. 8), the translational diffusion coefficient (D) is calculated, which relates directly to the average Brownian motion speed and afterwards, via the Stokes-Einstein equation, the hydrodynamic radius is calculated. (Eq. 9)

$$G(\tau) = A * [1 + Bexp(-2\Gamma\tau)] \quad \text{(Eq. 6)}$$

$$\Gamma = Dq^2 \quad \text{(Eq. 7)}$$

$$q = \left(\frac{4\pi n}{\lambda_0}\right) * \sin\left(\frac{\theta}{2}\right) \quad \text{(Eq. 8)}$$

$$d(H) = \frac{kT}{3\pi\eta D} \qquad \text{(Eq.9)}$$

Where *A* and *B* are, respectively, baseline and intercept of the correlation function, τ is the time difference in the correlation function, *D* is the translational diffusion coefficient, *n* is the refractive index of the media, λ_0 is the wavelength of the laser, ϑ is the scattering angle, *k* is the Boltzmann's constant, *T* is the temperature in Kelvin and η is the viscosity of the media.

As can be seen, **DLS** can provide realistic hydro-dynamic diameter values, however it starts from a rather incorrect approximation for 2D materials, which is the assumption of the presence of only spherical particles (Fig 8a) in the Stokes-Einstein equation and, therefore, all the particles' geometries will be related to the hydrodynamic diameter of a sphere. Therefore, it is often more precise to refer to the obtained resulted as a "sphere with the same translation diffusion parameter as the particle" and in the case of 2D materials (Fig. 8b), the value obtained can be seen as an approximation of the lateral size of the bi-dimensional material studied.

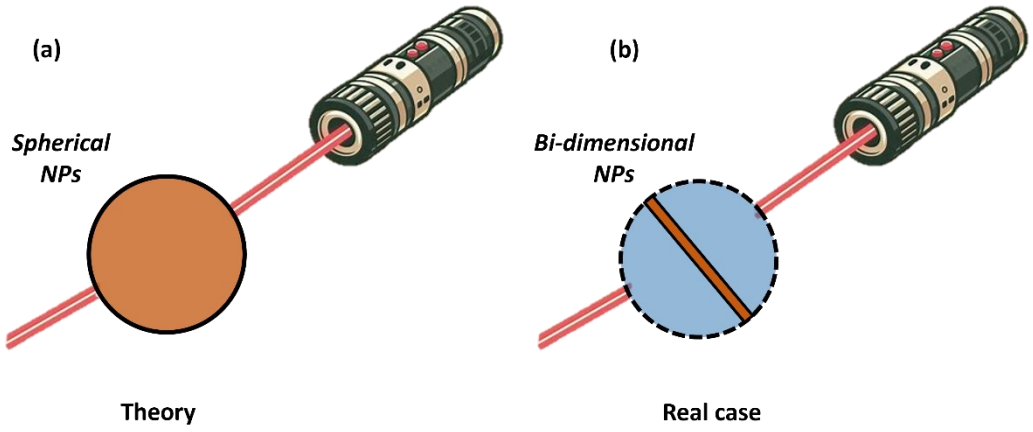

Figure 8. *(a) Theory vs (b) Real case of DLS measurements on nanoparticles and 2D materials*

On the other hand, **ZP** does not present the same issue since there are no geometry-related components in the formula to estimate the potential necessary

to move the nanomaterials. In fact, the equation used to obtain the value (Eq. 10) relates mostly to solvent properties and other tabulated values:

$$U_E = \frac{2 * \varepsilon * z * f(\kappa a)}{3\eta} \qquad \text{(Eq. 10)}$$

Where U_E represents the electrophoretic mobility, ε and η are the dielectric constant and viscosity of the solvent, z is the zeta potential and $f(\kappa a)$ is the so-called *Henry's function*. This function represents the thickness of the electric double layer around the nanoparticle in confront to the nanoparticle size and it is extremely dependent on the polarity of the solvent.

In general, the measurement exploits the surface charge of the nanoparticles, which derives from different sources, *i.e* surface functional group, inherent surface charge of the material or adsorption of charged species on the surface. This surface charge affects the distribution of ions around the nanoparticles forming an electric double layer. More specifically, two regions are distinguished around the nanoparticles, an inner region (Stern layer) and outer layer (diffuse layer). In the Stern layer, ions have a high concentration immediately around the nanoparticles, while in the diffuse layer there is a lower concentration of charges, which are exchanged continuously between this section and the bulk material. These layers are separated by an imaginary border (Fig. 9) at which boundary potentials are calculated.

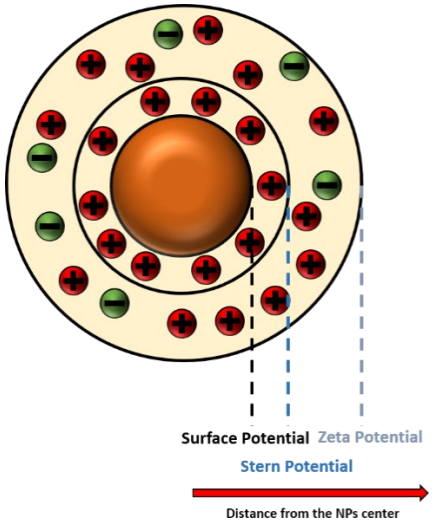

Figure 9. *Electric double layer around a spherical nanoparticle, highlight the inner and outer circle and the potential at the difference EDL "surfaces."*

2.3.1.2: UV-Vis spectroscopy

In a similar way to DLS, **UV-Vis spectroscopy** is a technique involving light sources, however UV-Vis and visible light are, instead, used and different wavelengths are scanned, in contrast with DLS. Using a desired detector, it is possible to measure the transmittance (T), percentage of the incident light reaching the detector, and correlate such value with the absorbance (A), calculated and expressed via the Lambert-Beer law. (Eq. 11)

$$A = \log_{10}\frac{1}{T} = \log_{10}\frac{I_0}{I} = C * \varepsilon * l \qquad \text{(Eq. 11)}$$

Where I_0 and I are the intensity of the light source before and after, respectively, passing through the sample, C is the concentration of the suspension, ε is the molar attenuation coefficient tabulated for most materials and l is the optical path length.

This technique can be used both qualitatively and quantitatively for the analysis of 2D material suspension. In the first case, it is possible to see the presence of excitonic peaks, especially for TMDCs, their shift difference towards lower wavelength compared to the bulk material and the change in spectra. Moreover, from the graph the concentration of a suspension can also be determined by using tabulated ε values at specific wavelengths using the Eq. 11. Additionally, with a simple data analysis, the band gap of a material can be found via the Tauc Plot. This analysis involves the conversion of wavelength to energies to create a new plot and the linear fit of the curve yields the band gap value.

2.3.1.3: Imaging: TEM and SEM microscopies

Microscopies techniques are also essential for the characterization of bi-dimensional material, as they provide information on the morphological features of the nanostructures. **Scanning Electron Microscopy** (**SEM)** and **Transmission Electron Microscopy (TEM)** are particularly valuable since they provide images of the morphology from the microscale to the nanoscale, allowing the analysis of the thickness and lateral size of a nanoparticle by simply looking at the image. They both exploit an electron beam penetrating through the sample, interacting with atoms to produce different signals that can be studied. For example, SEM focuses on studying secondary electron, backscattered electron and characteristic x-ray, (Fig 10a) while TEM makes use of the transmitted electron to obtain information on the samples (Fig 10b), causing a vast difference not only in the microscope themselves but also in type of information obtained from each technique. The use of these different phenomena makes the two microscopy's techniques vastly different from each other. SEM allows for tridimensional images and simple preparation, while it does not offer insights into the internal structure of the material and can reach several hundred nanometers resolution. TEM, on the other hand, provides 2D images, while being able to observe the internal structure of

the sample itself and achieving higher magnification compared to the SEM, up to few nanometers, however it suffers from lower flexibility in samples' preparation, while also needing much more complex and expensive instruments and instructions.

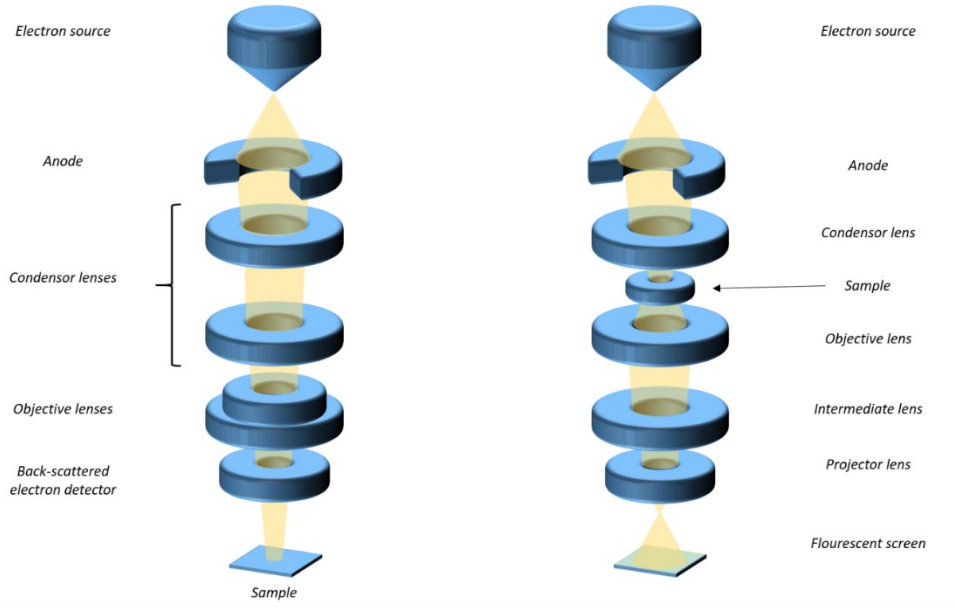

Figure 10. *Scheme of (a) a scanning electron microscope and of (b) a transmission electron microscope*

2.3.1.4: Powder XRD and Raman spectroscopy: Insight into the structure of a material

Lastly, **P-XRD** and **Raman** measurements are used to discern structural information of the material. The first technique is a standard material characterization methodology and exploits the diffraction of x-rays on an organized and repetitive crystalline structure to obtain a specific and recognizable pattern derived from the sample's structure. Raman spectroscopy is a technique

also used to analyze inorganic materials, as it allows the detection of the different and specific modes, specific to the sample itself, which are often not visible in the IR spectroscopy. In fact, Raman scattering, and IR spectroscopy are very similar techniques from a certain point of view, but very different at the same time, as they exploit two different phenomena. IR relies on the absorption of low energy radiation, infrared light, by the vibrational modes of a molecule, causing a shift in energy from the ground level to higher energy state in the vibrational levels. (Fig 11) This change can be observed at specific energy values, depending on where the absorption occurs, and each bond in each material has specific wavelength at which they resonate to absorb the incident light, therefore yielding a fingerprint specific to that material. On the other hand, Raman focuses as well on radiation absorption, but in this case, radiation has higher energy, a laser source, and therefore the excitation that takes place in the electronic states, instead of the vibrational ones. When light is absorbed in the electronic state, several possibilities arise. The absorption itself is studied in UV-Vis, but also decays from such states are studied and depending on the final state, the effect is different. In the case of decay from the excited state to the same initial energy level, the decay is called Rayleigh scattering, an elastic scattering, meaning no change in overall energy occur at the end of the whole transition. (Fig 11) While in the case the decay and the absorption do not match, there will be a difference in energy from the initial state, either a surplus or deficit, and a transfer to or from the vibrational mode will be necessary. This change in energy will result in a leaving photon at a different energy from the incident one, that can then be translated into signals. These phenomena are called Stokes or anti-Stokes effects, when the final wavelength has lower or higher energy respectively.[167]

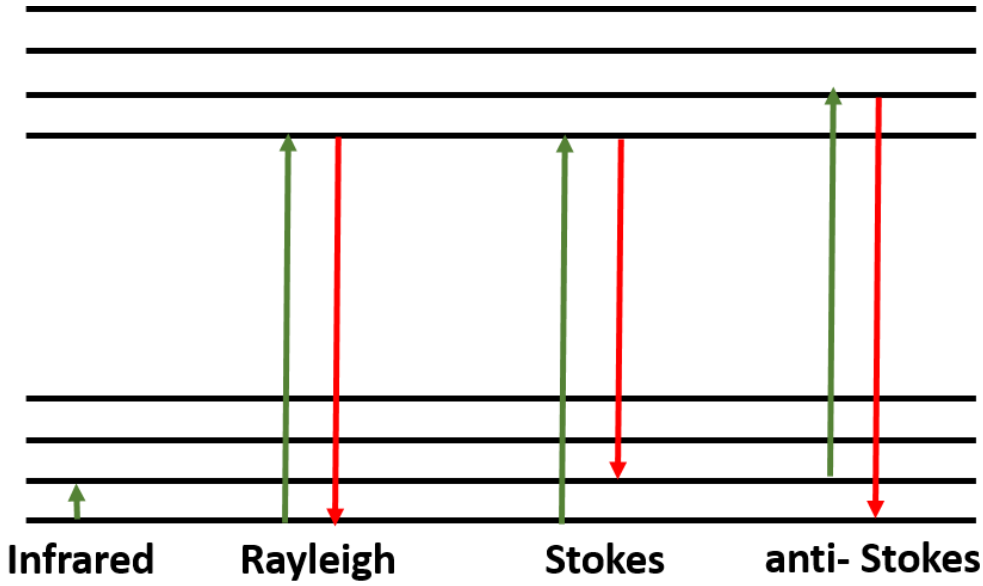

Figure 11. *Depiction of the absorption effect observed in IR spectroscopy and Raman scattering.*

Therefore, from this short explanation, it can be understood that the IR focuses on the variation of dipole moment of the material, while Raman on the polarization tensor's variation in the electronic cloud of the material. These effects have, often time, different selection rules, therefore, the use of one or the other technique should be done after careful consideration of the inherent symmetry of the material. Consequently, it is of utmost importance to understand which modes are Raman or IR active to properly use one, the other or both techniques. This can be done by applying the crystal group theory and by using the table related to the point group and checking the selection rules to determine which normal mode is active or not.

2.3.1.5: X-Ray Photoelectron Spectroscopy (XPS)

X-Ray Photoelectron Spectroscopy (**XPS**) is used for surface analysis of the materials and gives not only information on the elemental composition of the surface, but also on the chemical environment of an atom. This technique exploits

the photoelectric effect, where electromagnetic radiation, in this case x-rays, removes an electron bound in the electronic structure. This radiation needs to have high enough energy to remove an electron from the material structure, therefore the use of x-rays. (Eq.12)

$$h\nu = BE + KE + \Phi_{spec} \qquad \text{(Eq. 12)}$$

where hv is the X-ray source energy, BE is the binding energy of the electron in the electronic state, KE is the kinetic energy with which the electron is expelled by the atom and lastly Φ_{spec} is the work function of the spectrometer.

Specifically, what happens in an XPS machine is that the detector measures the kinetic energy of the exiting electrons and, since initial x-ray photos and work function are known, the binding energy is calculated. This value is fixed for the elements and does not change even when the x-ray source varies, since they are inherent properties of the orbital the electron was in and it would only change the kinetic energy of the exiting electron. (Fig 12a)

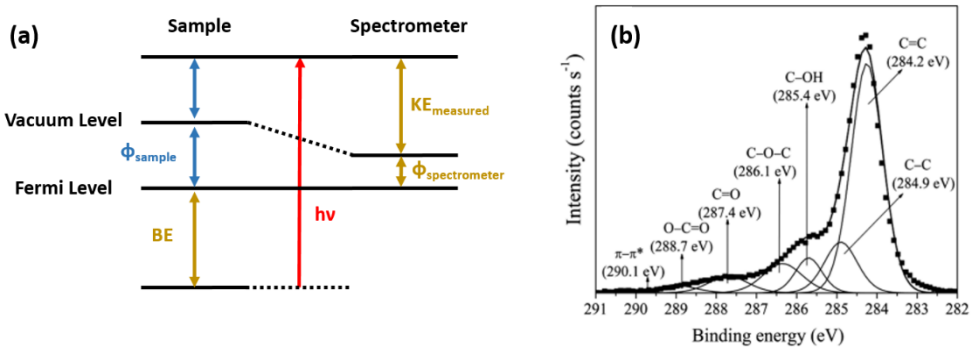

Figure 12. *(a) Energy diagram example of the equation 12, where the different energy compositions are considered. Fig 12b reprinted from Andreia Morais, Joao Paulo C. Alves, Francisco Anderson S. Lima, Monica Lira-Cantu, Ana Flavia Nogueira, Journal of Photonics for Energy, 5, 2015. Copyright 2015. SPIE Digital Library.*[124,168]

Once the binding energy is calculated, information about the surface composition of each element can be extrapolated. In fact, measurements of single element regions can be performed, and corresponding peaks can be studied. (Fig 12b, Carbon as an example) Moreover, it is possible to attribute and discern the different bonds underlying such peak, depending on their position. This can be done by considering the electron negativity and electron density around an atom; the larger the difference in electron negativity between two atoms bonded together, the larger the shift compared to the homo-nuclear bond. For example, in the C 1s region, the peak related to the C-C bond is always seen at 284.9 eV (Fig 12b), while, when there are bonds with other elements or even different kind of hybridization of the carbon, additional peaks will appear and show a shift to different binding energies, forming, in the overall peaks, shoulders. (Fig 12b) Taking oxygen as an example, a shift of 1.5 eV can be seen for single bond and of 3 eV for the case of a double bond.

2.3.2: Electrochemical characterization

Electrochemical characterizations are a very important class of analysis performed on 2D material and essential to determine their performance in specific sectors, such energy storage and electro-catalysis. For this reason, a short overview of some of the most common techniques used and why they are important for the characterization of those materials.

2.3.2.1: Voltametric techniques

Firstly, cyclic voltammetry (**CV**) and, from a certain perspective, linear sweep voltammetry (**LSV**) are the most used techniques to study redox processes. They are voltametric techniques that relies on a constant change of potential during the

measurements. CV's measurements study the redox processes, cycling in between a potential window to study both cathodic and anodic reactions. While the second methodology, LSV, focuses only on one of the two reaction branches, scanning from potential A to potential B, stopping once the final potential is reached. The following explanation applies also for LSV measurements, the explanation will focus on the ins and out of CVs measurements. Using the ferrocene (Fc)/ferrocenium (Fc^+) couple as an example (Fig 13), it is possible to observe peaks throughout the measurements, which vary depending on the species analyzed, and in the case of reversible species, as seen in Fig. 13, two close and well-defined peaks can be seen.

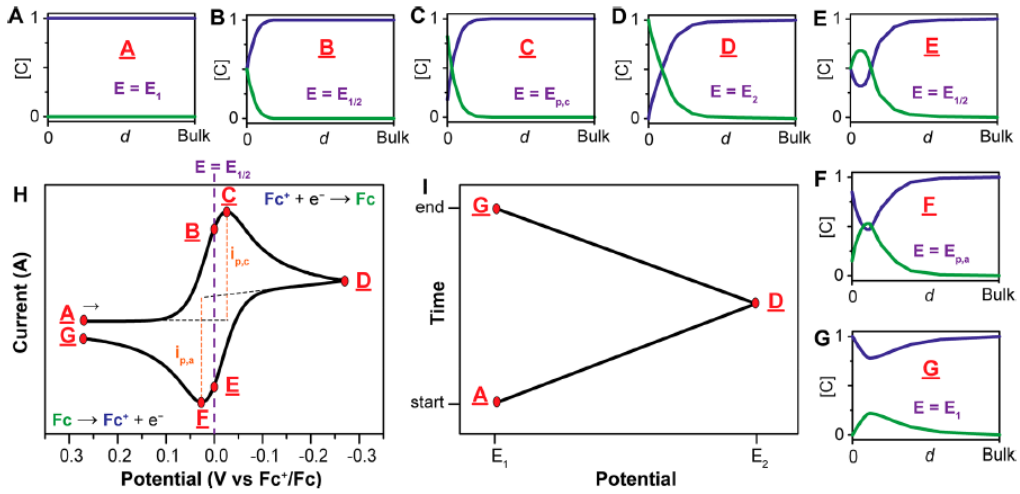

Figure 13. *(a)-(g) Concentration vs distant from the electrode graphs at different point in the cyclic voltammetry analysis (h) and the change in potential against time in the same measurement (I)*[169] *Reprinted with permission and under the scope of Author Choice open access license of ACS Publication from Elgrihi Noemie, J. Chem. Educ., 2018, 95, 2, 197-206, 10.1021/acs.jchemed.7b00361. Copyright 2018 American Chemical Society*[127]

This behavior can be explained and predicted by using the Nernst equation (Eq 13), which allows the understanding of how systems behave, whenever there is a change in species concentration and of potential, similarly to a snapshot performed at specific conditions.

$$E = E^0 - \frac{RT}{zF} \ln Q_r \qquad \text{(Eq. 13)}$$

Where E^0_{cell} is the standard potential for the cell, R is the universal gas costant, T is the temperature in Kelvin, z is the number of electrons exchanged during the reaction, F is the Faraday constant expressed in Coulomb per mole and Q_r is the reaction quotient of the cell reaction, often express, for simplicity sake, as the quotient between the concentration of the two species reacting.

Changing the potential will slowly affect the reaction rate and will progressively consume the reactant species on the electrode surface, gradually increasing the current. This is a kinetic regime, where the current is determined by how quickly the reactant is converted into product. As the potential increases or decreases and the reaction rate increases, the current reaches a peak where the diffusion of the material and its conversion are immediate. Afterward, increasing even further the potential, causes the concentration of reactant species on the electrode surface to decrease, decreasing the current and then forming a plateau afterward, this happens because the reaction rate is larger than the material diffusion to the surface. This is called diffusion regime and is described via the Randles-Sevcik equation (Eq. 14), where the dependence on the diffusion coefficient is expressed. Moreover, the dependence on the scan rate is introduced here and it can be observed that, in general, the current increases with increasing scan rate. This can be counterintuitive. However, the current is the definition of the charges passed per unit of time, and hence the increase via a higher scan rate can be observed. These regimes are of crucial importance to understanding the reaction kinetics and to obtain proper measurements, especially in electro-catalytic applications.

$$i_p = 2.69 * 10^5 * n^{3/2} * A * C * \sqrt{D * v} \qquad \text{(Eq. 14)}$$

Where i_p is the peak current, n is the electron number transferred during the process, A is the electrode area in cm^2, C is the concentration of the active species in mol/L, D is the diffusion coefficient in cm^2/s and v is the scan rate in V/s and the constant value at the beginning comes from a temperature related term and it is solved for a temperature of 25°C.

Varying the scan rate usually leads to an increase in current, according to Eq. 14, however the increase in rate can also provide insight into the reversibility of the reaction itself. (Fig. 14)

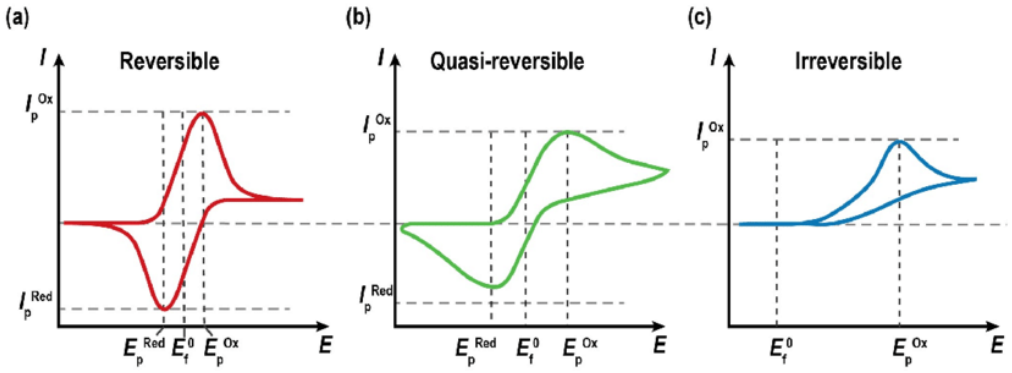

Figure 14. *Depiction of different CV profiles depending on the type of reaction occurring. (a) CV analysis of a reversible redox couple, (b) of a quasi-reversible redox couple and (c) lastly of an irreversible redox couple*[170] *Reprinted with permission and under the scope of open access license of Linköping University from Kosala Wijeratne Linköping University Electronic Press., 2018, p.93, 10.3384/diss.diva-152888. Copyright 2018 Linköping University.*

In fact, increasing the scan rate not only increases the current but can also significantly change the shape of the CV curve depending on the species reacting at the electrode. In fact, in a reversible reaction, the curve shape will remain similar at all rates (Fig. 14a) and the difference between the cathodic and anodic peak will be below 57 mV, value calculated from Eq. 14 considering E= $E_{1/2}$. However, there may be cases where the curves do not have the same shape and instead the two peaks are starting to drift apart from each other. (Fig. 14b) This case is called a semi-reversible reaction, where increasing the scan speed results in a more pronounced shift and separation of the two peaks, while still being

present. The last case, Fig 14c, is when the reaction is irreversible, meaning that after one of the two electrochemical cycles, the return scan will provide no redox peak. This is usually the case when the target species reacted or diffused quickly away from the electrode surface and therefore not being available for further.[169,171,172]

2.3.2.2: Galvanostatic measurements for energy storage devices

Another commonly used technique in electrochemistry and in battery science is Galvanostatic Charge Discharge. (**GCD**) This technique, conversely to LSV and CV, is a galvanostatic technique, meaning that a constant current is applied over time and the potential variation is measured. GCD is widely applied in cycle and capacity characterization of energy storage devices and often provides information on the type of storage mechanism present in the materials, in addition to data on resistance and capacity. (See Chapter 2.4.1) In general, this measurement is quite straightforward, since charges are injected into the material up until a specific voltage, however the shape of the as obtained curve can already provide several information.

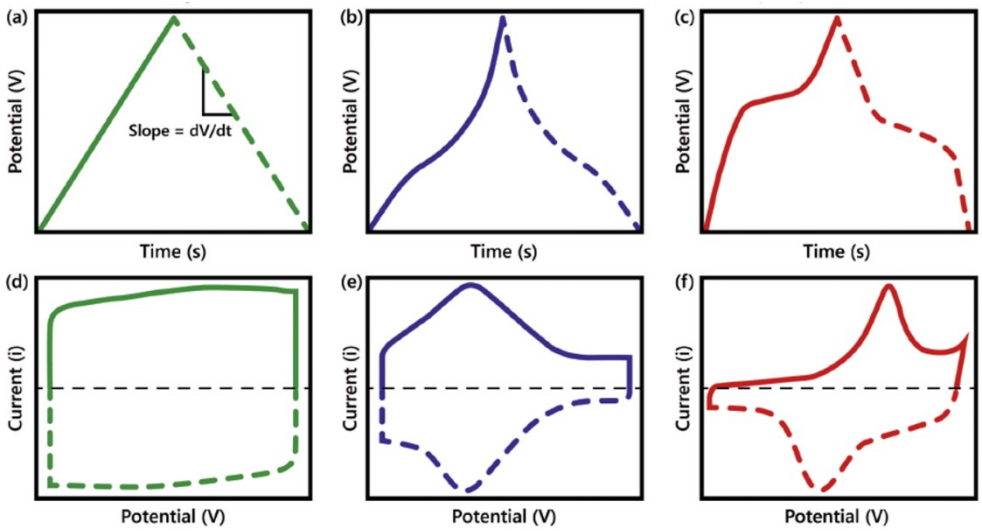

***Figure 15**. (a)(b)(b) GCD curves of electrode materials and (d)(e)(f) their respective CV curves*[173] *Reprinted from Tyler S Mathis, Narendra Kurra, Xuehang Wang, David Pinto, Patrice Simon, Yuri Gogotsi, Adv. Energy Material, 2019, 9, 1902007 with permission from Wiley. Copyright belongs to Wiley, 2019.*

From Fig.15, the GCD curves can suggest what kind of process is taking place. In Fig 15a a linear increase and decrease in voltage is observed, forming a regular triangular shape, and it can connected to the absence of any surface reaction, confirmed by checking the corresponding CV curve (Fig 15d) where no redox peaks are observed, hinting at an electric double layer type of mechanism. (Chapter 2.4.1) In contrast, in Fig. 15b and 15c, the presence of plateaus is observed, which is connected to surface and bulk chemical reactions, as it can also be seen in Fig. 15e and 15f respectively. In the CV analysis, two redox peaks can be seen in both cases, indicating a different charge storage mechanism, however these details will be discussed more in depth in the relative chapter (Chapter 2.4.1).

2.4: Applications: Supercapacitors and Hydrogen Evolution Reaction (HER)

The material studied in this thesis work weere then characterized and used keeping in mind two specific applications. The first one is related to energy storage, specifically in supercapacitors, devices which are in between batteries and capacitors, with present characteristics in between the two. (Fig. 16a) The second one is their use as catalyst for the hydrogen evolution reaction (HER) to produce green hydrogen, exploiting the already known properties of TMDC in such application. In the following Chapter, basic knowledge of supercapacitors energy storage and of electrocatalysis especially for the HER reaction. (Fig 16b)

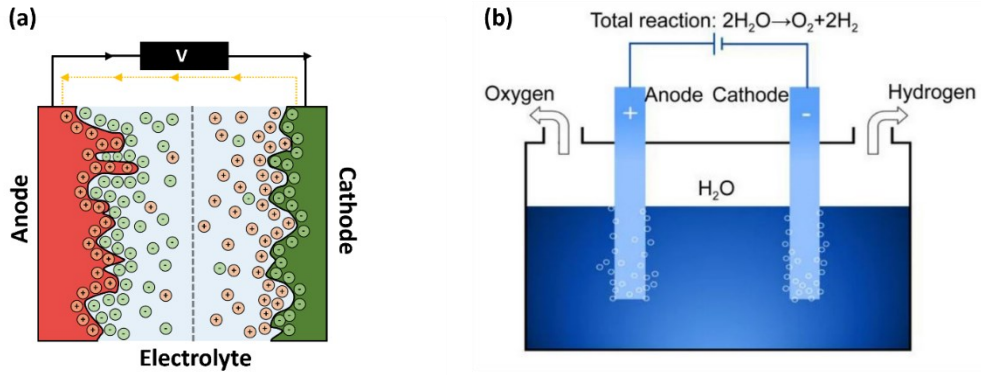

Figure 16. *(a) Scheme of an energy storage device*[174] *and (b) scheme of an electrolyzer*[175] *(b) Reprinted from Zhou, F., Zhou, Y., Liu, GG. et al. Recent advances in nanostructured electrocatalysts for hydrogen evolution reaction. Rare Met.* ***40****, 3375–3405 (2021), https://doi.org/10.1007/s12598-021-01735-y with permission from Springer Nature. Copyright belongs to Springer Nature, 2021.*

2.4.1: Energy storage: Supercapacitors

Supercapacitors (**SCs**) are part of the energy storage devices class and are the middle ground between batteries and capacitors. They borrow characteristics from both technologies and aim to provide the highest possible energy in the shortest amount of time and, thus, their use as supply and backup energy sources is quite useful, even though work needs to be done to achieve energy levels comparable to batteries' one. However, looking more in-depth at how these devices storage charges can help understand the reason for the properties of these devices.

SC devices are composed of two electrodes, a separator and an electrolyte, similar to a battery, but the energy storage mechanism takes place on the surface of the material itself. However, the energy storage mechanism may differ, depending on interactions taking place on the surface. They can be mainly of two types: the first one is based on non-faradic processes where the charges are bound electrostatically to the surface,[10,176,177] while the other process consist of faradic processes, meaning that a surface reaction takes place where an exchange of electrons is involved.[178–181] Since they are both surface processes, the increase in surface area highly influence the capacitance of the material and therefore there has been a lot of focus on improving this aspect of the material, however it has also been reported, in 2005 by Linoam et al.[182,183] that the size of the pores, especially nanopores with size of few nanometers, is important to improve the properties of the supercapacitors and further extend their surface area.

In general, considering their dependence on surface area, supercapacitors can be seen as capacitors themselves and therefore a rough estimation of their capacitance can be calculated by simply using the same formulas used in conventional systems. (Eq. 15)

$$C = \frac{\varepsilon_0 \varepsilon * \mathrm{A}}{d} \qquad \text{(Eq. 15)}$$

Where ε and ε_0 are respectively the electrolyte dielectric constant and the vacuum dielectric constant, A is the surface area of the electrode and d is the distance between the two condenser's plates or electrodes.

This was the initial assumption made by Helmholtz in 1879, where he was considering only a layer of closely packed counter ions balancing the surface charge of the electrode (Fig 17a). His theory was lacking from several points of view, such as neglecting further interaction between ions and solvent molecules, treating charges as point models and the simple assumption behind it, however he was the first one proposing an explanation for interaction of solid-liquid phases. Later on, Gouy-Chapman proposed a theory where ions were not static and could diffuse and move due to thermal motion.[184,185] This means that the charge distribution decreases the further away the distance from the electrode, therefore, allowing for the use of the Boltzmann distribution (Eq. 16) to describe the concentration of ions from the surface to the bulk of the solution. (Fig 17b)

$$n_i = n_i^0 \exp\left(\frac{-z_i e \varphi}{kT}\right) \qquad \text{(Eq.16)}$$

Where n_i^0 is the bulk concentration of the ion, z_i is the charge of the ion, e is the charge of an ionic species, ϕ is the potential, k is the Boltzmann constant, and T is the temperature.

This description was then further integrated by Otto Stern in the so-called Stern model, which is similar to the one used these days.[186–188] The model draws from the two previous theories and considers a thin, closely packed layer of counter ions at the electrode surface, with minimal distance to the surface. This equals their ionic radius itself, therefore considering the size of the ions directly into the model. It also includes a diffusion layer where solvated ions can approach the electrode and be still affected by the charged electrode. (Fig 17c)

Lastly, subsequent scientists further refined Stern's model and addressed the inherent issues the model initially had and gave explanation to other surface effects, such ion adsorption or surface reaction. To this matter, Grahame introduced the definition of "specially adsorbed ions" which includes the previously described ions that, after losing their solvation shell, approach the surface to react with it, giving rise to the pseudo capacitance.[189–191] Moreover, Grahame introduced the current separation in three layer of the Helmholtz-Stern model. The Inner Helmholtz plane (**IHP**), encompassing all the ions in close proximity to the surface with an average distance equal to the average diameter of the ions themselves, which is called Inner Helmholtz layer or simply Stern Layer. Then there is an Outer Helmholtz layer (**OHP**) which encompasses an area where the solvated ion interacts with the surface and aligns around it, whose imaginary border passes thorough the center of the ion at its minimal distance point. Lastly, there is the diffusion layer where solvated ions are free to move around but with low to null interaction with the surface of the electrode. (Fig 17d)

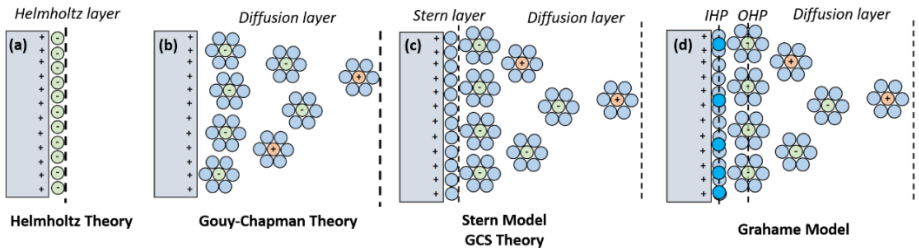

***Figure 17**. Evolution of electric double layer models in the year, starting from (a) the Helmholtz model to (b) the Gouy-Chapan model, (c) the Stern model or GCS (Gouy-Chapman-Stern) theory and lastly (d) the Grahame correction*

The last depiction provides a comprehensive description of the processes taking place on the surface and allows for a distinction between the different sources from which capacitive behavior can arise in supercapacitors. In fact, there are two main types of supercapacitors, as mentioned before, based on faradic processes, pseudo capacitive SCs, and on non-faradic processes, namely so called ELDC. The first process is typical of metal oxides and conductive polymer, where a surface redox reaction takes place, while the second is more common in carbonaceous

species, with graphene and nanotubes as examples, where charges are simply oriented like in a capacitor. There have also been reports, where each electrode focuses on one of the two storage mechanisms in a so called asymmetric geometry, and sometimes using directly a typical battery electrode, instead of pseudo capacitive, called a “capattery” or a “super battery”, merging together properties of both worlds to achieve even further enhanced performances.

Regardless of the storage mechanism in supercapacitor, the formula to calculate the specific capacitance is the same, derived from the classic capacitance formula, which is function of the charges and potential applied.[10,173,181] (Eq. 17)

$$C_s = \frac{\Delta Q}{\Delta V * m} = I \int_0^t 1/V(t)dt \qquad \text{(Eq. 17)}$$

Where I is the current density used in galvanostatic measurement, 1/V(t) is the potential variation in function of time and the time is generally considered from the beginning of the measurement to the end. The charges are calculated via GCD graph, examples in Fig. 14, and the Eq. 17 is a general way to consider and calculate capacitance values, not depending on the shape of the measurement. However, in the case of an ideal supercapacitor (perfectly triangular shape) or with a quasi-triangular shape, a simpler formula can be used to calculate the specific capacitance. (Eq. 18)

$$C_S = \frac{I * t_{dis}}{\Delta V} \qquad \text{(Eq. 18)}$$

Where I is the current density used during the measurement, t_{dis} is the discharge time of the curve and ΔV is the potential window used in the same measurement. This is a very commonly used formula even for not ideal supercapacitor, which can lead to overestimation of the capacitance, therefore Eq. 15 is suggest being used in that case.

Once the capacitance values are obtained, it is possible to calculate both energy (Eq. 19) and power (Eq. 20) from which a Ragone plot can be built. (Fig 20) This calculation must be performed using two-electrode measurements, since the Ragone plot is often used to compare the characteristic and performances of devices with each other, even though it is possible to calculate this value for a bare electrode, comparing then material with one another.

$$E_g = \frac{1}{M}\int_0^{id} iVdt = \frac{C_s * V^2}{2} \qquad \text{(Eq 19)}$$

$$P_g = \frac{E_g}{t_d} \qquad \text{(Eq. 20)}$$

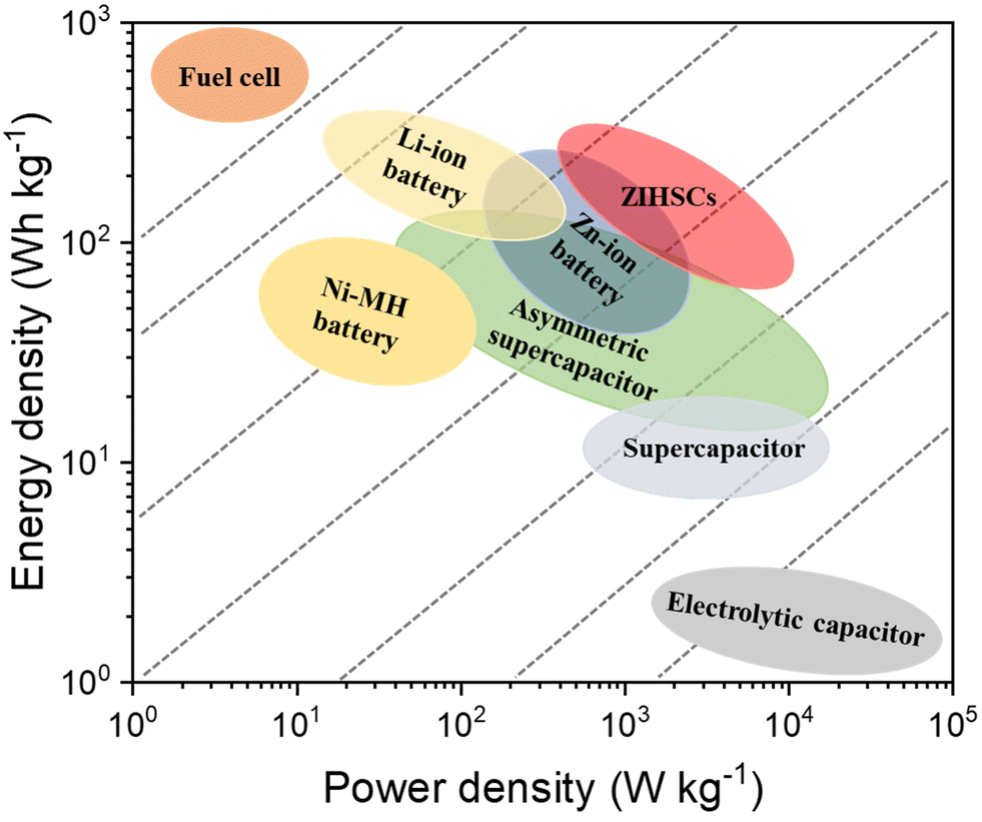

Figure 18. *Ragone plot with highlight of the typical power and energy densities values for class of energy storage devices*[192,193]

2.4.2: Electro catalysis: Hydrogen Evolution Reaction (HER)

Hydrogen is a very important material for the energy transition, because of its low impact on the ecosystem when burnt and its energy density. However, it is an energy vector, meaning that it can only transport energy from one place to another. Therefore, it must be produced by some external process in one place to be transported and used somewhere else as combustible to be of use. The most common methodology used to produce hydrogen, currently, is the steam reforming procedure, but this process consumes fossil fuels to produce the desired product but also large quantities of CO_2. Consequently, a green, efficient, and renewable way to produce hydrogen must be found. Among the most promising options, water electrolysis is the most appealing due to its ability to produce H_2 from a very common source and because it is also the combustion product of the energy vector, therefore closing the loop. Although particular attention must be paid to the energy used for this reactions, since using nonrenewable sources would not reduce the effective environmental impact of such process.[194–196]

Water electrolysis is composed of two reaction: hydrogen reduction (Eq. 21, Eq. 22) and water oxidation to oxygen (Eq. 23, Eq. 24), however in this section, only the hydrogen evolution reaction (**HER**) part will be focus on.[197–199]

HER (Acidic): $2H^+ + 2e^- \longrightarrow H_2$ (Eq. 21)

HER (Basic / Neutral): $4H_2O + 4e^- \longrightarrow 2H_2 + 4OH^-$ (Eq. 22)

OER (Acidic / Neutral): $2H_2O \longrightarrow 4e^- + 4H^+ + O_2$ (Eq. 23)

OER (Basic): $4OH^- \longrightarrow \ O_2 + 2H_2O + 4e^-$ (Eq. 24)

Looking at the basics of the HER, the reaction is a multi-step process catalyzed reaction where two electrons are exchanged. It is composed of two main steps: 1) the adsorption of H^+ or H_2O on the surface (depending on the solvent pH), called Volmer step (Fig 19, Eq. 25), and 2) the desorption of the final H_2 molecule via chemical (Tafel step, Fig 19, Eq. 26) or electrochemical (Heyrovsky, Fig. 19, Eq. 27) step.[200–203]

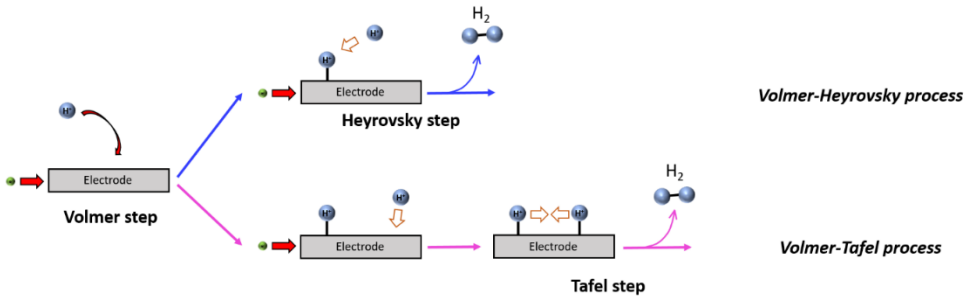

Figure 19. *Scheme of Hydrogen Evolution reaction with highlight on the possible rds steps and possible mechanism routes*

$$H^+ + e^- \longrightarrow H^* \quad \textbf{Volmer step} \qquad \text{(Eq. 25)}$$

$$H^* + H^+ + e^- \longrightarrow H_2 \quad \textbf{Tafel step} \qquad \text{(Eq. 26)}$$

$$2H^* \longrightarrow H_2 \quad \textbf{Heyrovsky step} \qquad \text{(Eq. 27)}$$

Each one of these steps can be the rate-determining and it depends greatly on the catalyst used, since the reaction must use a catalyst to overcome the kinetic barrier to start producing molecular hydrogen without reaching extreme condition. Finding the ideal catalyst is challenging, because it involves solving performances issues, but also durability and costs, therefore it is usually a very complicated task to do. However, Volcano plots,[204,205] constructing keeping in mind the Sabatier principles and DFT calculations, are a way to have an idea of the performances of

some specific metals for the reaction, where basically the best catalyst is the one that bind H^+ strong enough to avoid adsorption problems and not too strong to avoid poisoning of the material. (Fig 20)

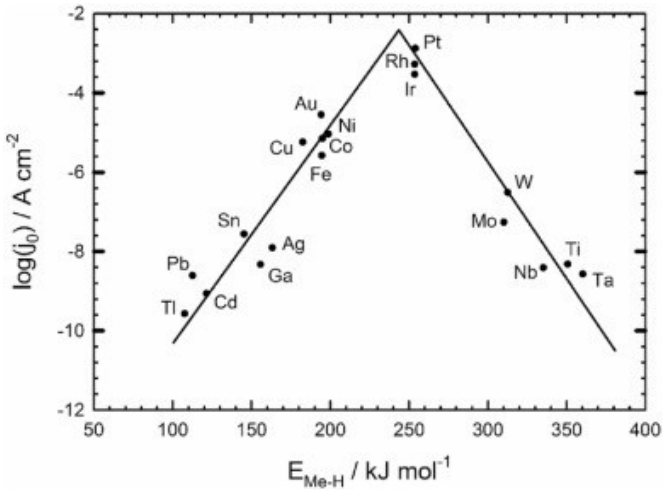

Figure 20. *Volcano plot for HER reactio0.n*[205] *Reprinted from Sara M. Stratton, Shengjie Zhang, Matthew M Montemore, Surface Science Report, 78, 2023, 3 with permission from Elsevier. Copyright belongs to Elsevier, 2023*

As expected, noble metals are in the optimum range for HER reaction and Pt/C is considered the benchmark catalyst for such a reaction with very low over potential and Tafel slopes below 40 mV/dec. However, considering the growing need of energy, even with a low loading of Pt on a support, the need and the cost for such material will increase even further, thus reducing the appeal for noble metals, due to their inherent high cost. Other transition metal are then the key to sustain an increasing interest and need in hydrogen production and among this catalyst such TMDC[76,206–209], metal borides[143], and other metals[210], but also mixtures of catalyst such as Ni-Fe[211], Ni/NiO[212,213], Ni/g-C_3N_4[214] and others.[203,215,216]

Chapter 3: Publications

In the following paragraphs, the publications on which this thesis work is based are reported. *Main author* and *shared authorship works* are the ones contributing to the dissertation, but also *co-author works* show the application, and further collaboration underwent during the doctoral period. Each publication is introduced by a short context section, describing, and expanding on the work conducted as author during the publication period. Moreover, the specific contribution I performed are highlighted to clearly differentiate my work from the co-authors' one. Below a concise summary and description of each type of publication and the general contribution for such literature work is provided, to avoid repetition throughout the short introductions.

Main Authorship:

A main authorship work encompasses and organizes work done by the candidate over several months or years. The candidate is primarily responsible for a large amount of the experimental, interpretation and writing work. Results are discussed on a regular basis with the author co-authors, especially Prof. Teresa Gatti. Manuscript drafts are mostly written and produced by the main author, with continuous feedback and correction from the co-authors, unless otherwise stated in the description part.

Shared Authorship:

A shared authorship work involves cooperative work done by two or more authors that contributed equally to one or several areas of the work, such experimental data gathering, data interpretation and manuscript preparation. This type of work proofs a strong communication between the different main authors and a continuous discussion between them and the different co-authors, in order to

further elevate the quality of the work. Manuscript drafts are prepared according to deliverables set by each of the main co-authors and are then corrected and processed via continuous feedback between them and all co-authors.

Co-Authorship:

A co-authorship work pertains to the publication done by another author, where the candidate has performed one or more task that helped further improve the quality of the research. Such tasks can vary from experimental ones to draft reviewing or writing ones. The main author takes the lead in manuscript writing and the co-author provides targeted contributions, suggestions or reviewing a specific section of the work to refine and elevate the final publication.

3.1: Publication's list:

Publication n°1:

Main Authorship.

Crisci M., Dolcet P., Yang J., Salerno M., Belteky P., Kukovecz A., Lamberti F., Agnoli S., Osella S., Gross S., Gatti T. "Design Principles and Insights into the Liquid Phase Exfoliation of Alpha MoO_3 for the Production of Colloidal 2D Nano Inks in green Solvents", *Journal of Physical Chemistry C*, **2022**, *126*, 404-415

Publication n°2:

Main Authorship.

Crisci M., Boll F., Merola L., Johannes Pflug J., Liu Z., Gallego J., Lamberti F., Gatti T. "Nanostructure 2D WS_2@PANI nanohybrids for electrochemical energy storage", *Frontiers in Chemistry*, **2022**, DOI: 10.3389/fchem.2022.1000910. (Gold Open Access)

Publication n°3:

Main Authorship.

Crisci M., Felix B., Domenici S., Gallego J., Smarsly B., Lamberti F., Wang M., Rubino A., Gatti T. "Easy direct Functionalization of 2D MoS_2 applied in Covalent Hybrids with PANI as dual blend Super-capacitive Materials", **2024**, *under revision.*

Publication n°4:

Shared Authorship.

Pozzati M., Boll F., **Crisci M.**, Domenici S., Smarsly B., Gatti T., Wang M. "Systematic Investigation on the Surfactant-Assisted Liquid-Phase Exfoliation of

MoS_2 and WS_2 in Water for Sustainabl 2D Material Inks", *Physical Status Solidi RLL*, **2024.** DOI: 10.1002/pssr.202400039

Publication n°5:

Co-Authorship.

Wang M., Osella S., Torre B., **Crisci M.**, Schmitz F., Altieri R., Di Fabrizio E., Amenitsch H., Sartori B., Liu Z., Gatti T., Lamberti F. "Stabilizing Layered BiOBr Photoelectrocatalyst by Van der Waals Heterojunction Strategy," *ChemCatChem*, **2024**, *e202400282*

Publication n°6:

Co-Authorship.

Domenici S., Micheli S., **Crisci M.**, Rohnke M., Hergert H., Allione M., Wang M., Smarsly B., Klar J. P., Lamberti F., Cimetta E., Ceseracciu L., Gatti T. "Hybrid piezoresistive 2D MoS_2/PEGDA/PANI covalent hydrogels for the sensing of low-to-medium pressure", *Small Structures*, **2024**, DOI: 10.1002/sstr.202400131. (Gold Open Access).

Publication n°7:

Co-Authorship.

Pozzati M., Boll F., **Crisci M.**, Domenici S., Scotognella F., Smarsly B., Gatti T., Wang M. "Water-Based Bi_2S_3 Nano Inks obtained with Surfactant-assisted Liquid Phase Exfoliation and their direct processing into Thin Films", *Colloids and Interfaces*, **2024**, *8*, 28-40 (Gold Open Access).

Publication n°8:

Co-Authorship.

Wang M., Langer M., Altieri R., **Crisci M.**, Osella S., Gatti T. "Two-dimensional layered Heterojunction for Photo-electrocatalysis," *ACS Nano*, **2024**, *18*, 9245-9284

Publication n°9:

Co-Authorship.

Wang M., **Crisci M.**, Pavan M., Liu Z., Gallego J., Gatti T. "New Insights into the Surfactant-Assisted Liquid Phase Exfoliation of Bi_2S_3 for Electrocatalytic Applications", *Catalysts*, **2023**, *13*, 551-563 (Gold Open Access).

Publication n°10:

Co-Authorship.

Wang M., Osella S., Brescia R., Liu Z., Gallego J., Cattelan M., **Crisci M.**, Agnoli S., Gatti T. "2D MoS_2/BiOBr van der Waals heterojunction by liquid phase exfoliation as photo-electrocatalysts for hydrogen evolution", *Nanoscale*, **2023**, *15*, 522-531

Publication n°11:

Co-Authorship.

F. Boll, M. Fadda, M. Happel, M. Crisci, A. Athanassiou, B. Smarsly, F. Bella, F. Lamberti, G. Perotto, **T. Gatti* "**Multicomponent synergistic contribution in nano-engineered nano-fibers for flexible energy storage," *ACS Appl. Energy Mater.*, **2024**. 7, 4733

Publication n°12:

Co-Authorship.

F. Boll, **M. Crisci**, L. Merola, F. Lamberti, B. Smarsly, T. Gatti. **"**Assessing the effect of stabilization and carbonization temperatures on electrochemical performance of electro-spun carbon nanofibers*," Adv. Energy Sustain. Res.,* **2023** 4, DOI: 10.1002/aesr.202300121. (Gold Open Access).

3.1.1: Conference contribution

Poster Presentation n°1:

"Liquid exfoliation of hydrothermally synthesized MoO_3 meso-structures in low toxicity solvents for the production of green 2D materials inks"

Crisci M., Dolcet P., Belteky P., Kukovecz A., Lamberti F., Gross S., Gatti T.

Chem2DMat, **2021**, Online conference

Poster Presentation n°2

"2D transition metal dichalcogenide-conductive polymer hydrogel for flexible energy storage devices"

Crisci M., Boll F., Pflug J., Merola L., Gatti T.

Graphene2022, **2022**, Aachen (Germany)

Oral Presentation n°1:

"2D transition metal dichalcogenide-conductive polymer hydrogel for flexible energy storage"

Crisci M., Boll F., Pflug J., Merola L., Gatti T.

EMRS, **2022**, Varsaw (Poland)

Oral Presentation n°2:

"Electroactive 2D TMDC based polymer hybrid and hydrogel"

Crisci M., Domenici S., Pflug J., Boll F., Gatti T.

MatSUS, **2023**, Valencia (Spain)

Oral Presentation n°3:

"Electroactive 2D TMDC based polymer hybrid and hydrogel"

Crisci M., Domenici S., Pflug J., Boll F., Gatti T.

MRS, **2023**, San Francisco (USA)

3.2: Publication n°1

Design Principles and Insights into the Liquid Phase Exfoliation of Alpha MoO_3 for the Production of Colloidal 2D Nano Inks in green Solvents

Authors: **Crisci M.**, Dolcet P., Yang J., Salerno M., Belteky P., Kukovecz A., Lamberti F., Agnoli S., Osella S., Gross S., Gatti T.

Before this publication, extensive work on the exfoliation of graphene and other initial 2D materials was performed[136,217–219], while the use of MoO_3 as possible candidate for such application was still investigated. In general, the LPE, the usual technique used for ink production, has several parameters to consider to obtain a concentrated and stable colloidal ink. The number of parameters makes this easy technique, complicated to properly optimize. Among these solvents are one of the major to take into account and already several researcher reported work on this matter: *Hanlon D. et al.*[146] have studied the exfoliation of MoO_3 in high boiling point solvents, such as NMP, DMSO and DMF, using shear exfoliation, proving that the aforementioned solvents give the best results both in term of concentration and 2D material thickness, confirming the thread seen also for other 2D materials. However, the use of high boiling, expensive and potentially dangerous solvents, is a big detriment for actual application of the material, therefore the quest to successfully obtain high concentration inks using more environmentally friendly solvents continued. *Ji F.* et al.[220] proposed and tested more commonly available solvents, such as ethanol and isopropyl alcohol, using also a pre-grinding step to improve the yield, while also *Datta R.S. et al.*[221], *Etman A.S. et al.*[222] and *Sricharan M. et al.*[223] reported use of low boiling point solvents to exfoliate such material, with different degree of success.

With these considerations, **publication n°1** needs to be seen as a continuation on this research thread, focused on obtained high yield and small MoO_3 flakes using

green and sustainable solvent and studying the effect of different exfoliation instruments. α-MoO_3 was synthesized using a straightforward hydrothermal procedure already reported in literature[224], and it was used to produce 2D materials inks, where solvents were changed (water, acetone, 2-butanone, water/isopropanol mixture) and the exfoliation instrument. The solvents used in these work were decided following the Hansen Solubility Parameter theory (HSP) to try the efficacy of using such theoretical background to predict potential solvent for the exfoliation of 2D material, as reported in some literature work.[143,145,225] The inks' sheet size and stability was characterized via DLS and Zeta Potential measurements, however it must be pointed out that DLS, as techniques itself, is precise only for spherical particles, therefore the use of such methodology is a rough estimation of what can be observed with further specific characterization. Optical properties were evaluated via UV-Vis analysis, while the morphology was studied via TEM and SEM images and confronted with the previously used DLS measurements. Lastly, the powder obtained from the inks were further characterized via Raman spectroscopy, XRD, SAED, AFM and XAS, specifically EXAFS and XANES using the synchrotron irradiation at SOLEIL. These last measurements helped shine light on the atom position and local environment of the Mo atoms and their level of distortion and bond length before and after exfoliation. Lastly, DFT calculations were used to gain deeper insights on the exfoliation final effect on the material and the results were compared with the one of the materials obtained beforehand, to find matches between theory and experimental work.

In general, the aim of this work was to use a mixture of theoretical and experimental approaches to gain deep insight on the exfoliation process and structural changes of 2D α-MoO_3, using more commonly available and standard for 2D materials characterization, while also exploring different approaches to gain deeper insight in the exfoliation process and therefore leading the way in the use of such techniques for the characterization of 2D materials.

My role in the whole process is the one described beforehand in the *Main Authorship* section, but more specifically experimental work and most of the characterization were performed by the candidate, comprehensive as well of the XAS data, which were, however, further analyzed by one the co-author *Dolcet Paolo.*

THE JOURNAL OF PHYSICAL CHEMISTRY C
A JOURNAL OF THE AMERICAN CHEMICAL SOCIETY

pubs.acs.org/JPCC Article

Design Principles and Insights into the Liquid-Phase Exfoliation of Alpha-MoO_3 for the Production of Colloidal 2D Nano-inks in Green Solvents

Matteo Crisci, Paolo Dolcet, Jijin Yang, Marco Salerno, Péter Bélteky, Ákos Kukovecz, Francesco Lamberti, Stefano Agnoli, Silvio Osella,* Silvia Gross,* and Teresa Gatti*

Cite This: *J. Phys. Chem. C* 2022, 126, 404−415 Read Online

ACCESS | Metrics & More | Article Recommendations | Supporting Information

ABSTRACT: The interest in layered 2D nanomaterials has witnessed an impressive growth in the last years, bringing to the discovery of many new species and methods for their preparation. The liquid-phase exfoliation (LPE) of crystalline bulk powders is certainly the most suitable method for scaled-up production, allowing also the convenient access to solution processing techniques for the direct utilization of the produced 2D material colloidal inks. Given the large number of reports on LPE processes for different 2D materials, today, it is necessary to specifically define the results of similar investigations, so as to provide the scientific community with clear guidelines for identifying design rules and applying standardized procedures. In this work, we present a systematic study on the LPE process for α-MoO_3, a stable high band gap semiconductor, which in its 2D form has been employed for many purposes, ranging from catalysis to energy/optoelectronic devices and sensing. We investigate the effect of different low-toxicity solvents and instruments for its LPE and provide new insights into the structural and electronic properties of the resulting 2D nano-inks in a joint experimental−computational effort, which will represent a solid source of information for the future implementation of liquid-dispersed layered α-MoO_3 nanosheets in different fields.

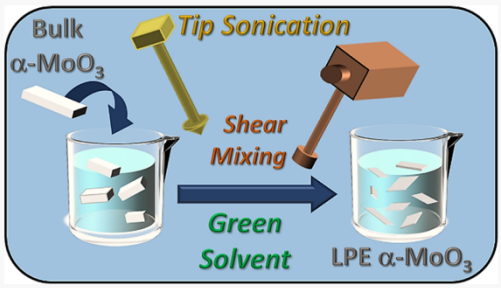

1. INTRODUCTION

In the past years, many research efforts have been directed toward the identification of species that can be used in substitution of the so-called critical raw materials for different vital applications, with the aim of preventing a global supply crisis driven by the progressive increasing demand of technological items.[1] In this context, metal oxide semiconductors emerge as a valuable platform to obtain new substitute materials, considering their chemical stability and ease of tunability in functional properties, achievable through different methods, ranging from doping to dimensional variation from the bulk to the diversified nanoforms.[1]

Molybdenum trioxide (MoO_3) emerges as a suitable candidate for this role: Mo is indeed a non-critical raw material, and its oxide is an interesting semiconductor, characterized by a high band gap, high work function, and notable environmental stability.[2−7] This material attracts interest for a very wide range of applications: there are numerous reports on its use for electro-, thermo-, and photochromism,[8−11] catalysis,[12,13] Li-ion batteries[14,15] and solar cells,[16,17] demonstrating its versatility in different functions.

MoO_3 can display three main crystalline phases, namely, the highly stable α- and *h*-phases and the metastable β-phase. In these phases, MoO_6 octahedra are always present as basic structural units, but they differ in their relative connectivity. In the α-one, the MoO_6 octahedra organize in order to form an orthorhombic cell that results from the overlap of different MoO_3 layers, where they are connected by sharing oxygen corners, while these layers are held together by van der Waals forces. The β-phase is a metastable monoclinic phase that resembles the structure of ReO_3, while the *h*-phase has a hexagonal structure where the octahedra are connected *via* corner sharing oxygen atoms that form long linear chains.[18,19] The α-phase is the most investigated one due to its layered structured, which makes α-MoO_3 similar to other layered materials, such as the transition metal dichalcogenides

Received: October 25, 2021
Revised: December 17, 2021
Published: December 29, 2021

https://doi.org/10.1021/acs.jpcc.1c09221
J. Phys. Chem. C 2022, 126, 404−415

(TMDs) MoS_2 and WS_2 and the corresponding selenides and tellurides,[20] making it suitable for exfoliation processes leading to the formation of the corresponding material in a two-dimensional (2D) form. 2D MoO_3 is an emerging 2D material, together with other 2D metal oxides, investigated for similar purposes as the three-dimensional (3D) counterpart, but offering more promising perspectives in terms of high surface to volume ratio, which favors interfacial exchanges with charges or molecules, adsorbates, and other nanomaterials.[21−24]

The liquid-phase exfoliation (LPE) is a particularly convenient top-down process for the production of 2D materials as colloidal inks, suitable for subsequent direct utilization or processing, which can be carried out through shear mixing (SM) or tip sonication (TS) in a liquid-dispersed phase.[25−29] Several liquid media can be employed for this purpose, the most effective generally being organic high boiling point solvents, such as *N*-methylpyrrolidone (NMP),[30,31] or dimethylformamide[32,33] and dimethyl sulfoxide,[34,35] which have all led to 2D material inks with very high concentration, but that hold considerable drawbacks related to the difficulties in removing them during processing and to the toxicity and high cost issues.[36,37] For this reason, research aiming at resorting to non-toxic solvents during LPE,[38] such as water[39−42] or alcohols,[43,44] is progressively attracting increasing interest from the scientific community. However, these green solvents, when used as the sole dispersants, have some limitations connected to the relatively low concentration in final 2D materials that they allow to reach, being often necessary to resort to the assistance of surfactants to improve their stability,[36] which can then compromise the electronic properties of solution-processed thin films through their insulating effect.

In this work, we present a systematic investigation on the LPE of α-MoO_3 crystalline powder in a series of green solvents characterized by relatively low boiling points without the help of any dispersant, allowing us to define the best media to produce good quality 2D α-MoO_3 nano-inks. We also compare the effect of resorting to SM or TS as exfoliating instruments and of protracting the process for different times while looking in detail at the physicochemical and morphological properties of the resulting colloids. Advanced structural analysis achieved by resorting to X-ray absorption spectroscopy (XAS) provides new insights into the structure of α-MoO_3 2D nanosheets, which have been never reported before, to the best of our knowledge. These data, combined with density functional theory (DFT) investigations, allow us to shed new light onto the properties of this emerging 2D semiconductor,[45] which might serve as guidelines for its future implementation in energy-related or optoelectronic devices as well as for its use in sensing and catalysis.

2. MATERIALS AND METHODS

All chemicals were purchased from Sigma-Aldrich and used without any further purification. α-MoO_3 was synthesized using an already reported procedure developed by some of us.[46] Technical grade isopropanol (IPA) was used for LPE. UV−visible (UV−vis) absorption spectra of the colloidal inks were recorded on a Goebel Uvikon spectrometer using a quartz cuvette of 1 cm optical length. Raman spectra were recorded on a Bruker Senterra instrument using a 514 nm laser excitation source. The samples were prepared by drop-casting the suspensions over a silicon slide and then analyzed. Zeta potential (ZP) was measured on a Malvern Zetasizer Nano-ZS device. The samples were measured in Rotilabo precision glass cuvettes with a light path of 10 mm and a volume of 3.5 mL. High-resolution transmission electron microscopy (HR-TEM) images and selective area electron diffraction (SAED) patterns were acquired on a FEI Tecnai G2 20 X Twin TEM operating at 200 kV. Powder X-ray diffraction (P-XRD) analysis was performed at ambient temperature with a PANalytical B.V. X'Pert PRO diffractometer employing Cu Kα1 radiation. The instrument operated at 40 kV and 40 mA using a 1° divergence slit for the incident beam. Atomic force microscopy (AFM) and Kelvin probe force microscopy (KPFM) were both carried out on an MFP-3D atomic force microscope by Asylum Research-Oxford Instruments, using NCHV probes, of highly doped (0.01−0.025 Ω cm) n-type (An-doped) silicon, with a nominal cantilever resonance frequency of 320 kHz and a tip apex radius of curvature 8 nm, operated in the Nap (i.e., double-pass) mode at a typical elevation height of 50 nm. X-ray photoelectron spectroscopy (XPS) measurements were performed in a custom-designed ultra-high vacuum chamber, working at a base pressure of 10^{-9} mbar, equipped with a non-monochromatized dual-anode DAR 400 X-ray source, a 5-channeltrons, and an Omicron EA 125 electron analyzer. The XPS data were collected at room temperature with an Al Kα line (1486.7 eV) using 0.1 energy steps, 0.5 s dwell time, and 20 eV pass energy. The calibration was based on the binding energy (B.E.) of the Au4f7/2 line at 83.9 eV with respect to the Fermi level. The standard deviation for the B.E. values was 0.15 eV. The reported B.E. was corrected for the B.E. charging effects, assigning the B.E. value of 284.6 eV to the C 1s line of carbon. XAS spectra were collected at the SAMBA beamline of the SOLEIL synchrotron facility (Gif-sur-Yvette, France). Data were collected at the Mo K-edge using a Si(220) crystal monochromator for energy selection (energy resolution ca. 6×10^{-15}). Powdered samples were pressed into pellets, using cellulose as a binder, and measured in the transmission mode, using Oxford ionization chambers as detectors. The samples in liquid suspension were recorded in the fluorescence mode, exploiting a 35-elements Ge detector.

2.1. LPE of α-MoO_3 Powder. To produce the bulk α-MoO_3 suspension in a liquid environment, 1 g of the powder material was dispersed in 100 mL of the chosen solvent (water, IPA/water 6:4 v/v, acetone, and 2-butanone). Then, the resulting slurry was pre-sonicated for 30 min in a bath sonicator (Elma, Elmaosonic P) in order to disperse completely the material. This was then followed by LPE *via* SM (on an IKA T 25 digital Ultra-Turrax instrument), operating at 8000 rpm or *via* tip TS (on a Bandelin Sonopuls HD2200 instrument) operated at 80% power using pulses of 3 s on/3 s off. Both operations were carried out for three different times (2, 4, and 8 h). Once the LPE process was completed, liquid cascade centrifugation was applied to separate the different species in suspension based on relative size and thickness, so as to isolate a final colloid containing the most exfoliated fraction. The resulting suspension was thus centrifuged first at 1500 rpm (210 rcf) for 1 h, and then the supernatant was carefully removed and centrifuged again at 3000 rpm (837 rcf) for 1 h. This final supernatant was recovered as the target colloidal ink and used for characterizations. The concentration of these final inks was calculated by either drying 10 mL of the suspension in a previously weighed Petri dish and calculating the difference in weight or filtering 5 mL of the suspension through a previously weighed

https://doi.org/10.1021/acs.jpcc.1c09221
J. Phys. Chem. C 2022, 126, 404−415

PTFE filter and calculating the difference in weight after drying the filter in a vacuum oven at 40 °C overnight.

2.2. Computational Analysis of Bulk and 2D α-MoO_3. The α-MoO_3 3D orthorhombic crystal structure was considered as the input structure for *ab initio* calculations carried out at the DFT periodic protocol within the PWscf package of the Quantum Espresso 5.1 program.[47] Geometry optimization was performed with scalar relativistic pseudopotentials,[48] with the PBEsol functional,[49] together with a wave function and a density cutoff of 50 and 400 Ry, respectively. A 18 × 6 × 18 *k*-sampling was considered for the analysis of the first Brillouin zone, and band structures, density of states (DOS), and work function shift were analyzed. From the optimized 3D α-MoO_3 structure, a 2D slab has been extracted, and the geometry was optimized at the same level of theory with now a 18 × 1 × 18 *k*-sampling (the *y*-axis has been considered as the direction normal to the plane of the slab).

For the *ab initio* X-ray absorption near edge structure (XANES) calculations, the parallel version of the FDMNES package was used.[50,51] The FDMNES code features the real-space monoelectronic calculations. The final state was calculated using the finite different method (FDM) of the FDMNES code; this method is a full potential one and introduces no approximation on the shape of the potential. The XANES contributions of the Mo sites were calculated using a cluster radius of 7 Å. A convolution procedure was applied to the calculated spectra to account for the core hole lifetime and multi-electron excitations.

3. RESULTS AND DISCUSSION

In previous works, different conditions for the LPE of α-MoO_3 were reported, employing different solvents such as NMP,[52] various alcohols,[14,53] and water/surfactant mixtures.[54,55] It is possible to predict the LPE suitability of a solvent by resorting to several models, such as by considering the surface tension compatibility and the Hildebrand parameters.[56] However, the mostly used and reliable way is to apply the Hansen solubility parameter (HSP) theory, commonly employed in polymer chemistry to predict the solubility, but demonstrated to work well also for LPE 2D materials.[56−59] The HSP theory states that the smaller is the interaction radius between the material and the solvent, the better will be the stability (eq 1)[60]

$$R_a = \sqrt{4(\delta_{d2} - \delta_{d1}) + (\delta_{p2} - \delta_{p1}) + (\delta_{h2} - \delta_{h1})} \quad (1)$$

where δ_{d2} is the dispersive component for the material chosen, δ_{d1} is the dispersive component for the solvent, δ_{p2} and δ_{p1} are the polar components for the material and the solvent, respectively, and δ_{h2} and δ_{h1} are the hydrogen bonding contribution of the two.

Therefore, in order to minimize the R_a value and then increase the compatibility between a solvent and a material, the dispersive, polar, and hydrogen bonding parameters have to be as close as possible to each other. Based on this theory, in this work, a pre-screening of different solvents was performed to ascertain the relative α-MoO_3 compatibility and determine which solvent should perform better. Among the examined solvents, water, a mixture of IPA and water, acetone and butanone were selected. The first one was chosen mainly for its absence of toxicity and to test the possibility to exfoliate α-MoO_3 directly in water without the use of any surfactant, while the other ones were chosen because of low R_a ratio, with 2-butanone being the most promising one (see Table 1 for a summary of the HSPs for the here investigated solvents and for α-MoO_3, as well as the calculated R_a values).

Table 1. HSPs for the Different Solvents Used in This Work and for α-MoO_3 and Relative R_a Calculated between Each Solvent and the Oxide Employing eq 1

solvent/material	δ_p	δ_d	δ_h	R_a
H_2O	18.1	17.1	16.9	13.8
IPA/H_2O (6:4 v/v)	16.7	10.5	16.6	10.6
2-butanone	16	9	5.1	4.0
acetone	15.5	10.4	7	5.2
α-MoO_3	17.8	8	6.5	

In addition to varying the liquid medium, the type of instrument (either SM or TS) and the exfoliation time (2, 4, 8 h) were also tuned to perform a systematic study and identify the optimal conditions for the LPE of α-MoO_3. Figure 1 summarizes the overall process and different conditions applied: powder bulk α-MoO_3 produced via hydrothermal synthesis[46] dispersed in the selected liquid media undergoes LPE in the different established conditions, and the final mixture after exfoliation is subjected to multiple steps of liquid cascade centrifugation at an increasing speed to selectively precipitate the non-exfoliated products (pellets) before obtaining a final colloidal ink of the most exfoliated α-MoO_3 material, used for further characterizations (see the experimental details of this process in the Materials and Methods section).

Table 2 summarizes the different data obtained for the various prepared LPE inks. By first looking only at the final colloid concentrations, it is possible to highlight different trends in relation to the instrument and solvent employed. For the samples exfoliated in water, shorter LPE times resulted to be more suitable in yielding higher concentration inks. For the ketones (acetone and 2-butanone) instead, the final ink concentrations increase with the LPE time for almost all samples; however, this concentration is always lower compared to that obtained for the water exfoliated sample (for certain samples in 2-butanone, the concentration was too low to be effectively measured by weighing the dried residue). These values should be compared to other literature data: Hanlon et al.[52] reported an optimal yield of 0.17 mg/mL for LPE α-MoO_3 in pure IPA, while Dutta et al.[53] reported a yield of 0.33 mg/mL in ethanol/water. These numbers appear to be in perfect agreement with the order of magnitudes for LPE yield found by us, with some of ours even exceeding them slightly (e.g., SM in H_2O).

The ZP data, also summarized in Table 2, allow us to estimate the colloidal stability of each final LPE MoO_3 ink. By examining them, it is possible to state a good match with the HSP theory used to actually select the liquid media. Indeed, the ZP values for 2-butanone and acetone suspensions have the highest values, between −30 and −45 mV, indicating long-term stable colloids, while the ZP values for water are in the range of −25 and −40 mV, indicating a medium-/short-term stability and those in IPA/water have values lower than −20 mV, hinting at relatively low-stability colloids prone to coagulation in a shorter timeframe.

In order to characterize further the obtained LPE α-MoO_3 colloids, we carried out additional analyses, namely Raman and UV−vis absorption spectroscopy and TEM/AFM. Raman scattering is widely employed to ascertain the changes into

https://doi.org/10.1021/acs.jpcc.1c09221
J. Phys. Chem. C 2022, 126, 404−415

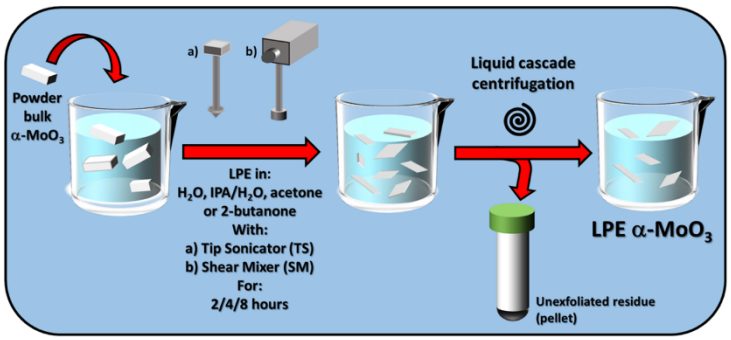

Figure 1. Schematic representation of the LPE process for α-MoO_3 described in this work and parameters whose effect was investigated, namely, type of the exfoliating instrument, liquid medium, and exfoliation time.

Table 2. Summary of the Different LPE α-MoO_3 Inks, Exfoliation Times, Employed Instruments and Relative Concentrations, ZPs, and E_{gap}

solvent 1 (v/v)	solvent 2 (v/v)	LPE time (h)	LPE method	concentration (mg mL^{-1})	ZP[a] (meV)	E_{gap}[b] (eV)
H_2O		2	TS	0.27	−39 ± 1.2	3.62
H_2O		4	TS	0.34	−34 ± 2.1	3.64
H_2O		8	TS	0.24	−36 ± 1.6	3.68
IPA (6)	H_2O (4)	2	TS	0.36	−19 ± 2.9	3.07
IPA (6)	H_2O (4)	4	TS	0.24	−16 ± 0.9	3.05
IPA (6)	H_2O (4)	8	TS	0.13	−9 ± 0.6	3.05
2-butanone		2	TS		−42 ± 8.5	2.90
2-butanone		4	TS	0.015	−47 ± 0.8	3.00
2-butanone		8	TS	0.045	−42 ± 2.8	3.17
acetone		2	TS	0.06	−30 ± 2.1	3.06
acetone		4	TS	0.015	−35 ± 1.5	3.04
acetone		8	TS	0.045	−49 ± 1.9	2.97
H_2O		2	SM	0.57	−43 ± 3.4	3.60
H_2O		4	SM	0.47	−27 ± 1.7	3.61
H_2O		8	SM	0.40	−32 ± 1.6	3.65
IPA (6)	H_2O (4)	2	SM	0.19	−16 ± 1.0	3.05
IPA (6)	H_2O (4)	4	SM	0.21	−15 ± 0.3	3.06
IPA (6)	H_2O (4)	8	SM	0.19	−11 ± 0.7	3.07
2-butanone		2	SM		−33 ± 1.6	3.05
2-butanone		4	SM		−37 ± 1.7	3.09
2-butanone		8	SM		−31 ± 0.6	3.12
acetone		2	SM	0.02	−31 ± 0.4	3.00
acetone		4	SM	0.02	−15 ± 0.5	2.99
acetone		8	SM	0.07	−25 ± 0.6	3.00

[a]The values reported here are an average of three different measurements. [b]Calculated from the Tauc plot derived from the UV−vis absorption spectra reported in Figure 2.

phonon modes when a dimensional reduction is carried in a layered material progressing from the pure 3D to the 2D form. In many 2D materials such as MoS_2,[61,62] WS_2,[63] and graphene,[64,65] Raman spectroscopy has been demonstrated to be one of the most powerful tools to state the number of layers present in a sample. However, for the characterization of layered MoO_3, this technique does not provide significant information to distinguish the 2D form from the bulk. A comparison between the bulk α-MoO_3 powder Raman spectra and those of some representative exfoliated samples is reported in Figure S1 of the Supporting Information (SI). In these spectra, the signals at 996 and 666 cm^{-1} and at wavenumbers <400 cm^{-1} show a slight red shift following dimensional reduction, which could be however within the Raman error, although it has been theoretically predicted[45] (the attribution of the signals to the different Raman modes is clarified in Table S1). Normalization on the most intense symmetric stretching mode of the terminal oxygen atoms or the doubly connected bridge−oxygen Mo−O−Mo at 818 cm^{-1} does not also highlight any change in relative intensity ratios with other modes, thus confirming that Raman for this specific layered material is not the suitable technique to ascertain the dimensional reduction, as it was shown before.[13,66]

UV−vis absorption spectra were acquired for all the LPE α-MoO_3 colloidal inks, as summarized in Figure 2, to verify whether a change in the energy of the optical band gap (E_{gap}) of α-MoO_3 can be detected following exfoliation, applying the

https://doi.org/10.1021/acs.jpcc.1c09221
J. Phys. Chem. C 2022, 126, 404−415

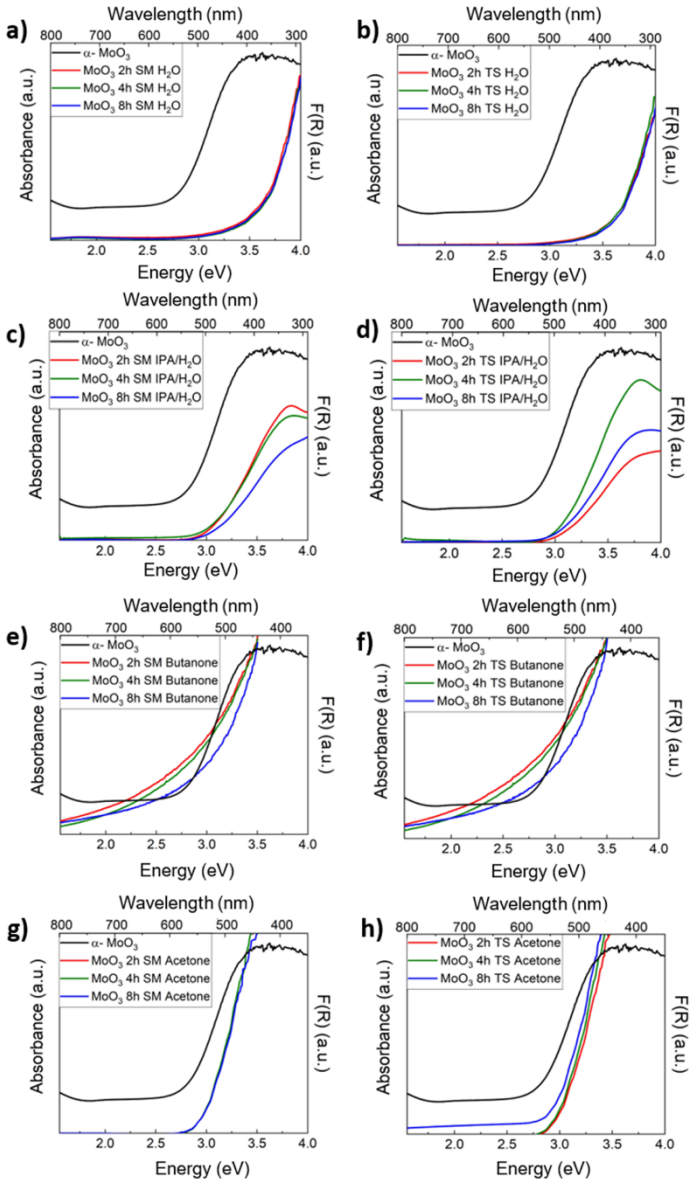

Figure 2. (a–h) UV–vis absorption spectra of the different LPE α-MoO_3 inks produced in this work employing multiple liquid media and SM or TS as the mechanical exfoliation method. The spectrum of bulk α-MoO_3 was recorded on the solid powder through reflectance spectroscopy, and it is reported in every graph for the sake of comparison.

Tauc method[46,67] to calculate its value at the absorption onset (all E_{gap} values are reported in Table 1).

In TMDCs, this technique normally allows to follow the blue shift of the excitonic transition during exfoliation, in agreement with the quantum confinement effect;[68,69] however, α-MoO_3 does not present any excitonic absorption whose position can be probed by UV–vis. Despite that, UV–vis can still be used to determine the band gap and its energy shift. The as-synthesized bulk α-MoO_3 has a measured indirect band gap of 2.8 eV, while all the LPE suspensions show an increase in this value from hundreds of meV up to almost 1 eV (Table 1). This indicates that possibly some samples might have undergone a dimensional reduction (e.g., the samples in pure H_2O, Figure 2a,b), while others might feature a quasi-2D

https://doi.org/10.1021/acs.jpcc.1c09221
J. Phys. Chem. C 2022, 126, 404–415

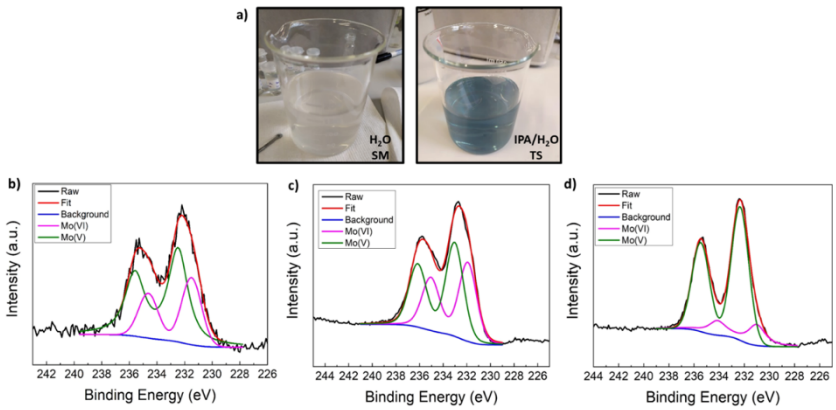

Figure 3. (a) Pictures of the LPE α-MoO_3 colloids in pure H_2O prepared via SM (left) and IPA/H_2O prepared via TS (right). XPS analysis of (b) as-synthesized α-MoO_3 powder, (c) LPE MoO_3 in H_2O prepared via SM, and (d) LPE MoO_3 in IPA/H_2O prepared via TS.

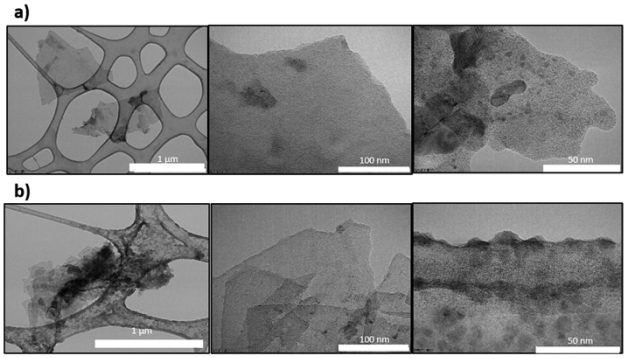

Figure 4. HR-TEM images of representative LPE α-MoO_3 colloids. (a) Samples in H_2O obtained via SM for 8 h and (b) samples in IPA/H_2O obtained via TS for 4 h.

structure (such as those in butanone, Figure 2e–f), as also previously reported in the literature.[70] To further investigate the variation in the electronic properties of α-MoO_3 following LPE, KPFM was performed to probe the work function (WF) of the material. The KPFM data on the samples with the largest optical band gap (colloids in H_2O and IPA/H_2O) show an average value for the WF of 4.56 ± 0.56 eV, which appears decreased as compared to the values obtained from the bulk material[46] of 5.11 ± 0.50 eV, indicating a shift of the Fermi level toward the vacuum level, as expected following quantum confinement toward the 2D form.[71]

Despite the wide band gap of some of the prepared LPE α-MoO_3 inks (namely, the ones in pure H_2O and IPA/H_2O mixture), remarkable changes in the color to the naked eye result depending on both the solvent and instrument employed for the LPE. Figure 3a shows the two significant cases of the inks produced in IPA/H_2O via TS and in H_2O via SM, respectively: while the latter is transparent, in line with the expectations considering the band gap of the material, the former presents a blue coloration. Since no significant traces of an absorption in the red zone of the visible spectrum are detected in the optical absorption spectra (Figure 2d), we expect that this coloration might be due to the presence of a relatively low quantity of Mo(V) moieties/oxygen vacancies, which can anyway contribute to change drastically the color of the ink.[72,73] In order to state the presence of Mo(V) in the blue-shaded ink, XPS measurements were performed (spectra of the molybdenum zone are reported in Figure 3b–d). From the XPS analysis, it is possible to clearly highlight that in the bulk α-MoO_3 material, some Mo(V) moieties were already present (Figure 3b). However, after LPE with the two different exfoliating devices (SM or TS), the quantity of Mo(V) sites slightly increases in the SM experiment (Figure 3c), but their concentration is perhaps not high enough to show their typical coloration in the resulting colloid. On the contrary, in the TS case (Figure 3d), a considerable increase in Mo(V) contribution in the photoemission spectrum is detected, thus explaining unambiguously the blue color of the suspension. Such an increase in the number of defect sites is most likely related to the harsher LPE conditions that result from the use of the TS method, known to cause flakes breaking other than exfoliation only,[74,75] compared to the milder SM. It is particularly interesting to notice that such a blue coloration emerges as a predominant effect only at very high quantities of

https://doi.org/10.1021/acs.jpcc.1c09221
J. Phys. Chem. C 2022, 126, 404–415

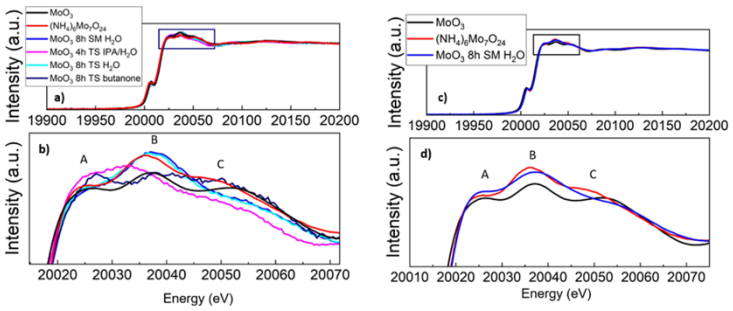

Figure 5. XANES spectra of (a) LPE α-MoO_3 colloidal inks with (b) relative zoom in the post-Mo-edge features. (c) XANES spectra of LPE α-MoO_3 powder obtained after drying the ink produced in H_2O after 8 h SM with relative zoom on the post-Mo-edge features in (d). In all the spectra, an internal comparison with the spectra of the precursors α-MoO_3 and AHM is also reported (measured as powders) for the sake of comparison.

Mo(V) moieties in the materials, indicating that the nanostructures in suspensions can withstand a high degree of Mo(V) atoms (or oxygen vacancies). In addition, the coloration results more intense in alcohol-based mixtures: this can be explained by the slightly reducing characteristic of the alcohol that likely promoted the formation of reduced species[76,77] during the exfoliation process [this phenomenon seems to increase when the samples are left in light, which might trigger the further Mo(VI) reduction by means of IPA].

To compare the variation in the electronic properties studied through UV−vis absorption with the effective nanomorphology of the resulting LPE α-MoO_3 colloids, HR-TEM analysis was performed to understand the size and dimension of the particles in suspension. Representative ink samples were selected to perform this analysis (see Figures 4 and S2) based on their higher concentration with respect to other inks and optical band gap opening (either large or small). From the TEM images, it can be seen that the sheet lateral size can reach dimensions up to 1 μm and that the material has been successfully exfoliated in some samples (see Figure 4a,b), especially in the H_2O LPE samples, which are also those reporting the highest opening of the optical band gap (Table 2). From a closer look at the images at high magnifications from Figure 4, it is possible to highlight the atomic morphology of the nanosheet planes: particularly in Figure 4a, showing the aspect of the LPE samples in H_2O, the atomic order appears to be altered compared to what should be expected from the starting crystalline α-MoO_3, hinting at a partial loss in crystallinity after LPE and at the concomitant formation of an amorphous phase in certain zones of the 2D nanosheets. Also, in the IPA/H_2O ink, this amorphous phase seems to be partially present (Figure 4b), together with crystalline domains, pointing at an amorphization of the material in the presence of water during LPE. On the other hand, the TEM images of the LPE sample in butanone (Figure S2) clearly show that the low E_{gap} increase with respect to the bulk α-MoO_3 is due to a non-efficient production of few-layered species. The presence of an amorphous component can be further detected by carrying out P-XRD analysis of the LPE α-MoO_3 dried material: Figure S3 shows a comparison between the diffractograms of bulk α-MoO_3 and of the exfoliated samples in H_2O (SM 8 h) and in IPA/H_2O (TS 4 h), from which, in the two latter samples, the emergence of the typical α-MoO_3 reflexes from a large amorphous background is clearly detected which is not present at all in the former. On the other hand, SAED analysis carried out locally on individual nanosheets on the TEM grid shows the presence of crystalline features (Figure S4), although these reflexes are coincident with high 2θ value reflexes in the P-XRD patterns of α-MoO_3, while the main material reflexes remain buried in the central part of the SAED pattern and are thus not distinguishable.

Once the information about the dimension and morphology of the LPE materials was obtained through TEM, the investigation was focused on understanding the thickness of the nanosheets, and to this aim, AFM analysis was performed (the results are displayed in Figure S5 in the Supporting Information). Through this analysis, it was possible to track nanosheet thicknesses varying within a narrow range, from bilayers (≈1.8 nm) to five to six layers (≈5−6 nm), further demonstrating that in the case of the colloidal samples in H_2O and IPA/H_2O, the LPE was successful.

To gain further insights into the atomic arrangement of the obtained LPE α-MoO_3 colloids produced via LPE in different liquid media, XAS measurements were performed at the SAMBA beamline of the SOLEIL synchrotron (Gif-sur-Yvette, France) directly on the colloidal inks and on the solid material obtained after drying the ink in H_2O produced *via* SM, being this one the most promising in terms of the 2D aspect ratio, and the results were compared to those obtained for the α-MoO_3 precursor in solid form and also for the precursor of this last one, namely, ammonium heptamolybdate (AHM). Next, the XANES spectra are first discussed, allowing us to unravel the atomic configuration around the Mo atoms, that is, their coordination sphere in the 2D nanosheets as compared to the bulk material. The recorded spectra are shown in Figure 5 for both the colloidal inks and the dried powder in comparison with the α-MoO_3 precursor and AHM, with both these references known to feature an octahedral coordination geometry around the Mo atoms. The liquid suspensions in Figure 5a show features similar to those of bulk α-MoO_3, in particular, a pre-edge feature at around 20.07 keV representing the forbidden 1 s → 4d transition in Mo atoms.[78] This transition becomes more pronounced when there is an overlap between O p-orbitals and Mo d-orbitals, with a high degree of distortion greatly improving such an overlap and subsequently the intensity of the pre-edge feature. By comparing this peak across the different samples, it is possible to evidence that those obtained by LPE in H_2O and IPA/H_2O show a less

https://doi.org/10.1021/acs.jpcc.1c09221
J. Phys. Chem. C 2022, 126, 404−415

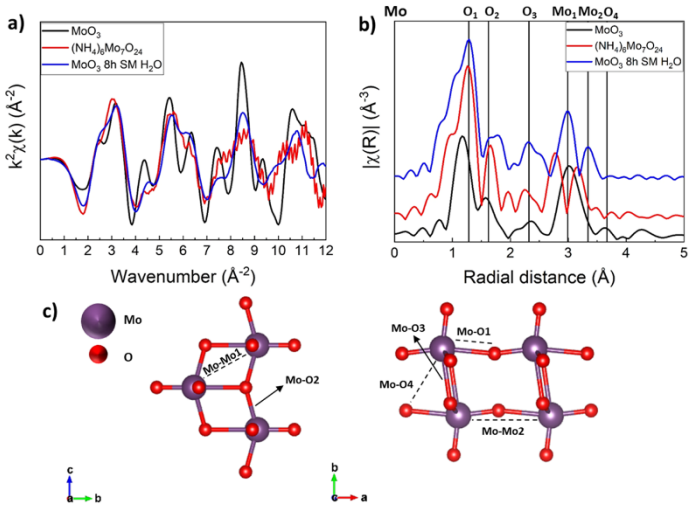

Figure 6. (a) EXAFS spectra and (b) not-corrected Fourier transformed EXAFS spectra of LPE α-MoO_3 powder obtained after drying the ink in H_2O prepared through 8 h SM. The internal comparison with the spectra of the precursors α-MoO_3 and AHM is also reported. (c) Details of the α-MoO_3 crystal structure highlighting the atomic distances probed by the EXAFS analysis (left: view along the *a*-axis; right: view along the *c*-axis).

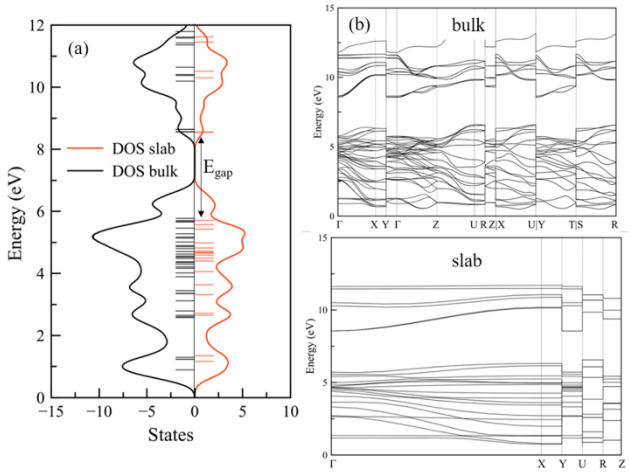

Figure 7. (a) Total DOS for the bulk (black line) and slab (red line) of α-MoO_3. The horizontal lines refer to the eigenvalues. (b) Band structure along the first Brillouin zone for both bulk and slab α-MoO_3.

intense pre-edge feature, indicating the existence of a higher symmetry compared to the reference compounds α-MoO_3 and AHM, while that in butanone gives rise to a more intense signal in the same zone, indicating a more distorted structure. By analyzing the main edge feature, information on the type of Mo site can be gathered: in general, octahedrally coordinated Mo features three main peaks, indicated in Figure 5 as A (20.025 keV), B (20.037 keV), and C (20.055 keV). These originate from the MoO_6 octahedra (a structure composed of four long Mo−O bonds and two shorter Mo═O bonds) sharing edges, and their relative intensity differs depending on the different Mo sites present in these polyoxoanion structures.[79] These sites are called 1, 1′, and 2: the first two represent a Mo atom sharing the edges with three other Mo atoms, with a slightly difference in Mo−O bond length, while site 2 represents a Mo atom surrounded by 6 MoO_6 octahedra.[79] For this latter site in particular, the intensity of peak B is much less intense as compared to sites 1 and 1′. Specifically, in the spectra presented here, it is possible to notice how the LPE samples in H_2O feature an increase in intensity and small shift toward lower energy in peak B, in direct relation to the absence of type 2 sites, and a decrease in intensity in peak C, which is connected both to the Mo coordination and to the second O shell around Mo. Those two

https://doi.org/10.1021/acs.jpcc.1c09221
J. Phys. Chem. C 2022, 126, 404−415

variations altogether account for a decrease of type 2 sites and a decrease in long-range interactions between different Mo and O, which can be related to a decrease in dimensionality. In addition, this sample also show a slight shift of the absorption edge position toward lower energies, compatible with the presence of the Mo(V) moieties detected *via* XPS. The presence of these reduced species has an even more profound effect on the sample in IPA/H_2O prepared via TS since the edge position is also shifted but, more relevantly, feature B is strongly shifted and overlaps with peak A.

Comparison has to be made then with the XANES spectra of a dried powder obtained from the best 2D colloid available among the here analyzed (namely, the H_2O 8 h SM, Figure 5d), where it is possible to observe, upon drying, a clear change in the spectrum: the pre-edge and edge features resemble those in the AHM spectra, rather than α-MoO_3, indicating distorted octahedra around the Mo(VI) centers. Compared to the crystalline α-MoO_3, peak A slightly increases in intensity, while peak C decreases: those combined observations suggest a change in ratio between sites 1 and 1′ (see the different computed site contributions in Figure S6), overall pointing to a partial restacking of the 2D nanosheets once they are not anymore in the colloidal state.

The extended X-ray absorption fine structure (EXAFS) part of the XAS spectrum was further analyzed for the dry sample (for the inks, this was not possible given the very low signal-to-noise ratio). This analysis provides information about bond lengths around the scattering atom, and changes in those lengths are detected for the here investigated materials when going from bulk α-MoO_3 to the 2D MoO_3 nanosheets (see Figure 6 and Table S2 in the Supporting Information for a list of the estimated bond lengths). While the first coordination shell resulted similar to the bulk oxide in terms of Mo−O lengths, in the second coordination sphere, both Mo−O and Mo−Mo bonds are considerably shorter in the 2D LPE α-MoO_3 powder compared to the bulk material. A similar effect can be attributed to a certain strain existing within the 2D nanosheets, as evidenced previously for TMDs,[80] and provides new interesting insights into the structure of few-layer α-MoO_3, which can have an effect on the optical and electronic properties of this low-dimensional material, as it has been highlighted also for 2D TMDs.[81]

To gain deeper insights into the experimental data, computational analyses on the 3D bulk structure of α-MoO_3 and the 2D slab were performed, and the results reported in Figure 7. After geometry optimization of both bulk and slab structures, very similar bond lengths as measured by EXAFS were obtained, with a maximum error of 0.23 Å for the Mo−O1 distance in the bulk and of 0.62 Å for the Mo−O3 distance in the slab. Since this bond distance is in the direction of the vacuum in the slab, it should not strongly affect the electronic properties here reported. Interestingly, we observe only slight variation in the DOS going from bulk to slab, with a main decrease in intensity rather than energy position. Yet, a band opening of around 50 meV was obtained at the Gamma point, from a value of 2.79 eV for the bulk to 2.85 eV for the slab. The band gap opening in is excellent agreement with the measured UV data. The discrepancy between some experimental values and the computation arises from two factors, namely, that all the calculations were performed in vacuum, for a single-layer structure, and without considering the effect of the different solvents on the electronic properties. Nevertheless, a large shift in the work function value has been computed, with values of 5.36 and 4.96 eV going from bulk to slab, which is again in excellent agreement with the measured values, and suggests a shift toward the vacuum for the slab, as well as the low importance of the solvent nature in determining the electronic properties of the slab (the solvent is important for LPE but does not affect the gap or WF shift). This is directly related to the quantum confinement effect which rises when the dimensionality of a system is decreased, thus shifting the Fermi level toward the vacuum.[71]

4. CONCLUSIONS

In this work, we describe a detailed analysis of the LPE process for the layered oxide α-MoO_3, a wide band gap semiconducting material that is attracting increasing attention for a variety of functional purposes, ranging from (opto)-electronics to electrochromism, energy storage, and catalysis.[45] Considering such attention that is progressively receiving by the scientific community active in the field of 2D materials research, it is timely to provide a comprehensive study as the present one, in which the parameters for the efficient LPE of α-MoO_3 targeting the production of its 2D colloids in low-environmental impact liquid media are thoroughly explored, allowing us to identify the best operating conditions. The use of water-based solvents results to be the right condition to ensure the formation of few-layer nanosheets, correlated with an opening of the optical band gap and a shift in the Fermi level in the direction of vacuum, being both electronic peculiarities of the dimensional reduction.[82] The yield in the LPE 2D material is still relatively modest, but it could be improved by resorting to pre-treatments on bulk α-MoO_3 such as the pre-intercalation of water molecules, followed by a series of freeze−thaw cycles that cause water freezing expansion, as it has been reported previously by Li et al.[83]

In parallel to this characterization, for the first time, we report here the results of a XAS investigation that compares the bulk and 2D form of α-MoO_3, allowing us to evidence extremely precise structural parameters at the atomic level. This points out at the potential of this technique to probe the local environment in 2D nanosheets, suggesting how this could be in the future more widely implemented also on other 2D materials to shine better light on structure−property relationships. Finally, through theoretical investigation, we strengthen the validity of the experimental results, effectively clarifying such relationships in the here analyzed α-MoO_3 with different dimensionalities.

This work will serve as a valuable tool in the hand of other investigators interested at applying 2D α-MoO_3 nanosheets in functional applications, resorting to this material as a colloidal ink, a pre-requisite for enabling in the future large-area processing and industrial scale implementation.[41]

■ ASSOCIATED CONTENT

Supporting Information

The Supporting Information is available free of charge at https://pubs.acs.org/doi/10.1021/acs.jpcc.1c09221.

Raman spectra and Raman mode assignment for LPE α-MoO_3; absorption spectra of LPE α-MoO_3 thin films and SEM images of their cross section; additional HR-TEM images and AFM analysis of LPE α-MoO_3; XRD and SAED spectra of LPE α-MoO_3; bond distances and other parameters obtained from EXAFS spectra; and

https://doi.org/10.1021/acs.jpcc.1c09221
J. Phys. Chem. C 2022, 126, 404−415

comparison between experimental and calculated XANES spectra (PDF)

AUTHOR INFORMATION

Corresponding Authors

Silvio Osella − *Chemical and Biological Systems Simulation Lab, Center of New Technologies, University of Warsaw, 02-097 Warsaw, Poland;* orcid.org/0000-0001-8541-1914; Email: s.osella@cent.uw.edu.pl

Silvia Gross − *Institute for Chemical Technology and Polymer Chemistry, Karlsruhe Institute of Technology (KIT), D-76131 Karlsruhe, Germany; Department of Chemical Sciences, University of Padua, 35131 Padova, Italy;* orcid.org/0000-0003-1860-8711; Email: silvia.gross@unipd.it

Teresa Gatti − *Center for Materials Research, Justus Liebig University, 35392 Giessen, Germany;* orcid.org/0000-0001-5343-8055; Email: teresa.gatti@phys.chemie.uni-giessen.de

Authors

Matteo Crisci − *Center for Materials Research, Justus Liebig University, 35392 Giessen, Germany*

Paolo Dolcet − *Institute for Chemical Technology and Polymer Chemistry, Karlsruhe Institute of Technology (KIT), D-76131 Karlsruhe, Germany;* orcid.org/0000-0001-9583-9375

Jijin Yang − *Department of Chemical Sciences, University of Padua, 35131 Padova, Italy*

Marco Salerno − *Materials Characterization Facility, Italian Institute of Technology, 16163 Genova, Italy*

Péter Bélteky − *Interdisciplinary Excellence Centre, Department of Applied and Environmental Chemistry, University of Szeged, H-6720 Szeged, Hungary*

Ákos Kukovecz − *Interdisciplinary Excellence Centre, Department of Applied and Environmental Chemistry, University of Szeged, H-6720 Szeged, Hungary;* orcid.org/0000-0003-0716-9557

Francesco Lamberti − *Department of Chemical Sciences, University of Padua, 35131 Padova, Italy;* orcid.org/0000-0003-1720-8038

Stefano Agnoli − *Department of Chemical Sciences, University of Padua, 35131 Padova, Italy;* orcid.org/0000-0001-5204-5460

Complete contact information is available at: https://pubs.acs.org/10.1021/acs.jpcc.1c09221

Notes

The authors declare no competing financial interest.

ACKNOWLEDGMENTS

M.C. and T.G. acknowledge the financial support from the European Commission through the H2020 FET-PROACTIVE-EIC-07-2020 project LIGHT-CAP (project number 101017821). S.O. acknowledges the Polish National Agency for Academic Exchange under the Bekker program (grant no. PPN/BEK/2020/1/00053/U/00001). This research was carried out with the support of the Interdisciplinary Center for Mathematical and Computational Modeling at the University of Warsaw (ICM UW) under grant no G83-28. S.G., F.L., and M.C. acknowledge the "Centro Levi Cases" of the University of Padova for financial support (AMONRA project). S.G. gratefully thank the Deutsche Forschungsgemeinschaft (DFG, German Research Foundation)—for funding a "Mercator Fellowship" position within the SFB 1441—Project-ID 426888090 at KIT Karlsruhe and the DAAD for a visiting professorship (2021) at the Justus Liebig Universität Giessen. P.D. acknowledges the support by the state of Baden-Württemberg through bwHPC and the DFG through grant no INST 40/575-1 FUGG (JUSTUS 2 cluster). SOLEIL synchrotron facility is kindly acknowledged for provision of beamtime (Proposal 20201498). We thank Emiliano Fonda, SAMBA beamline scientist, for technical support during the remote beamtime.

REFERENCES

(1) Gatti, T.; Lamberti, F.; Mazzaro, R.; Kriegel, I.; Schlettwein, D.; Enrichi, F.; Lago, N.; Di Maria, E.; Meneghesso, G.; Vomiero, A.; et al. Opportunities from Doping of Non-Critical Metal Oxides in Last Generation Light-Conversion Devices. *Adv. Energy Mater.* **2021**, *11*, 2101041.

(2) Greiner, M. T.; Helander, M. G.; Tang, W.-M.; Wang, Z.-B.; Qiu, J.; Lu, Z.-H. Universal Energy-Level Alignment of Molecules on Metal Oxides. *Nat. Mater.* **2012**, *11*, 76−81.

(3) Greiner, M. T.; Lu, Z.-H. Thin-Film Metal Oxides in Organic Semiconductor Devices: Their Electronic Structures, Work Functions and Interfaces. *NPG Asia Mater.* **2013**, *5*, No. e55.

(4) Meyer, J.; Hamwi, S.; Kröger, M.; Kowalsky, W.; Riedl, T.; Kahn, A. Transition Metal Oxides for Organic Electronics: Energetics, Device Physics and Applications. *Adv. Mater.* **2012**, *24*, 5408−5427.

(5) Zhu, Y.; Yao, Y.; Luo, Z.; Pan, C.; Yang, J.; Fang, Y.; Deng, H.; Liu, C.; Tan, Q.; Liu, F.; et al. Nanostructured MoO3 for Efficient Energy and Environmental Catalysis. *Molecules* **2020**, *25*, 2942.

(6) Yu, X.; Marks, T. J.; Facchetti, A. Metal Oxides for Optoelectronic Applications. *Nat. Mater.* **2016**, *15*, 383−396.

(7) Guo, Y.; Robertson, J. Origin of the High Work Function and High Conductivity of MoO3. *Appl. Phys. Lett.* **2014**, *105*, 222110.

(8) Dixit, D.; Madhuri, K. V. Electrochromism in MoO3 Nanostructured Thin Films. *Superlattices Microstruct.* **2021**, *156*, 106936.

(9) Novak, T. G.; Kim, J.; Tiwari, A. P.; Kim, J.; Lee, S.; Lee, J.; Jeon, S. 2D MoO3 Nanosheets Synthesized by Exfoliation and Oxidation of MoS2for High Contrast and Fast Response Time Electrochromic Devices. *ACS Sustain. Chem. Eng.* **2020**, *8*, 11276−11282.

(10) Arvizu, M. A.; Morales-Luna, M.; Pérez-González, M.; Campos-Gonzalez, E.; Zelaya-Angel, O.; Tomás, S. A.; Arvizu, B. M. A.; Mx, M. C. Influence of Thermal Annealings in Argon on the Structural and Thermochromic Properties of MoO 3 Thin Films. *Int. J. Thermophys.* **2017**, *38*, 51.

(11) Szkoda, M.; Trzciński, K.; Klein, M.; Siuzdak, K.; Lisowska-Oleksiak, A. The Influence of Photointercalaction and Photochromism Effects on the Photocatalytic Properties of Electrochemically Obtained Maze-like MoO3 Microstructures. *Sep. Purif. Technol.* **2018**, *197*, 382−387.

(12) Ma, Y. T.; Ma, S. Y.; Tang, J.; Wu, Z. G.; Shi, J.; Zhao, Y.; Wang, Y.; Pei, S. T. Constructed Heterostructured SnS@MoO3 Hollow Nanotubes and Detected Sensing Properties towards TEA. *Vacuum* **2021**, *184*, 109939.

(13) Datta, R. S.; Haque, F.; Mohiuddin, M.; Carey, B. J.; Syed, N.; Zavabeti, A.; Zhang, B.; Khan, H.; Berean, K. J.; Ou, J. Z.; et al. Highly Active Two Dimensional α-MoO3-: X for the Electrocatalytic Hydrogen Evolution Reaction. *J. Mater. Chem. A* **2017**, *5*, 24223−24231.

(14) Zhang, H.; Gao, L.; Gong, Y. Exfoliated MoO3 Nanosheets for High-Capacity Lithium Storage. *Electrochem. Commun.* **2015**, *52*, 67−70.

(15) Zhu, K.; Wang, X.; Liu, J.; Li, S.; Wang, H.; Yang, L.; Liu, S.; Xie, T. Novel Amorphous MoS2/MoO3/Nitrogen-Doped Carbon Composite with Excellent Electrochemical Performance for Lithium

https://doi.org/10.1021/acs.jpcc.1c09221
J. Phys. Chem. C 2022, 126, 404−415

Ion Batteries and Sodium Ion Batteries. *ACS Sustain. Chem. Eng.* **2017**, *5*, 8025−8034.
(16) Razmyar, S.; Sheng, T.; Akter, M.; Zhang, H. Low Temperature Photocatalytic Hydrogen Addition to Two-Dimensional MoO3 Nanoflakes from Isopropyl Alcohol for Enhancing Solar Energy Harvesting and Conversion. *ACS Appl. Nano Mater.* **2019**, *2*, 4180−4192.
(17) Avigad, E.; Etgar, L. Studying the Effect of MoO3 in Hole-Conductor-Free Perovskite Solar Cells. *ACS Energy Lett.* **2018**, *3*, 2240−2245.
(18) de Castro, I. A.; Datta, R. S.; Ou, J. Z.; Castellanos-Gomez, A.; Sriram, S.; Daeneke, T.; Kalantar-zadeh, K. Molybdenum Oxides − From Fundamentals to Functionality. *Advanced Materials*; Wiley-VCH Verlag, 2017.
(19) Ren, H.; Sun, S.; Cui, J.; Li, X. Synthesis, Functional Modifications, and Diversified Applications of Molybdenum Oxides Micro-/Nanocrystals: A Review. *Cryst. Growth Des.* **2018**, *18*, 6326−6369.
(20) Manzeli, S.; Ovchinnikov, D.; Pasquier, D.; Yazyev, O. V.; Kis, A. 2D Transition Metal Dichalcogenides. *Nat. Rev. Mater.* **2017**, *2*, 17033.
(21) Kumbhakar, P.; Chowde Gowda, C.; Mahapatra, P. L.; Mukherjee, M.; Malviya, K. D.; Chaker, M.; Chandra, A.; Lahiri, B.; Ajayan, P. M.; Jariwala, D.; et al. Emerging 2D Metal Oxides and Their Applications. *Mater. Today* **2021**, *45*, 142−168.
(22) Guan, M.; Wang, Q.; Zhang, X.; Bao, J.; Gong, X.; Liu, Y. Two-Dimensional Transition Metal Oxide and Hydroxide-Based Hierarchical Architectures for Advanced Supercapacitor Materials. *Front. Chem.* **2020**, *8*, 390.
(23) Browne, M. P.; Sofer, Z.; Pumera, M. Layered and Two Dimensional Metal Oxides for Electrochemical Energy Conversion. *Energy Environ. Sci.* **2019**, *12*, 41−58.
(24) Timmerman, M. A.; Xia, R.; Le, P. T. P.; Wang, Y.; Elshof, J. E. ten. Metal Oxide Nanosheets as 2D Building Blocks for the Design of Novel Materials. *Chem.—Eur. J.* **2020**, *26*, 9084−9098.
(25) Hernandez, Y.; Nicolosi, V.; Lotya, M.; Blighe, F. M.; Sun, Z.; De, S.; McGovern, I. T.; Holland, B.; Byrne, M.; Gun'Ko, Y. K.; et al. High-Yield Production of Graphene by Liquid-Phase Exfoliation of Graphite. *Nat. Nanotechnol.* **2008**, *3*, 563−568.
(26) Hu, G.; Kang, J.; Ng, L. W. T.; Zhu, X.; Howe, R. C. T.; Jones, C. G.; Hersam, M. C.; Hasan, T. Functional Inks and Printing of Two-Dimensional Materials. *Chem. Soc. Rev.* **2018**, *47*, 3265−3300.
(27) Huang, Y.; Pan, Y.-H.; Yang, R.; Bao, L.-H.; Meng, L.; Luo, H.-L.; Cai, Y.-Q.; Liu, G.-D.; Zhao, W.-J.; Zhou, Z.; et al. Universal Mechanical Exfoliation of Large-Area 2D Crystals. *Nat. Commun.* **2020**, *11*, 1−9.
(28) Backes, C.; Higgins, T. M.; Kelly, A.; Boland, C.; Harvey, A.; Hanlon, D.; Coleman, J. N. Guidelines for Exfoliation, Characterization and Processing of Layered Materials Produced by Liquid Exfoliation. *Chem. Mater.* **2017**, *29*, 243−255.
(29) Blake, P.; Brimicombe, P. D.; Nair, R. R.; Booth, T. J.; Jiang, D.; Schedin, F.; Ponomarenko, L. A.; Morozov, S. V.; Gleeson, H. F.; Hill, E. W.; et al. Graphene-Based Liquid Crystal Device. *Nano Lett.* **2008**, *8*, 1704−1708.
(30) Wang, H.; Su, X.; Song, T.; Li, Z.; Zhao, Y.; Lou, H.; Wang, J. Scalable Exfoliation and Dispersion of Few-Layer Hexagonal Boron Nitride Nanosheets in NMP-Salt Solutions. *Appl. Surf. Sci.* **2019**, *488*, 656−661.
(31) Gupta, A.; Arunachalam, V.; Vasudevan, S. Liquid-Phase Exfoliation of MoS2 Nanosheets: The Critical Role of Trace Water. *J. Phys. Chem. Lett.* **2016**, *7*, 4884−4890.
(32) Han, G.-Q.; Liu, Y.-R.; Hu, W.-H.; Dong, B.; Li, X.; Chai, Y.-M.; Liu, Y.-Q.; Liu, C.-G. WS2 Nanosheets Based on Liquid Exfoliation as Effective Electrocatalysts for Hydrogen Evolution Reaction. *Mater. Chem. Phys.* **2015**, *167*, 271−277.
(33) Gomez, C. V.; Guevara, M.; Tene, T.; Villamagua, L.; Usca, G. T.; Maldonado, F.; Tapia, C.; Cataldo, A.; Bellucci, S.; Caputi, L. S. The Liquid Exfoliation of Graphene in Polar Solvents. *Appl. Surf. Sci.* **2021**, *546*, 149046.
(34) Esfandiari, M.; Mohajerzadeh, S. Formation of Large Area WS2 Nanosheets Using an Oxygen-Plasma Assisted Exfoliation Suitable for Optical Devices. *Nanotechnology* **2019**, *30*, 425204.
(35) El Garah, M.; Bertolazzi, S.; Ippolito, S.; Eredia, M.; Janica, I.; Melinte, G.; Ersen, O.; Marletta, G.; Ciesielski, A.; Samorì, P. MoS2 Nanosheets via Electrochemical Lithium-Ion Intercalation under Ambient Conditions. *FlatChem* **2018**, *9*, 33−39.
(36) Hu, C.-X.; Shin, Y.; Read, O.; Casiraghi, C. Dispersant-Assisted Liquid-Phase Exfoliation of 2D Materials beyond Graphene. *Nanoscale* **2021**, *13*, 460−484.
(37) Vook, R. W. Theories Of Nucleation And Growth Of Thin Films. In *Thin Film Technologies and Special Applications*; Hunter, W. R., Ed.; SPIE, 1982; Vol. *0346*, pp 2−8.
(38) Paolucci, V.; D'Olimpio, G.; Lozzi, L.; Mio, A. M.; Ottaviano, L.; Nardone, M.; Nicotra, G.; Le-Cornec, P.; Cantalini, C.; Politano, A. Sustainable Liquid-Phase Exfoliation of Layered Materials with Nontoxic Polarclean Solvent. *ACS Sustain. Chem. Eng.* **2020**, *8*, 18830−18840.
(39) Parvez, K.; Worsley, R.; Alieva, A.; Felten, A.; Casiraghi, C. Water-Based and Inkjet Printable Inks Made by Electrochemically Exfoliated Graphene. *Carbon* **2019**, *149*, 213−221.
(40) McManus, D.; Vranic, S.; Withers, F.; Sanchez-Romaguera, V.; Macucci, M.; Yang, H.; Sorrentino, R.; Parvez, K.; Son, S.-K.; Iannaccone, G.; et al. Water-Based and Biocompatible 2D Crystal Inks for All-Inkjet-Printed Heterostructures. *Nat. Nanotechnol.* **2017**, *12*, 343−350.
(41) Hu, G.; Kang, J.; Ng, L. W. T.; Howe, R. C. T.; Jones, C. G.; Hersam, M. C.; Hasan, T.; Tawfique, H. Functional Inks and Printing of Two-Dimensional Materials. *Chem. Soc. Rev.* **2018**, *47*, 3265−3300.
(42) Lin, Z.; Liu, Y.; Halim, U.; Ding, M.; Liu, Y.; Wang, Y.; Jia, C.; Chen, P.; Duan, X.; Wang, C.; et al. Solution-Processable 2D Semiconductors for High-Performance Large-Area Electronics. *Nature* **2018**, *562*, 254−258.
(43) Yuan, H.; Liu, X.; Ma, L.; Gong, P.; Yang, Z.; Wang, H.; Wang, J.; Yang, S. High Efficiency Shear Exfoliation for Producing High-Quality, Few-Layered MoS2 Nanosheets in a Green Ethanol/Water System. *RSC Adv.* **2016**, *6*, 82763−82773.
(44) Liu, H.; Xu, L.; Liu, W.; Zhou, B.; Zhu, Y.; Zhu, L.; Jiang, X. Production of Mono- to Few-Layer MoS2 Nanosheets in Isopropanol by a Salt-Assisted Direct Liquid-Phase Exfoliation Method. *J. Colloid Interface Sci.* **2018**, *515*, 27−31.
(45) Radha, S. K.; Crowley, K.; Holler, B. A.; Gao, X. P. A.; Lambrecht, W. R. L.; Volkova, H.; Berger, M.-H.; Pentzer, E.; Pachuta, K. G.; Sehirlioglu, A. Ultrathin 2D-Oxides: A Perspective on Fabrication, Structure, Defect, Transport, Electron, and Phonon Properties. *J. Appl. Phys.* **2021**, *129*, 220903.
(46) Dalle Feste, P.; Crisci, M.; Barbon, F.; Tajoli, F.; Salerno, M.; Drago, F.; Prato, M.; Gross, S.; Gatti, T.; Lamberti, F. Work Function Tuning in Hydrothermally Synthesized Vanadium-Doped MoO3 and Co3O4 Mesostructures for Energy Conversion Devices. *Appl. Sci.* **2021**, *11*, 2016.
(47) Giannozzi, P.; Baroni, S.; Bonini, N.; Calandra, M.; Car, R.; Cavazzoni, C.; Ceresoli, D.; Chiarotti, G. L.; Cococcioni, M.; Dabo, I.; et al. QUANTUM ESPRESSO: A Modular and Open-Source Software Project for Quantum of Materials. *J. Phys. Condens. Matter* **2009**, *21*, 395502.
(48) Hamann, D. R. Optimized Norm-Conserving Vanderbilt Pseudopotentials. *Phys. Rev. B: Condens. Matter Mater. Phys.* **2013**, *88*, 85117.
(49) Terentjev, A. V.; Constantin, L. A.; Pitarke, J. M. Dispersion-Corrected PBEsol Exchange-Correlation Functional. *Phys. Rev. B: Condens. Matter Mater. Phys.* **2018**, *98*, 214108.
(50) Bunău, O.; Joly, Y. Self-Consistent Aspects of x-Ray Absorption Calculations. *J. Phys. Condens. Matter* **2009**, *21*, 345501.
(51) Guda, S. A.; Guda, A. A.; Soldatov, M. A.; Lomachenko, K. A.; Bugaev, A. L.; Lamberti, C.; Gawelda, W.; Bressler, C.; Smolentsev, G.; Soldatov, A. V.; et al. Optimized Finite Difference Method for the Full-Potential XANES Simulations: Application to Molecular

https://doi.org/10.1021/acs.jpcc.1c09221
J. Phys. Chem. C 2022, 126, 404−415

Adsorption Geometries in MOFs and Metal−Ligand Intersystem Crossing Transients. *J. Chem. Theory Comput.* **2015**, *11*, 4512−4521.
(52) Hanlon, D.; Backes, C.; Higgins, T. M.; Hughes, M.; O'Neill, A.; King, P.; McEvoy, N.; Duesberg, G. S.; Sanchez, B. M.; Pettersson, H.; et al. Production of Molybdenum Trioxide Nanosheets by Liquid Exfoliation and Their Application in High-Performance Supercapacitors. *Chem. Mater.* **2014**, *26*, 1751−1763.
(53) Dutta, S.; Pal, S.; De, S. Mixed Solvent Exfoliated Transition Metal Oxides Nanosheets Based Flexible Solid State Supercapacitor Devices Endowed with High Energy Density. *New J. Chem.* **2019**, *43*, 12385−12395.
(54) Smith, R. J.; King, P. J.; Lotya, M.; Wirtz, C.; Khan, U.; De, S.; O'Neill, A.; Duesberg, G. S.; Grunlan, J. C.; Moriarty, G.; et al. Large-Scale Exfoliation of Inorganic Layered Compounds in Aqueous Surfactant Solutions. *Adv. Mater.* **2011**, *23*, 3944−3948.
(55) Sricharan, M.; Gupta, B.; Moolayadukkam, S.; Matte, H. S. S. R. Exfoliation in a Low Boiling Point Solvent and Electrochemical Applications of MoO 3. *Beilstein J. Nanotechnol.* **2020**, *11*, 662−670.
(56) Cunningham, G.; Lotya, M.; Cucinotta, C. S.; Sanvito, S.; Bergin, S. D.; Menzel, R.; Shaffer, M. S. P.; Coleman, J. N. Solvent Exfoliation of Transition Metal Dichalcogenides: Dispersibility of Exfoliated Nanosheets Varies Only Weakly between Compounds. *ACS Nano* **2012**, *6*, 3468−3480.
(57) Hernandez, Y.; Lotya, M.; Rickard, D.; Bergin, S. D.; Coleman, J. N. Measurement of Multicomponent Solubility Parameters for Graphene Facilitates Solvent Discovery. *Langmuir* **2010**, *26*, 3208−3213.
(58) Coleman, J. N.; Lotya, M.; O'Neill, A.; Bergin, S. D.; King, P. J.; Khan, U.; Young, K.; Gaucher, A.; De, S.; Smith, R. J.; et al. Two-Dimensional Nanosheets Produced by Liquid Exfoliation of Layered Materials. *Science* **2011**, *331*, 568−571.
(59) Paolucci, V.; Emamjomeh, S. M.; Nardone, M.; Ottaviano, L.; Cantalini, C. Two-Step Exfoliation of WS2 for NO2, H2 and Humidity Sensing Applications. *Nanomaterials* **2019**, *9*, 1363.
(60) Hansen, C. *Hansen Solubility Parameters A User's Handbook*, 2nd ed.; CRC press, 2007.
(61) Li, H.; Zhang, Q.; Yap, C. C. R.; Tay, B. K.; Edwin, T. H. T.; Olivier, A.; Baillargeat, D. From Bulk to Monolayer MoS2: Evolution of Raman Scattering. *Adv. Funct. Mater.* **2012**, *22*, 1385−1390.
(62) Liu, G.; Komatsu, N. Readily Available "Stock Solid" of MoS_2 and WS_2 Nanosheets through Solid-Phase Exfoliation for Highly Concentrated Dispersions in Water. *ChemNanoMat* **2016**, *2*, 500−503.
(63) Lu, C.; Ma, J.; Si, K.; Xu, X.; Quan, C.; He, C.; Xu, X. Band Alignment of WS2/MoS2 Photoanodes with Efficient Photoelectric Responses Based on Mixed Van Der Waals Heterostructures. *Phys. Status Solidi* **2019**, *216*, 1900544.
(64) Ciesielski, A.; Samorì, P. Graphene via Sonication Assisted Liquid-Phase Exfoliation. *Chem. Soc. Rev.* **2013**, *43*, 381−398.
(65) Claramunt, S.; Varea, A.; López-Díaz, D.; Velázquez, M. M.; Cornet, A.; Cirera, A. The Importance of Interbands on the Interpretation of the Raman Spectrum of Graphene Oxide. *J. Phys. Chem. C* **2015**, *119*, 10123−10129.
(66) Ji, F.; Ren, X.; Zheng, X.; Liu, Y.; Pang, L.; Jiang, J.; Liu, S. 2D-MoO 3 Nanosheets for Superior Gas Sensors. *Nanoscale* **2016**, *8*, 8696.
(67) Kim, M.; Alfano, A.; Perotto, G.; Serri, M.; Dengo, N.; Mezzetti, A.; Gross, S.; Prato, M.; Salerno, M.; Rizzo, A.; et al. Moisture Resistance in Perovskite Solar Cells Attributed to a Water-Splitting Layer. *Commun. Mater.* **2021**, *2*, 1−12.
(68) Zheng, S.-W.; Wang, L.; Wang, H.-Y.; Xu, C.-Y.; Luo, Y.; Sun, H.-B. Observation of Quantum-Confined Exciton States in Monolayer WS 2 Quantum Dots by Ultrafast Spectroscopy. *Nanoscale* **2021**, *13*, 17093.
(69) Wang, X.; Liu, Y.; Ren, J.; Dou, K.; Shi, X.; Zhang, R. A Revised Mechanism of Band Gap Evolution of TMDC Nanotubes and Its Application to Janus TMDC Nanotubes: Negative Electron and Hole Compressibility. *J. Mater. Chem. C* **2021**, *9*, 8920−8929.
(70) Liu, H.; Lee, C. J. J.; Jin, Y.; Yang, J.; Yang, C.; Chi, D. Huge Absorption Edge Blue Shifts of Layered α-MoO3 Crystals upon Thickness Reduction Approaching 2D Nanosheets. *J. Phys. Chem. C* **2018**, *122*, 12122−12130.
(71) Katan, C.; Mercier, N.; Even, J. Quantum and Dielectric Confinement Effects in Lower-Dimensional Hybrid Perovskite Semiconductors. *Chem. Rev.* **2019**, *119*, 3140−3192.
(72) Siokou, A.; Leftheriotis, G.; Papaefthimiou, S.; Yianoulis, P. Effect of the Tungsten and Molybdenum Oxidation States on the Thermal Coloration of Amorphous WO3 and MoO3 Films. *Surf. Sci.* **2001**, *482*−*485*, 294−299.
(73) Morales-Luna, M.; Tomás, S. A.; Arvizu, M. A.; Pérez-González, M.; Campos-Gonzalez, E. The Evolution of the Mo5+ Oxidation State in the Thermochromic Effect of MoO3 Thin Films Deposited by Rf Magnetron Sputtering. *J. Alloys Compd.* **2017**, *722*, 938−945.
(74) Di Berardino, C.; Bélteky, P.; Schmitz, F.; Lamberti, F.; Menna, E.; Kukovecz, Á.; Gatti, T. Controlled Size Reduction of Liquid Exfoliated Graphene Micro-Sheets via Tip Sonication. *Cryst* **2020**, *10*, 1049.
(75) Tyurnina, A. V.; Tzanakis, I.; Morton, J.; Mi, J.; Porfyrakis, K.; Maciejewska, B. M.; Grobert, N.; Eskin, D. G. Ultrasonic Exfoliation of Graphene in Water: A Key Parameter Study. *Carbon* **2020**, *168*, 737−747.
(76) Yang, L. C.; Gao, Q. S.; Tang, Y.; Wu, Y. P.; Holze, R. MoO2 Synthesized by Reduction of MoO3 with Ethanol Vapor as an Anode Material with Good Rate Capability for the Lithium Ion Battery. *J. Power Sources* **2008**, *179*, 357−360.
(77) Pal, A.; Shah, S.; Devi, S. Microwave-Assisted Synthesis of Silver Nanoparticles Using Ethanol as a Reducing Agent. *Mater. Chem. Phys.* **2009**, *114*, 530−532.
(78) Macis, S.; Rezvani, J.; Davoli, I.; Cibin, G.; Spataro, B.; Scifo, J.; Faillace, L.; Marcelli, A. Structural Evolution of MoO3 Thin Films Deposited on Copper Substrates upon Annealing: An X-Ray Absorption Spectroscopy Study. *Condens. Matter* **2019**, *4*, 41.
(79) Tougerti, A.; Berrier, E.; Mamede, A.-S.; La Fontaine, C.; Briois, V.; Joly, Y.; Payen, E.; Paul, J.-F.; Cristol, S.S. Synergy between XANES Spectroscopy and DFT to Elucidate the Amorphous Structure of Heterogeneous Catalysts :TiO2 -SupportedMolybdenum Oxide Catalysts. *Angew. Chem., Int. Ed.* **2013**, *52*, 6440−6444.
(80) Rhodes, D.; Chae, S. H.; Ribeiro-Palau, R.; Hone, J. Disorder in van Der Waals Heterostructures of 2D Materials. *Nat. Mater.* **2019**, *18*, 541−549.
(81) Scalise, E.; Houssa, M.; Pourtois, G.; Afanas'ev, V.; Stesmans, A. Strain-Induced Semiconductor to Metal Transition in the Two-Dimensional Honeycomb Structure of MoS2. *Nano Res.* **2011**, *5*, 43−48.
(82) Yang, A.; Blancon, J.-C.; Jiang, W.; Zhang, H.; Wong, J.; Yan, E.; Lin, Y.-R.; Crochet, J.; Kanatzidis, M. G.; Jariwala, D.; et al. Giant Enhancement of Photoluminescence Emission in WS2-Two-Dimensional Perovskite Heterostructures. *Nano Lett.* **2019**, *19*, 4852−4860.
(83) Li, C.; Wang, T.; Wu, Y.; Ma, F.; Zhao, G.; Hao, X. Fabrication of Two-Dimensional Nanosheets via Water Freezing Expansion Exfoliation. *Nanotechnology* **2014**, *25*, 495302.

https://doi.org/10.1021/acs.jpcc.1c09221
J. Phys. Chem. C 2022, 126, 404−415

Supporting Information for:

Design Principles and Insights into the Liquid-Phase Exfoliation of Alpha-MoO_3 for the Production of Colloidal 2D Nano-Inks in Green Solvents

Matteo Crisci,[1] Paolo Dolcet,[2] Jijin Yang,[3] Marco Salerno,[4] Péter Bélteky,[5] Ákos Kukovecz,[5] Francesco Lamberti,[3] Stefano Agnoli,[3] Silvio Osella,[6] Silvia Gross,[2,3] Teresa Gatti[1]

[1] Center for Materials Research, Justus Liebig University, Heinrich-Buff-Ring 17, 35392 Giessen, Germany

[2] Institute for Chemical Technology and Polymer Chemistry, Karlsruhe Institute of Technology (KIT), D-76131, Karlsruhe, Germany

[3] Department of Chemical Sciences, University of Padua, via Marzolo 1, 35131 Padova, Italy

[4] Materials Characterization Facility, Italian Institute of Technology, Via Morego 30, 16163 Genova, Italy

[5] Interdisciplinary Excellence Centre, Department of Applied and Environmental Chemistry, University of Szeged, Rerrich Béla tér 1, H-6720 Szeged, Hungary

[6] Chemical and Biological Systems Simulation Lab, Center of New Technologies, University of Warsaw, Banacha 2C, 02-097 Warsaw, Poland

Table of Contents

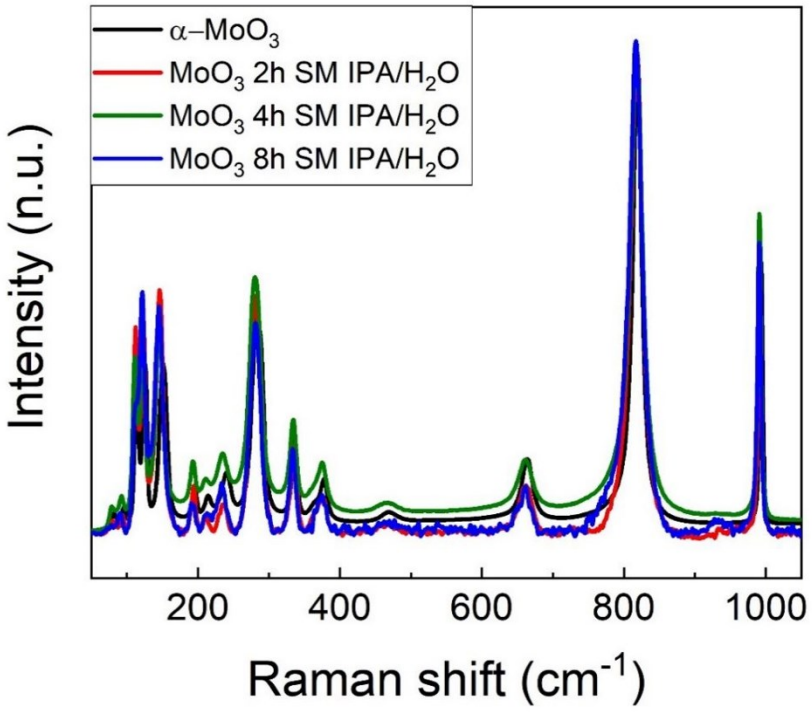

Figure S1. Representative normalized Raman spectra for bulk and LPE α-MoO_3.

Table S1. Raman modes assignment for α-MoO_3.[1]

Raman Shift (cm^{-1})	**Mode**	**Assignment**
996	A_g, B_{1g}	ν O=Mo
818	B_{2u}	ν O_2Mo
666	B_{2g}, B_{3g}	ν O_3Mo
472	B_{2u}	
374	B_{1g}	δ O=Mo
338	A_g, B_{1g}	δ OMo_3
286	B_{2g}	δ O=Mo
246	B_{3g}	δ OMo_2
218	A_g	
198	B_{2g}	

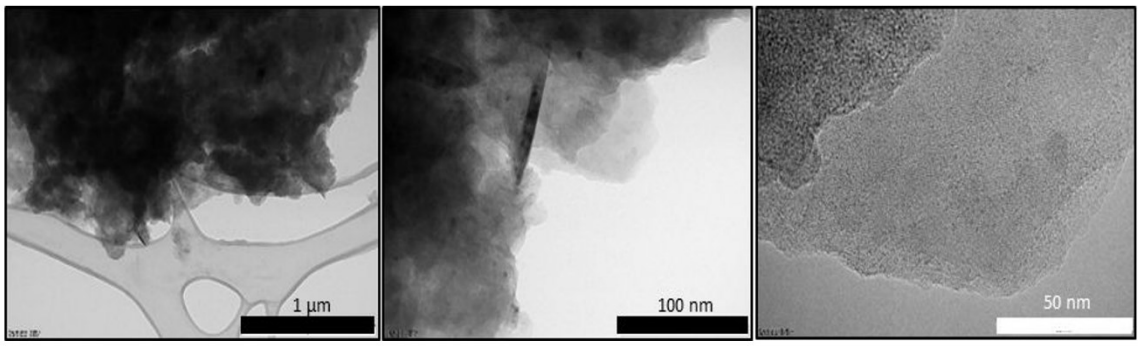

Figure S2. HR-TEM images of LPE α-MoO_3 colloids obtained in butanone after 8 h TS.

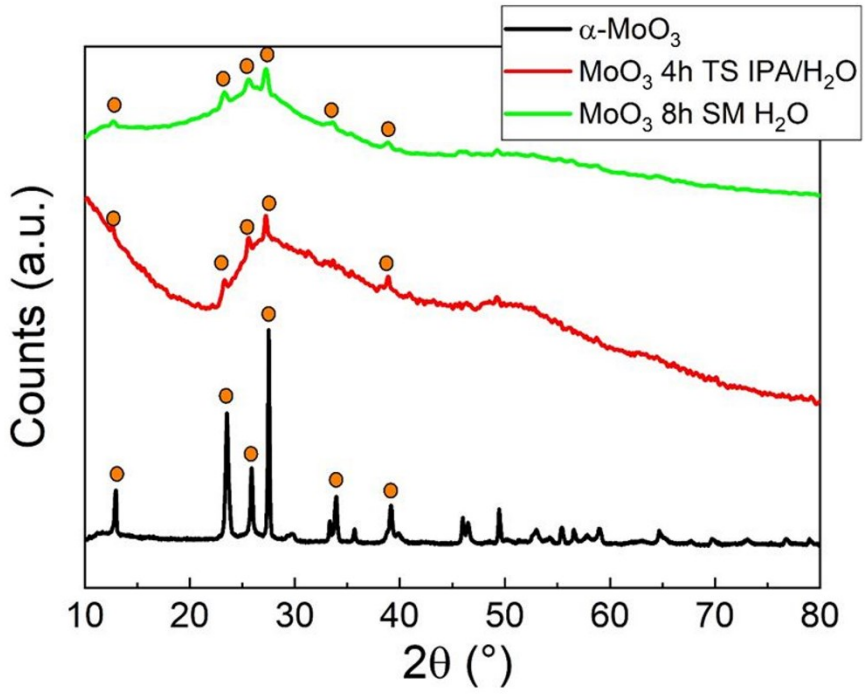

Figure S3. P-XRD patterns for dried LPE α-MoO_3 colloids obtained in H_2O after 8 h SM and in IPA/H_2O after 4 h TS compared to the P-XRD pattern of the bulk α-MoO_3 used as starting material.

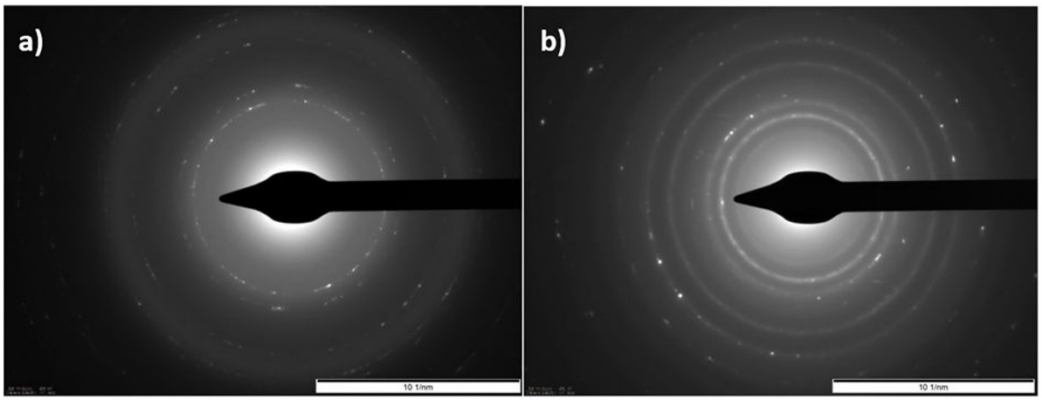

Figure S4. SAED patterns collected on the LPE α-MoO_3 nanosheets shown in Figure 4 in the main manuscript text: a) 8 h SM H_2O and b) 4 h TS IPA/H_2O

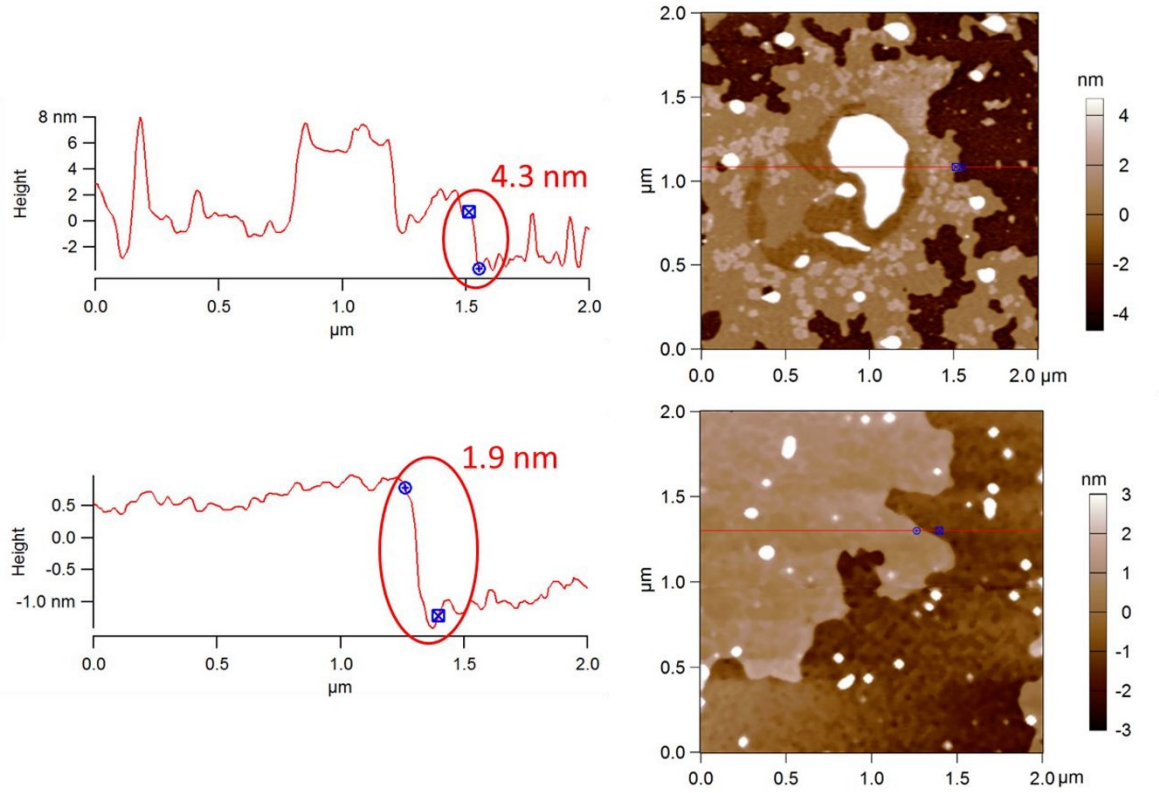

Figure S5. Representative AFM images for 2D α-MoO_3 derived from LPE in a,b) H_2O for 8 h via SM and in c,d) IPA/ H_2O for 4 h via TS.

Table S2. Bond distances and parameters obtained from the fitting of the FT-EXAFS spectra in Figure 6.

Sample	Scatterer	Distance (Å)	Number	Sigma Debye-Waller factor (10^{-3}) (Å^2)	Enot E_0 (eV)	R-factor (%)
MoO_3_8h_SM_H_2O	O1	1.71 ± 0.01	2	3.7 ± 0.4	-8.07 ± 1.58	0.9
	O2	2.03 ± 0.01	2	9.4 ± 1.4		
	O3	2.33 ± 0.01	2	9.5 ± 2.2		
	O4	3.18 ± 0.02	4	8.8 ± 1.2		
	Mo1	3.28 ± 0.02	2	8.8 ± 1.2		
	Mo2	3.65 ± 0.02	2	7.8 ± 2.5		
MoO_3	O1	1.73 ± 0.02	2	4.8 ± 1.8	-1.26 ± 4.03	4.5
	O2	1.96 ± 0.02	2	5.2 ± 1.4		
	O3	2.27 ± 0.03	2	6.3 ± 5.2		
	O4	3.37 ± 0.03	4	5.9 ± 2.1		
	Mo1	3.41 ± 0.02	2	5.9 ± 2.1		
	Mo2	4.01 ± 0.02	2	8.6 ± 2.2		
AHM	O1	1.74 ± 0.01	2	1.8 ± 0.5	2.94 ± 3.01	5.0
	O2	1.95 ± 0.01	2	3.8 ± 1.6		
	O3	2.19 ± 0.02	2	12.8 ± 4.4		

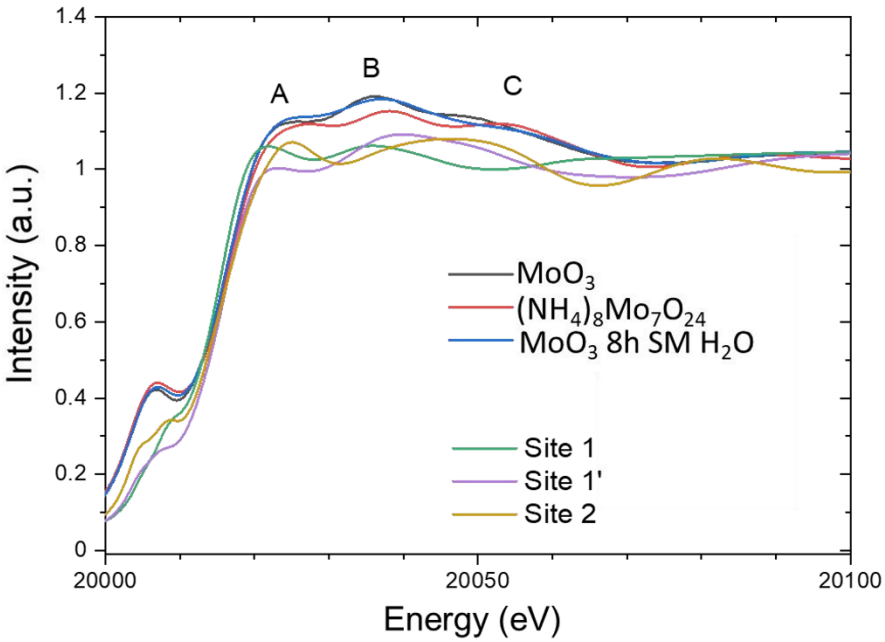

Figure S6. Comparison between experimental XANES spectra in Figure 5c,d and calculated ones for site 1,1´and 2.

References

3.3: Publication n°2

Systematic Investigation on the Surfactant-Assisted Liquid-Phase Exfoliation of MoS_2 and WS_2 in Water for Sustainable 2D Material Inks

Authors: Pozzati M.*, Boll F.*, **Crisci M.***, Domenici S., Smarsly B., Gatti T., Wang M.

From my first publication on the topic, exfoliation has evolved and explored different other options, outside of simply changing the solvents. This is still a valid methodology, but the issues with high boiling point solvents still stand and research is moving in different directions to solve the issue. The first idea is to directly remove the need of a solvent; therefore, methodologies such as scotch tape[96,98,100,101] and ball milling[226–228] have found their way into the exfoliation technology once again. *Zhang C. et al.*[229] also developed an additional way to exfoliate 2d materials using a SiC intermediate and by applying a shear force to the mixture of two components, leading to the high yield and quality of the as obtained 2d materials. However, despite this, the liquid phase exfoliation is often the most convenient due to its ease of use and up scalability, molten salts[230,231] has been used to exfoliate some materials, but it is not suitable for example, in the case of TMDCs. Rhodiasolv series of solvents has been studied by *Paolucci V. et al*[232]*.* and *Occhiuzzi J. et al.*[233,234] and these solvents could be a good alternative to NMP or DMF, due to their eco friendliness, whilst being good for exfoliation, with the only drawback of the economical large scale application. Therefore, the most convenient solvents remain alcohols and water, this last one, however, has the issue of not having matching parameters with TMDCs, therefore additives are often used to obtain stable and concentrated inks.[235–238] The research group of *Casiraghi C.* worked a lot using pyrene based surfactant[235,239], proving their

efficacy in the exfoliation even at low concentration, opening another door to research on the sector.[240]

Following the surfactant-based exfoliation, in **publication n°2** we focused, together with my collaborator, in the study of two different TMDCs exfoliated in water with different surfactant, SDS, SDBS and SHS, at different concentration. These three alkyl compounds have been used in different works as stabilizers; however, a comprehensive literature work was missing with a comparison between the three. Therefore, **publication n°2** founds its niche in this context. The bulk material was exfoliated using TS at different concentrations: their values were chosen in accordance with the CMC of SDS and applied to all the material-surfactant combinations tested. The exfoliated ink was tested according to the procedures established in **publication n°1**: initially the suspensions were analyzed via DLS, ZP and UV-Vis to assess size, stability and optical properties from which band gap and size reduction effects were calculated. Moreover, the powder obtained via freeze drying where then analyzed with Raman spectroscopy to study the fingerprints of the materials: here the MoS_2 and WS_2 excitons were observed and a slight shift, associated with the dimensional reduction of the material[241–243], were observed therefore indexing at a layer reduction of the material. This was confirmed once again using TEM microscopy where few layered materials could be seen.

Therefore, this paper adds information on the liquid phase exfoliation of well renowned TMDC, using as commonly used surfactants, by systematically studying the effect of concentration and alkyl chain length, as well as providing a convenient platform where a comparison and use of the three different surfactants can be found.

This paper is a shared authorship between *Felix Boll*, *Micael*a *Pozzato,* and *me*. Each one of the shared authors contributed significantly to the experimental and writing of the publications, with slightly different tasks for each one. The exfoliations were performed by a systematic and well-organized system where all

the three authors participated, while each one of us also focused on analyzing the inks using one technique each. Lastly, the writing part was led by *Micaela Pozzati*, while the two other authors contributed extensive sections and correction of the manuscript.

RESEARCH ARTICLE

physica status solidi pss rrl
www.pss-rapid.com

Systematic Investigation on the Surfactant-Assisted Liquid-Phase Exfoliation of MoS_2 and WS_2 in Water for Sustainable 2D Material Inks

Micaela Pozzati, Felix Boll, Matteo Crisci, Sara Domenici, Bernd Smarsly, Teresa Gatti, and Mengjiao Wang**

MoS_2 and WS_2 have gathered significant attention due to their tunable properties and wide range of applications. Liquid-phase exfoliation (LPE) is a facile method to prepare 2D MoS_2 and WS_2. Currently, the principally employed solvents for LPE of MoS_2 and WS_2 are expensive and toxic, and have high boiling points. These drawbacks encourage to find more sustainable alternatives to the liquid medium used for the preparation of 2D material inks. Water is the best option, but surfactants are necessary for LPE in water, since MoS_2 and WS_2 are hydrophobic. Organic molecules with amphoteric character such as sodium dodecyl sulfate, sodium dodecylbenzene sulfonate, and sodium hexadecyl sulfonate (SHS) are selected as suitable candidates for the role. However, the study of these surfactants used in LPE is barely systematically reported. In this work, a detailed investigation is presented on their impact on the LPE of MoS_2 and WS_2, which are representatives of transition-metal dichalcogenides. By characterizing and qualifying the products from average number of layers, it is found that all the surfactants work efficiently to exfoliate MoS_2 and WS_2 into few layers, and SHS stabilizes the 2D layers better than the other two. However, in terms of yield and relative surfactant concentration, a real trade-off is not identified between maximized quantity of exfoliated materials and minimized surfactant concentration, which prompts to select the colloidal ink based on the specific further needs for processing.

1. Introduction

Transition-metal dichalcogenides (TMDs) have gathered significant attention in a wide range of applications, such as energy storage, sensing, and optoelectronics.[1–3] In this broad family of materials, MoS_2 and WS_2 play important roles due to the possibility of preparing the 2D layered counterparts, which possess specific electronic and optical properties.[4–7] As shown in **Figure 1**, MoS_2 and WS_2 contain a layer of metal atoms sandwiched between two sulfur layers, and these sandwiched layers are linked to each other by van der Waals (vdW) forces in the bulk.[8–12] Due to the unique layered structure, it is possible to use top-down methodologies which are more scalable, versatile, and cost-effective compared to the bottom-up methods.[9] Therein, liquid-phase exfoliation (LPE) is commonly used to produce 2D layered materials. This procedure consists in delaminating the layers of the material dispersed in a solvent by mechanical forces such as ultrasonication and high shear mixing.[13] For instance, in the sonication-assisted LPE, the sonication generates the growth and collapse of microbubbles of the solvents, thus resulting in shock waves. These waves can produce shear forces on the bulk materials, break the vdW interactions between the layers of the 2D structures, and form layered materials eventually.[14,15] The type of solvent plays an important role on the yield and quality of the 2D materials. Typically, organic solvents such as N-methyl-2-pyrrolidone, dimethyl sulfoxide, and *N*,*N*-dimethyl formamide are the most commonly used in exfoliating MoS_2 and WS_2. However, they are expensive and toxic, and have high boiling point.[16–18] To avoid these disadvantages, water is applied as an alternative. Since most of the TMDs are hydrophobic, surfactants are needed to stabilize the 2D nanocrystals in water.

In LPE, ionic surfactants are applied for stabilizing the samples and thus increase the production yield in 2D layered colloids in water.[19,20] Thanks to the electrostatic forces, the ionic surfactants can compensate the vdW attraction between the layers of the material, thus preventing the restacking.[21,22] There are different kinds of surfactants that can be used in this process and

M. Pozzati, S. Domenici, T. Gatti, M. Wang
Dipartimento Scienza Applicata e Tecnologia (DISAT)
Politecnico di Torino
Corso Duca degli Abruzzi 24, 10129 Torino, Italy
E-mail: teresa.gatti@polito.it; mengjiao.wang@polito.it

F. Boll, M. Crisci, B. Smarsly, T. Gatti
Center for Materials Research (LaMa)
Justus Liebig University
Heinrich-Buff-Ring 17, 35392 Giessen, Germany

The ORCID identification number(s) for the author(s) of this article can be found under https://doi.org/10.1002/pssr.202400039.

DOI: 10.1002/pssr.202400039

ADVANCED SCIENCE NEWS
www.advancedsciencenews.com

physica status solidi pss rrl
www.pss-rapid.com

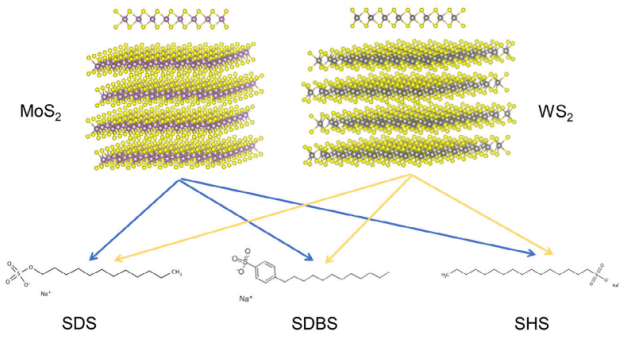

Figure 1. Structures of the two-layered TMDs considered in this study (MoS_2 and WS_2) in their semiconducting H-phase and modular structures of surfactants SDS, SDBS, and SHS.

the most reported one for MoS_2 and WS_2 is an anionic surfactant, namely sodium dodecyl sulfate (SDS), whose chemical structure is shown in Figure 1b.[23] It is characterized by a C_{12} alkyl chain that tends to aggregate on the nanosheets surface, avoiding the restacking.[20,24] Surfactants with a similar structure as SDS have been applied in LPE as well. Sodium dodecylbenzene sulfonate (SDBS) is also used as stabilizing agent. It is reported that the nonpolar benzene rings in SDBS combine with the 2D layers with a strong bind energy, thus improving at the same time the colloidal stability and yield in 2D MoS_2 in an aqueous solution.[25,26] Additionally, since it is reported that the length of the alkyl chain can have an impact on the stability of the dispersion, we have identified sodium hexadecyl sulfonate (SHS) as a new potential surfactant for stabilizing 2D nano-inks, considering its long C_{16} alkyl chain.[27] Plenty of previous studies suggest that the concentration of the surfactant has a great impact on the dispersion quality and final concentration.[20] Therefore, to tune, the concentration of the surfactants will be important for optimizing the LPE of MoS_2 and WS_2.

In this work, we perform a systematic investigation about the influence of the surfactant type and concentration on the quality of exfoliated MoS_2 and WS_2. As shown in Figure 1, three different surfactants, SDS, SDBS, and SHS have been selected for this study. These organic surfactants have a critical micellar concentration (CMC), and it was reported that surfactants can play a more efficient role in LPE when their concentration is less than the CMC.[28] However, some other reports have shown that the surfactant concentration has negligible influence on the yield and quality of exfoliated samples.[23] This confliction encourages us to systematically investigate the relationship between surfactant concentration and the exfoliated samples by LPE. Considering the CMC of SDS, SDBS, and SHS are respectively 8.2, 2.7, and 0.55 mM,[29–32] we chose the CMC of SDS as the highest surfactant concentration and set the concentrations to 8.2, 4.1, 2.0, 1.0, and 0.5 mM for comparison. By testing the UV–vis absorption, Raman spectra, zeta potential (ZP), we were able to compare the quality of the exfoliated MoS_2 and WS_2 in the aspect of layer thickness and stability. Eventually, the production yield is calculated for all the exfoliated samples. It is found that the thickness of the layers is not tightly related to the surfactant type and concentration, as almost all the samples are few layered for MoS_2 and mostly monolayered for WS_2. Meanwhile, SHS performs better than the other two surfactants in stabilizing the nanosheets, since LPE MoS_2 and WS_2 colloids have long-term stability with SHS.

2. Results and Discussion

The suspensions of MoS_2 and WS_2 were obtained with the surfactant-assisted LPE method described in Experimental Section, and the MoS_2 or WS_2 samples were labeled by the surfactant type and concentration. Transmission electron microscope (TEM) measurements were performed on selected MoS_2 and WS_2 suspensions to characterize the morphology of the exfoliated samples in detail. In **Figure 2**a, it is evident that the exfoliated MoS_2 are thin nanosheets with a lateral size of more than 500 nm. In Figure 2b, the TEM image with higher magnification displays a thin side view of less than 10 nm of the nanosheets. Since the interlayer spacing of MoS_2 is 0.615 nm, we expect that the exfoliated samples have less than 16 layers.[33] Figure 2c shows a TEM image of the exfoliated WS_2 nanosheets of more than 500 nm lateral size. In Figure 2d, it is easy to find the thickness of the WS_2 nanosheets of around 5 nm from the wrinkled part, which implies that the obtained WS_2 nanosheets have less than 8 layers.[34]

The effect of the surfactant on the optical properties of exfoliated MoS_2 was studied by UV–vis absorption spectroscopy. **Figure 3** shows the UV–vis normalized absorption spectra of LPE MoS_2 with SDS, SDBS, and SHS at different concentrations. All the spectra have shown the four characteristic excitons of MoS_2 at around 670 nm for the A exciton, 610 nm for the B exciton, 450 nm for the C exciton, and 395 nm for the D exciton, confirming the existence of the 2D layered material. Spectral changes are observed while varying the concentration of the surfactant. Therein, *A* and *B* excitons stands for direct excitonic transitions occurring at the *K* points in the first Brillouin zone, due to

ADVANCED SCIENCE NEWS
www.advancedsciencenews.com

physica status solidi rrl
www.pss-rapid.com

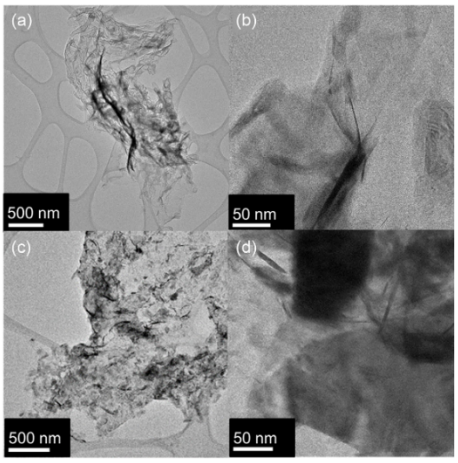

Figure 2. TEM images of a,b) MoS_2 SDBS 1.0 mM and c,d) WS_2 SDS 0.5 mM.

the spin–orbit splitting of the top of the valence band. *C* and *D* excitons are related to the optical transitions from the deep valence band to the conduction band.[35] In Figure 3a, the slope in the region between the *B* exciton and the *C* exciton becomes sharper while increasing the surfactant concentration, indicating smaller and thinner nanosheets. In addition, the value of *A* exciton is closely related to the size of the product. As listed in **Table 1**, the position of the *A* exciton tends to shift to shorter wavelength while increasing the concentration, revealing smaller and thinner nanosheets as well.[20,36–38] It has to be mentioned that there is no linear relationship between ligand concentration and absorption intensity, since the linear increase of surfactant concentration does not result in the linear increase of sample concentration, which have direct influence on the absorbance intensity. While the relationship between product yield and concentration of the surfactant will be discussed in the following content.

In addition, the bandgap of the nano-colloids was calculated with the Tauc plot equation (Equation (1)):

$$(\alpha h\nu)^{1/n} = A\,(h\nu - E_g) \tag{1}$$

where α is the absorption coefficient, h is the Plank constant, ν is the frequency, E_g is the bandgap energy, and n is 2 for the indirect bandgap materials such as few-layered MoS_2 and WS_2.[39] The values obtained are listed in Table 1. It is obvious that all the exfoliated MoS_2 have a larger bandgap range of 1.38–1.65 eV compared to the bulk MoS_2 (1.2 eV).[40] When comparing values between different surfactants, SHS in general results in higher bandgap compared to other surfactants, which means MoS_2 can be exfoliated into thinner layers when SHS is applied. While comparing the values between different concentration of the same surfactant, higher concentration of surfactant tends to produce the samples with higher bandgap, which means thinner nanosheets.[41] At last, the MoS_2 SHS 8.2 mM sample features the broadest bandgap of 1.65 eV, which means it likely contains nanosheets with the smallest average number of layers among all the LPE MoS_2 samples.

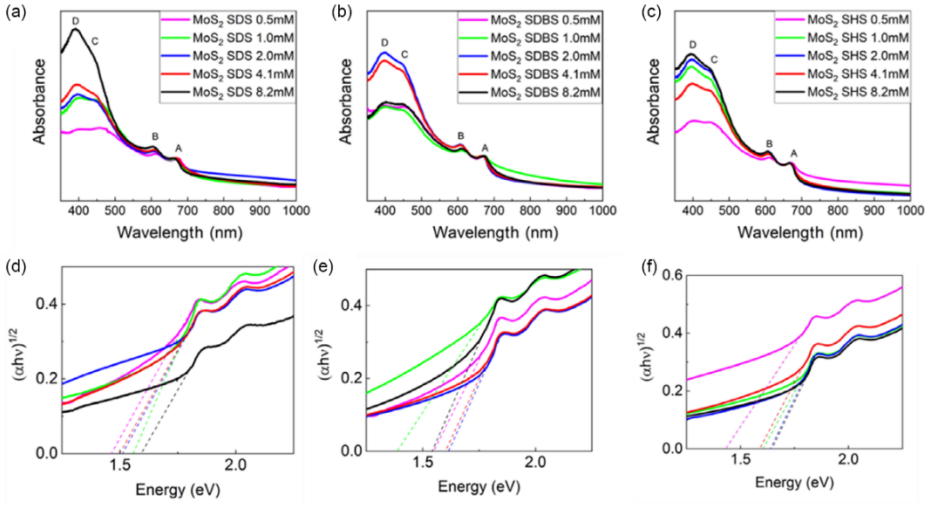

Figure 3. UV–Vis absorption spectra and corresponding Tauc plots of exfoliated MoS_2 with a,d) SDS, b,e) SDBS, and c,f) SHS.

ADVANCED SCIENCE NEWS
www.advancedsciencenews.com

physica status solidi rrl
www.pss-rapid.com

Table 1. Positions of A exciton and bandgap values for LPE MoS_2 samples with the three different surfactants.

Surfactant	Surfactant concentration [mM]	A exciton [nm]	Bandgap [eV]
	8.2	664.6	1.59
	4.1	671.1	1.50
SDS	2.0	668.9	1.51
	1.0	671.1	1.56
	0.5	673.4	1.46
	8.2	672.1	1.54
	4.1	670.1	1.60
SDBS	2.0	667.8	1.62
	1.0	672.1	1.38
	0.5	672.2	1.55
	8.2	667.8	1.65
	4.1	668.9	1.58
SHS	2.0	668.9	1.64
	1.0	669.3	1.61
	0.5	672.2	1.43

The UV–vis spectra of WS_2 are shown in **Figure 4**a–c. We can observe the presence of the four characteristic excitons of WS_2 (*A*: ≈630 nm; *B*: ≈522 nm; *C*: ≈460 nm; and *D*: ≈430 nm) in all the spectra while varying the surfactant type and concentration, revealing the success of exfoliation in all the experiments.[38] Specifically, in Figure 4d, it is shown that the bandgap of exfoliated WS_2 increases from 1.42 to 1.74 eV with the increasing concentration of SDS from 0.5 to 8.2 mM. Therefore, higher concentration of SDS results in the exfoliated WS_2 with broad bandgap and thinner layers of the samples on average. In contrast, for SDBS and SHS, difference in concentration has negligible influence on the bandgap of the samples, as shown in Figure 4e,f, and the bandgap of the samples by SDBS and SHS is around 1.74 eV. However, there is an exception of WS_2 SHS 8.2 mM, which shows a bandgap of 1.43 eV. This might be because 8 mM is much more than the suitable concentration of SHS to exfoliate WS_2 and results in thicker layers than other concentrations. Although the concentrations from 0.5 to 4.1 mM are all more than the CMC of SHS (0.5 mM), we still obtained WS_2 thin layers. It means that for the exfoliation of WS_2 with SHS, the concentration of SHS is not limited to the CMC. This result is different from the exfoliation of MoS_2 with SHS, which all results in thick MoS_2 layers, as shown in Table 1. This might be because the different hydrophobicity of WS_2 and MoS_2 results in different interaction intensity between the TMDs and SHS.[42] All the A-exciton positions and bandgap values are listed in **Table 2**, for the sake of comparison.

Exfoliation from the bulk to a 2D layered material results in a change of chemical structure and electronic properties on the surface of the samples. Therefore, Raman spectroscopy is used as an effective technique for identifying the change in surface chemical bonding and characterizing these exfoliated MoS_2 and WS_2. As shown in **Figure 5**a–c, all the exfoliated MoS_2 samples display two characteristic peaks: the peak at around 383 cm^{-1} is assigned to the E_{2g} mode, while the peak at around 408 cm^{-1} is assigned to the A_{1g} mode.[43,44] E_{2g} and A_{1g} are related to the in-plane and out-of-plane vibrations within the stacked layers. The shift between the two peak positions at ≈383 and ≈408 cm^{-1} can be used to identify the number of layers in that exfoliated MoS_2 particles, since the thickness of the materials is correlated with the frequency.[43–46]

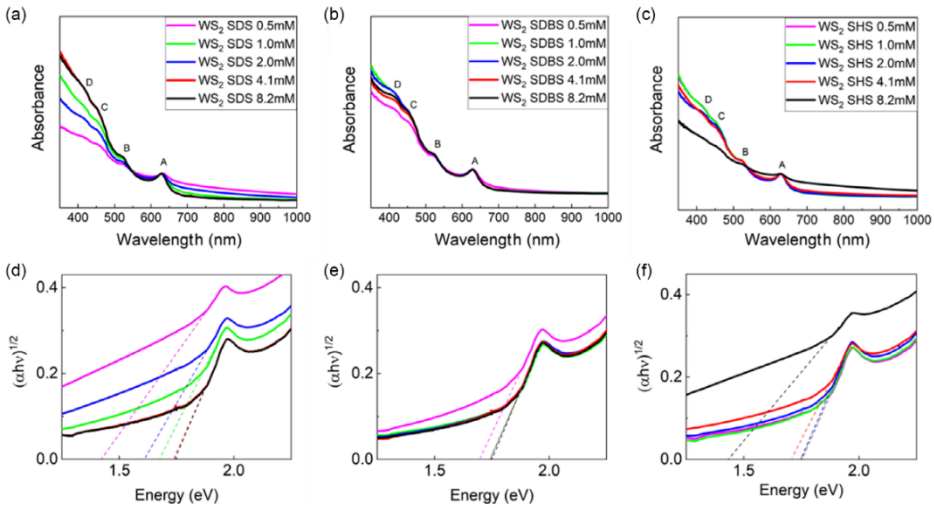

Figure 4. UV–Vis absorption spectra and corresponding Tauc plots of exfoliated WS_2 with a,d) SDS, b,e) SDBS, and c,f) SHS.

ADVANCED SCIENCE NEWS
www.advancedsciencenews.com

physica status solidi rrl
www.pss-rapid.com

Table 2. Positions of A exciton and bandgap values for LPE WS_2 samples with the three different surfactants.

Surfactant	Surfactant concentration [mM]	A-exciton position [nm]	Bandgap [eV]
	8.2	629.3	1.74
	4.1	629.3	1.74
SDS	2.0	630.3	1.61
	1.0	630.9	1.67
	0.5	632.1	1.42
	8.2	629.3	1.74
	4.1	629.3	1.74
SDBS	2.0	628.2	1.75
	1.0	628.2	1.74
	0.5	630.3	1.70
	8.2	628.2	1.43
	4.1	630.3	1.70
SHS	2.0	629.3	1.75
	1.0	629.3	1.75
	0.5	629.3	1.75

Table 3. Distance between E_{2g} and A_{1g} Raman peaks in LPE MoS_2 samples.

Surfactant	Surfactant concentration [mM]	$\Delta\nu$ [cm^{-1}]
	8.2	24.4
	4.1	25.1
SDS	2.0	24.6
	1.0	25.7
	0.5	25
	8.2	25
	4.1	24.9
SDBS	2.0	25.1
	1.0	25.0
	0.5	25.4
	8.2	25
	4.1	25
SHS	2.0	25
	1.0	25
	0.5	25.5

For monolayered MoS_2, at an excitation wavelength of 532 nm, a difference between the A_{1g} and the E_{2g} peak at 18 cm^{-1} is expected. Few layered materials have shifts from 18 to 25 cm^{-1}. Above 25 cm^{-1} samples are expected to be multilayered/bulk-like material. In **Table 3**, the distance of the two Raman peaks is shown for all samples with the three different surfactants and from 0.5 up to 8.2 mM. Apart from SDS 8.2 mM, SDS 2.0 mM, and SDBS 4.1 mM, all other samples show a shift of 25 cm^{-1} or bigger, which is a characteristic of a multilayered material. However, it is important to consider that a certain degree of restacking of the layers is expected during sample preparation, since for the Raman analysis the suspensions are evaporated and the residual dried particles are measured.[47]

Figure 5d–f summarizes the Raman spectra of all the exfoliated WS_2 samples. For all the samples, the peaks relative to

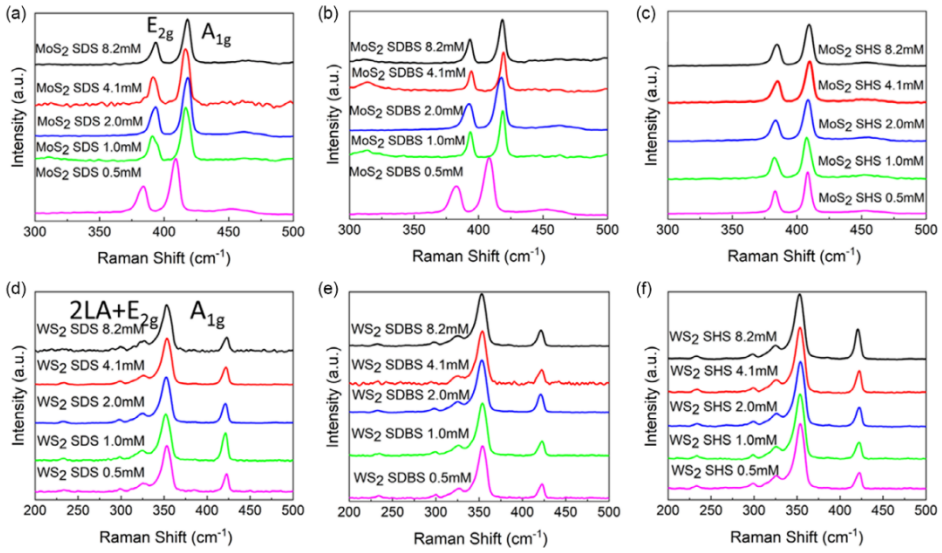

Figure 5. Raman spectra of LPE a–c) MoS_2 and d–f) WS_2.

ADVANCED SCIENCE NEWS
www.advancedsciencenews.com

physica status solidi rrl
www.pss-rapid.com

Table 4. $(2LA + E_{2g})/A_{1g}$ ratios in LPE WS_2 samples.

Surfactant	Surfactant concentration [mM]	$(2LA + E_{2g})/A_{1g}$ ratio
	8.2	3.38
	4.1	2.66
SDS	2.0	2.35
	1.0	1.69
	0.5	2.58
	8.2	3.67
	4.1	3.67
SDBS	2.0	2.90
	1.0	3.81
	0.5	3.34
	8.2	2.17
	4.1	3.00
SHS	2.0	3.40
	1.0	3.90
	0.5	4.05

Table 5. Product concentration and yield for LPE MoS_2 calculated from Lambert–Beer law and from weighted freeze-dried samples.

Surfactant	Surfactant concentration [mM]	Product concentration by UV–vis absorption [mg mL^{-1}]	Product concentration by freeze-drying [mg mL^{-1}]	Yield [%]
	8.2	0.028		0.28
	4.1	0.051		0.51
SDS	2.0	0.077		0.77
	1.0	0.021		0.21
	0.5	0.027		0.27
	8.2	0.085		0.85
	4.1	0.08		0.8
SDBS	2.0	0.093		0.93
	1.0	0.11		1.1
	0.5	0.043		0.43
	8.2	0.032	0.36	0.32
	4.1	0.042		0.42
SHS	2.0	0.027	1.35	0.27
	1.0	0.021		0.21
	0.5	0.061		0.61

$2LA + E_{2g}$ and A_{1g} vibrational modes can be observed, at around 355 and 417 cm^{-1}, respectively.[48,49] As reported by other works present in the literature, the increasing ratio of $(2LA + E_{2g})/A_{1g}$ is due to the decreasing the atomic layers of WS_2 nanosheets.[50] For bulk WS_2, the $(2LA + E_{2g})/A_{1g}$ ratio is around 0.5, while the ratio of monolayered WS_2 reaches above 2. When the ratio value is between 1 and 2, WS_2 nanosheets are present as few-layer-stacked particle layers.[51] As shown in Figure 5d–f and **Table 4**, independent from the type and concentration of the surfactant, all the exfoliated WS_2 samples are adequate for producing monolayer WS_2, except the case of SDS at a concentration of 1.0 mM where a few-layered system was obtained. This might be due to the restacking of the exfoliated samples during the preparation and Raman spectroscopy measurement. In general, for WS_2, we were able to show that all surfactants can produce water-based WS_2 suspension containing highly exfoliated nanosheets and the effect of restacking of the nanosheets is not apparent at the solid state.

ZP measurements were performed to characterize the stability of the obtained colloidal suspensions after LPE. As shown in **Figure 6**, all the samples of MoS_2 and WS_2 provide a ZP value lower than −20 mV, indicating that all the suspensions are colloidally stable and the suspended nanosheets negatively charged. However, when the ZP values are between −20 and −30 mV, the samples show a short-term stability, and a gradual sedimentation of materials was observed after several days. While samples with −30 mV ZP values show a long-term stability up to several months.[52] Specifically, for MoS_2, the application of SDS and SDBS mostly results in a short-term stability, independently from the surfactant concentration, since the ZP values are in the range of −20 and −30 mV, while SHS can increase the stability of the suspension dramatically, with the ZP values of SHS as −30 mV. In contrast, WS_2 suspensions show long-term stability with most of the investigated surfactants and concentrations, except with 1.0 mM SDS. Interestingly, the blue lines in Figure 6 clearly show that with SHS, the suspensions of both MoS_2 and WS_2 gain better stability than that of SDS and SDBS. When studying the impact of surfactant nature on the colloidal stability of the suspensions, no strict rule can be concluded by comparing

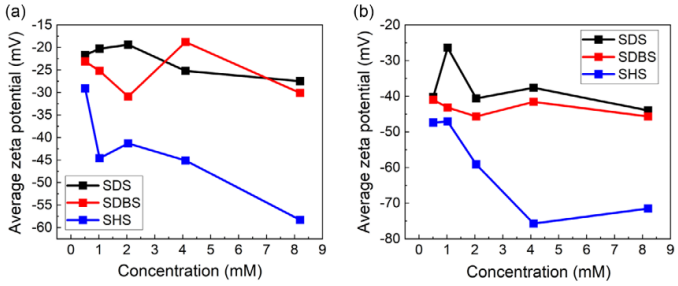

Figure 6. ZP trends for a) MoS_2 and b) WS_2 samples with different type and concentration of surfactants.

ADVANCED SCIENCE NEWS
www.advancedsciencenews.com

physica status solidi pss rrl
www.pss-rapid.com

Table 6. Product concentration and yield for LPE WS_2 calculated from Lambert–Beer law and from weighted freeze-dried samples.

Surfactant	Surfactant concentration [mM]	Product concentration by UV–vis absorption [mg mL^{-1}]	Product concentration by freeze-drying [mg mL^{-1}]	Yield [%]
	8.2	0.068		0.68
	4.1	0.097		0.97
SDS	2.0	0.13	0.23	1.3
	1.0	0.11		1.1
	0.5	0.23		2.3
	8.2	0.12	1.25	0.85
	4.1	0.12		0.8
SDBS	2.0	0.14		0.93
	1.0	0.11		1.1
	0.5	0.12		1.2
	8.2	0.33	0.56	3.3
	4.1	0.11		1.1
SHS	2.0	0.12		1.2
	1.0	0.10		1.0
	0.5	0.098		0.98

the variable parameters. However, there is still a rough trend showing that, with all the surfactants used for MoS_2 and WS_2 exfoliation, higher concentrations increase the colloidal stability of the samples.

The yield in the exfoliated material is another important standard to evaluate the effect of the surfactants and the corresponding experimental parameters used. As described in Section "Calculation Methods of the Sample Concentration," UV–vis spectra are used to quantify the yield and final concentration of each suspension. The product concentration and the corresponding yield of MoS_2 and WS_2 are calculated and listed in **Table 5** and **6**, respectively. The product concentration values changed with surfactant type and concentration, as shown from the trends reported in **Figure 7**. For MoS_2 inks, SDBS results in a better product concentration, compared to the other two surfactants. With a surfactant concentration of 1.0 mM, it was possible to obtain an optimized MoS_2 concentration of 0.11 mg mL^{-1} and the highest yield of 1.1%. In contrast, for WS_2 inks there is no clear evidence showing that the type or the concentration of the surfactants has a relationship with the product concentration and yield. However, we are still able to find the best parameter with SHS 8.2 mM, which can result in an outstanding product concentration of 0.33 mg mL^{-1} and yield of 3.3% compared to other surfactant parameters. These results are comparable to the published works.[53,54] Meanwhile, for some selected samples with relatively high concentration, we were able to obtain the actual concentration from freeze-drying the suspensions. Interestingly, the concentration calculated from freeze-drying method is higher than the concentration obtained from UV–vis spectra. This might be due to the presence of residual surfactants left on the samples after prolonged dialysis, which indicates that the surfactant is tightly anchored on the nanosheet surfaces. These surfactants are necessary to hinder the aggregation of the exfoliated layers when the samples are extracted from inks, though they might influence the future application of the exfoliated products.[55]

3. Conclusion

In conclusion, a systematic study was conducted on the surfactant-assisted LPE of MoS_2 and WS_2 in water. With the aid of three different ionic surfactants (SDS, SDBS, and SHS), exfoliations were carried out in water to produce sustainable colloidal suspensions. By charactering the samples with different techniques, we were able to compare the quality of the exfoliated 2D MoS_2 and WS_2 nanosheets contained in the inks in terms of layer thickness, colloidal stability, and product yield.

For MoS_2, since most experimental parameters result in multilayer samples, the best parameters can be chosen considering the sample stability and product yield. Specifically, 8.2 mM SHS results in the best stability for LPE MoS_2 suspensions, while 1.0 mM SDBS can result in the highest yield of the product. Depending on the target application for the produced ink, one can thus decide whether to proceed with a colloid containing surfactant amount, which is relevant for certain purposes such as use in electronic or energy-related applications.

As for what concerns LPE WS_2, almost all the parameter combinations result in monolayered product, except 8.2 mM SHS, which anyway provides the highest yield in suspended WS_2. And, 4.1 mM SHS is likely the preferred choice to provide the

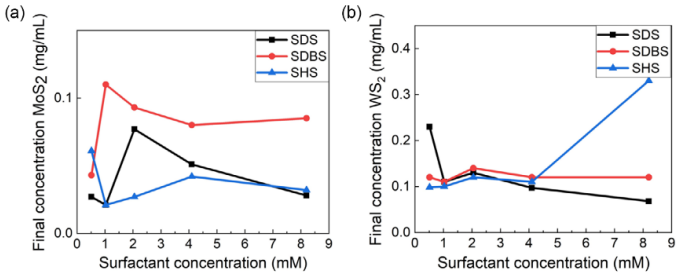

Figure 7. Product concentration trends for a) LPE MoS_2 and b) LPE WS_2 samples.

ADVANCED SCIENCE NEWS
www.advancedsciencenews.com

physica status solidi pss rrl
www.pss-rapid.com

most stable suspension of layered WS_2 in water. Considering that the CMC of SHS is only 0.55 mM, our results surprisingly indicate that the best concentration of SHS in the LPE of MoS_2 and WS_2 is indeed highly above the CMC. As to the product yield, the all the experiments reported in this work obtain a yield of less than 3.3%, which is comparable but does not outperform other published works. Therefore, modifications such as new surfactants with different length of carbon chains and functional groups, or longer exfoliation time, are necessary to increase the product yield. With the detailed provision of a wide scenario of experimental conditions from which to select one's needs for a specific application, such as processing of thin films, nanochemistry, or even biomedicine, this study will constitute a useful tool for further research in the field of sustainable production of 2D material inks.

4. Experimental Section

Materials and LPE Process: MoS_2 (99%), WS_2 (99%), SDS, and SDBS were purchased from Sigma Aldrich and used without further purification. SHS was purchased from TCI Chemicals and used without further purification. All the exfoliations were performed using a tip sonicator and the samples were cooled down to 0 °C with an ice bath during the process. LPE was carried out on a Bandelin Sonopuls tip sonicator, operating with 80% power using pulses of 1 s on/1 s off for 4 h. In all the experiments, the suspension volume was kept fixed at 150 mL with a concentration of the bulk materials of 10 mg mL^{-1}. The concentration of all the surfactants was 8.2, 4.1, 2.0, 1.0, and 0.5 mM. After the sonication step, liquid cascade centrifugation was applied at two different rates. The suspensions obtained after the sonication were centrifuged for 30 min at 1500 rpm and, after keeping the supernatants, those were further centrifuged for 30 min at 3000 rpm with a Universal 320 Hettich centrifuge. Ultrapure water was obtained with the Milli-Q Direct Water Purification System. The detailed parameters of all the experiments performed in this work are listed in Table S1, Supporting Information.

Characterization: UV–visible (UV–vis) absorption spectra of the colloidal inks were recorded on a Goebel Uvikon spectrometer using a quartz cuvette of 1 cm optical length from 350 to 1000 nm with a scan interval of 0.25 nm. Raman spectra were recorded on a Bruker Senterra instrument using a 532 nm laser excitation source with a 2 mW of power, 6 s of integration, and 60 co-additions. The samples were prepared by drop-casting the suspensions over a silicon slide and then analyzed. ZP was measured on a Malvern Zetasizer Nano-ZS device three times and the results were averaged to obtain the final results. The samples were measured in Rotilabo precision glass cuvettes with a light path of 10 mm and a volume of 3.5 mL. TEM images were recorded using a non-aberration-corrected TALOS F200X (ThermoScientific, Eindhoven, Netherland) operated at 200 kV. Images were recorded on a 16Mpxls CMOS camera with a 1 s exposure time.

Calculation Methods of the Sample Concentration: UV analysis was employed to calculate the final concentration of the 2D materials. A calibration line was obtained using a set of dilutions from a suspension with a known concentration, obtained after filtration. The slope of the calibration line corresponded to the extinction coefficient of the dispersed material. The final concentrations of the MoS_2 and WS_2 were obtained with the Lambert–Beer law (Equation (2))

$$A = \varepsilon bc \tag{2}$$

where A stands for absorbance of the material, ε is the extinction coefficient of the dispersed nanosheets, and c is the concentration of the suspension. In this work, we used the absorption value of the A exciton as A. ε was obtained from the calibration lines from several standard MoS_2 and WS_2 suspensions with known concentrations. For MoS_2, the calculated ε was 7.85 mg mL^{-1} cm, while for WS_2 the ε was 3.91 mg mL^{-1} cm.

The other method used to obtain the final concentration was freeze-drying. Before freeze-drying, dialysis was performed using cellulose dialysis bag (Carl Roth) 14 kDa, filling each bag with 20–25 mL of the desired suspension and closing both sides with a plastic pin once filled. The bag was then left in a suitable Becker with Milli-Q water for 3 days, changing 3 times per day the water. Freeze-drying was performed at −10 °C for 16 h and a pressure of 1 mPa.

Supporting Information

Supporting Information is available from the Wiley Online Library or from the author.

Acknowledgements

M.P., F.B., and M.C. contributed equally to this work. This research was funded by the ERC StG project JANUS BI (grant agreement no. 101041229). M.W. and T.G. also thank Fondazione Compagnia di San Paolo for financial support through the "Bando TRAPEZIO - Paving the way to research excellence and talent attraction". T.G. further acknowledges Fondazione Compagnia di San Paolo for the support through the Starting Grant ERC program. M.C., F. B., and T.G. also acknowledge the support of the European Commission through the H2020 FET-PROACTIVE-EIC-07-2020 project LIGHT-CAP (grant no. 101017821). The authors declare no conflict of interest.

Conflict of Interest

The authors declare no conflict of interest.

Data Availability Statement

The data that support the findings of this study are available from the corresponding author upon reasonable request.

Keywords

2D materials, colloidal inks, green chemistry, surfactant-assisted liquid-phase exfoliations, sustainabilities, transition-metal dichalcogenides

Received: January 31, 2024
Revised: February 20, 2024
Published online:

[1] S. Ott, N. Wolff, F. Rashvand, V. J. Rao, J. Zaumseil, C. Backes, *Chem. Mater.* **2019**, *31*, 8424.
[2] X. Geng, J. Yi, *Nano-Sized Multifunctional Materials: Synthesis, Properties and Applications*, Elsevier, Amsterdam **2019**, pp. 117–144.
[3] Y. Guan, H. Yao, H. Zhan, H. Wang, Y. Zhou, J. Kang, *RSC Adv.* **2021**, *11*, 14085.
[4] C. Nie, J. Wang, B. Cai, B. Lai, S. Wang, Z. Ao, *Appl. Catal., B* **2024**, *340*, 123173.
[5] Z. Liang, R. Shen, Y. H. Ng, P. Zhang, Q. Xiang, X. Li, *J. Mater. Sci. Technol.* **2020**, *56*, 89.
[6] A. Sebastian, R. Pendurthi, T. H. Choudhury, J. M. Redwing, S. Das, *Nat. Commun.* **2021**, *12*, 693.
[7] C. Lan, C. Li, J. C. Ho, Y. Liu, *2D WS2: From Vapor Phase Synthesis to Device Applications*, Vol. *7*, Blackwell Publishing Ltd., Hoboken **2021**.

[8] M. H. Kang, D. Lee, J. Sung, J. Kim, B. H. Kim, J. Park, *Comprehensive Nanoscience and Nanotechnology*, Elsevier, Amsterdam **2019**, pp. 55–90.
[9] S. Pinilla, J. Coelho, K. Li, J. Liu, V. Nicolosi, *Two-Dimensional Material Inks*, Vol. *7*, Nature Research, London **2022**, pp. 717–735.
[10] J. N. Coleman, M. Lotya, A. O'neill, S. D. Bergin, P. J. King, U. Khan, K. Young, A. Gaucher, S. De, R. J. Smith, I. V. Shvets, S. K. Arora, G. Stanton, H.-Y. Kim, K. Lee, G. T. Kim, G. S. Duesberg, T. Hallam, J. J. Boland, J. J. Wang, J. F. Donegan, J. C. Grunlan, G. Moriarty, A. Shmeliov, R. J. Nicholls, J. M. Perkins, E. M. Grieveson, K. Theuwissen, D. W. Mccomb, P. D. Nellist, et al., *Science* **2011**, *331*, 568.
[11] R. J. Smith, P. J. King, M. Lotya, C. Wirtz, U. Khan, S. De, A. O'Neill, G. S. Duesberg, J. C. Grunlan, G. Moriarty, J. Chen, J. Wang, A. I. Minett, V. Nicolosi, J. N. Coleman, *Adv. Mater.* **2011**, *23*, 3944.
[12] M. Chhowalla, H. S. Shin, G. Eda, L. J. Li, K. P. Loh, H. Zhang, *Nat. Chem.*, **2013**, *5*, 263.
[13] C. Backes, T. M. Higgins, A. Kelly, C. Boland, A. Harvey, D. Hanlon, J. N. Coleman, *Guidelines for Exfoliation, Characterization and Processing of Layered Materials Produced by Liquid Exfoliation*, Vol. *29*, American Chemical Society, Washington **2017**, pp. 243–255.
[14] Y. Xu, H. Cao, Y. Xue, B. Li, W. Cai, *Liquid-Phase Exfoliation of Graphene: An Overview on Exfoliation Media, Techniques, and Challenges*, Vol. *8*, MDPI AG, Basel **2018**.
[15] Z. Li, R. J. Young, C. Backes, W. Zhao, X. Zhang, A. A. Zhukov, E. Tillotson, A. P. Conlan, F. Ding, S. J. Haigh, K. S. Novoselov, J. N. Coleman, *ACS Nano* **2020**, *14*, 10976.
[16] A. Jawaid, D. Nepal, K. Park, M. Jespersen, A. Qualley, P. Mirau, L. F. Drummy, R. A. Vaia, *Chem. Mater.* **2016**, *28*, 337.
[17] C. X. Hu, Y. Shin, O. Read, C. Casiraghi, *Dispersant-Assisted Liquid-Phase Exfoliation of 2D Materials Beyond Graphene*, Vol. *13*, Royal Society of Chemistry, London **2021**, pp. 460–484.
[18] H. Tao, Y. Zhang, Y. Gao, Z. Sun, C. Yan, J. Texter, *Scalable Exfoliation and Dispersion of Two-Dimensional Materials-An Update*, Vol. *19*, Royal Society of Chemistry, London **2017**, pp. 921–960.
[19] T. Ivanković, J. Hrenović, *Arch. Ind. Hyg. Toxicol.* **2010**, *61*, 95.
[20] A. Griffin, K. Nisi, J. Pepper, A. Harvey, B. M. Szydłowska, J. N. Coleman, C. Backes, *Chem. Mater.* **2020**, *32*, 2852.
[21] Y. J. Lee, L. Huang, H. Wang, M. L. Sushko, B. Schwenzer, I. A. Aksay, J. Liu, *Colloids Interface Sci. Commun.* **2015**, *8*, 1.
[22] S. De, S. Malik, A. Ghosh, R. Saha, B. Saha, *RSC Adv.* **2015**, *5*, 65757.
[23] A. Gupta, V. Arunachalam, S. Vasudevan, *J. Phys. Chem. Lett.* **2015**, *6*, 739.
[24] H. Domínguez, *J. Phys. Chem. B* **2007**, *111*, 4054.
[25] Z. Guan, C. Wang, W. Li, S. Luo, Y. Yao, S. Yu, R. Sun, C. P. Wong, *Nanotechnology* **2018**, *29*, 425702.
[26] A. Roy, P. Kalita, B. Mondal, *J. Mater. Sci.: Mater. Electron.* **2023**, *34*.
[27] B. Zhang, M. Wang, M. Ghini, A. E. M. Melcherts, J. Zito, L. Goldoni, I. Infante, M. Guizzardi, F. Scotognella, I. Kriegel, L. De Trizio, L. Manna, *ACS Mater. Lett.* **2020**, *2*, 1442.
[28] B. Abreu, B. Almeida, P. Ferreira, R. M. F. Fernandes, D. M. Fernandes, E. F. Marques, *J. Colloid Interface Sci.* **2022**, *626*, 167.
[29] S. A. Markarian, L. R. Harutyunyan, R. S. Harutyunyan, *J. Solution Chem.* **2005**, *34*, 361.
[30] Y. Moroi, K. Motomura, R. Matuura, *The Critical Micelle Concentration of Sodium Dodecyl Sulfate-Bivalent Metal Dodecyi Sulfate Mixtures in Aqueous Solutions*.
[31] K. Yang, L. Zhu, B. Xing, *Environ. Sci. Technol.* **2006**, *40*, 4274.
[32] N. Baccile, A. Poirier, *Microbial Biobased Amphiphiles (Biosurfactants): General Aspects on CMC, Surface Tension and Phase Behaviour*, Vol. *1*, Elsevier, Amsterdam **2022**, pp. 1–38.
[33] G. Solomon, R. Mazzaro, V. Morandi, I. Concina, A. Vomiero, *Crystals* **2020**, *10*, 1.
[34] H. C. Kim, H. Kim, J. U. Lee, H. B. Lee, D. H. Choi, J. H. Lee, W. H. Lee, S. H. Jhang, B. H. Park, H. Cheong, S. W. Lee, H. J. Chung, *ACS Nano* **2015**, *9*, 6854.
[35] A. Eghbali, A. A. Vyshnevyy, A. V. Arsenin, V. S. Volkov, *Biosensors* **2022**, *12*, 582.
[36] C. Backes, K. R. Paton, D. Hanlon, S. Yuan, M. I. Katsnelson, J. Houston, R. J. Smith, D. McCloskey, J. F. Donegan, J. N. Coleman, *Nanoscale* **2016**, *8*, 4311.
[37] A. Griffin, A. Harvey, B. Cunningham, D. Scullion, T. Tian, C. J. Shih, M. Gruening, J. F. Donegan, E. J. G. Santos, C. Backes, J. N. Coleman, *Chem. Mater.* **2018**, *30*, 1998.
[38] T. P. Nguyen, W. Sohn, J. H. Oh, H. W. Jang, S. Y. Kim, *J. Phys. Chem. C* **2016**, *120*, 10078.
[39] S. M. Winata, V. Fauzia, in *Journal of Physics: Conf. Series*, Institute of Physics, Bristol **2022**.
[40] G. A. Ermolaev, Y. V. Stebunov, A. A. Vyshnevyy, D. E. Tatarkin, D. I. Yakubovsky, S. M. Novikov, D. G. Baranov, T. Shegai, A. Y. Nikitin, A. V. Arsenin, V. S. Volkov, *NPJ 2D Mater. Appl.* **2020**, *4*, 21.
[41] G. S. Bang, K. W. Nam, J. Y. Kim, J. Shin, J. W. Choi, S. Y. Choi, *ACS Appl. Mater. Interfaces* **2014**, *6*, 7084.
[42] T. Krasian, W. Punyodom, P. Worajittiphon, *Chem. Eng. J.* **2019**, *369*, 563.
[43] H. Li, Q. Zhang, C. C. R. Yap, B. K. Tay, T. H. T. Edwin, A. Olivier, D. Baillargeat, *Adv. Funct. Mater.* **2012**, *22*, 1385.
[44] B. Adilbekova, Y. Lin, E. Yengel, H. Faber, G. Harrison, Y. Firdaus, A. El-Labban, D. H. Anjum, V. Tung, T. D. Anthopoulos, *J. Mater. Chem* **2020**, *8*, 5259.
[45] B. Chakraborty, H. S. S. R. Matte, A. K. Sood, C. N. R. Rao, *J. Raman Spectrosc.* **2013**, *44*, 92.
[46] M. W. Iqbal, K. Shahzad, R. Akbar, G. Hussain, *Microelectron. Eng.* **2020**, *219*, 111152.
[47] Y. Zhao, Y. Sun, M. Bai, S. Xu, H. Wu, J. Han, H. Yin, C. Guo, Q. Chen, Y. Chai, Y. Guo, *J. Phys. Chem. C* **2020**, *124*, 11092.
[48] H. R. Gutiérrez, N. Perea-López, A. L. Elías, A. Berkdemir, B. Wang, R. Lv, F. López-Urías, V. H. Crespi, H. Terrones, M. Terrones, *Nano Lett.* **2013**, *13*, 3447.
[49] A. Berkdemir, H. R. Gutiérrez, A. R. Botello-Méndez, N. Perea-López, A. L. Elías, C. I. Chia, B. Wang, V. H. Crespi, F. López-Urías, J. C. Charlier, H. Terrones, M. Terrones, *Sci. Rep.* **2013**, *3*, 1755.
[50] M. Crisci, F. Boll, L. Merola, J. J. Pflug, Z. Liu, J. Gallego, F. Lamberti, T. Gatti, *Front. Chem.* **2022**, *10*, 1.
[51] A. M. Abdelkader, I. A. Kinloch, *ACS Sustainable Chem. Eng.* **2016**, *4*, 4465.
[52] J. Kim, S. Kwon, D. H. Cho, B. Kang, H. Kwon, Y. Kim, S. O. Park, G. Y. Jung, E. Shin, W. G. Kim, H. Lee, G. H. Ryu, M. Choi, T. H. Kim, J. Oh, S. Park, S. K. Kwak, S. W. Yoon, D. Byun, Z. Lee, C. Lee, *Nat. Commun.* **2015**, *6*, 8294.
[53] D. Sahoo, B. Kumar, J. Sinha, S. Ghosh, S. S. Roy, B. Kaviraj, *Sci. Rep.* **2020**, *10*, 10759.
[54] L. Ma, Z. Liu, Z. L. Cheng, *Ceram. Int.* **2020**, *46*, 3786.
[55] C. Verma, C. M. Hussain, M. A. Quraishi, A. Alfantazi, *Green Surfactants For Corrosion Control: Design, Performance and Applications*, Vol. *311*, Elsevier B.V., Amsterdam **2023**.

WILEY-VCH

Supporting Information for:

Systematic investigation on the surfactant-assisted liquid phase exfoliation of MoS_2 and WS_2 in water for sustainable 2D material inks

Micaela Pozzati, Felix Boll, Matteo Crisci, Sara Domenici, Bernd Smarsly, Teresa Gatti and Mengjiao Wang**

Table S1. Parameters selected and varied during the LPE process for the two investigated TMDs.

TMD	Initial bulk concentration (mg/mL)	Surfactant	Surf. concentration (mM)	Exfoliation time
MoS_2, WS_2	10	SDS	8.2 4.1 2.0 1.0 0.5	3 h
MoS_2, WS_2	10	SDBS	8.2 4.1 2.0 1.0 0.5	3 h
MoS_2, WS_2	10	SHS	8.2 4.1 2.0 1.0 0.5	3 h

3.4: Publication n°3

Nanostructure 2D WS_2@PANI nanohybrids for electrochemical energy storage

Authors: **Crisci M.**, Boll F., Merola L., Johannes Pflug J., Liu Z., Gallego J., Lamberti F., Gatti T.

The use of bi-dimensional materials in supercapacitor has been reported extensively and their performances range vastly from tens of F/g to several hundred, depending on the type of synthesis, morphology and type of 2D material used.[11,206,244–246] TMDC, MoS_2 and WS_2 specifically, have been used as well in this context as energy storage devices.[16,247] The capacitance and properties of such materials depends greatly on the synthesis condition and their morphology, as well as the electrolyte used, for example *Mohan V.V. et al.*[248] proposed a high temperature hydrothermal synthesis were WS_2 nano-flowers were produced and reaching capacitances well above 100 F/g at high basic conditions. It is also possible to increase the capacitance of such 2D materials by producing blends and hybrid materials, combining several inorganic 2d materials together, usually TMDC/MXenes and graphene[9,10,249–252], or with other electro active materials[253–256], such as conductive polymers[8]. It is possible to perform further steps and combining together all of these different possibilities, producing a ternary blend as done by *Aftab J. et al*.[257] They used both GO and MoS_2 together with a pseudo-capacitor (MoO_2 in this case) and they managed to achieve capacitances over 1500 F/g in a 3 electrode set up and around 200 F/g in an asymmetric one. The use of three components, however, brings unclear interaction between all the components, despite the high performance. Therefore, easier methodologies to tune the capacitance of supercapacitors is to work and modify their morphology. As stated in the introductive part, supercapacitor store charges, and energy, on their material surface, in contrast with batteries, and therefore and high surface

area and more rough morphology allows for an increase in capacitance. Therefore, tuning this parameter is another valid option to further improve the properties of the final material.

With this context in mind, **Publication n°3** aims to provide additional insights into the binary blends using 2D materials and CPs, specifically focusing on the use of WS_2 and PANI as building blocks, as well as the effect of pseudo templating procedures. Specifically, a saturated NaCl water solution was used as media to produce the blends and its effect on the overall properties was studied. WS_2 was chosen, due to an already optimized procedure developed by *Felix Boll*, one of the co-authors.[258] First, the ink characterization was performed, following the established procedure reported in **publication n°1**. Zeta Potential and DLS were performed on the WS_2 inks, still paying attention to the disclaimer mentioned in the **publication n°1** about the use of such techniques, and optical data were gathered using UV-Vis and, there, the typical peaks, related to the excitonic transition in the structure were observed. XRD and Raman measurements were performed at every production step to follow the evolution of the final material: firstly, only information related to the 2D material are observed, but when the hybrid material was produced, signal belonging to the PANI were observed. Additionally, the final hybrids' morphology was characterized by SEM, showing a mixture of different morphologies, going from 2D sheets, cylindrical rods and web like filament connecting the various structures, and simultaneously bulk elemental analysis was performed via EDX. Following this analysis, surface elemental analysis via XPS was performed to discern the amount of the different elements, as well as their oxidation states and chemical bonds. Finally, the electrochemical properties of the materials were studied via GCD to obtain information about the charge storage properties, while EIS was used to study the resistance related to this surface process.

In conclusion, this work reports on the possibility to use pseudo templating procedure to further tune the morphology and, consequently, the electrochemical

storage capabilities of 2D-materials and CPs based binary blends, trailblazing the way forward for the application of such methodology to other systems.

In this paper the synthesis of the material and basic characterization (Raman and XRD) was performed by my student Jonas Pflug and by me, while I also performed the electrochemical characterization and XRD, SEM and EDX analysis. Felix Boll also contributed to the paper by sharing his knowledge on the synthesis of WS_2.

frontiers | Frontiers in Chemistry

TYPE Original Research
PUBLISHED 08 September 2022
DOI 10.3389/fchem.2022.1000910

OPEN ACCESS

EDITED BY
Hai-Chao Chen,
Qingdao University, China

REVIEWED BY
Pingping Yu,
Jiangnan University, China
Mao-Cheng Liu Liu,
Lanzhou University of Technology, China

*CORRESPONDENCE
Teresa Gatti,
teresa.gatti@phys.chemie.uni-giessen.de

SPECIALTY SECTION
This article was submitted to Electrochemistry, a section of the journal Frontiers in Chemistry

RECEIVED 22 July 2022
ACCEPTED 23 August 2022
PUBLISHED 08 September 2022

CITATION
Crisci M, Boll F, Merola L, Pflug JJ, Liu Z, Gallego J, Lamberti F and Gatti T (2022), Nanostructured 2D WS_2@PANI nanohybrids for electrochemical energy storage.
Front. Chem. 10:1000910.
doi: 10.3389/fchem.2022.1000910

Nanostructured 2D WS_2@PANI nanohybrids for electrochemical energy storage

Matteo Crisci[1,2], Felix Boll[1,2], Leonardo Merola[1,3], Jonas Johannes Pflug[1], Zheming Liu[3], Jaime Gallego[1,2], Francesco Lamberti[4] and Teresa Gatti[1,2]*

[1]Institute of Physical Chemistry, Justus Liebig University, Giessen, Germany, [2]Center for Materials Research, Justus Liebig University, Giessen, Germany, [3]Nanochemistry Department, Istituto Italiano di Tecnologia, Genova, Italy, [4]Department of Chemical Sciences, University of Padova, Padova, Italy

2D materials are interesting flat nanoplatforms for the implementation of different electrochemical processes, due to the high surface area and tunable electronic properties. 2D transition metal dichalcogenides (TMDs) can be produced through convenient top-down liquid-phase exfoliation (LPE) methods and present capacitive behaviour that can be exploited for energy storage applications. However, in their thermodynamically stable 2H crystalline phase, they present poor electrical conductivity, being this phase a purely semiconducting one. Combination with conducting polymers like polyaniline (PANI), into nanohybrids, can provide better properties for the scope. In this work, we report on the preparation of 2D WS_2@PANI hybrid materials in which we exploit the LPE TMD nanoflakes as scaffolds, onto which induce the *in-situ* aniline polymerization and thus achieve porous architectures, with the help of surfactants and sodium chloride acting as templating agents. We characterize these species for their capacitive behaviour in neutral pH, achieving maximum specific capacitance of 160 F/g at a current density of 1 A/g, demonstrating the attractiveness of similar nanohybrids for future use in low-cost, easy-to-make supercapacitor devices.

KEYWORDS

2D material, transition metal dichacogenide, nanohybrid, nanostructuring, energy storage

Introduction

Electrochemical energy storage is a central topic in current technology-oriented research (Zhang, 2013; Dutta et al., 2022) and the need to develop devices for different type of applications, ranging from automotive (Xu et al., 2020; Rajagopal et al., 2022) up to wearable electronics (Sumboja et al., 2018) and health monitoring platforms (Chen et al., 2020), triggers the continuous search for novel active materials that can satisfy these variable price and performance/durability demands. In this context, two-dimensional (2D) materials are attracting considerable attention, due to their high surface area and highly tunable electronic and electrochemical properties (Cui et al., 2020), as well as

convenient methods for their large scale production. In particular, the top-down liquid-phase exfoliation (LPE) of bulk layered crystals (Hernandez et al., 2008; Nicolosi et al., 2013; Paton et al., 2014) is a very promising production method, allowing to obtain 2D nanosheets in colloidal form, i.e., as functional inks (Hu et al., 2018; Tian, 2021; Pinilla et al., 2022), suitable for the subsequent processing of solid-state architectures.

Among the many different 2D materials that have been produced and studied in the last decade, 2D transition metal dichalcogenides (TMDs) display interesting electronic and mechanical properties for use in energy storage systems (Cherusseri et al., 2019): in fact, the combination of large surface area and variable oxidation states opens up the possibility to store charges through both the electrical double layer and the pseudocapacitive mechanisms. Unfortunately, the most thermodynamically stable crystalline phase of TMDs, i.e., the 2H phase, is semiconducting, strongly limiting the charge/discharge potential achievable from these nanomaterials. The metastable metallic 1T phase can be alternatively produced through LPE by pre-treating the bulk crystalline material with organolithium compounds (Qian et al., 2020), but concerns about stability under prolonged operation in devices are still an open issue (Tang and Jiang, 2015; Jenjeti et al., 2021). An alternative to the use of bare 2D TMDs comes from the combination of these last ones with other (electro)active functional materials, into composite or nanohybrid (Osella et al., 2021; Versaci et al., 2022) structures. Since many years, conducting polymers represent a valuable option for this type of functional hybridization approach: they are low-cost and light-weight materials, they can be pre-synthesized or directly polymerized *in-situ* and they feature a wide range of convenient electronic properties, which can be exploited for energy conversion and storage applications (Sajedi-Moghaddam et al., 2017). Polyaniline (PANI) in particular, represents a sort of benchmark material for the construction of easy-to-make electrochemical energy storage platforms, due to its excellent environmental and thermal stability, coupled to the high electrical conductivity, typical of the emeraldine salt form, obtained when polymerization is carried out in acidic conditions (Beygisangchin et al., 2021).

In this work, we study nanohybrids of 2D WS_2, prepared from LPE of bulk WS_2 powder in environmentally friendly water/isopropanol mixtures (LPE WS_2), and *in situ* polymerized PANI (defined from now on 2D WS_2@PANI), for electrochemical energy storage. Similar composite materials have been studied by Jelinek and co-workers in a recent contribution, targeting the formation of microporous frameworks, in which efficient ion diffusion takes place, and revealing interesting performance in a symmetric supercapacitor architecture (De Adhikari et al., 2021). In order to obtain well-integrated and porous nanoarchitectures, we here adopt a templating strategy that makes use of two different ionic surfactants, namely sodium dodecyl sulphate (SDS) and sodium cholate (NaCh), to promote the effective mixing of the 2D nanosheets and the conducting polymer and of sodium chloride, to tune the morphology and nanostructure of the hybrids, following an example already reported for pure PANI electrodes by Anbalagan and Sawant (2016). The choice of these two specific surfactants is based on their well-known and largely studied ability to efficiently disperse in water-based environments many low-dimensional materials and, in particular, TMDs, as thoroughly discussed in a recent, very comprehensive review on the topic (Hu et al., 2021). The thus obtained different hybrid species are characterized for their structural and electrochemical performance, revealing important structure-to-property-to-function relationships which can be exploited to identify the most promising combinations for use in supercapacitor-like devices.

Experimental section

Materials and methods

All chemicals and solvents were purchased from Sigma-Aldrich and used without any further purification. Raman spectra were recorded on a Bruker Senterra instrument using a 514 nm laser excitation source, a ×50 magnification lens, 2 mW laser power, a 5 s integration time and 20 co-additions. The samples were analysed in solution (LPE WS_2 and LPE WS_2 re-dispersed) or prepared by disposing powders over a silicon slide (Bulk WS_2 and filtered LPE WS_2) and then analysed. Powder X-ray diffraction (P-XRD) measurements were performed on PANanalytical B.V. Empyrean in the 5–75° range using a measurement step of 0.013° and hold time of 75 s. Transmission electron microscopy (TEM) was carried out on a JEOL-1100 transmission electron microscope with an acceleration voltage of 100 kV. The sample was prepared by dropping dilute suspensions of LPE WS_2 onto carbon film-coated 200 mesh copper grids. Scanning electron microscopy (SEM) was performed on a Zeiss Merlin instrument at a working potential of 4 kV. Energy-dispersive x-ray analysis (EDX) was performed on the same instrument at a working potential of 8 kV, an electron beam current of 8 nA and a X-Max 50 Silicon Drift Detector with 50 mm^2 active area and polymer window was used. Nitrogen physisorption experiments were performed at 77 K with an automated gas adsorption station Quadrasorb EVO by Quantachrome Instruments. Prior to the measurements, the samples were degassed in vacuum for 12 h at 50°C. The surface area was determined using the BET method, and the pore size distributions were calculated *via* the nonlocal density functional theory (NLDFT) approach, using the adsorption branch of the isotherm. X-ray photoelectron spectroscopy (XPS) measurements were conducted with a PHI 5000 VersaProbe II Scanning ESCA Microprobe (Physical Electronics) with monochromatized Al Kα X-ray source in

high power mode (beam size 1,300 µm × 100 µm, X-ray power: 100 W). Time steps of 50 ms, a step size of 0.2 eV and an analyzer pass energy of 46.95 eV were used for measuring the detail spectra. The sample surface was charge neutralized with slow electrons and argon ions, and the pressure was in the range from 10^{-7} to 10^{-6} Pa during the measurement. Data analysis was performed using the CasaXPS software.

Liquid-phase exfoliation of WS_2

For LPE, WS_2 powder with a particle size of 2 µm and a purity of 99% and sodium cholate hydrate (NaCh, from bovine and/or ovine bile) with a purity of 99% were employed. Up to a volume of 500 ml, LPE was carried out in a mixture of isopropanol and demineralized water at a ratio of 7:3 v/v. First, 1 mg/ml of NaCh was added to the solvent mixture and stirred until a clear solution was obtained. Afterwards, 10 mg/ml of the bulk WS_2 powder was added to the solution under continuous stirring for 10 min. The suspension was then further homogenized for 30 min in an ultrasonic bath. The LPE was carried out employing an IKA T25 digital Ultra-Turrax shear mixer at 8,000 RPM for 4 h, while the suspension was covered and cooled in an ice bath to avoid solvent evaporation. The final mixture was allowed to undergo gravitational sedimentation for 4 days, after which the colour changed from black to a yellow-brown nuance in the supernatant, which was thus separated from the precipitate (pellet). This final LPE WS_2 ink was filtered on an Omnipore-Teflon-Membrane (0.2 µm, from Merck Millipore), washed thoroughly on the filter with water to remove any NaCh residue and dried in vacuum, to determine the yield in 2D WS_2 (~2%). The LPE WS_2 was then recovered from the filter by re-dispersing it in isopropanol with the help of the ultrasonic bath and isolated as a powder after isopropanol evaporation under reduced pressure.

Synthesis of 2D WS_2@PANI hybrids

Pure PANI was synthesized through oxidative polymerization by first preparing a 0.1 M solution of aniline in 1 M HCl saturated with NaCl (brine). In another container, a 1.15 M solution of $K_2S_2O_8$ was prepared in 1 M HCl (also saturated with NaCl). Both solutions were then combined together and cooled to 0°C using an ice bath. After stirring for 30 min, the suspension was filtrated under vacuum and washed with 200 ml of 1 M HCl and twice with 25 ml of acetone. The formed product was dried at 40°C in a vacuum oven overnight. 0.4893 g of a dark green, almost black solid was obtained, which corresponds to a yield of 98%. For synthesis of the 2D WS_2@PANI hybrids, a slightly modified procedure was used: first the surfactant (1.25 mg/ml for SDS, 1.5 mg/ml for NaCh) was dissolved in 1 M HCl saturated with brine. Afterwards the respective amount of the LPE WS_2 powder (0.01, 0.02 and 0.05 equivalents compared to the used aniline) was added and dispersed by sonicating in an ultrasound bath at 37 Hz, 60% power for 15 min. Then, 0.245 ml of aniline were added to still form a 0.1 M solution. Afterwards, the mixture was combined with the same oxidant solution, as previously described, and the protocol continued as above. Since different WS_2/PANI molar ratio were prepared, Table 1 summarizes the relative quantities for each involved chemical and the quantity of product obtained.

Electrochemical testing

The electrochemical performance of the 2D WS_2@PANI hybrids was characterized by galvanostatic charge-discharge (GCD) and electrochemical impedance spectroscopy (EIS) using a three-electrode set up based on a glassy carbon electrode (GC) as working electrode (WE), a platinum wire as counter electrode (CE) and an Ag/AgCl reference electrode (RE). The data have been then translated against the reversible hydrogen electrode (RHE), for the sake of clarity. The tests were performed on an Autolab PGSTAT302 equipped with the Nova (2.1.1.) software. The WE was prepared as follows: an ink of 5 mg/ml of active material was produced by weighting the desired hybrid and dispersing it in 2 ml of H_2O/EtOH (1:1 v/v). Afterwards 60 µl of Nafion (30 µl/ml of ink) were added to the suspension and the final ink was sonicated in ultrasonic bath (40% power, room temperature, 37 kHz frequency) for 1 h. Afterwards, 5 µl of the resulting ink were drop casted on top of the GC WE and dried in oven at 100°C for 1 h before use. The measurements were performed in 0.5 M Na_2SO_4 electrolyte. GCD measurements were performed in the voltage range 0–0.8 V at the different current densities of 0.2, 0.5, 1, 2, 5, 10 A/g. Based on the GCD curve, specific capacitance (C_S) for the single electrode material was calculated using the equation:

$$C_s = \frac{I*\Delta t}{m*\Delta V} \quad (1)$$

where I is the discharge current applied, Δt is the discharge time of the curve, m is the mass of active material on the electrode and ΔV is the potential window. EIS measurements were carried out on a BioLogic SP 200 potentiostat at a constant potential mode of 0 V. Frequency range was varied between 200 kHz and 10 Hz at an amplitude of 5 mV.

Results and discussion

For the production of LPE WS_2, we have optimized a protocol that resorts to the use of shear mixing in green isopropanol/water solvent mixtures (Crisci et al., 2022) in the presence of NaCh as surfactant, to assist the mechanical

TABLE 1 Relative quantities (mg, mmol) for each involved reagent in the preparation of 2D WS_2@PANI nanohybrids and the quantity of product obtained.

WS_2/PANI molar ratio	$K_2S_2O_8$ (mg, mmol)	Surfactant (mg, mmol)	LPE WS_2 (mg, mmol)	Product (mg)
1:20 (+SDS)	919, 9.9	66, 0.2	35, 0.14	281
1:20 (+NaCh)	919, 9.9	77, 0.18	35, 0.14	370
1:50 (+SDS)	919, 9.9	66, 0.2	14, 0.06	331
1:50 (+NaCh)	919, 9.9	77, 0.18	14, 0.06	165
1:100 (+SDS)	919, 9.9	66, 0.2	7, 0.03	284
1:100 (+NaCh)	919, 9.9	77, 0.18	7, 0.03	345

exfoliation by properly adjusting the liquid medium surface tension. Optimization has mostly been addressed at reducing as much as possible the amount of surfactant, while still obtaining a good yield in exfoliated 2D material ink, as well as to be able to scale-up the production up to 500 ml per batch. Remarkably, this process is providing yields that are similar to those obtained by resorting to more classical LPE in high boiling solvents like N-methylpyrrolidone (NMP), while being undoubtedly more suitable from an environmental perspective for the future industrialization of similar inks (Hu et al., 2021). We have then proceeded through a filtration, accompanied by thorough washings, to remove all the surfactant and obtain a powder of the LPE WS_2, directly usable for the preparation of the 2D WS_2@PANI nanohybrids. Although NaCh is also employed within this last process, we had the need to remove the native one, being interested also in testing another surfactant, namely SDS, to compare the effect of the two different molecular structures on the quality of the 2D WS_2@PANI species.

In order to rule out the extensive re-aggregation of the individual few-layers WS_2 nanosheets during filtration and to demonstrate the reversibility of such aggregation following a simple re-dispersion step in ultrasonic bath, we have carried out a thorough Raman analysis, following the detailed description reported in the work of Terrones and coworkers (Berkdemir et al., 2013). The results of this analysis are displayed in Supplementary Figure S1 of the Supplementary Material (SM). By examining the position and relative intensity of the 2LA + E^12g peak in the range 350–375 cm^{-1} and of the A_{1g} peak in the range 410–430 cm^{-1}, it is possible to estimate the average number of layers present in a given WS_2 sample. In Supplementary Figure S1, we show the spectra of the starting bulk WS_2 in powder compared to that of the LPE WS_2 ink in liquid, of the filtered LPE WS_2 ink (as powder) and of the re-dispersed nanomaterial in 1 M HCl in brine in the presence of freshly added surfactant (as a suspension). In these spectra, the two Raman modes under investigation change significantly in position when going from the bulk to the LPE material (the 2LA + E^12g mode shifts from 348 to 364 cm^{-1} and the A_{1g} mode from 413 to 433 cm^{-1}). Also in the filtered material, they never return to the original bulk position, although a slight shift to lower wavenumbers is detectable after filtration. The average number of layers in the nanosheets can be quantified by considering the ratio between the intensities of the 2LA + E^12g mode and the A_{1g} mode. This ratio is lower than 1 (0.95) in bulk WS_2 and increases to a value higher than 2 (2.08) in the LPE WS_2, indicating the production of nanosheets with an average number of layers between 1 and 3, thus a highly exfoliated nanomaterial. TEM images of this material (Supplementary Figure S2) demonstrate their few-layers nature (possibly some mono, bi and tri-layer species are distinguishable), although strong aggregation at the solid-state (i.e., in this case on the TEM grid) takes place, making difficult to distinguish individual flakes. In the filtered species, we observe a decrease of the ratio to values similar to the bulk (0.95), which anyway reconverts to 1.6 in the re-dispersed powder, typical of 2–5 layers nanosheets (Berkdemir et al., 2013), thus again mostly 2D layered species.

The procedure adopted to prepare nanostructured 2D WS_2@PANI hybrids is depicted in Figure 1A, in which the effective mixing between the nanosheets and aniline is ensured by the presence of one of the two investigated surfactants (SDS or NaCh) and the formation of porous architectures is templated by the concomitant action of NaCl crystals (Anbalagan and Sawant, 2016) during the *in situ* oxidative polymerization, triggered by potassium persulfate used as the oxidant. The trapped NaCl crystals are then removed after thorough washings of the filtered composite materials, leaving behind the target 2D WS_2@PANI hybrids. Other than varying the surfactant, we have also tuned the relative molar ratio between LPE WS_2 and aniline, to produce hybrids with different stoichiometries, ranging from 1:20 to 1:50 and up to 1:100.

All the samples have been investigated through Raman and P-XRD analysis, of which prototypical spectra and diffractograms are reported in Figures 1B,C, respectively. The results are compared with the Raman spectra and P-XRD patterns of the two individual components, namely LPE WS_2 and pure PANI, also prepared with the NaCl templating method. From Raman, we can distinguish in the nanohybrid the presence of the two previously discussed 2LA + E^12g and A^{1g} modes of layered WS_2, with positions unvaried with respect to LPE WS_2

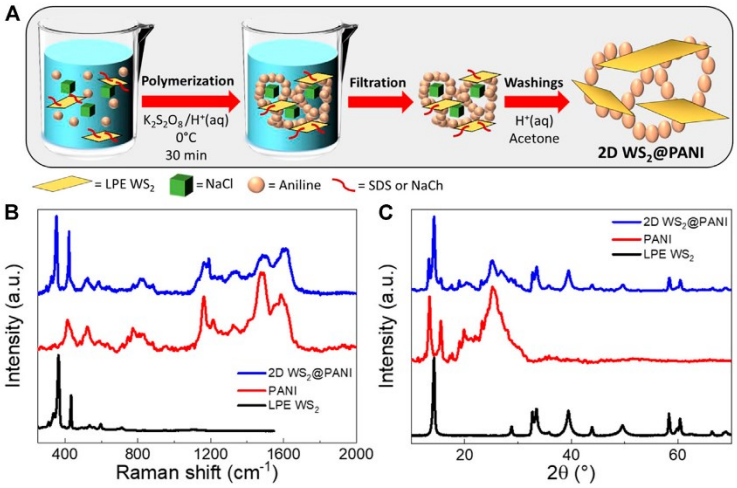

FIGURE 1
(A) Schematic representation of the template-assisted synthesis of nanostructured 2D WS_2@PANI nanohybrids. **(B)** Raman spectra and **(C)** P-XRD diffractograms of the nanostructured 2D WS_2@PANI nanohybrids, of template-assisted synthesized pure PANI and of LPE WS_2 (the P-XRD pattern of this last one has been obtained from the filtered powder).

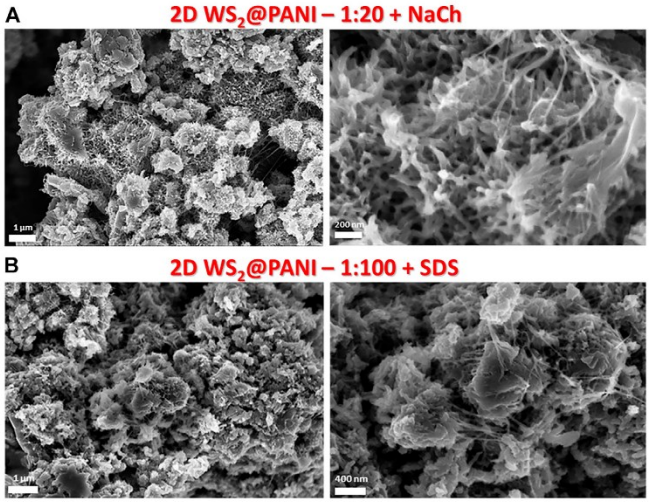

FIGURE 2
SEM images at different magnifications of prototypical nanostructured 2D WS_2@PANI nanohybrids obtained with different LPE WS_2/PANI molar ratios and with different surfactants favouring the proper mixing of the two individual components in the composite. **(A)** 2D WS_2@PANI with 1:20 molar ratio prepared in the presence of NaCh as surfactant. **(B)** 2D WS_2@PANI with 1:100 molar ratio prepared in the presence of SDS as surfactant.

10.3389/fchem.2022.1000910

and intensity ratio typical of highly exfoliated material, although not precisely determinable due to overlapping of the A_{1g} mode with a vibration of PANI (out of plane deformation of the ring structure). Concerning the PANI component in the hybrids, we can observe a change in the relative intensities of the two signals at around 1,600 cm^{-1} (stretching of the conjugated C-C bonds in the quinoid form) and at around 1,480 cm^{-1} (stretching of the C=N bond) with respect to pure PANI, likely indicating a change in the supramolecular structure of the polymeric/oligomeric chains, although extremely complex to exactly determine (Trchová et al., 2014; Stejskal et al., 2017). P-XRD also confirms the presence of the two crystalline components in the hybrids, although no particular additional information can be inferred, if not that residual NaCl is not present in the sample at detectable levels (the typical intense reflex of this last one at $2\theta = 31.7^{\circ}$ is absent in the diffractograms).

The templating and nano-structuring effect of the particular synthetic method here employed is well recognizable from the SEM characterization of the resulting nanohybrid materials. First of all, it should be pointed out that the mixing effect of the surfactant is essential to not achieve phase separation during the *in situ* aniline polymerization in the presence of the LPE WS_2 flakes, as it is testified by the SEM image reported in Supplementary Figure S3 (right) of the SM. This was recorded on a 1:20 2D WS_2@PANI sample, for which individual and aggregated 2D material flakes emerge within a background of the sole polymer scaffold (a SEM detail of the nanomorphology of pure PANI is also provided in the same figure, left, for the sake of comparison). The tendency to self-aggregate is indeed typical of the LPE WS_2 material when casted from the liquid phase onto substrates, as it can be seen from the SEM image also reported in Supplementary Figure S3 (bottom image).

Then, what clearly emerges from SEM images reported in Figure 2 and in Supplementary Figures S4, S5, is a certain difference in the nanomorphology of the different hybrids, obtained in the presence of either NaCh or SDS as the compatibilizer. In particular, for the NaCh-based 2D WS_2@PANI hybrids we can distinguish already at the lowest 2D WS_2/PANI ratio (1:20, Figure 2A) the formation of fractal-like nanostructures, most likely due to the NaCl-templated growth of PANI on the surface of the 2D WS_2 nanosheets, coupled to filaments of the same polymer connecting different areas. These peculiar morphological characteristics are further maintained in the samples with higher 2D material/polymer ratios (Supplementary Figure S4). On the contrary, in the hybrids synthesized in the presence of SDS, the formation of similar complex nano-architectures is only detectable within the 1:100 2D WS_2@PANI sample (Figure 2B), while at the higher TMD contents, the presence of aggregated TMD flakes separated from PANI aggregates is distinguishable. These data might indicate a different ability of the two surfactants to act as proper compatibilizers between the two materials in the composites. In particular, the more extended molecular structure of NaCh,

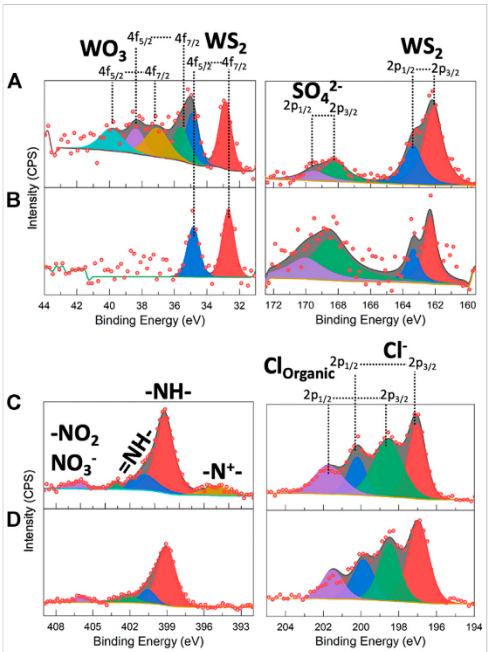

FIGURE 3
XPS spectra of **(A,C)** 2D WS_2@PANI with 1:20 molar ratio prepared in the presence of SDS and **(B,D)** 2D WS_2@PANI with 1:20 molar ratio prepared in the presence of NaCh in the W 4f, S 2p (top panels) and N 1s and Cl 2p (bottom panels) regions.

compared to the mostly linear one of SDS, seems to better provide efficient intermixing between the 2D WS_2 nanosheets and the conjugated polymer. Further studies are anyway necessary to better understand this behaviour. In addition, it is worthy to specify that the formation of the peculiar filament-like nanostructures in these composites is most likely attributed to the use of the saturated brine solution during the synthesis. During this process, NaCl crystallizes from the saturated solution and then re-dissolves during the washings, allowing the formation of short chains and filaments of PANI between the different polymeric domains.

Although the degree of nano-structuring in the synthesized hybrids seems to point out at different overall surface areas for the various type of samples, physisorption data were not varying significantly across both the NaCh- and SDS-based series. Type III N_2 physisorption isotherms were found for all the investigated species (a prototypical one is reported in Supplementary Figure S6), indicating the presence of mostly macropores and surface areas from Brunauer–Emmett–Teller (BET) analysis all in the range 23–27 m^2/g, thus considerably lower than what found for similar species recently (up 70 m^2/g in the work of De Adhikari

TABLE 2 Comparison between atomic % of different elements in 2D WS2@PANI nanohybrids as obtained from XPS and EDX analysis.

At. %	C	N	O	Cl	W	S	S/W ratio	Cl/N ratio
2D-WS2@PANI 1:20 + SDS								
XPS	76.4	11.3	6.1	4.1	0.15	2.05	13.6	0.4
EDX	82.5	10.5	1.1	3.5	0.3	0.4	1.33	0.33
2D-WS2@PANI 1:20 + NaCh								
XPS	74.7	7.8	7.5	4	0.1	0.8	12	0.5
EDX	85.2	10.7	0.8	1.3	0.8	1.2	1.5	0.12

et al. (2021). We completed the compositional analysis of the 2D WS_2@PANI hybrids by comparing XPS and SEM-EDX data for the 1:20 samples prepared in the presence of both SDS and NaCh as compatibilizers. XPS spectra of the tungsten, sulphur, nitrogen and chlorine regions of these species are reported in Figure 3, while the entire spectra are displayed in Supplementary Figure S6, for the sake of completeness. From the W 4f region of the SDS-based hybrid, it is clearly distinguishable the presence of tungsten oxide species together with the native sulphide (Figure 3A). As the oxide is not detectable from P-XRD, it must be related to the sole surface, coming from the there-happening partial oxidation of WS_2. These oxidized species are not detected in the XPS spectrum of the NaCh-based hybrid (Figure 3B), in which only the signals of WS_2 are present: we can therefore argue that the PANI nanostructures seen in the SEM images of the latter and not in those of the former (at least not in the 1:20 sample), act as an effective protecting layer against the surface oxidation of the TMD nanosheets. The S 2p region shows in both samples the presence of WS_2 and of sulfate species, which are most likely related to residues of the oxidant used for PANI polymerization. From N 1s region, it is detected the PANI component in the hybrids, characterized by mostly -NH- and = NH- groups along the chains coming from the aromatic and quinoid polymer forms, but also from small cationic and oxidized nitrogen species, particularly in the SDS-based sample. The level of PANI p-doping can be inferred by analysing the Cl 2p region, where both chloride ions and organic chloride (i.e., chloride directly bonded to carbon atoms) can be distinguished (still, uncertainty would remain on whether some of the chloride signals are not originating from not perfectly washed away NaCl used during the synthesis, although no sodium signal is seen in the XPS spectra, Supplementary Figure S7, indicating the lack of this element on the surface). Qualitatively, the spectra of the two species are not differing significantly, but it is possible to quantify the atomic percentage of the various elements and calculate from that the Cl/N ratio, which is directly related to the extent of doping, since chlorides act as counter-ions for the doped form of the polymer.

In Table 2, we show this quantitative data for the 1:20 SDS- and NaCh-based 2D WS_2@PANI hybrids, calculated from both XPS and SEM-EDX analysis, with the former providing information on the surface composition while the latter of the bulk. As it can be inferred from this numbers, the Cl/N ratio is slightly higher in the NaCh-based sample, although here no clear signal of $-N^+$- species (that are counterions of Cl^- in the p-doped PANI) are present in the N 1s region (Figure 3C).

The S/W ratio could provide some information on the stoichiometry of the WS2 component, although this number is strongly influenced by the presence of the oxidant residues (SO_4^{2-}) and of the sulphate polar head in SDS molecules. Indeed, this ratio is considerably high on the surface, where mot likely these sulphur-containing species are prevalently located, while in the bulk it is closed to the expected value (2), with a slight under-stoichiometric tendency that might be related to sulphur-vacancies present on the 2D WS2 nanosheets (most likely on the edges). Supplementary Figure S8 reports the SEM-EDX maps of the different analysed elements in the 1:20 2D WS2@PANI hybrids prepared in the presence of SDS and NaCh. Here, we can notice the inhomogeneous nature of the former composite, characterized by areas in which WS2 seems confined (W and S signals distribution), while the PANI component is present everywhere (N, C and Cl signals). These data further reinforce the previous speculation made from simple observation of the SEM micrographs, i.e., the low extent of intimate mixing between the two materials in the SDS-containing 1:20 2D WS2@PANI hybrid. On the other hand, for the NaCh-containing hybrid, we can further confirm from Supplementary Figure S7 the highly homogenous nature, with the W and S signals extending over a large part of the mapped area as are those of N and C.

The series of synthesized 2D WS2@PANI hybrids has been characterized for its electrochemical performance in light of the charge storage capability at neutral pH (Figure 4), by investigating them through GCD. The materials have been displaced in the form of powder samples on a GC electrode with the help of Nafion as binder to ensure their safe and stable attachment. The choice of operating at neutral pH is specific for the perspective of employing them in wearable electronics, although it is well known that PANI-based species demonstrate higher capacitances in strongly acidic media (Li et al., 2009).

Figures 4A,B display the calculated CS from GCD curves (Supplementary Figure S9, Figures 4C,D) as a function of the current density for the composites prepared in the presence of, respectively, NaCh and SDS at the different 2D WS2/PANI ratios.

The performance of the two NaCh-containing samples featuring the lowest amount of PANI (1:20 and 1:50) is rather similar and always surpassing that of pure PANI up to high current densities. Remarkably, the CS value at 1 A/g of the 1:20 sample is 160 F/g, thus almost doubling that of pure PANI. In addition, this value is also slightly higher than the CS value at such current density reported by De Adhikari et al. (2021) from similar hybrid materials (140 F/@ 1 A/g) featuring even higher surface areas,

10.3389/fchem.2022.1000910

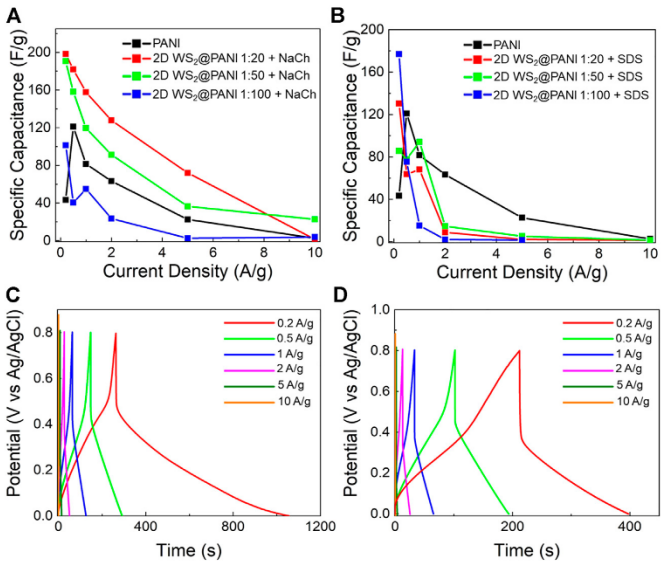

FIGURE 4
Electrochemical performance of 2D WS2@PANI nanohybrids at neutral pH (in 0.5 M Na2SO4 electrolyte). Specific capacitance as a function of current density for 2D WS2@PANI nanohybrids at different molar ratios prepared in the presence of **(A)** NaCh and **(B)** SDS. The data for pure PANI are also provided for the sake of comparison. GCD curves at increasing current densities for **(C)** the 1:20 2D WS2@PANI nanohybrid prepared in the presence of NaCh and **(D)** for pure PANI.

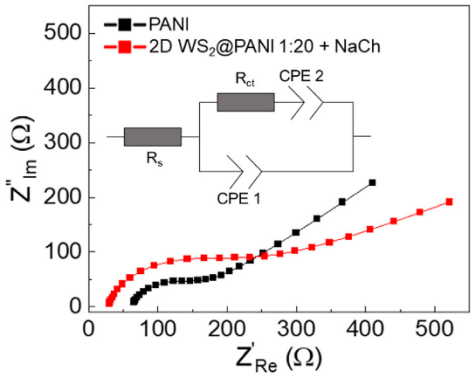

FIGURE 5
EIS analysis-derived Nyquist plots with relative equivalent circuit for the NaCh-based 1:20 2D WS2@PANI nanohybrid and for pure PANI as measured after GCD analysis.

pointing out at the existence of other effects governing the capacitive behaviour in these systems. However, the same cannot be observed for the SDS-based samples, which overall have worst performances than the pristine PANI reference, with the exception of the extremely low current densities regime. The present data seem to confirm the generally lower quality of the constituent materials mutual mixing and nano/microstructure in the SDS-based composites in comparison with the NaCh-based ones, which translates in a poorer electrochemical charge storage ability. The WS2 surface oxidation detected by XPS in these systems, might also be a partial cause of their poor performance, as generally the oxide is less conductive than the sulphide (Liu et al., 2015). Since the capacitive behaviour of pure 2D WS2 is almost negligible (and for this reason not shown here), the results obtained for the 1:20 2D WS2@PANI hybrid prepared in presence of NaCh point out at a notable cooperative effect between the TMD nanosheets and the conducting polymer, which allows to overperform both the individual species involved. This is even more evident when considering that by increasing the conducting polymer content, and thus going more in the

TABLE 3 Fitted values from the EIS characterization of the NaCh-based 1:20 2D WS_2@PANI nanohybrid and for pure PANI after GCD analysis.

Sample	Rs (Ω)	Rct (Ω)	CPE1 (S)	N1	Cdl (uF)	CPE2 (S)	N2
PANI	63	89	1.49e-6	0.87	0.39	0.00051	0.45
2D WS2@ PANI	29	113	7.79e-7	0.89	0.24	0.00076	0.29

direction of a mostly polymer-based active material, the energy storage capability worsens progressively and becomes even lower than that of pure PANI (in the 1:100 sample).

To better characterize the electrochemical behaviour of the champion composite (i.e., the 1:20 2D WS2@PANI + NaCh), we examined more in detail the GCD curves of this material at increasing current densities (Figure 4C). The GCD curves allow to appreciate the longer discharge time typical of the hybrid in comparison to the pure PANI reference (Figure 4D), which contribute to the higher CS measured for the former. In addition, their asymmetric shape is a sign of the pseudocapacitive behaviour of these materials over the range of current densities examined (Chen et al., 2013).

Stability is a key issue when dealing with modified electrodes: delamination of the coating may occur during measurements and EIS is a really sensitive tool for this scope (Jorcin et al., 2006). To further try to understand the long-term energy storage properties of the NaCh-based 1:20 2D WS2@PANI nanohybrid (the best performing sample) in comparison with the reference PANI sample, EIS analysis was carried out on the electrode after GCD characterization, working in the same electrolyte medium, with the relative Nyquist plots reported in Figure 5. Cyclability of the electrodes was indeed an unsuccessful method to understand durability, since it was visually clear that the active materials were progressively detaching from GC during scans. The results of EIS thus provide information about the electrode-electrolyte interface, i.e., the kinetics of the charge transfer mechanisms happening between WS2 and PANI, as well as about the electrode surface area. The experimental data are fitted using a Randles modified cell (Nguyen and Breitkopf, 2018), choosing a constant phase element (CPE) for modeling the double layer capacitance and the Warburg element (Lamberti et al., 2013): in this way the non-ideality of the whole system can be modeled emphasizing the role of each constituent in the composite electrode. In particular, Rs refers to the saturated resistance, Rct is the charge transfer resistance associated to the sodium cations discharge in the underlying GC electrode, the CPE1 is the associated double layer capacitance and CPE2 represents the Warburg element related to the semi-infinite linear diffusion of the ions from the electrolyte towards the electrode. Fitted values are reported in Table 3. The associated Cdl values from the CPE1 values are calculated using the equations reported in reference (Bard and Faulkner, 2000).

The Rct for pure PANI is slightly smaller than the one of the 2D WS_2@PANI best sample (113 vs. 89 Ω), reflecting a reduced conductivity for the TMD-modified PANI electrode: this result suggests a slower charge discharge at the modified electrode after prolonged GCD characterization. This result is also justified by the steeper slope of the Nyqvist plot (i.e., smaller Warburg impedance) for the pristine PANI sample: the diffusion of ions towards the working electrode is therefore strongly limited by the presence of WS_2. Furthermore, the presence of a depressed semicircle in both samples (and therefore the use of a CPE instead of an ideal C) accounts for the inhomogeneity of the surface as supported by SEM analysis (Figure 2): more specifically, one expects to find a quasi-tridimensional surface (Mulder et al., 1990). This is the case of the hybrid sample at least, where a fractal morphology is found. However, the N1 fitted value for the two samples (0.87 for PANI sample and 0.89 for the 2D WS_2@PANI sample) is almost the same thus corroborating the idea that the surface roughness for the two samples is comparable (as also suggested by BET analysis). The delimitation occurred after intense electrochemical characterization accounts for the decrease of about 40% of the value of the Cdl for the composite electrode (0.39 uF for pristine PANI and 0.24 uF for 2D WS_2@PANI sample) that reflects a smaller surface area for this sample.

The EIS results as a whole suggest that capacitive measurements are not conservative for the electrodes as they have been here characterized (i.e., by relatively simple deposition on a GC) and in order to obtain durable devices, it will be necessary to develop an optimized process for their preparation. We further proof this issue by carrying out multiple cycles of charge/discharge on two prototypical composites (the 1:20 2D WS_2@PANI hybrids prepared with both NaCh and SDS) at 1 A/g current density. The results, reported in Supplementary Figure S10 over 100 cycles, show how an almost immediate drop in C_S of almost 30% takes place after only 10 cycles, likely due to progressive detachment of the active material from the GC electrode during cycling. In general, anyway, we can observe a slightly higher stability of the NaCh-based composite, confirming the better agglomeration between the components in this active material. The incorporation within a gel matrix of the 2D WS_2@PANI hybrid material is indeed the next step that we are currently exploring in order to produce stable supercapacitors retaining the capacitive properties found in the current study.

Conclusion

In this work, we report on a series of electro-active composite materials between LPE WS_2 nanoflakes and *in-situ* polymerized

PANI with large interest for application into the next-generation of low-cost, light-weight energy storage devices. We show how the use of different compatibilizers can strongly influence the level of mixing between the two components and consequently the surface properties, with strong implications into charge accumulation mechanisms. In addition, the concomitant effect of using a simple, inexpensive and easy-to-remove templating agent like NaCl during the synthetic process, allows to tune the nano-structuring of the resulting species, with peculiar morphological features emerging in combination with the compatibilizer, which have likely a large influence on the observed capacitive behaviour.

The combined physico-chemical and electrochemical characterization of these species provides significant hints on the structure-property-function relationships, which will serve for the design of even more active nano-structured energy storage materials. Our future plans include their integration into flexible supercapacitor architectures by previous incorporation into hydrogel scaffolds, targeting the field of wearable technologies, which will likely cover a large portion of the market for electronic products in the up-coming decades.

Data availability statement

The raw data supporting the conclusion of this article will be made available by the authors, without undue reservation.

Author contributions

MC, FB, JP, and LM prepared the materials and studied their properties. JG carried out XPS analysis. ZL performed TEM characterization. TG supervised the work and wrote the manuscript. All authors have revised the final manuscript.

Funding

This work was supported by the European Commission through the H2020 FET-PROACTIVE-EIC-07-2020 project LIGHT-CAP (project number 101017821).

Conflict of interest

The authors declare that the research was conducted in the absence of any commercial or financial relationships that could be construed as a potential conflict of interest.

Publisher's note

All claims expressed in this article are solely those of the authors and do not necessarily represent those of their affiliated organizations, or those of the publisher, the editors and the reviewers. Any product that may be evaluated in this article, or claim that may be made by its manufacturer, is not guaranteed or endorsed by the publisher.

Supplementary material

The Supplementary Material for this article can be found online at: https://www.frontiersin.org/articles/10.3389/fchem.2022.1000910/full#supplementary-material

References

Anbalagan, A. C., and Sawant, S. N. (2016). Brine solution-driven synthesis of porous polyaniline for supercapacitor electrode application. *Polymer* 87, 129–137. doi:10.1016/j.polymer.2016.01.049

Bard, A. J., and Faulkner, L. R. (2000). *Electrochemical methods: Fundamentals and applications*. 2nd Edition. New York: John Wiley & Sons.

Berkdemir, A., Gutiérrez, H. R., Botello-Méndez, A. R., Perea-López, N., Elías, A. L., Chia, C.-I., et al. (2013). Identification of individual and few layers of WS2 using Raman Spectroscopy. *Sci. Rep.* 3, 1755. doi:10.1038/srep01755

Beygisangchin, M., Abdul Rashid, S., Shafie, S., Sadrolhosseini, A. R., and Lim, H. N. (2021). Preparations, properties, and applications of polyaniline and polyaniline thin films a review. *Polym. (Basel).* 13, 2003. doi:10.3390/polym13122003

Chen, W., Rakhi, R. B., and Alshareef, H. N. (2013). Facile synthesis of polyaniline nanotubes using reactive oxide templates for high energy density pseudocapacitors. *J. Mat. Chem. A* 1, 3315–3324. doi:10.1039/C3TA00499F

Chen, X., Villa, N. S., Zhuang, Y., Chen, L., Wang, T., Li, Z., et al. (2020). Stretchable supercapacitors as emergent energy storage units for health monitoring bioelectronics. *Adv. Energy Mat.* 10, 1902769. doi:10.1002/aenm.201902769

Cherusseri, J., Choudhary, N., Sambath Kumar, K., Jung, Y., and Thomas, J. (2019). Recent trends in transition metal dichalcogenide based supercapacitor electrodes. *Nanoscale Horiz.* 4, 840–858. doi:10.1039/C9NH00152B

Crisci, M., Dolcet, P., Yang, J., Salerno, M., Bélteky, P., Kukovecz, Á., et al. (2022). Design principles and insights into the liquid-phase exfoliation of alpha-MoO3 for the production of colloidal 2D nano-inks in green solvents. *J. Phys. Chem. C* 126, 404–415. doi:10.1021/acs.jpcc.1c09221

Cui, H., Guo, Y., Ma, W., and Zhou, Z. (2020). 2 D materials for electrochemical energy storage: Design, preparation, and application. *ChemSusChem* 13, 1155–1171. doi:10.1002/cssc.201903095

De Adhikari, A., Shauloff, N., Turkulets, Y., Shalish, I., and Jelinek, R. (2021). Tungsten-Disulfide/polyaniline high frequency supercapacitors. *Adv. Electron. Mat.* 7, 2100025. doi:10.1002/aelm.202100025

Dutta, A., Mitra, S., Basak, M., and Banerjee, T. (2022). A comprehensive review on batteries and supercapacitors: Development and challenges since their inception. *Energy Storage*, e339. doi:10.1002/est2.339

Hernandez, Y., Nicolosi, V., Lotya, M., Blighe, F. M., Sun, Z., De, S., et al. (2008). High-yield production of graphene by liquid-phase exfoliation of graphite. *Nat. Nanotechnol.* 39 (3), 563–568. doi:10.1038/nnano.2008.215

Hu, C.-X., Shin, Y., Read, O., and Casiraghi, C. (2021). Dispersant-assisted liquid-phase exfoliation of 2D materials beyond graphene. *Nanoscale* 13, 460–484. doi:10.1039/D0NR05514J

Hu, G., Kang, J., Ng, L. W. T., Zhu, X.i, Howe, R. C. T., Jones, C. G., et al. (2018). Functional inks and printing of two-dimensional materials. *Chem. Soc. Rev.* 47, 3265–3300. doi:10.1039/C8CS00084K

Jenjeti, R. N., Kumar, R., Sellam, A., and Sampath, S. (2021). High stability of 1T-phase $MoS_{2x}Se_{2(1-x)}$ monolayers under ambient conditions. *J. Phys. Chem. C* 125, 8407–8417. doi:10.1021/acs.jpcc.1c00212

Jorcin, J.-B., Aragon, E., Merlatti, C., and Pébère, N. (2006). Delaminated areas beneath organic coating: A local electrochemical impedance approach. *Corros. Sci.* 48, 1779–1790. doi:10.1016/j.corsci.2005.05.031

Lamberti, F., Ferraro, D., Giomo, M., and Elvassore, N. (2013). Enhancement of heterogeneous electron transfer dynamics tuning single-walled carbon nanotube forest height and density. *Electrochim. Acta* 97, 304–312. doi:10.1016/j.electacta.2013.02.119

Li, H., Wang, J., Chu, Q., Wang, Z., Zhang, F., and Wang, S. (2009). Theoretical and experimental specific capacitance of polyaniline in sulfuric acid. *J. Power Sources* 190, 578–586. doi:10.1016/j.jpowsour.2009.01.052

Liu, H., Han, N., and Zhao, J. (2015). Atomistic insight into the oxidation of monolayer transition metal dichalcogenides: From structures to electronic properties. *RSC Adv.* 5, 17572–17581. doi:10.1039/C4RA17320A

Mulder, W. H., Sluyters, J. H., Pajkossy, T., and Nyikos, L. (1990). Tafel current at fractal electrodes: Connection with admittance spectra. *J. Electroanal. Chem. Interfacial Electrochem.* 285, 103–115. doi:10.1016/0022-0728(90)87113-X

Nguyen, T. Q., and Breitkopf, C. (2018). Determination of diffusion coefficients using impedance spectroscopy data. *J. Electrochem. Soc.* 165, E826–E831. doi:10.1149/2.1151814jes

Nicolosi, V., Chhowalla, M., Kanatzidis, M., Strano, M., and Coleman, J. (2013). Liquid exfoliation of layered materials. *Science* 340, 1226419. doi:10.1126/science.1226419

Osella, S., Wang, M., Menna, E., and Gatti, T. (2021). (INVITED) Lighting-up nanocarbons through hybridization: Optoelectronic properties and perspectives. *Opt. Mater. X* 12, 100100. doi:10.1016/j.omx.2021.100100

Paton, K. R., Varrla, E., Backes, C., Smith, R. J., Khan, U., O'Neill, A., et al. (2014). Scalable production of large quantities of defect-free few-layer graphene by shear exfoliation in liquids. *Nat. Mat.* 13, 624–630. doi:10.1038/nmat3944

Pinilla, S., Coelho, J., Li, K., Liu, J., and Nicolosi, V. (2022). Two-dimensional material inks. *Nat. Rev. Mat.*. doi:10.1038/s41578-022-00448-7

Qian, Z., Jiao, L., and Xie, L. (2020). Phase engineering of two-dimensional transition metal dichalcogenides. *Chin. J. Chem.* 38, 753–760. doi:10.1002/cjoc.202000064

Rajagopal, S., Pulapparambil Vallikkattil, R., Mohamed Ibrahim, M., and Velev, D. G. (2022). Electrode materials for supercapacitors in hybrid electric vehicles: Challenges and current progress. *Condens. Matter* 7, 6. doi:10.3390/condmat7010006

Sajedi-Moghaddam, A., Saievar-Iranizad, E., and Pumera, M. (2017). Two-dimensional transition metal dichalcogenide/conducting polymer composites: Synthesis and applications. *Nanoscale* 9, 8052–8065. doi:10.1039/C7NR02022H

Stejskal, J., Mrlík, M., Plachý, T., Trchová, M., Kovářová, J., and Li, Y. (2017). Molybdenum and tungsten disulfides surface-modified with a conducting polymer, polyaniline, for application in electrorheology. *React. Funct. Polym.* 120, 30–37. doi:10.1016/j.reactfunctpolym.2017.09.004

Sumboja, A., Liu, J., Zheng, W. G., Zong, Y., Zhang, H., and Liu, Z. (2018). Electrochemical energy storage devices for wearable technology: A rationale for materials selection and cell design. *Chem. Soc. Rev.* 47, 5919–5945. doi:10.1039/C8CS00237A

Tang, Q., and Jiang, D. (2015). Stabilization and band-gap tuning of the 1T-MoS2 monolayer by covalent functionalization. *Chem. Mat.* 27, 3743–3748. doi:10.1021/acs.chemmater.5b00986

Tian, X. (2021). Direct ink writing of 2D material-based supercapacitors. *2D Mat.* 9, 012001. doi:10.1088/2053-1583/ac3f43

Trchová, M., Morávková, Z., Bláha, M., and Stejskal, J. (2014). Raman spectroscopy of polyaniline and oligoaniline thin films. *Electrochim. Acta* 122, 28–38. doi:10.1016/j.electacta.2013.10.133

Versaci, D., Canale, I., Goswami, S., Amici, J., Francia, C., Fortunato, E., et al. (2022). Molybdenum disulfide/polyaniline interlayer for lithium polysulphide trapping in lithium-sulphur batteries. *J. Power Sources* 521, 230945. doi:10.1016/j.jpowsour.2021.230945

Xu, C., Dai, Q., Gaines, L., Hu, M., Tukker, A., and Steubing, B. (2020). Future material demand for automotive lithium-based batteries. *Commun. Mat.* 1, 99. doi:10.1038/s43246-020-00095-x

Zhang, S. (2013). Status, opportunities, and challenges of electrochemical energy storage. *Front. Energy Res.* 1, 8. doi:10.3389/fenrg.2013.00008

Supplementary Material for:

Nanostructured 2D WS_2@PANI nanohybrids for electrochemical energy storage

Matteo Crisci,[1,2] Felix Boll,[1,2] Jonas Johannes Pflug,[1] Leonardo Merola,[1,3] Zheming Liu,[4] Jaime Gallego,[1,2] Francesco Lamberti,[3] Teresa Gatti[1,2*]

[1] Institute of Physical Chemistry, Justus Liebig University, Heinrich-Buff-Ring 17, 35392 Giessen, Germany

[2] Center for Materials Research, Justus Liebig University, Heinrich-Buff-Ring 17, 35392 Giessen, Germany

[3] Department of Chemical Sciences, University of Padova, via Marzolo 1, 35131 Padova, Italy

[4] Nanochemistry Department, Istituto Italiano di Tecnologia, via Morego 30, 16163 Genova, Italy

Table of Contents

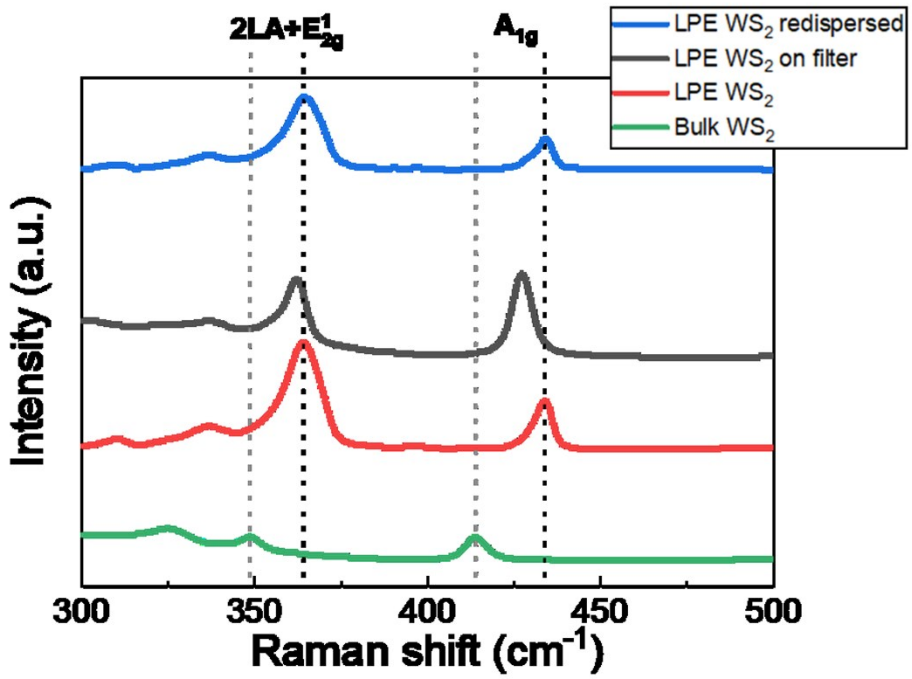

Figure S1. Raman spectra LPE WS_2 pre- and post-filtration and after redispersion of the filtrated material in 1 HCL in brine in the presence of a freshly added surfactant. The spectrum of bulk WS_2 powder is also shown for the sake of comparison.

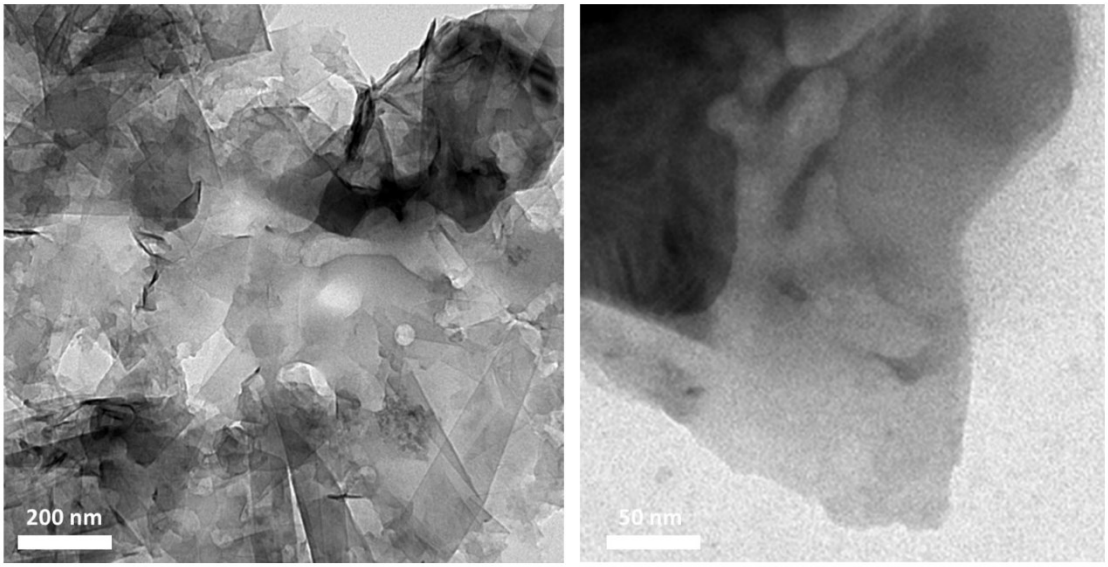

Figure S2. TEM images of LPE WS_2.

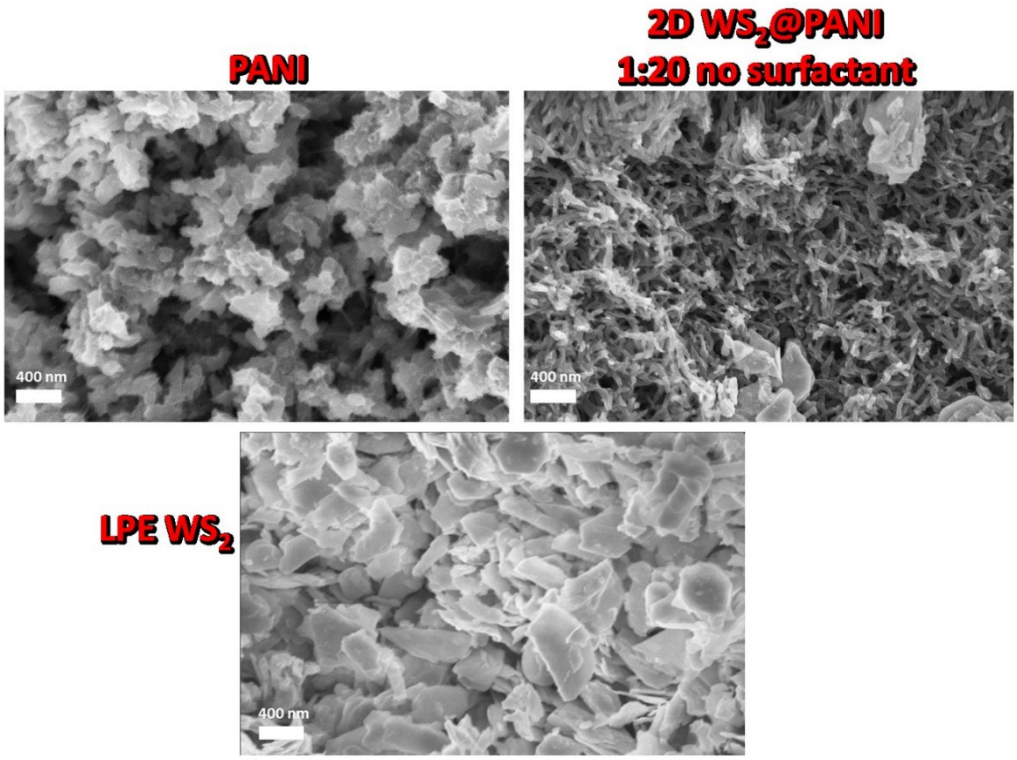

Figure S3. SEM images of template-assisted oxidatively polymerized pure PANI, of a 2D WS2@PANI nanohybrid prepared without the addition of any surfactant and of LPE WS_2 casted from the colloidal phase onto a substrate.

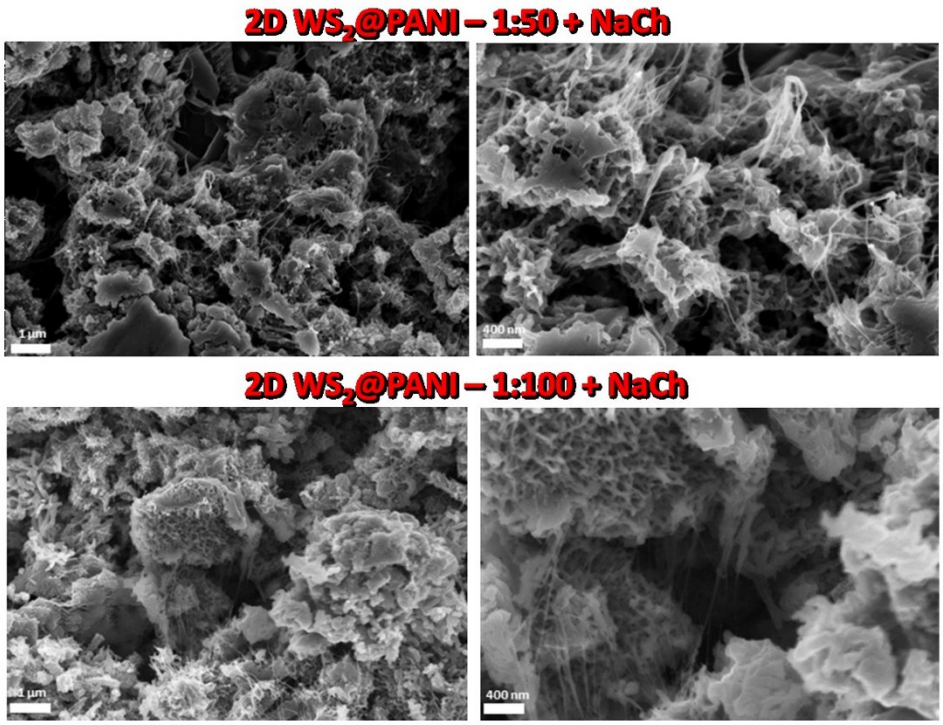

Figure S4. SEM images of 2D WS2@PANI nanohybrids obtained with different LPE WS_2/PANI molar ratios in the presence of NaCh.

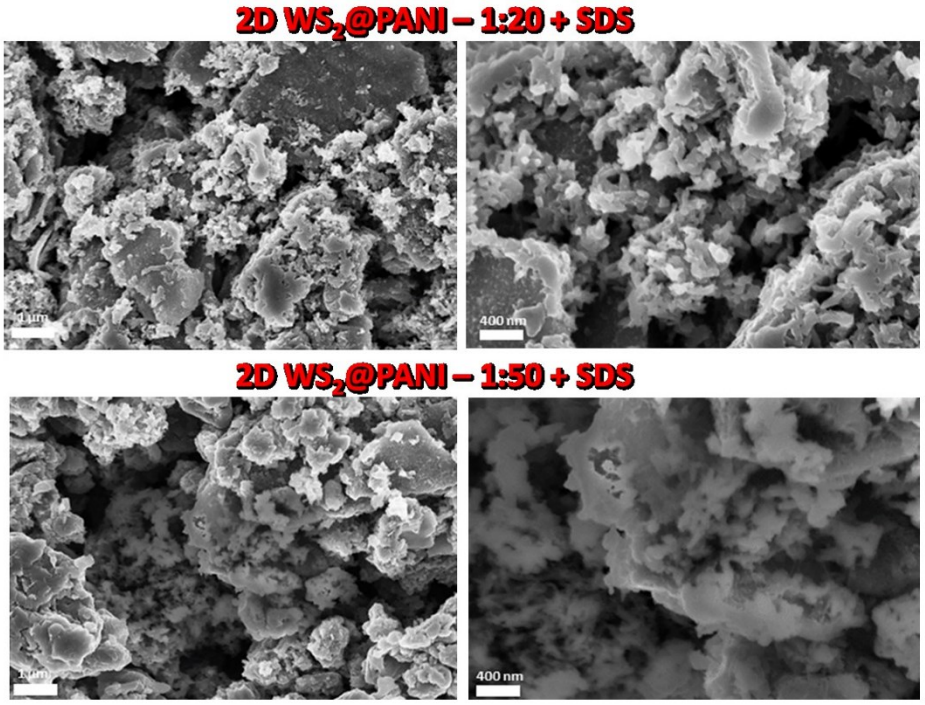

Figure S5. SEM images of 2D WS2@PANI nanohybrids obtained with different LPE WS_2/PANI molar ratios in the presence of SDS.

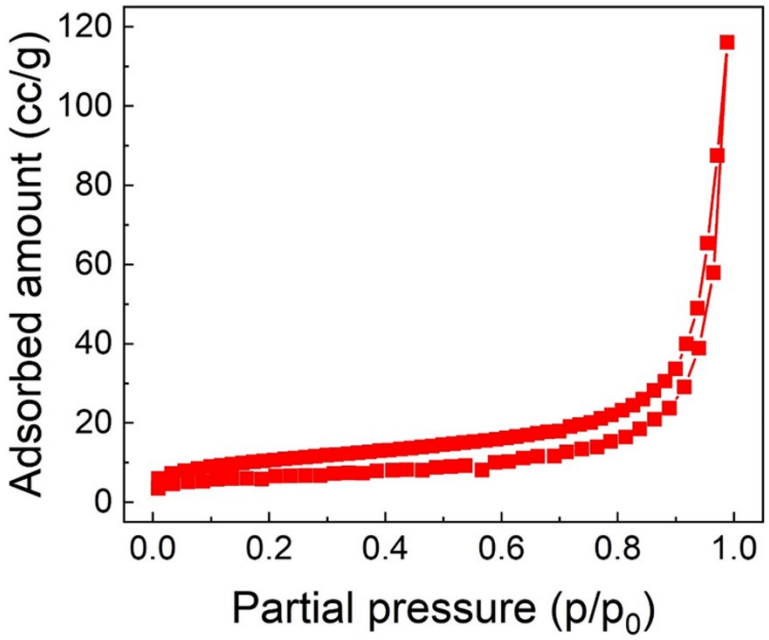

Figure S6. a) N_2 (77 K) physisorption isotherm of a prototypical 2D WS2@PANI nanohybrid. The total surface area is calculated from the adsorption and desorption branches using the NLDFT method.

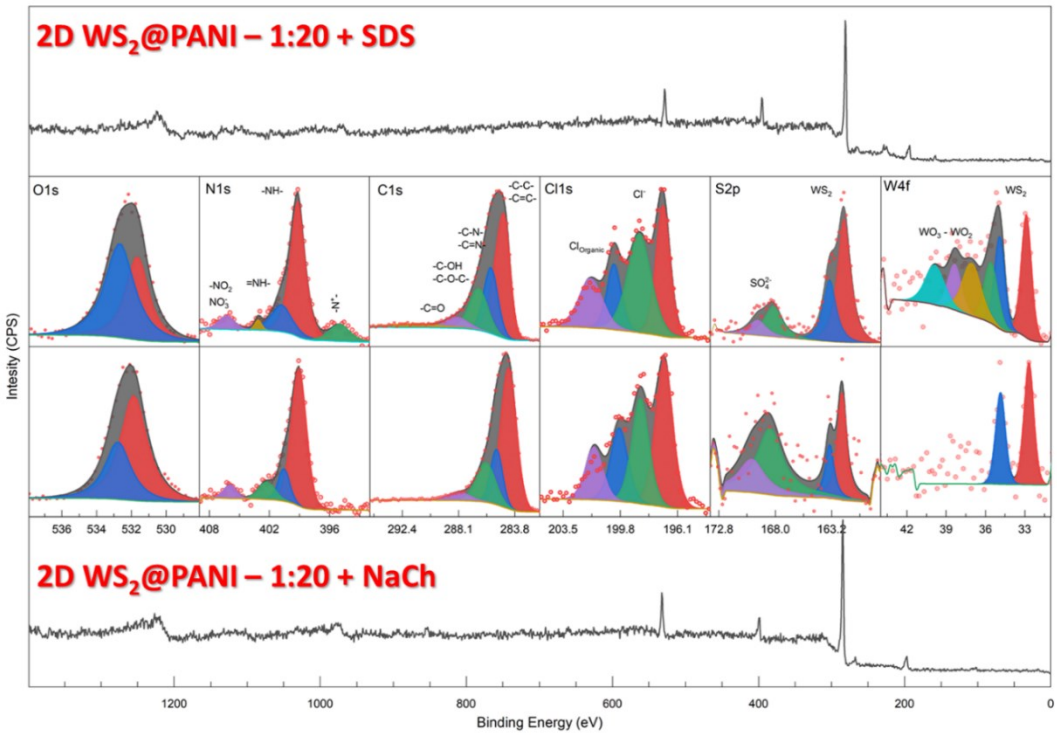

Figure S7. Full XPS spectra of 1:20 2D WS2@PANI nanohybrids prepared in the presence of SDS and NaCh.

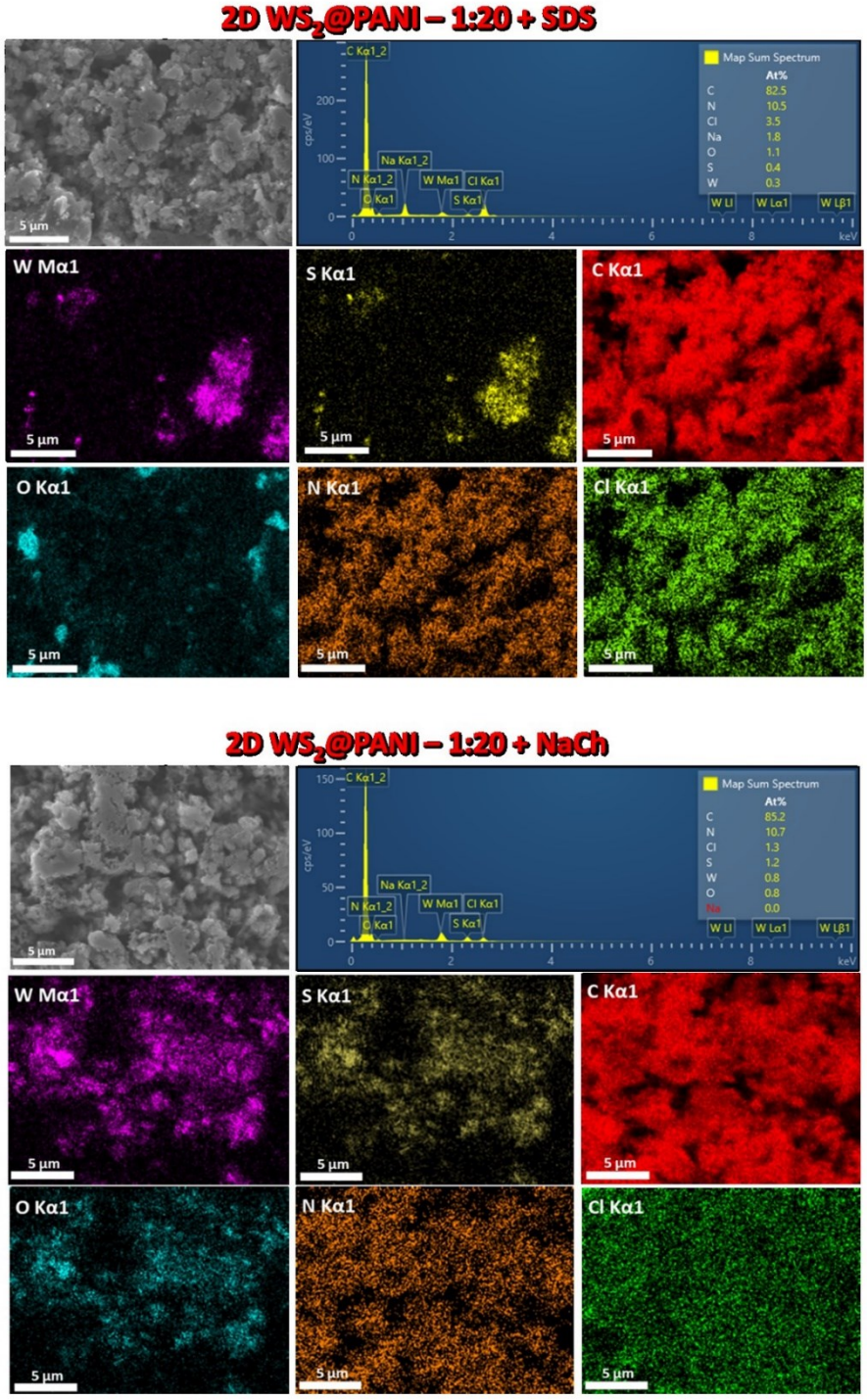

Figure S8. EDX maps of different elements in 1:20 2D WS_2@PANI nanohybrids prepared in the presence of SDS and NaCh.

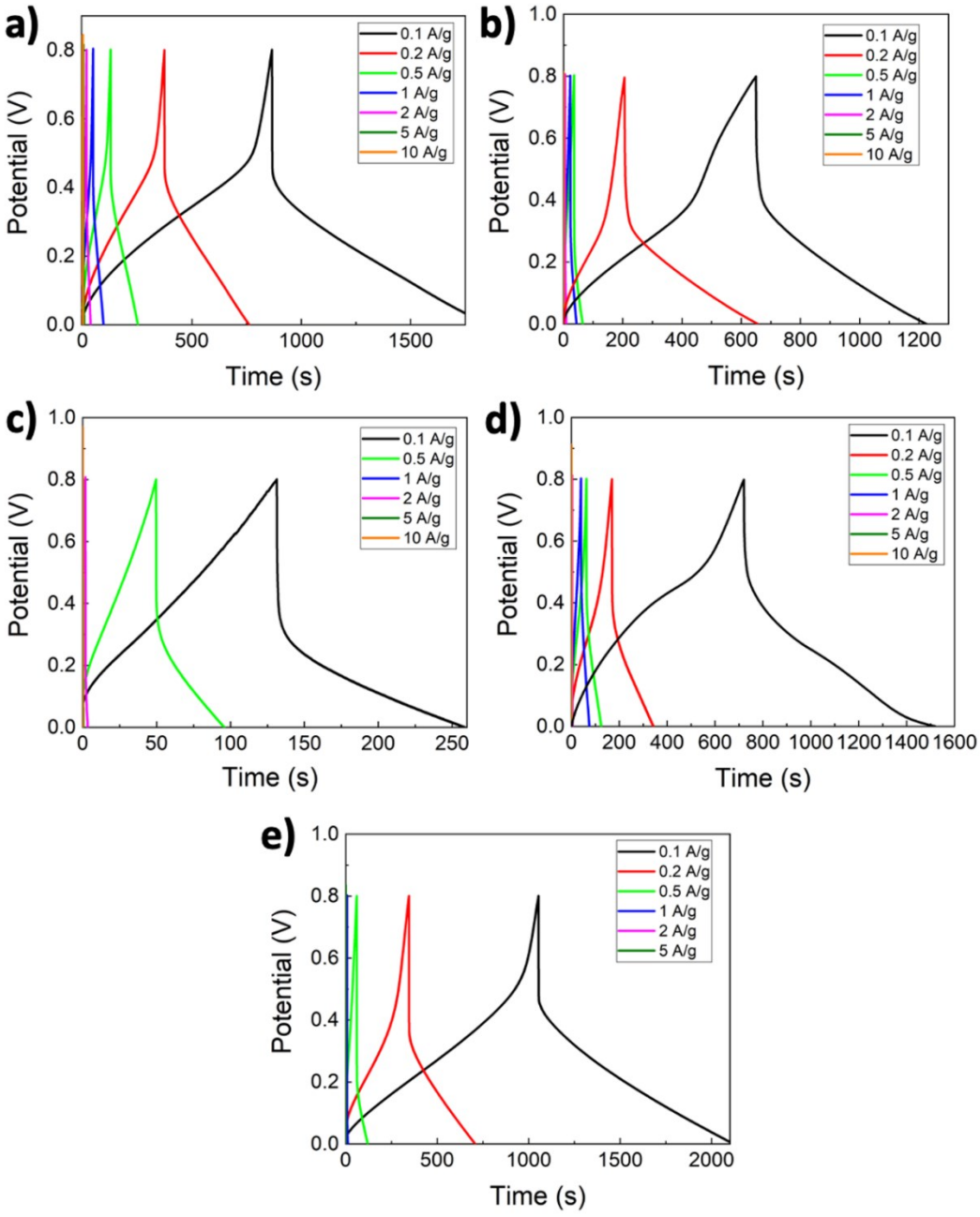

Figure S9. GCD curves at increasing current densities for different 2D WS2@PANI nanohybrids: a) 1:50 + NaCh, b) 1:100 + NaCh, c) 1:20 + SDS, d) 1:50 + SDS, e) 1:100 + SDS.

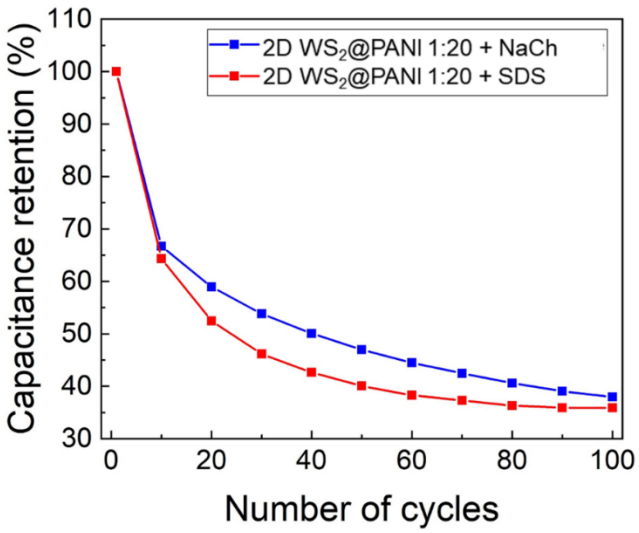

Figure S10. Cyclability of the 1:20 2D WS_2@PANI nanohybrids prepared in the presence of SDS and NaCh measured at a current density of 1 A/g over 100 cycles in a three electrode system (with the active materials deposited on the GC electrode).

3.5: Publication n°4

Easy direct functionalization of 2D MoS_2 applied in Covalent Hybrids with PANI as dual Super-capacitive Blends

Authors: **Crisci M.**, Boll F., Domenici S., Gallego J., Smarsly B., Lamberti F., Wang M., Rubino A., Gatti T.

As reported in the previous introduction, 2D materials have been used extensively as supercapacitors and their performance depends on the number of components on the blend and the actual materials. Moreover, functionalization is also another option to tune the properties of the materials. For example, MoS_2 can be functionalized in different ways. One option is to lock either the 1T phase from transitioning back to the thermodynamically stable 2H phase.[259–261] This was reported, for example, by *Kulkarni B. et al*[262] and *Tang Q. et al*.[263] as well as other groups.[264,265] In this case, the first report experimented with phase locking via carboxylic group, while the second studied through DFT methodologies the surface coverage and the effect of several functional group on the phase transition. Click chemistry and thiol based functionalization[265–268] are also methodologies investigated to add functional group on the MoS_2 surface. Nucleophilic functionalization is also another methodology used to both lock the phases and to introduced functional moieties on the 2D sheet moieties; *Vishnoi P et al.*[269] and *Zhang H. et al.*[264] and many other researchers[270–272] reported the use of iodine based compounds to functionalized the electron rich surface of 1T phase. *Vishnoi P et al.* made a further step by using aryl compounds and studying the functionalization degree based on the group in para compared to the iodine leaving group.

Considering the large possibility of the functionalization and the expertise gathered in binary hybrid production, **publication n°4** focuses on putting together these two different fields: specifically, functionalization of 1T-MoS_2. Specifically,

aryl-based functionalization of the TMDC is performed and used to create anchor point for the surface polymerization of PANI, combined with the brine-based process, the goal of the work is to study the effect of such additional steps to the overall performance of the material. The overall project can be divided into 3 main sections: production of functionalized 1T-MoS_2, synthesis of the binary compound material and electrochemical analysis. The first part consists in the exfoliation and functionalization study of the TMDC material, using chemical exfoliation, and using lithium as expanding agent. The ink was characterized using the techniques and protocols suggested and established in the **publication n°1**. Therefore, UV-Vis, DLS and Zeta Potential were used as basic characterization. After the lyophilization, the 2D material powder was characterized using XRD, Raman, XPS, SEM and TEM analysis. All of these characterizations were essential to discern the quantity of both phases and their morphology as well as verifying possible contamination, coming from the procedure. Generally speaking, the as produced 1T phase showed an initial percentage of around 70% while after functionalization and air exposure it dropped as low as 35-40%, both pointing at the slow phase transition of the material and the effect of phase locking of the functionalization. This step was further characterized via TGA and IR spectroscopy, which allowed both to estimate the surface functionalization and to verify the presence of the C-S bond, key proof of the molecular grafting. Subsequently, the hybrid materials were synthesized using both functionalized and non-functionalized material, obtaining in both cases a very similar powder: the characterizations, here performed (XRD, SEM, Raman spectroscopy), confirmed the main contribution of the polymer and similar fingerprint throughout the samples were also observed. Therefore, the difference between the different powders was studied via electrochemical measurements, specifically CVs, GCD, EIS and durability tests. in order, 3 electrodes measurements were first performed to assess the basic properties of the material and to properly choose a suitable potential range using both CVs and GCDs, while 2 electrodes set up, specifically a Swagelog cell, were performed afterward to simulate and study the materials in a more applicative environment without bogging down in the

production of a device, which has inherently several criticality coming from not only the material, but also the geometry and production procedure. Lastly, used electrodes were studied once again with SEM images to assess changes and differences compared to pristine electrodes and try to evaluate the morphological effect of the brine pre-treatment.

In this paper, all the materials and samples were prepared by me, as well as their structural, morphological, and electrochemical analyses. Specifically, I performed XRD, Raman spectroscopy, DLS, ZP, XPS, SEM, EDX and the electrochemical measurements, while some of the aforementioned analysis, such as TGA and TEM, were performed by external collaborators. The candidate also performed data processing and manuscript writing.

Easy direct functionalization of 2D MoS_2 applied in covalent hybrids with PANI as dual blend supercapacitive materials

*Matteo Crisci[1,2], Felix Boll[1,2], Sara Domenici[2,3], Jaime Gallego[1,2], Bernd Smarsly[1,2], Mengjiao Wang[3], Francesco Lamberti[4-5], Andrea Rubino[6], Teresa Gatti[2,3]**

[1]Institute of Physical Chemistry, Justus Liebig University, Heinrich Buff Ring 17, 35392, Giessen, Germany

[2]Center for Materials Research, Justus Liebig University, Heinrich Buff Ring 16-17, 35392, Giessen, Germany

[3]Deparment of Applied Science and Technology, Politecnico di Torino, C.so Duca degli Abruzzi 24, 10129, 10129 Torino, Italy

[4] Department of Chemical Sciences, University of Padova, Via Marzolo 1, 35131 Padova, Italy

[5]Department of Industrial Engineering, University of Padova, Via Gradenigo 6a, 35131, Padova, Italy

[6] Functional Nanosystems, Istituto Italiano di Tecnologia, Via Morego 30, 16163 Genova, Italy

E-mail: teresa.gatti@polito.it

Abstract

The pressing demand for more sustainable energy provision and the ongoing transition towards renewable resources underline the critical need for effective energy storage solutions. To address this challenge, scientists persistently explore new compounds and hybrids to address this challenge and in such dynamic research field, 2D materials, particularly transition metal di-chalcogenides (TMDCs), show great potential for electrochemical storage uses. Simultaneously, also conductive polymers (CPs) are interesting and versatile super capacitors materials, especially PANi who has been extensively studied for this purpose, however, both CPs and TMDCs have their own drawbacks. Therefore, in this work, we present a powerful method to combine the two aforementioned compounds and produce covalent hybrids starting from aniline functionalized few-layers 1T-MoS_2, attained by a facile functionalization using iodo-compounds and then by grafting polyaniline (PANI).

The hybrids attain 70 F/g specific capacitance in a pseudo device set up, coupled with a robust capacitance retention well over 80% for up to 5000 cycles. These findings demonstrate the potential of similar composites to work as active components for novel, innovative energy storage technologies. At the same time, the successful synthesis marks the efficacy of direct covalent grafting of conductive polymer on the surface of 2D TMDCs for stable functional materials.

Keywords

2D MoS_2, nanohybrid, covalent functionalization, polyaniline, capacitive material

1. Introduction

The global shift towards sustainable energy systems is driving an increasing demand for high-performance energy storage solutions. Among the various technologies available, supercapacitors have gained significant attention due to their high-power density, rapid charge-discharge cycles, and long cycle life..[1,2] However, the development of materials capable of providing both high energy density and cycle stability remains a key challenge. This has led researchers to explore novel material combinations, particularly the blending of two-dimensional (2D) materials with conductive polymers (CPs), to enhance the electrochemical performance of supercapacitors.[3–9]

CPs are often pseudo-capacitive, possess good electrical conductivity and intrinsic capacitance and are easy to produce. Polyaniline (PANi), a widely studied conducting polymer, has been considered a promising candidate for supercapacitor electrodes due to its pseudocapacitive properties, ease of synthesis, and low cost.[10–13] However, PANi suffers from significant degradation over multiple charge-discharge cycles[12,14], primarily due to structural changes during the redox process, which leads to a rapid decline in capacitance. This limits its practical application in energy storage devices, necessitating strategies to improve its cycle life and stability.

On the other hand, 2D-MoS_2, a transition metal dichalcogenide (TMDCs), has been extensively studied and emerged as an energy storage material, due to its van der Waals and layered structure, allowing for easy ions' intercalation and the high surface area achievable.[15–18] However, MoS_2, particularly in its semiconducting 2H phase, exhibits low electrical conductivity, which limits its ability to deliver high power density, which can be partially improved by using the relative 1T phase, which however is metastable. Additionally, the aggregation of MoS_2 nanosheets during cycling can further reduce its performance over time, therefore spacers can additionally help to reduce this effect.

To address these issues, combining the strengths of both materials in a hybrid system has emerged as a promising approach. By blending MoS_2 nanosheets with PANi, it is possible to harness the high surface area and ion intercalation capability of MoS_2 alongside the pseudocapacitive behavior of PANi. Such hybrids can improve the overall electrochemical performance, particularly in terms of capacitance retention and cycle stability[19–21], by mitigating the weaknesses of each component material. In this work, we present a novel approach to the covalent functionalization of MoS_2 nanosheets with PANi, aiming to create a hybrid material that exhibits enhanced supercapacitive performance. The direct covalent grafting of PANi onto the surface of exfoliated MoS_2 ensures a robust interaction between the two materials, improving charge transfer and structural integrity during cycling. This hybrid structure not only enhances the conductivity of MoS_2 by maintaining the material in its highly conductive 1T phase, but also stabilizes the PANi polymer, thereby improving its cycle life.

Based on this background knowledge, we report a new synthetic protocol for preparing nanohybrids by grafting PANI onto a functionalized 2D MoS_2 NSs (MoS_2@PANI) demonstrating specific capacitances of up to 70 F/g in a pseudo-device system and exhibit capacitance retention of over 80% after 5000 cycles, underscoring the potential of MoS_2-PANi hybrids as next-generation super capacitive materials. This work highlights the efficacy of combining functionalization[22] to obtain specific moieties on the 2D materials and its grafting orientation of conductive polymers, resulting in

a robust integration of the two materials,[23] and addressing the long-standing challenges of energy storage, paving the way for the development of more efficient and durable super capacitors.[12]

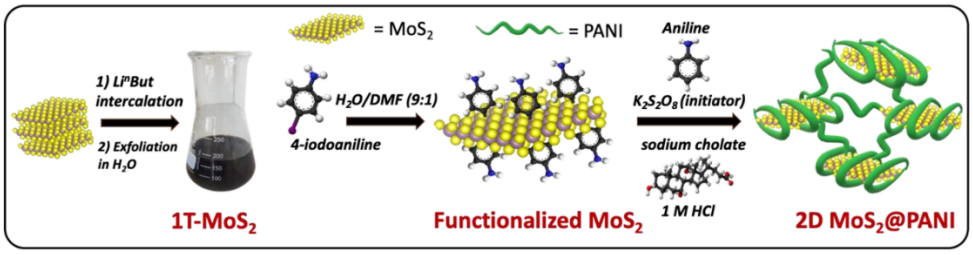

Figure 1. Sketch of the whole synthetic process towards covalent 2D MoS_2/PANI nanohybrids, including chemical exfoliation, 4-iodoaniline functionalization and PANI covalent grafting.

2. Results and discussion

The layered material was obtained by adapting a literature chemical exfoliation procedure, where n-butyllithium was used as an electron donor reactant to foster the phase transition from the 2H-phase, typically existing in the bulk powder, to the 1T-phase, as described in the Experimental Section. The exfoliated MoS_2, obtained from the resulting aqueous-base ink via freeze drying, has been characterized by powder X-ray diffraction (P-XRD) and Raman analysis (see Figure S1 in the Supporting Information – S.I.). From Raman spectra, it is possible to observe signatures of both the 1T and 2H phases of MoS_2, while the P-XRD showed the typical reflex of 1T MoS_2 at 8° and the presence of surface oxide, due probably to the oxidation caused by the exfoliation process (see S.I. for further discussion). Considering the Raman results, X-ray photoelectron spectroscopy (XPS) measurements were also performed to evaluate the quality of the synthesized material and its composition. As displayed in Figure 2a, the Mo 3d region in the XPS spectra shows different signals, which were fitted using three different components for Mo and one for S respectively, since the S 2s is present in this region as well. Seven peaks were found at 225.8, 228.1, 229.1, 231.3, 232.2, 232.7 and 235.6 eV, that were attributed respectively to S 2s, Mo(1T) $3d_{5/2}$, Mo(2H) $3d_{5/2}$, Mo(1T) $3d_{3/2}$, Mo(2H) $3d_{3/2}$, MoO_x $3d_{5/2}$ and MoO_x $3d_{3/2}$.[24–26] It is important to note that 1T-MoS_2 related peaks are shifted towards lower binding energy compared to the 2H-MoS_2 due to the higher electron density

and, therefore, it is possible to distinguish between the two MoS_2 phases, being the different peaks circa 1 eV apart.[27] Based on this result, the ratio between the two phases was calculated from the performed fittings and it suggests an estimated distribution of 70% 1T-MoS_2 and 30% of 2H-MoS_2. The study of S 2p spectral range can give similar information as the Mo 3d (Figure 2b). This signal has two major peaks at around 162 eV and 168 eV, and they were divided into several different components. The first one has 4 main contributions at 160.9, 162, 162.1 and 163.2 eV, which can be attributed to $2p_{3/2}$ and $2p_{1/2}$ metal-sulphur bonds, confirmed as well by the difference between the two orbitals (1.18 eV on average for 2p orbitals). The difference in these peaks comes from the presence of both MoS_2 phases and their significant difference in electron density, that influences not only the shift of the Mo 3d orbital but also of the S 2p one. In addition to these fittings attributed to Mo-S bonds, the peak observed at 170, 169.1 and 170.3 eV were further resolved in the two S 2p orbitals and were attributed to superficial SO_4^{2-}, a common impurity in S based compounds due to air exposure. The high percentage of 1T-phase significantly changes the material properties, allowing for its dissolution in water and easy functionalization in such media, despite the presence of some 2H phase in the final product.

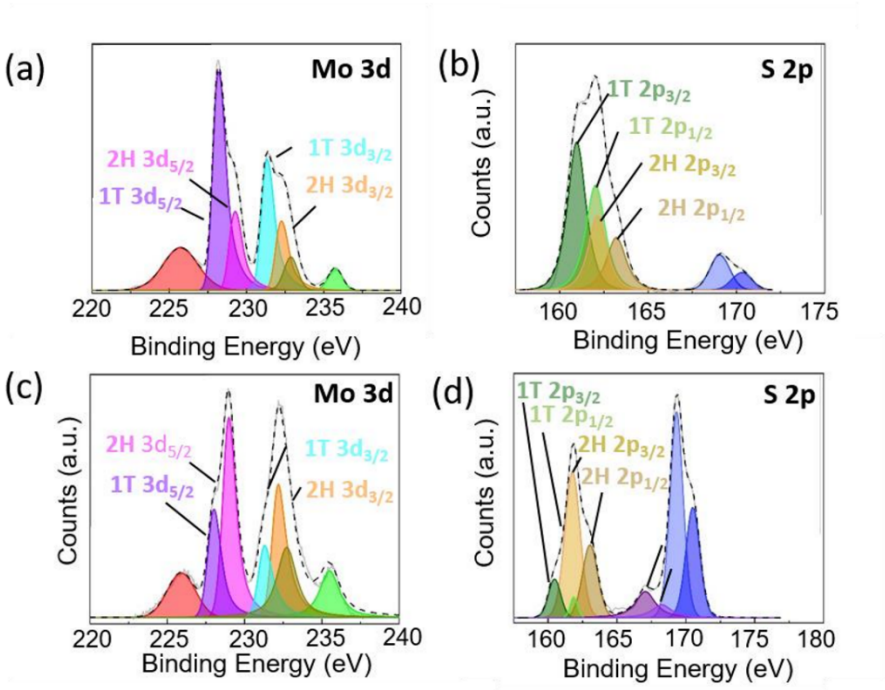

Figure 2. (a)-(d) XPS spectra of 1T-MoS_2 prepared by chemical exfoliation and functionalized for 1 day with 4-iodoaniline. Fitted Mo 3d region before (a) and after (c) functionalization (including the underlying S 2s peak). Fitted S 2p region before (b) and after (d) functionalization

With these information acquired, the as-produced 1T-MoS_2 ink was then used for the direct arylation step (Figure 1), following a previously reported procedure.[28] Therein, *p*-iodoaniline was used in large excess as a functionalizing agent and the grafting onto 1T-MoS_2 electron rich sulfur atoms was facilitated due to the weak C-I bond in the reagent. However, electron donating moieties in di-substituted iodo-aryls, such as $–NH_2$ groups, proved to lead to a lower surface grafting compared to electron withdrawing moieties.[28] This effect can be explained using the Hammett parameters theory for di-substituted aryls, where functional groups with a negative Hammett value (electron donating) increase the electron density on the aryl, stabilizing the forming carbo-cation after the –I leaving group and therefore rendering it less reactive.[29–31] To compensate this effect, which opposes the functionalization process, working conditions for this reaction were tuned, testing different reaction

times (1, 3 and 7 days, respectively) and increasing the temperature to 40 °C from the previously reported room temperature, to fasten the kinetics of the reaction. After the end of the reaction, the material was collected and purified according to the procedure described in the Experimental Section. Evidence of covalent functionalization was confirmed through XPS spectra of both pristine and MoS_2 with the functionalization reaction of 1 day (see Figure 2a-d). In the Mo3d range, the functionalization's impact on the two materials' phases is evident (Figure 2c). Post deconvolution, a significant increase in 2H-phase compared to 1T is detected, with proportion reaching 65% and 35%, respectively. The S 2p binding energy region provides further valuable information on the functionalization. The main peaks were divided into several different components in a similar way as reported beforehand. (Figure 2d). After the functionalization, additional peaks were detected at 167 and 168.2 eV. These two components are shifted in comparison to normal C-S bonds assignation, usually reported at 164 eV ,[32] however these deconvolutions are still assignable to organic C-S bonds and the shift can be again attributed to the different electron density around the element, pointing at the covalent functionalization of MoS_2 with aniline moieties. Similarly, the N 1s XPS profile, shown in Figure S2, further corroborates the aniline decoration of the MoS_2 surface, since two sharp peaks at 394.6 and 398.9 eV can be deconvoluted and attributed, respectively, to Mo 3p and to aniline oligomers (or to polyaniline) according to the NIST XPS database[33].

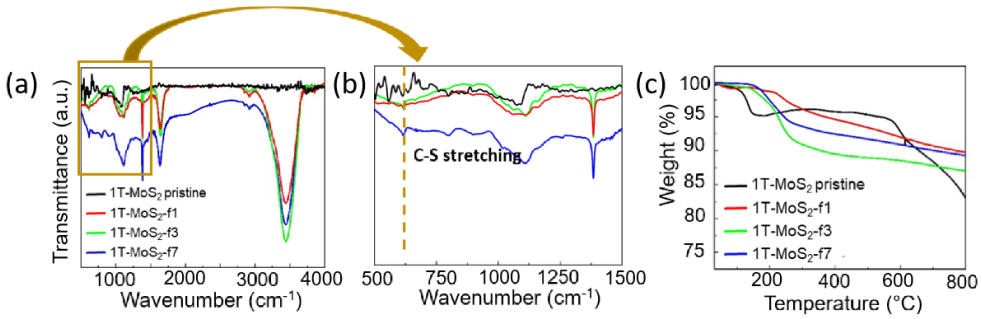

Figure 3. (a)-(b) IR analysis and (c) TGA of the different functionalized samples at different reaction times.

Another evidence of the presence of organic C-S bonds in the materials is provided by the infrared (IR) spectroscopy analysis represented in Figure 3a. In the fingerprint region, between 500 and

1000 cm^{-1}, it is possible to detect a peak at 620 cm^{-1} (Fig. 3b) that appears after the reaction, but it does not clearly increase with the reaction time. This feature corresponds to the C-S stretching[34] and is a consequence of the covalent grafting of the aniline moieties directly on the MoS_2 surface, while the lack in increase, connected to a major presence of the moiety, can be attributed to the surface saturation and consequent formation of oligomeric branches instead of new C-S bonds. Several other peaks were observed at 3430, 1632, 1394 and 1108 cm^{-1}, attributed to N-H stretching, N-H bending, C-C stretching, and C-N stretching modes, respectively. These findings additionally point towards the presence of aniline moieties on the surface of the material.

Finally, thermogravimetric analysis (TGA) was carried out on the functionalized MoS2 to investigate the presence of organic functional moieties on the surface of the material (Figure 2f). An initial downward slope at around 120 °C characterizes the pristine 1T-MoS_2 sample, attributed to the realize of interstitial water, followed by a slight increase in the weight % of the material. This effect could derive from an effect called tumescence, where the material upon heating, behaves similarly to a pitch, forming bubbles that can give a false interpretation of the weight before the bubbles' removal. This is further confirmed by mass spectrometry data associated with the TGA measurements, where only a sharp peak at 18 m/*z* peak was observed around the same temperature, which corresponds to the molecular mass of water (see Figure S3). On the other hand, the functionalized material shows a sharp decrease in mass between 180 and 300 °C. This effect, spanning for more than 100 °C, is the index of a gradual and slow degradation of organic species. While pure aniline typically evaporates at around 180 °C, in this case, the effect can be attributed to a more complex decomposition process rather than the mere detachment of individual aniline moieties from the NSs[35,36]. In fact, this degradation is likely to be attributed to oligomers of aniline. Specifically, whenever the surface of the 2D material has been already functionalized, further addition of monomers can be done on top of the already existing grafted aniline moieties, starting to create oligomers, which are usually called nano-branches, and these compounds decompose in a similar way to polyaniline, as observed in the thermograms in Figure 2f .[35,36] Once the surface functionalization reaches a certain extent, the excess

of iodo-aniline will preferentially react with already grafted aniline moieties and form PANI-like oligomers on the surface. However, this phenomenon can often lead to a broad and uncontrollable size dispersion of the oligomers on the surface. For this reason, in Figure 2f the 3 days functionalization (MoS_2-*f3*) shows a higher mass loss compared to the 7 days one (MoS_2-*f7*), since the former most probably features a higher degree of oligomers on the surface. Overall, already 1-day of reaction (MoS_2-*f1*) was enough to reach a functionalization degree of 3.6% (in mass fraction, see Table S1). When the reaction time was increased, the functionalization degree was estimated to reach up to 9.5% per S atom, but this high value can also be attributed to the formation of branches, as previously mentioned.

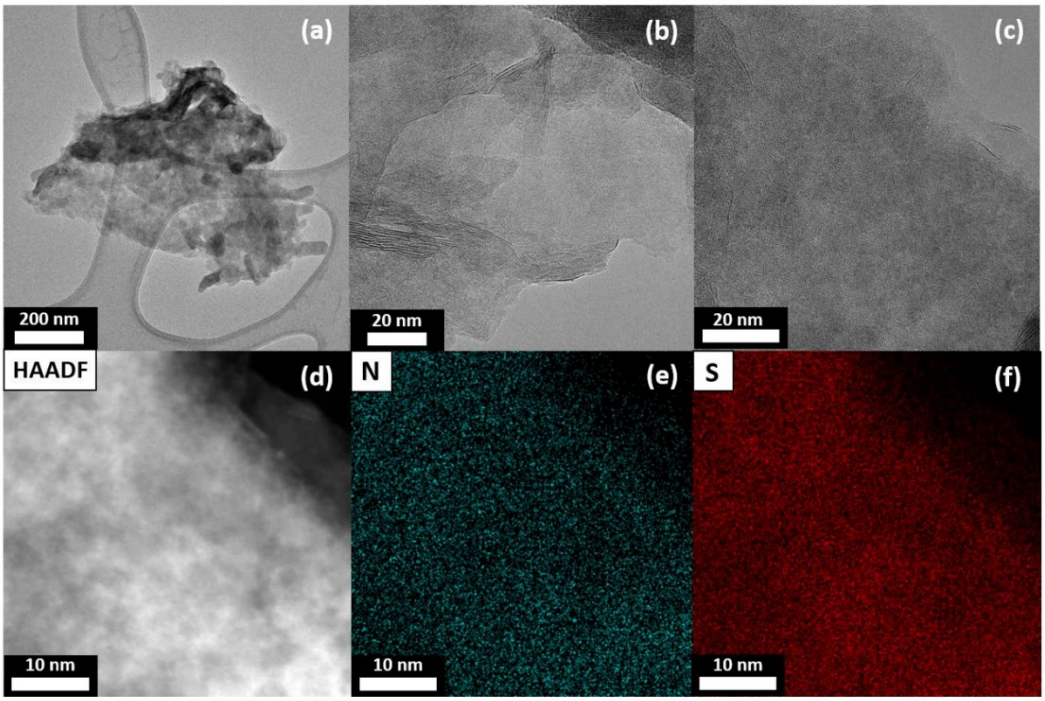

Figure 4. (a-b-c) HR-TEM image of the MoS_2-f1 (i.e. after 1 day functionalization), associated to the corresponding (d)-(f) STEM-EDX image, nitrogen and sulfur elemental maps.

Transmission electron microscopy (TEM) imaging was employed to characterize the NSs morphology and composition after aniline functionalization. From high-resolution TEM (HRTEM, Figure 4a-b-c), it is possible to observe a few layered material and different regions where both the

2H and the 1T-phase of the material were detected (Figure S4), confirming the results from the XPS fittings (Figure 2a-d) on the presence of both phases in the material, which can even co-exist in a single flake. In addition, scanning TEM (STEM) coupled to energy dispersive x-ray analysis (STEM-EDX) characterization (Figure 4d-f) confirms the presence of both nitrogen and sulfur on the functionalized NSs, with a highly homogeneous distribution of both elements, hinting at an ordered surface decoration of the layered nanomaterial with aniline or its oligomers.

Starting from the aniline-decorated MoS_2 flakes obtained after 1 day of functionalization (MoS_2-f1), 2D MoS_2/PANI hybrids (MoS_2-f1@PANI) were prepared, following the procedure described in the Experimental Section and sketched in Figure 1. In particular, hybrids with 1:20 molar ratio between the inorganic (functionalized-MoS_2) and organic (PANI) components were synthesized using both pristine 1T phase and functionalized one. Briefly, the conducting polymer was prepared *in situ*, by adding aniline and the oxidizing agent, ammonium peroxidisulfate (APS), as reactants to the dispersed MoS_2-f1 NSs and the final hybrid was collected as a powder after purification, they were called respectively MoS2(1T)@PANI 1:20 and MoS2-f1@PANI 1:20. The as-synthesized materials were characterized with Raman spectroscopy, P-XRD analysis, scanning electron microscopy (SEM) and EDX and details are discussed in the S.I. (Figure S5). In summary, after polymerization of PANI around the 2D material, the only peaks in the Raman analysis and reflexes in the P-XRD visible are the one related to the polymer, while SEM pictures show a rod like morphology, typical of the PANI structure (Figure S6). On the other hand, EDX reveals the presence of both Mo and S in the material together with C and Cl, confirming the presence of all the expected atomic components in the hybrids. Nitrogen is not seen due to overlap with the EDX signal of carbon, however chlorine is an indirect indicator of the nitrogen presence, since chlorine is the anionic dopant in the PANI emeraldine structure, counterbalancing the positive charges of the -NH-$^+$ moieties.

After characterizing the structural and morphological properties of the MoS_2-f1@PANI hybrid, which was easily produced by the 3-steps exfoliation-functionalization-polymerization procedure previously described, its electrochemical behavior was tested in order to investigate the potential for

use in supercapacitor-like devices. For comparison, a reference hybrid, termed MoS_2(1T)@PANI, was prepared by in-situ polymerization of aniline in the presence of pristine 1T-MoS_2. Initial analyses were carried out in a 3-electrodes system to study the properties of the hybrid materials and comparing them to the pristine components, using H_2SO_4 0.5 M as the electrolyte (see more details in the Experimental Section). Cyclic voltammetry (CV) analysis was first performed to select the potential range suitable for subsequent galvanostatic charge-discharge (GCD) measurements. From Figure 4a, it is possible to notice that in almost all samples the PANI redox peaks appear between 0.25 V and 0.5 V (*vs* RHE), therefore GCD measurements performed in this potential window will exploit the pseudo-capacitive storage mechanism related to this redox couple. However, in the hybrid containing the pristine 1T-MoS_2, there is an evident shift and broadening of the PANI oxidative peak towards higher potentials, from 0.4 V to 0.7 V (Figure 5a). This shift could be explained by an anti-synergistic effect between the inorganic and organic components in the nanohybrid. Previous studies have extensively reported the effect of dopants and additives on the redox behavior of PANI, with inorganic acid being the most reported as the dopants that can change the properties of the conducting polymer. However, there are some examples of inorganic materials[37–39] used in combination with PANI that significantly change the polymer redox properties. Similarly, 1T-MoS_2 may act as an additive for PANI, with its negative surface charge influencing the redox properties of the polymer chains. In contrast, no similar effect is observed when the functionalized material is used (MoS_2-f1@PANI), which behaves instead like pure PANI, thanks to the direct connection between polymeric part and the inorganic part. This result hints at a different type of interaction between the conducting polymer and the inorganic nanomaterial, compared to the case of the non-grafted hybrid.

With the clear information on redox behavior of the examined systems and by comparing it with previous literature reports, the potential window between 0 and 0.8 V vs RHE was set to explore the capacitive properties of the nanohybrids.[40] GCD curves were subsequently obtained within this potential range, primarily exhibiting nearly ideal shapes, as depicted in Figures 5b and S7. These curves typically formed a triangular pattern, with distinct charge and discharge phases. From the cycle

performance, we can observe a negligible iR drop, which is usually related to the internal resistance of the system. As counter evidence, potentiostatic electrochemical impedance spectroscopy (PEIS) analysis was performed and from the relative Nyquist plots (Figures 5c) a clear difference between the two hybrids emerges. In both cases, the analysis reveals a semicircle at high frequencies, followed by a straight line at lower frequencies, hinting at a similar processes happening at the applied potential.[41,42] The functionalized material (MoS_2-f1@PANI) shows a smaller semicircle, compared to the MoS_2(1T)@PANI, corresponding to a lower charge transfer resistance (R_{ct}) and the exact values can be estimated by fitting the corresponding circle with a suitable model. (Fig 5c) Moreover, the conductivity can also be extrapolated from these values and, assuming a similar thickness for both electrodes, the conductivity values supports a better charge mobility in the functionalized material. All the values obtained are shown in the S.I. in Table S2 and suggest a larger internal resistance for the MoS_2(1T)@PANI hybrid compared to the MoS_2-f1@PANI sample, arising from several factors. One of these is the stabilization of the 1T-MoS_2 metallic phase in the MoS_2-f1@PANI hybrid, since the 1T phase of MoS_2 is renowned for being highly conductive, especially in comparison to the 2H phase of the same material.[15,17] Therefore, the phase locking via functionalization[43,44] protect any further transition to the 2H phase that can occur due to air exposure and continuous cycling. Moreover, the direct covalent grafting of PANi onto the functionalized MoS_2 nanosheets in MoS_2-f1@PANi significantly improves charge transfer across the hybrid interface. This is due to the stronger electronic coupling between the PANi and MoS_2 layers, which facilitates more efficient electron transport pathways. In contrast, the pristine MoS_2(1T)@PANi sample relies on weaker interactions between the polymer and the MoS_2 nanosheets, leading to higher R_{ct} values. Lastly, the differences in the polymerization of PANi on the functionalized vs. not functionalized MoS_2 nanosheets also play a role. In the MoS_2-f1@PANi hybrid, the covalent bonding ensures uniform polymerization and better integration of PANi with MoS_2, further contributing to lower charge transfer resistance. The less organized structure in the MoS_2(1T)@PANi system leads to greater impedance. Thus, the differences in conductivity between the functionalized and unfunctionalized systems, along with the nature of the

covalent bonding in MoS_2-f1@PANi, contribute to the observed differences in charge transfer resistance.

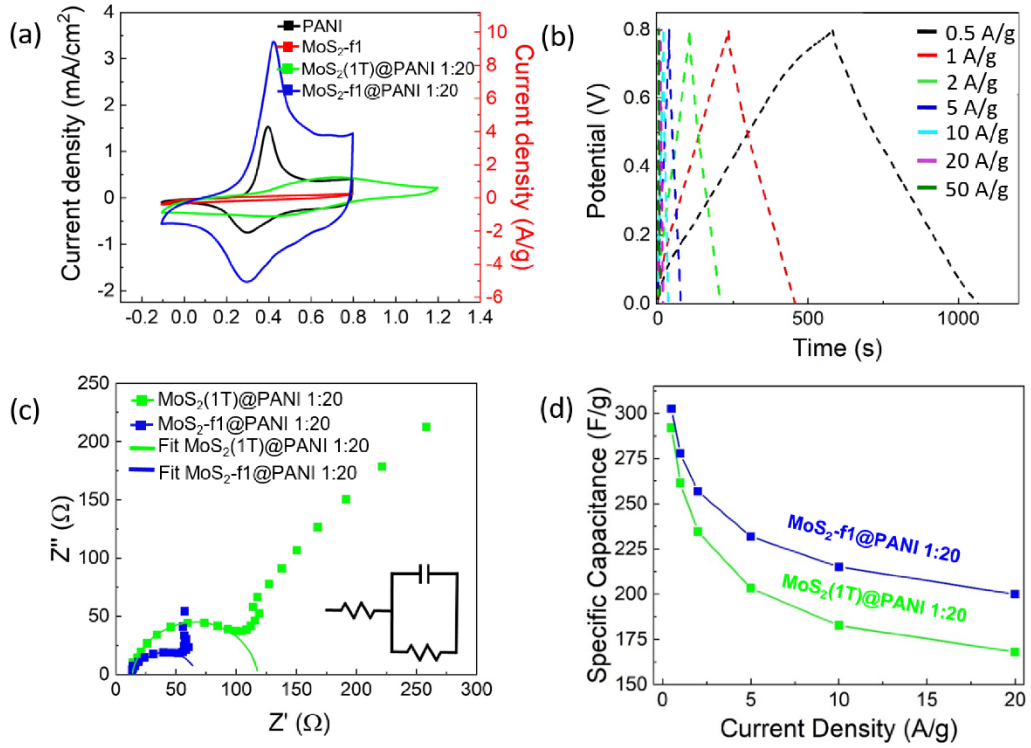

Figure 5. Three-electrodes electrochemical characterization of the covalently grafted and non-grafted 2D MoS_2/PANI hybrids. (a) CVs of hybrids and individual components. (b) GCD curves for the grafted MoS_2-f1@PANI hybrid at different current densities (see Figure S7 in the S.I. for the corresponding curves of the non-grafted sample). (c) PEIS analysis and (d) specific capacitance calculated for the two hybrid materials.

The GCD results displayed in Figure 4b and Figure S7 were used to calculate the values plotted in Figure 5d, using Equation 1 reported in the Experimental Section. The hybrids showed a similar specific capacitance (C_s) at low current density (0.5 A/g) of 302.5 F/g for the functionalized material-based hybrid, and of 291 F/g for the un-functionalized reference, with only a 3.5% difference between the two species. However, at increasing applied current, the difference becomes more pronounced, reaching a 16% difference in C_s at 20 A/g, with 200 F/g for MoS_2-f1@PANI and 168 F/g for

MoS_2(1T)@PANI, pointing at a significant improvement in performance promoted by the surface functionalization.

Given the promising results in a 3-electrodes setup, further tests were conducted in a 2-electrodes system to more realistically assess the performance of the nanohybrids in an actual supercapacitor-like device. The system chosen for the two electrodes test was assembled in a Swagelok cell, to simulate a device setting with symmetric features and current collectors made of 10 mm diameter Toray paper discs (see Experimental section). In this conditions, both MoS_2-fl@PANI and MoS_2(1T)@PANI species were tested. In addition, two further hybrids were modified by applying NaCl saturated solution (brine) as an additive during the PANI polymerization process, as described in Figure 1, in order to tune functional properties (the two new hybrids are named by simply adding "brine" at the end of MoS_2-fl@PANI and MoS_2(1T)@PANI, for the sake of clarity). The additional salt has no effect on the overall hybrids' morphology (see Figure S8), but it has been reported to possibly improve the electrochemical performances. NaCl crystals act as pseudo templates (Figure 6a,b), as reported in previous works,[4,45] and facilitate additional connection between the polymer chains, potentially further boosting the capacitive behavior of the hybrids. GCD measurements were performed (Figure S9) and from them, C_s values were calculated (Figure 6c). The trend observed in the 3-electrodes set-up electrochemical characterization is still visible in the pseudo-device setting, however a small increase can be seen initially in some samples, that can be attributed to an complete stabilization of the composite after the first measurements. Specifically, the hybrid based on the covalently functionalized 2D MoS_2 shows a higher C_s compared to the one based on pristine 1T-MoS_2, namely 25% greater at 0.5 A/g and 45% at 10 A/g current densities. Moreover, the addition of the NaCl pseudo-template during the synthesis yielded materials with higher C_s (maximum values of 71.1 A/g and 58.8 A/g for MoS_2-fl@PANI and MoS_2(1T)@PANI, respectively) compared to the one without this pretreatment, proving once again the positive effect of the functionalization of the material, finally obtaining a maximum capacitance for the functionalized and brine treated samples of 71.1 F/g at 0.5 A/g.. This improvement in C_s also results in a larger power and energy density

(Figure 6d) for the hybrids prepared in the presence of brine, with 8 kW/Kg power density and energy density of 4.5 Wh/Kg for the MoS_2-f1@PANI best sample (Table S3).

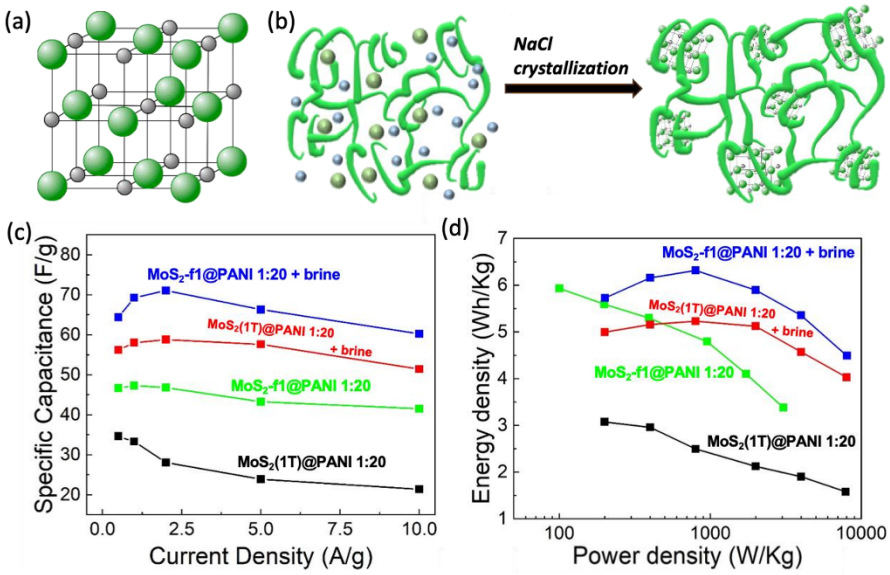

Figure 6. Effect of saturated NaCl (brine) addition during 2D MoS_2/PANI hybrids synthesis on capacitive behavior in a 2-electrodes set-up. (a) NaCl crystal structure and (b) proposed pseudo-templating mechanism of NaCl during aniline polymerization. (c) C_s calculated from GCD curves of the hybrids and (d) Ragone plot for the same samples.

To gain insights into performance retention of the investigated pseudo-capacitors, durability tests were performed on all the above reported samples for over 5000 cycles (Figure 7a). Here, the brine-based samples showed a much steeper C_s drop in the early cycles compared to the others, while C_s decreases gradually for the two hybrids prepared without brine, until MoS_2-f1@PANI stabilizes at around 84% retention (best C_s at 5000 cycles among all the functional electrodes tested). To further investigate the peculiar deterioration of the brine-based samples, pre- and post-mortem morphological analysis on the electrodes were performed with SEM imaging.

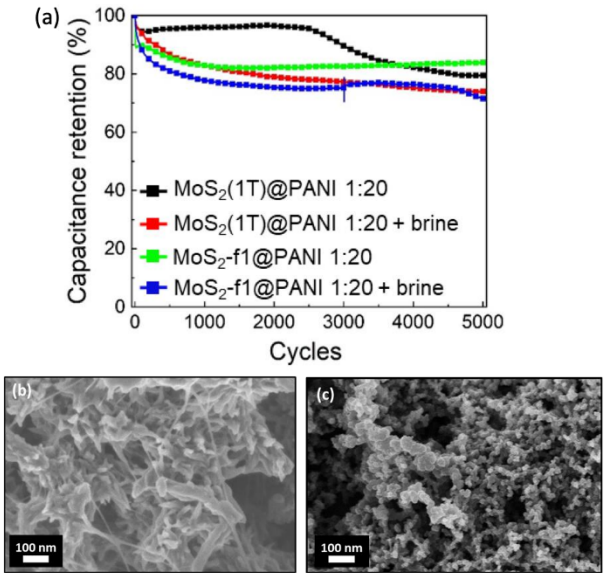

Figure 7. (a) Capacitance retention of the different material in a 2-electrodes set-up. SEM images before (b) and after (c) cycling for MoS_2-f1@PANI + brine.

From SEM image before cycling (Figure 7b), it is possible to observe the presence of thin nanometric polymer-based interconnections within the microstructure of the electrode material. Similar morphological details are not present in the sample prepared without brine, which makes them specific features of the templated samples. However, after cycling these features disappear (Figure 6c), index that they are connected to the charge storage mechanism. We attribute both the increase in C_s and its sharp initial drop during cycling to this morphological variation observed in the nanohybrids prepared with the NaCl pseudo-template. The additional presence of these wires expands the surface where the electrolyte can interact, but, at the same time, the continuous cycling at relatively high current density brings to a rapid degradation of these filaments, leading to a loss in C_s already after 200 cycles. This deterioration in the charge storage performance can be explained in the context of the PANI degradation mechanism, which often encompasses a phase transition corresponding to a morphology change, due to the reversible redox reaction happening in the polymer chains during cycling.[14,46] Therefore, this process may also lead to the disappearance of the nanowires connecting different areas of the composite material, thus reducing the available surface for the energy storage process. This hypothesis is verified by post-mortem SEM images on all samples

(Figure 6c and S10), from which a change in morphology is observed and the degradation of the nanostructure after the cycling occurs. Samples based on pristine 1T-MoS_2 showed the largest morphological difference before and after cycling, with wide areas of the material transitioned to an amorphous microstructure. Simultaneously, the brine pre-treated samples exhibited a lower degree of the amorphous phase, while the filamentous connections disappeared, supporting the aforementioned observations (Figure 7b and 7c).

Based on the above analysis, the brine treatment appears to positively affect the overall charge storage performance of the hybrid materials, significantly enhancing their C_s. However, this improvement also contributes to a faster capacitance drop in the material. This issue could potentially be addressed by implementing slower cycling conditions or by establishing thicker connections between the polymer chains via longer reaction time, thus reducing the influence of the degradation process, while once again the functionalization proved to yield better composite in comparison to the non functionalized samples.

In general, this work produces binary blends starting from a flexible and easy functionalization step of 2D materials. This process was often used before with graphene[47–49] using diazonium salts, as well as with other 2D materials, such as MXenes[50] and other TMDCs[44,51,52]. This procedure, using iodo-compounds, is not as common but utilize the same principles, therefore the possibilities for its applications are as wide as diazonium based functionalizations.

The blending with conductive polymers improves the performance of the single components and their stability. However, blends in literature are often prepared by using three or more components (Table 1) and therefore, they can not be compared easily. It is also clear how the 3rd components, usually a carbonaceous material, greatly increase the electrochemical properties, however our work focuses on the optimization of the interaction between the two basic components, opening the possibility to reach even higher electrochemical performances adding another additive to the mixture to enhance performances and cycle retentions.

***Table 1**. Literature comparison of the here proposed material with some other binary/ternary blends*

	Cs	Cycle Stability (2 Electrodes)	Ref
MoS_2/PANI//CC	452 F/g (0.2 A/g)	87% (1000 cycles)	[53]
MoS_2/PANI/MnO	469 F/g (1 A/g)	94.1 % (4000 cycles)	[54]
MoS_2/PANI/Graphene	699 F/g (0.2 A/g)	98.3 % (500 cycles)	[55]
MoS_2/PANI	274 A/g (1 A/g)	42% (1000 cycles)	[40]
MoS_2/PANI/CNT	532 A/g (1 A/g)	83% (1000 cycles)	
MoS_2/PANI	348 F/g (0.5 mA/cm^2)	/	[56]
MoS2/PANI	390 (0.8 A/g)	86 % (1000 cycles, 3 Electrodes)	[20]
1T@2H-MoS_2/PANI	618 F/g (0.5 A/g)	98% (8000 cycles)	[57]
MoS_2-ex/PANI	277 F/g (0.5 A/g)	98% (10000 cycles)	[58]
MoS_2-NH_2/PANI	326.4 F/g (A/g)	96% (10000 cycles)	[59]
MoS_2-f1/PANI	302.5 F/g (0.5 A/g)	84% (5000 cycles)	This work

3. Conclusions

In summary, this study elucidates two distinct ways for bolstering 2D materials used in electrochemical energy storage. The synthesis of hybrid nanostructures between layered MoS_2 and PANI is reported. This is accomplished by resorting to both pristine 1T-MoS_2 and an easily produced functionalized variant of the MoS_2. The functionalization process occurs under gentle conditions, employing a readily available reagent. It introduces covalently bound aniline moieties, which can be exploited to further tune the structure of the 2D nanosheets by grafting PANI directly on the surface. This functionalization methodology exploits known electrophilic chemistry, which can be also applied to other 2D materials, as long as the preconditions are met and allowing for material tailoring depending on the final applications desired. Notably, the as-synthesized MoS_2-f1@PANI covalent

hybrids show better charge storage performance compared to the non-functionalized system in the same way, reaching a specific capacitance of 302.5 F/g at 0.5 A/g in a 3-electrodes configuration and demonstrating the power of the grafting approach to improve functionality. Additionally, our investigation also shows that a templating NaCl treatment during synthesis can further improve electrochemical storage capacity, up to 71.5 F/g at 2 A/g in a 2-electrodes set-up, compared to 46 F/g for an analogous sample prepared without such pre-treatment.

Our results align quite well with those from other 2D material/conducting polymer hybrid systems, providing valuable insights into enhancing 2D materials-based energy storage platforms. We propose an easy-to-make and straightforward method for the covalent functionalization/hybridization of 2D TMDCs. This method can be exploited to produce functional electrodes for reaching high C_s at high current density, while maintaining good storage retention over prolonged cycling. Additionally, these hybrids can be easily casted on top of carbon collectors, and, in a similar way, they could be processed on other substrates, even flexible ones, in order to produce a range of energy-storage devices for multiple electronic applications.

Experimental Section

Materials preparation

MoS_2, Aniline, $(NH_4)_2S_2O_8$ and N-butyl lithium (Li^nBut) were purchased from Sigma Aldritch and used without any further purification. p-iodoaniline was purchased from TCI Chemicals and used without any further purification. 1 M HCl was prepared by dilution of concentrated HCl (36-38 wt. %) with deionized water and used without any further treatment.

1T MoS_2 production. 1T-MoS_2 was produced by a slightly modified lithiation procedure reported in literature.[60,61] A three-neck round bottom flask was connected to an Ar Schlenk line and cleaned following standard Schlenk line procedure (cycles of vacuum, heating, and Ar flux), after which 1 g of bulk MoS_2 and a magnetic stirrer were added under Ar flux in the round bottom flask and left drying under vacuum for 1 hour at 40 °C. After drying, the glassware was cooled down using an ice

bath, and then 4 mL of dry hexane was added, using an Ar purged syringe, to the glassware under moderate stirring. Subsequently, 6 mL of Li^{n}But in hexane was added in a similar way to the round bottom flask. The ice bath then, was removed and the solution was left stirring for 3 days at room temperature. At the end of the reaction, the hexane solution was recuperated using hexane as solvent and centrifuged at 6000 rpm for 20 minutes, removing the supernatant and adding fresh hexane each time. This procedure was performed three times, and the final tubes were left drying under vacuum at 40 °C overnight. Subsequently, 800 mg of the as lithiated MoS_2 were added to 400 mL of deionized water and exfoliated using a tip-sonicator (TS, Bandelin Sonoplus), operating at 80% power output with 1 s on / 1 s off cycles for 2 hours while kept at 0 °C with an ice bath. The suspension was then centrifuged at 6000 rpm for 20 minutes and the supernatant was kept for further work. Furthermore, a set amount was freeze-dried to obtain 1T-MoS2 powder for further characterization and to calculate the concentration of the suspension, which was 1 mg/mL on average.

1T-MoS_2 functionalization. The functionalization was carried out using a previously reported procedure in literature: briefly, a large excess of p-iodoaniline were added to 25 mL of NMF (usually 10 equivalents of the calculated MoS_2 used for the reaction) and left stirring for 15 minutes at 300 rpm to produce a homogenous pink solution. Afterward, the iodo-aniline solution was added to 100 mL of MoS_2 suspension in a round bottom flask and left stirring for 7 days at 40 °C. After the reaction concluded, the suspension was filtered on a PTFE filter (Omnipore, 200 μm), washed twice with 20 mL of distilled water, once with 10 mL of DMF and lastly with 10 mL of acetone and put in vacuum oven at 40 °C to dry overnight and recuperated the day after.

MoS_2@PANI hybrids. MoS_2 and PANI hybrids are synthesized according to a common procedure for the PANI polymer. Briefly, two solutions are prepared: in the first one, 10 mg of MoS_2 based material and 12 mg of sodium cholate are added to 6 mL of 1 M HCl and sonicated for 15 minutes in an ultrasonic bath (USB) at 37 Hz at room temperature. 1T-MoS_2 suspension is prepared for MoS_2(1T)@PANI, and functionalized 1T-MoS_2 suspension is prepared for MoS_2-f1@PANI. Afterward, 114 μL of aniline (1.25 mmol) were added to this suspension and stirred for another 15

minutes. Simultaneously, another solution was prepared by dissolving 0.3131 g of ammonium peroxydisulfate (APS, 1.1 eq of aniline) in 6 mL of 1 M HCl.

Depending then on the experiment, NaCl was added to both solutions until saturation was reached. The sample as produced has an additional "brine" added to their name and they are respectively: MoS_2(1T)@PANI 1:20 + brine and MoS_2-f1@PANI 1:20 + brine. Once preparation was over, the aniline/MoS_2 solution was placed in an ice bath to cool it down and the APS solution was then added to it while stirring and left reacting for 1 hour. After the reaction, the material was filtered using a paper filter and washed thoroughly with 1 M HCl and, eventually, with 10 mL of acetone and dried in a vacuum oven at 40 °C overnight.

Structural, chemical and morphological characterization

Raman spectra were recorded on a Bruker Senterra instrument using a 532 nm laser as excitation source with a power of 0.2 mW, integration time of 5 s and 60 co-addition per measurement. P-XRD measurements were performed on a PANanalytical B.V. Empyrean in the 5°-75° 2θ range using a step size of 0.013° and an integration time of 100 s. TGA was run on a Netzsch STA409PC instrument, using ≈ 20 mg per measured sample. Measurements were performed under inert atmosphere and were heated between 30 °C to 800 °C with a ramp of 10°C min^{-1}. SEM was performed on a Zeiss Merlin instrument at an acceleration potential of 4 kV, 20 µm beam aperture, and at several different magnifications. The secondary electrons were measured using an in-lens detector and a work distance of 2 mm. HRTEM imaging was conducted with a non-aberration-corrected Transmission Electron Microscope (TALOS F200X, Thermo Scientific, Eindhoven, The Netherlands) operating at 200 kV. The images were acquired using a 16-megapixel CMOS camera with an exposure time of 1 second. EDX was performed with the same instrument at an acceleration potential varying from 8 kV to 10 kV, a current of 8 nA and 60 µm beam aperture using an X-Max 50 Silicon Drift detector with 50 mm^2 active equipped with a polymer window. XPS measurements were conducted with a PHI 5000 VersaProbe IV Scanning ESCA Microprobe (Physical Electronics) with monochromatized Al Kα 1486.6 eV X-ray source in high power mode (beam diameter 200 µm, X-ray power: 50 W, X-ray

lamp voltage: 15 kV). Samples were prepared by filling a Teflon sample cap and attaching them to the XPS sample holder with an isolating tape. A time steps of 50 ms, a step size of 0.2 eV and an analyzer pass energy of 27 eV were used for measuring the detail spectra, while a pass energy of 140 eV were used for the survey spectra. The sample surface was charge neutralized with slow electrons and argon ions, and the pressure was in the range from 10^{-7} Pa to 10^{-6} Pa during the measurement. Data analysis was performed using the CasaXPS software, using an asymmetric Gaussian-Lorentzian function (A(0.35, 0.4, 0) GL(20)) to fit the MoS_2 3d orbitals, while the MoOx 3d and the S 2p orbitals were fitted with a SGL(80) and GL(10) function respectively.

Electrochemical characterization. CV was performed in a 3-electrodes set-up using glassy carbon as working, Ag/AgCl as reference, and a Pt wire as counter electrode on an Autolab PGSTAT302 equipped with an impedance module. The potential window was chosen by analyzing around the OCP with 100 mV steps until the CE dropped below 95% and confirming the results via CV, resulting in the potential window between 0 V and 0.800 V vs Ag/AgCl. PEIS was measured on a fresh electrode at constant potential (OCP), frequency range varying from 1 MHz to 1 Hz, amplitude of 10 mV and 10 points/dec. Lastly, PEIS were measured at different potentials (0 V and 0.1 V vs Ag/AgCl) after the measure and used for further analysis. GCD measurements were performed between -0.2 V and 0.6 V vs Ag/AgCl (ΔV: 0.8 V) at different current densities (0.1 A/g to 20 A/g). Specific capacitance was calculated from these measurements using the Equation 1:

$$C_s = \frac{I*\Delta t}{m*\Delta V} \qquad \text{Eq. 1}$$

Where I is the discharge current applied, Δt is the discharge time, m is mass in g of active material and ΔV is the potential window used.

Two electrode measurements were performed using a symmetric setup on Swagelok cell using a BioLogic SP150 potentiostat. Electrodes were prepared by coating a 10 mm (Swagelok) Toray paper carbon disk with a paste made from the active material, acetylene black and PVDF (mass ratio 8:1:1 respectively) and a glass fiber separator, where tree drops of electrolyte solution (H_2SO_4 0.5 M) were casted. GCD measurement were also performed from 0 V to 0.8 V (ΔV: 0.8 V) using current densities

(0.1 A/g, 0.2 A/g, 0.5 A/g, 1 A/g, 2 A/g, 5 A/g, 10 A/g). Lastly, stability test was performed on fresh electrodes at 2 A/g for 5000 cycles and capacitance retention and faradic efficiency were calculated from the mentioned measurements using the EC Lab program. C_s was calculated by using the aforementioned methodology. Faradic efficiency was calculated by dividing the amount of charge for the discharge and charge part of the GCD curve and reporting them over the course of the cycles. Lastly, Ragone plot was calculated using the Equations 2 and 3 for the energy density (J/g) and the power density (W/g) respectively:

$$E_s = \frac{C_s V^2}{2} \quad \text{Eq. 2}$$

$$P_s = \frac{E_s}{t_d} \quad \text{Eq 3}$$

Where C_s is the specific capacitance in F/g calculated beforehand, V is the voltage window used for the measurements, E_s is the energy density and t_d is the discharge time of the GCD curve.

Acknowledgments

The authors acknowledge the financial support of the European Commission through the H2020 FET-PROACTIVE-EIC-07-2020 project LIGHT-CAP (grant agreement no. [101017821]) and of the European Research Council through the ERC StG project JANUS BI (grant agreement no. [101041229]).

References

[1] M. Pershaanaa, S. Bashir, S. Ramesh, K. Ramesh, *J. Energy Storage* **2022**, *50*, 104599.

[2] D. P. Chatterjee, A. K. Nandi, *J. Mater. Chem. A* **2021**, *9*, 15880.

[3] Y. Xu, B. Liu, C. Dong, H. Feng, Y. Wei, X. Zhang, *Eur. J. Inorg. Chem.* **2023**, *26*, e202200569.

[4] M. Crisci, F. Boll, L. Merola, J. J. Pflug, Z. Liu, J. Gallego, F. Lamberti, T. Gatti, **2022**, DOI 10.3389/fchem.2022.1000910.

[5] R. Zeng, Z. Li, L. Li, Y. Li, J. Huang, Y. Xiao, K. Yuan, Y. Chen, *ACS Sustain. Chem. Eng.* **2019**, *7*, 11540.

[6] Z. Song, Z. Wang, R. Yu, *Small Methods* **2023**, 2300808.

[7] Z. Song, Z. Wang, R. Yu, *Small Methods* **2024**, *8*, 2300808.

[8] H. Ribeiro, J. P. C. Trigueiro, P. S. Owuor, L. D. Machado, C. F. Woellner, J. J. Pedrotti, Y. M.

Jaques, S. Kosolwattana, A. Chipara, W. M. Silva, C. J. R. Silva, D. S. Galvão, N. Chopra, I. N. Odeh, C. S. Tiwary, G. G. Silva, P. M. Ajayan, *Compos. Sci. Technol.* **2018**, *159*, 103.

[9] C. Zhao, X. Jia, K. Shu, C. Yu, G. G. Wallace, C. Wang, *J. Mater. Chem. A* **2020**, *8*, 4677.

[10] S. U. Rahman, P. Röse, A. U. H. A. Shah, U. Krewer, S. Bilal, *Polym. 2020, Vol. 12, Page 2212* **2020**, *12*, 2212.

[11] H. Tian, S. Zhu, F. Xu, W. Mao, H. Wei, Y. Mai, X. Feng, *ACS Appl. Mater. Interfaces* **2017**, *9*, 43975.

[12] Q. Zhang, A. Zhou, J. Wang, J. Wu, H. Bai, *Energy Environ. Sci.* **2017**, *10*, 2372.

[13] F. Lai, Z. Fang, L. Cao, W. Li, Z. Lin, P. Zhang, **n.d.**, DOI 10.1007/s11581-020-03438-3.

[14] H. Tang, Y. Ding, C. Zang, J. Gu, Q. Shen, J. Kan, *Int. J. Electrochem. Sci.* **2014**, *9*, 7239.

[15] O. Öztürk, E. Gür, *ChemElectroChem* **2024**, *11*, e202300575.

[16] S. Manzeli, D. Ovchinnikov, D. Pasquier, O. V. Yazyev, A. Kis, *Nat. Rev. Mater. 2017 28* **2017**, *2*, 1.

[17] M. Ali, A. M. Afzal, M. W. Iqbal, S. Mumtaz, M. Imran, F. Ashraf, A. Ur Rehman, F. Muhammad, *Int. J. Energy Res.* **2022**, *46*, 22336.

[18] S. Balendhran, S. Walia, H. Nili, J. Z. Ou, S. Zhuiykov, R. B. Kaner, S. Sriram, M. Bhaskaran, K. Kalantar-Zadeh, *Adv. Funct. Mater.* **2013**, *23*, 3952.

[19] C. Oueiny, S. Berlioz, F. X. Perrin, *Prog. Polym. Sci.* **2014**, *39*, 707.

[20] J. Wang, Z. Wu, K. Hu, X. Chen, H. Yin, *J. Alloys Compd.* **2015**, *619*, 38.

[21] V. Babel, B. L. Hiran, *Polym. Compos.* **2021**, *42*, 3142.

[22] X. Chen, C. Bartlam, V. Lloret, N. Moses Badlyan, S. Wolff, R. Gillen, T. Stimpel-Lindner, J. Maultzsch, G. S. Duesberg, K. C. Knirsch, A. Hirsch, *Angew. Chemie Int. Ed.* **2021**, *60*, 13484.

[23] T. Gatti, N. Vicentini, M. Mba, E. Menna, *European J. Org. Chem.* **2016**, *2016*, 1071.

[24] H. Huang, Y. Cui, Q. Li, C. Dun, W. Zhou, W. Huang, L. Chen, C. A. Hewitt, D. L. Carroll, *Nano Energy* **2016**, *26*, 172.

[25] M. Acerce, D. Voiry, M. Chhowalla, *Nat. Nanotechnol.* **2015**, *10*, 313.

[26] D. Tang, J. Li, Z. Yang, X. Jiang, L. Huang, X. Guo, Y. Li, J. Zhu, X. Sun, *Chem. Eng. J.* **2022**, *428*, 130954.

[27] H. Li, H. Li, Z. Wu, L. Zhu, C. Li, S. Lin, X. Zhu, Y. Sun, *J. Mater. Sci. Technol.* **2022**, *123*, 34.

[28] P. Vishnoi, A. Sampath, U. V. Waghmare, C. N. R. Rao, *Chem. – A Eur. J.* **2017**, *23*, 886.

[29] X. Creary, *Chem. Rev.* **1991**, *91*.

[30] P. W. Ayers, J. S. M. Anderson, J. I. Rodriguez, Z. Jawed, *Phys. Chem. Chem. Phys.* **2005**, *7*, 1918.

[31] R. M. O'Ferrall, *Adv. Phys. Org. Chem.* **2010**, *44*, 19.

[32] K. Xps, S. Sulfur, D. Fosforus, Y. Mempunyai, P. Yang Berbeza, K. S. Siow, L. Britcher, S. Kumar, H. J. Griesser, *Sains Malaysiana* **2018**, *47*, 1913.

[33] O. of D. I. (ODI), U. . D. of C. National Institute of Science and Technology (NIST), "https://srdata.nist.gov/xps/SpectraIdentifier," **2023**.

[34] *Encycl. Anal. Chem.* **2007**, DOI 10.1002/9780470027318.

[35] D. Lee, K. Char, *Polym. Degrad. Stab.* **2002**, *75*, 555.

[36] A. Kumar, A. Kumar, H. Mudila, K. Awasthi, V. Kumar, *J. Phys. Conf. Ser.* **2020**, *1531*, 012108.

[37] A. ul H. Ali Shah, N. Yasmeen, G. Rahman, S. Bilal, *Electrochim. Acta* **2017**, *224*, 468.

[38] A. ul H. A. Shah, S. Akhlaq, M. Sayed, S. Bilal, N. Ali, *Chem. Pap.* **2018**, *72*, 2523.

[39] K. Pandey, P. Yadav, I. Mukhopadhyay, *Phys. Chem. Chem. Phys.* **2014**, *17*, 878.

[40] M. Jasna, M. Muraleedharan Pillai, A. Abhilash, P. S. Midhun, S. Jayalekshmi, M. K. Jayaraj, *Carbon Trends* **2022**, *7*, 100154.

[41] V. Vivier, M. E. Orazem, *Chem. Rev.* **2022**, *122*, 11131.

[42] J. Huang, *Electrochim. Acta* **2018**, *281*, 170.

[43] Q. Tang, D. E. Jiang, *Chem. Mater.* **2015**, *27*, 3743.

[44] H. Zhang, T. D. Koledin, W. Xiang, J. Hao, S. U. Nanayakkara, N. H. Attanayake, Z. Li, M. V. Mirkin, E. M. Miller, *2D Mater.* **2021**, *9*, 015033.

[45] A. Chellachamy Anbalagan, S. N. Sawant, *Polymer (Guildf).* **2016**, *87*, 129.

[46] A. Q. Zhang, C. Q. Cui, J. Y. Lee, *Synth. Met.* **1995**, *72*, 217.

[47] G. L. C. Paulus, Q. H. Wang, M. S. Strano, *Acc. Chem. Res.* **2012**, *46*, 160.

[48] A. Sinitskii, A. Dimiev, D. A. Corley, A. A. Fursina, D. V. Kosynkin, J. M. Tour, *ACS Nano* **2010**, *4*, 1949.

[49] G. L. C. Paulus, Q. H. Wang, M. S. Strano, *Acc. Chem. Res.* **2013**, *46*, 160.

[50] D. Sabaghi, J. Polčák, H. Yang, X. Li, A. Morag, D. Li, A. S. Nia, S. Khosravi H, T. Šikola, X. Feng, M. Yu, *Adv. Energy Mater.* **2024**, *14*, DOI 10.1002/AENM.202302961.

[51] L. Daukiya, J. Teyssandier, S. Eyley, S. El Kazzi, M. C. Rodríguez González, B. Pradhan, W. Thielemans, J. Hofkens, S. De Feyter, *Nanoscale* **2021**, *13*, 2972.

[52] A. A. Mohamed, Z. Salmi, S. A. Dahoumane, A. Mekki, B. Carbonnier, M. M. Chehimi, *Adv. Colloid Interface Sci.* **2015**, *225*, 16.

[53] Y. Wang, X. Lv, S. Zou, X. Lin, Y. Ni, *RSC Adv.* **2021**, *11*, 10941.

[54] H. Heydari, M. Abdouss, S. Mazinani, A. M. Bazargan, F. Fatemi, *J. Energy Storage* **2021**, *40*, 102738.

[55] S. Palsaniya, H. B. Nemade, A. K. Dasmahapatra, *Polymer (Guildf).* **2018**, *150*, 150.

[56] S. Krithika, J. Balavijayalakshmi, *Mater. Today Proc.* **2022**, *50*, 17.

[57] R. Rahman, P. Rani, S. Ghosh, A. Midya, A. Pathak, T. K. Nath, *ACS Appl. Energy Mater.* **2023**, *6*, 11012.

[58] M. Tomy, M. A. Anu, T. S. Xavier, *Appl. Phys. A Mater. Sci. Process.* **2023**, *129*, 1.

[59] R. Zeng, Z. Li, L. Li, Y. Li, J. Huang, Y. Xiao, K. Yuan, Y. Chen, *ACS Sustain. Chem. Eng.*

Easy direct functionalization of 2D MoS_2 applied in covalent hybrids with PANI as dual blend supercapacitive materials

Matteo Crisci[1,2], Felix Boll[1,2], Sara Domenici[2,3], Jaime Gallego[1,2], Bernd Smarsly[1,2], Francesco Lamberti,[4-5] Mengjiao Wang[3], Andrea Rubino[6], Teresa Gatti[2,3]*

[1]*Institute of Physical Chemistry, Justus Liebig University, Heinrich Buff Ring 17, 35392, Giessen, Germany*

[2]*Center for Materials Research, Justus Liebig University, Heinrich Buff Ring 16-17, 35392, Giessen, Germany*

[3]*Deparment of Applied Science and Technology, Politecnico di Torino, C.so Duca degli Abruzzi 24, 10129, 10129 Torino, Italy*

[4] *Department of Chemical Sciences, University of Padova, Via Marzolo 1, 35131 Padova, Italy*

[5]*Department of Industrial Engineering, University of Padova, Via Gradenigo 6a, 35131, Padova, Italy*

[6] *Functional Nanosystems, Istituto Italiano di Tecnologia, Via Morego 30, 16163 Genova, Italy*

E-mail: teresa.gatti@polito.it

Table of Content

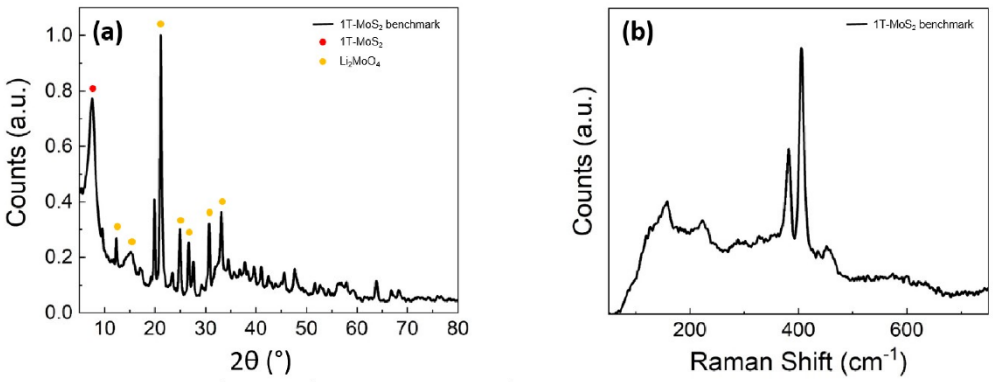

***Figure S1**.(a) P-XRD and (b) Raman measurements of exfoliated 1T-MoS2*

Figure S1 Discussion

Typical fingerprints of the MoS_2 1T-phase can be observed in the XRD diffractogram. The reflection at 8° can be ascribed to the 002 reflection of the material.[1–3] Additionally, reflections between 20° and 30° are observed and can be attributed to molybdate species. These could be formed by surface oxidation of the material during the exfoliation process. Typical peaks related to MoS_2 are present, i.e. the E_{2g} mode at 380 cm^{-1} and the A_{1g} mode at 404 cm^{-1}. Moreover, two further peaks at 157 cm^{-1} and 222 cm^{-1} were observed and can be indexed to J_1 and J_2 modes related to the 1T-MoS_2 phase.[3,4]

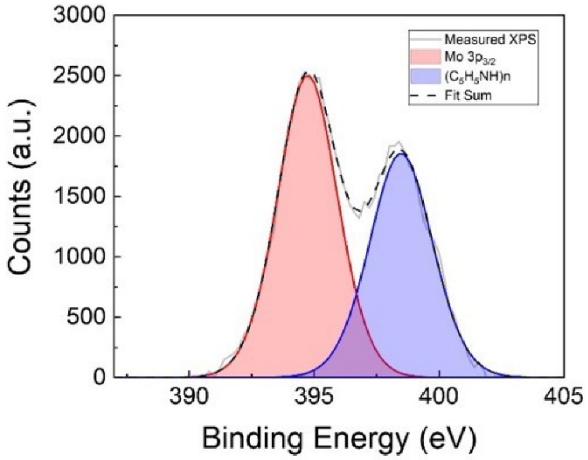

Figure S2. *XPS spectra of N 1s region of 1 day functionalized MoS*

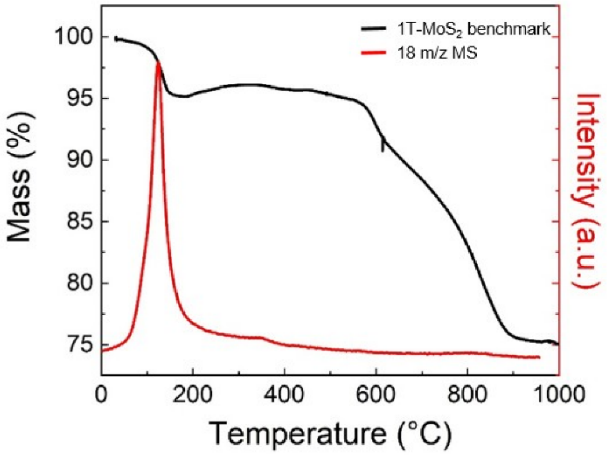

Figure S3. TGA-MS analysis of benchmark 1T-MoS2 and fragment corresponding to 18 m/z

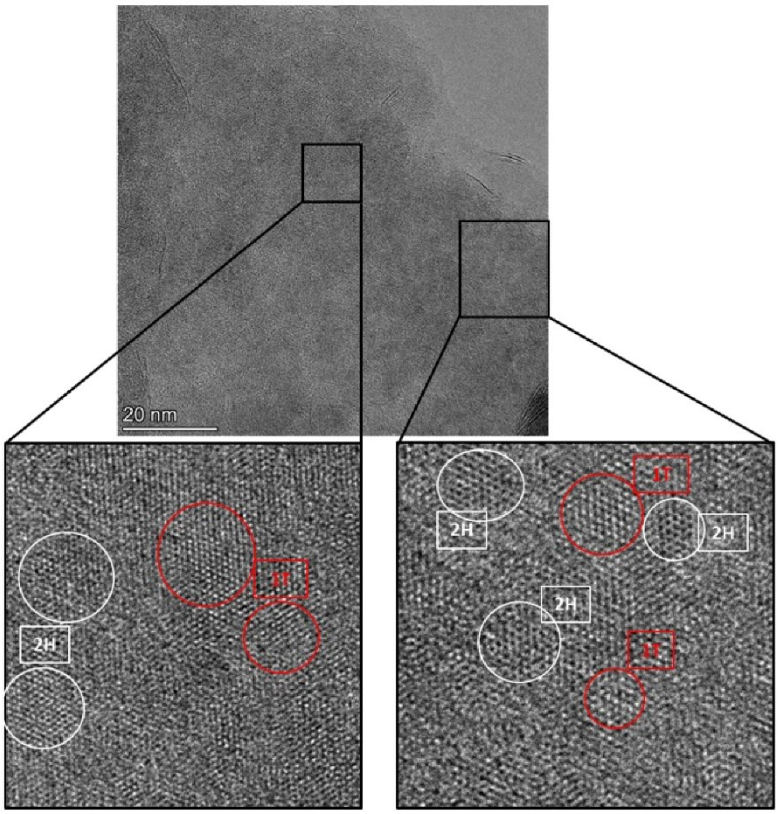

Figure S4. *TEM image of functionalized MoS_2 and high resolution zoom of the corresponding sample to show the different disposition of the atoms on the sheet (2H and 1T phase coexistence)*

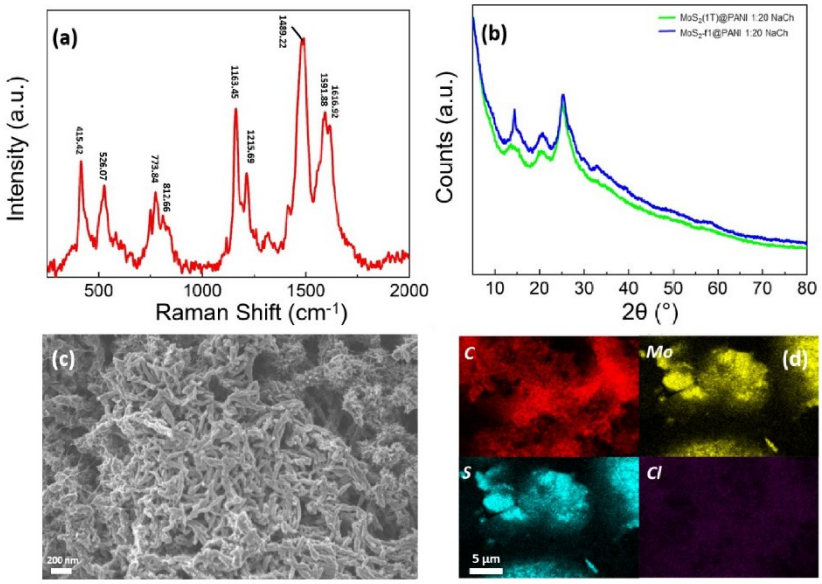

Figure S5. *(a) Raman spectra of MoS_2-f1@PANI. (b) P-XRD of the as produced materials. (c) Reference SEM picture of MoS_2-f1@PANI and (d) relative EDX maps.*

Figure S5 Discussion

The two peaks at 1616 cm^{-1} and 1591 cm^{-1} are respectively associated to the C-C stretching of the benzoic form and the C=C bond of the quinoid form. Right next to the quinoid form fingerprint, there is another signal at 1489 cm^{-1} that can be attributed to C=N stretching. Further modes at 1215 and 1163 cm^{-1} can be attributed to C-N and C-H bonds related to a mixed benzoic/quinoid structure of the material. Moreover, there is an additional artefact at 1314 cm^{-1} that can be associated with the localized charge on C-N bonds, however, this signal can shift depending on the chain length of the polymer. The last four observed peaks, at 812 cm^{-1}, 773 cm^{-1}, 526 cm^{-1} , and 415 cm^{-1} can be all attributed to C-H bonds and to C-C bond of the benzene/quinoid ring of the material.[5,6] In this region, also two main vibrational modes of MoS_2 should be present at around 380 cm^{-1} and 404 cm^{-1}, however, considering the 1 to 20 ratio between the inorganic and organic part in the hybrid material, they are probably covered by the signals of the conducting polymer and therefore no visible difference are observed in this context between the different hybrid materials. Similarly, P-XRD analysis were performed on both hybrid samples (Figure S5b) and, as in the Raman analysis, mainly reflections associated to PANI[7,8] were seen. Only the reflection at around 15° (2θ) can be attributed to both the (002) plane of MoS_2 and of the PANI. In the case of the reference with 1T-phase, this contribution comes predominantly from the conducting polymer; however, in the hybrid with functionalized MoS_2, a sharp reflection emerges at around 14.8° which can be associated with the aforementioned (002) plane of MoS_2. Eventually, the incorporation of the inorganic TMDC in the polymer was confirmed *via* scanning electron microscopy (SEM) and related energy dispersive X-ray (EDX) analysis, studying both the morphology and the elemental composition (Figure S5c-d, S6). A rod-like morphology is evident in the hybrid material, which is usually attributed to the PANI structure. However, no bi-dimensional

structures is observed, hinting at a complete coverage of the 2D material by the conductive polymer, reasonable considering the ratio between the two components.

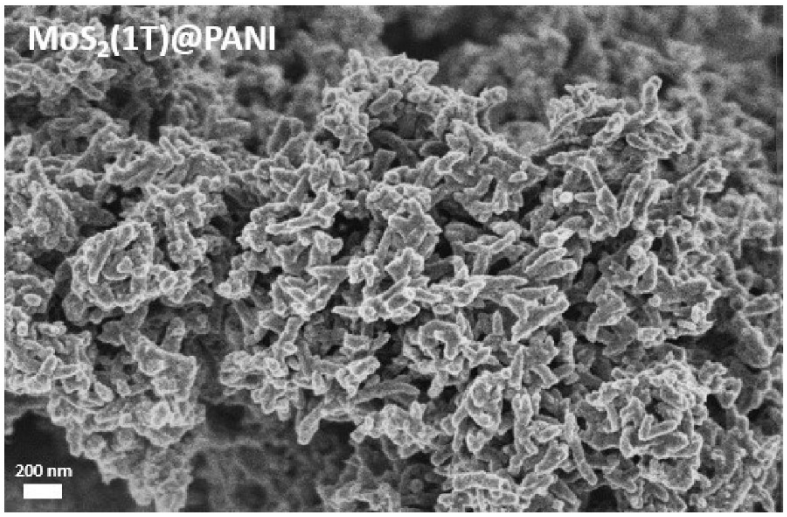

Figure S5. *SEM picture of hybrid material*

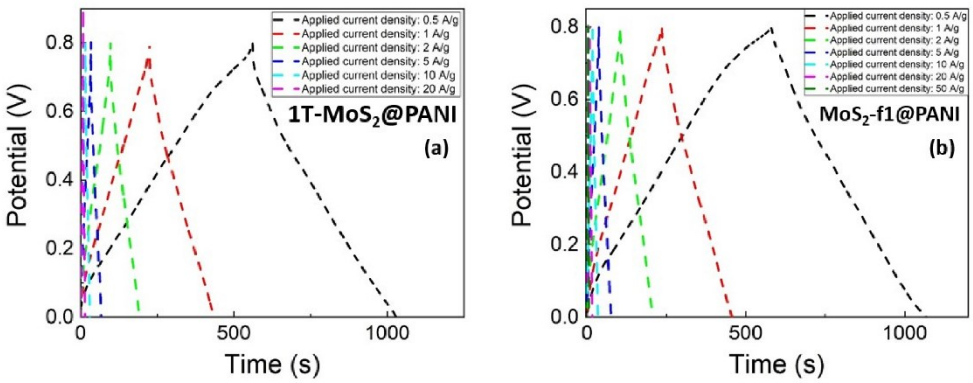

Figure S6. *GCD curves for the hybrid materials tested in 3 Electrode set up*

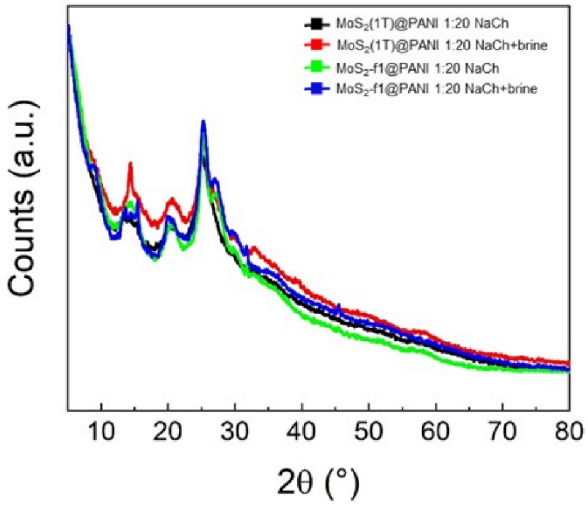

Figure S7. *P-XRD comparison of hybrid material, with and without brine treatment*

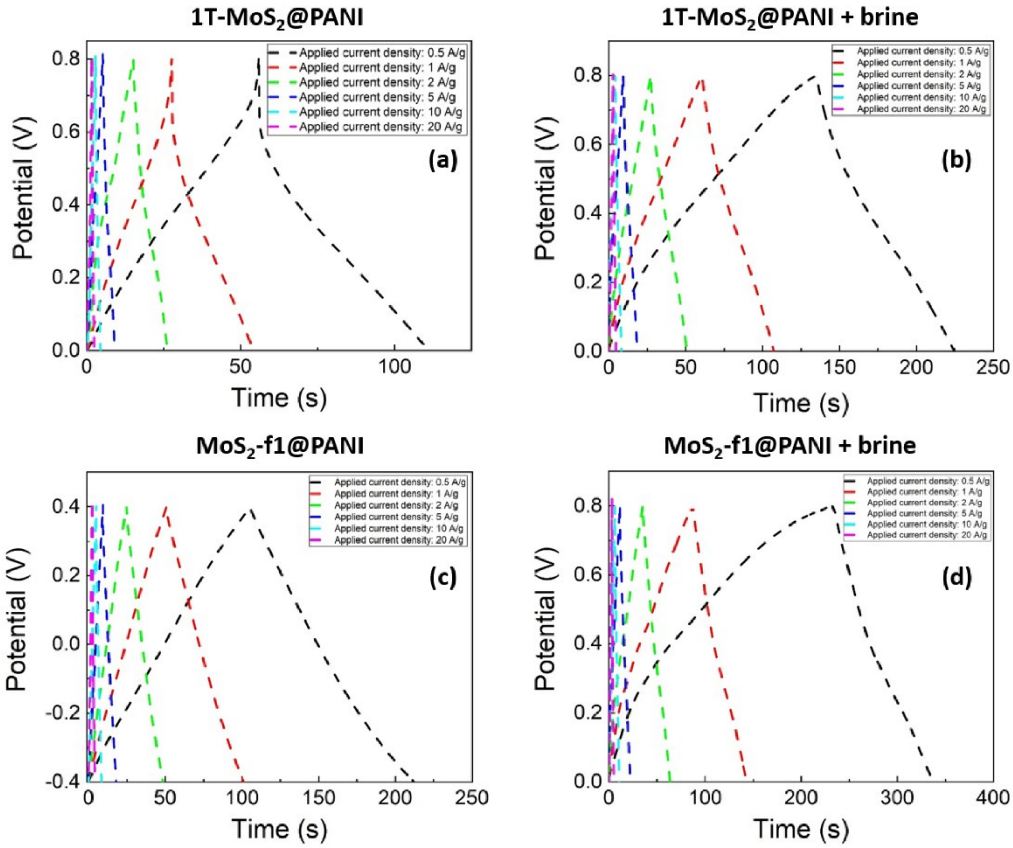

Figure S8. *GCD curves for the hybrid materials (with and without NaCl treatment) tested in a Swagelok cell*

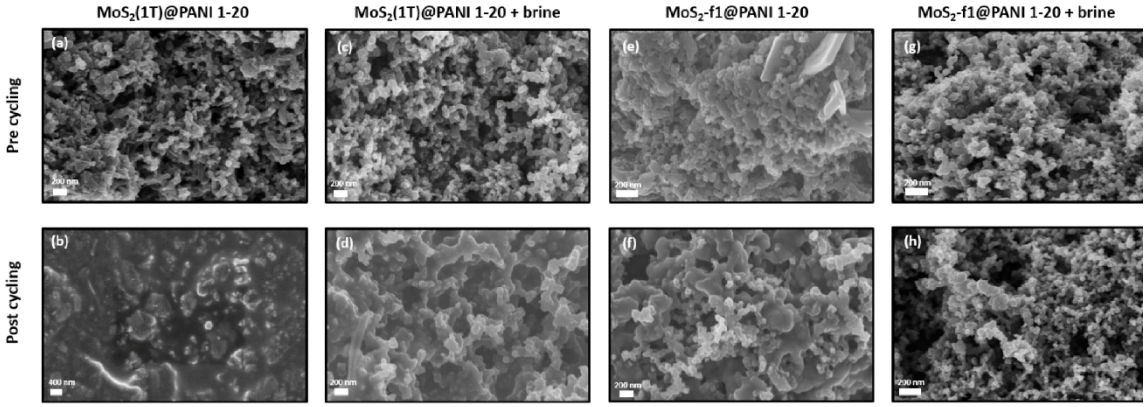

Figure S9. *SEM images of the used electrodes in Swagelok measurements, before and after cycling*

Table S1. Functionalization degree of 1T-MoS_2 nanosheets reacted with *para*-substituted iodoaniline for different time.

Reaction time (days)	Mass loss (%)	Functionalization degree per S atom (%)
1	4	3.6
3	10	9.6
7	7	6.5

Table S2. Resistance values obtained by fitting the impedance data with a standard cell circui and conductivity measurements obtained from the EIS data, assuming an electrode thickness of 100 µm.

Sample name	R_0 (Ω cm^2)	R_{ct} (Ω cm^2)	σ $(\Omega\ cm)^{-1}$
MoS_2(1T)@PANI	0.92	7.44	$1.34*10^{-3}$
MoS2-f1@PANI	1.11	3.62	$2.76*10^{-3}$

Table S3. Energy and power density values extrapolated from the Ragone plots for the four MoS_2/PANI hybrids tested in a two-electrodes set-up

Sample name	Energy density (Wh/kg)	Power density (kW/kg)
MoS_2(1T)@PANI	1.5	7.9
MoS_2-f1@PANI	3.4	3.1
MoS_2(1T)@PANI + brine	4.0	8.0
MoS_2-f1@PANI + brine	4.5	8.1

References

1 M. Acerce, D. Voiry and M. Chhowalla, *Nat. Nanotechnol.*, 2015, **10**, 313–318.

2 C. Zhang, Y. Zhang, Y. Zhang, X. Huang, Y. Li, J. Cao and C. Zhou, *Mater. Lett.*, 2022, **314**, 131794.

3 H. Li, H. Li, Z. Wu, L. Zhu, C. Li, S. Lin, X. Zhu and Y. Sun, *J. Mater. Sci. Technol.*, 2022, **123**, 34–40.

4 L. Li, J. Chen, K. Wu, C. Cao, S. Shi and J. Cui, *Nanomater. 2019, Vol. 9, Page 1366*, 2019, **9**, 1366.

5 M. Tagowska, B. Pałys and K. Jackowska, *Synth. Met.*, 2004, **142**, 223–229.

6 J. Malenfant, L. Kuster, Y. Gagné, K. Signo, M. Denis, S. Canesi and M. Frenette, *Chem. Sci.*, 2024, **15**, 701–709.

7 B. Li, D. Sun, B. Li, W. Tang, P. Ren, J. Yu and J. Zhang, *Langmuir*, 2020, **36**, 2209–2222.

8 S. Padmapriya, S. Harinipriya, K. Jaidev, V. Sudha, D. Kumar and S. Pal, *Int. J. Energy Res.*, 2018, **42**, 1196–1209.

3.6: Publication n°5

Stabilizing Layered BiOBr Photoelectrocatalyst by Van der Waals Heterojunction Strategy

Authors: Wang M., Osella S., Torre B., **Crisci M.**, Schmitz F., Altieri R., Di Fabrizio E., Amenitsch H., Sartori B., Liu Z., Gatti T., Lamberti F.

As reported in the previous chapters, HER has always been an interesting solution to substitute the production of hydrogen from fossil fuels to greener solutions and in this application MoS_2 has always proved to be an efficient catalyst and a good candidate for the substitution of Pt based catalysts. MoS_2 has been reported by several research group as a promising electrocatalyst for the production of hydrogen[175,273,274] with large differences between the 1T and 2H phases, with the first one often being considered the best one of the two for the evolution reaction. [275–278] However, there are also option to use the TMDC and other materials to enhance and fine tune the properties of the 2D material. Examples are the use of moS2 as a support and promoter, supported on some other materials and in heterostructures to obtain a synergistic effect on the final properties of the composite.

Following this line of thought, **publication n°5** aimed to obtain an heterostructure using both widely used electrocatalyst 1T-MoS_2 and photoactive BiOBr to achieve obtain photoelectrochemical hydrogen conversion, coupling the light absorbance of one material and the catalytic activity of the other to further bolster the properties of the material. The synthesis procedure was optimized from a precedent publication, **publication n° 4**, and the characterization was made via Raman and electron microscopies (TEM and SEM), while electrochemical characterization was performed via LSV and CVs in electrochemical (EC) and photoelectrochemical condition (PEC) using a mercury lamp a light source in this case. Moreover, to delve deeper into the mechanism

of reaction and the change of the two material, quasi in-situ WAXD experiments at the Electra Synchrotron in Trieste were performed after each electrochemical measurements and these analyses couple with theoretical calculations, performed by our collaborators, allowed us to deepen our understanding of the interactions between the two components.

My contribution in this paper was focused on the preparation of the 1T-MoS_2 material and the heterojunction with BiOBr, coupled with its characterization. Moreover, I took part in the experiments performed at the synchrotron, supporting the data gathering and analysis of the in-situ electrochemical WAXD measurement. In addition to that, data discussion, analysis and paper writing were also part of the contribution I gave to the publication.

Check for updates

ChemCatChem

Research Article
doi.org/10.1002/cctc.202400282

Chemistry Europe
European Chemical Societies Publishing

www.chemcatchem.org

Stabilizing Layered BiOBr Photoelectrocatalyst by Van Der Waals Heterojunction Strategy

Mengjiao Wang,*[a] Silvio Osella,[b] Bruno Torre,[a] Matteo Crisci,[c] Fabian Schmitz,[c] Roberto Altieri,[c] Enzo Di Fabrizio,[a] Heinz Amenitsch,[d] Barbara Sartori,[d] Zheming Liu,[e] Teresa Gatti,[a] and Francesco Lamberti*[f, g, h]

The photoelectrocatalytic (PEC) hydrogen evolution reaction (HER) holds immense promise as a clean and sustainable method for hydrogen production. However, finding a suitable catalyst which is efficient, stable and scalable still remains an open challenge. BiOBr is a 2D layered material studied as photoelectrocatalyst because of its suitable band gap for light absorption and potential for up-scalable production. However, its application in HER is not commonly reported, because of instability in a cathodic PEC environment, driven by a strong tendency to reduction to metallic bismuth. To solve this problem, 2D MoS_2 is used to induce the formation of a van der Waals (vdW) layered heterojunction (HJ) to stabilize the lattice of BiOBr during HER. By performing PEC HER with the HJs containing different ratios of MoS_2, it is found that the HJ with 1% MoS_2 can increase the stability of BiOBr, while the one with 50% MoS_2 can even accelerate the reduction of BiOBr to metallic bismuth. DFT calculations reveal that the interface between BiOBr and MoS_2 in the HJ with 1% MoS_2 tends to push active electrons on the sulfur atoms, thus favoring HER. On the other hand, in the 50% HJ, active electrons are prone to react with BiOBr to induce reduction. *In situ* wide-angle X-ray diffraction (WAXD) on the MoS_2/BiOBr HJs with 1% and 50% of MoS_2 allows to track the phase change and the phase transfer speed of BiOBr during PEC HER. Interestingly, when the HJ is illuminated with UV light, a lower amount of BiOBr is reduced to Bi under negative potential, due to the presence of photo-generated holes reacting with the extra electrons derived from the negative bias and preventing the BiOBr photon absorber to be further reduced.

Introduction

The photoelectrocatalytic hydrogen evolution reaction (PEC HER) is a fascinating and sustainable process, which harnesses sunlight and electric power to drive the production of hydrogen from water. However, several challenges such as efficiency, stability, cost and scalability still exist for optimizing photo-electrocatalysts for PEC HER.[1–3] BiOBr stands out as a promising photoelectrocatalyst with unique structural and electronic characteristics that make it well-suited for solar-driven applications.[4–6] Possessing a layered crystal structure with Bi_2O_2 layers separated by Br atoms, BiOBr has a peculiar electronic structure, which allows for efficient charge separation and migration, leading to enhanced PEC activity.[7] For instance, Ling et al. fabricated BiOBr nanosheet arrays on indium tin oxide as a photoanode and a transient current of 70 $\mu A/cm^2$ was detected at a bias of 0.9 V.[8] Wang et al. showed photocurrent density of 0.29 mA/cm^2 at 1.23 V vs. RHE for BiOBr.[9] Hu et al. used BiOBr nanosheets for PEC alcohol oxidation with the combination of Pt.[10] A BiOBr/Ti photoanode was used to degrade RhB under bias voltage of 0.7 V.[11] Meanwhile, its cost-effectiveness and

[a] *Dr. M. Wang, Dr. B. Torre, Prof. E. Di Fabrizio, Prof. T. Gatti*
Dipartimento Scienza Applicata e Tecnologia (DISAT)
Politecnico di Torino
Corso Duca degli Abruzzi 24, 10129, Torino, Italy
E-mail: mengjiao.wang@polito.it

[b] *Prof. S. Osella*
Chemical and Biological Systems Simulation Lab, Centre of New Technologies
University of Warsaw,
Ochota campus, Banacha 2 C, 02097 Warszawa, Poland

[c] *M. Crisci, F. Schmitz, R. Altieri*
Institute of Physical Chemistry and Center for Materials Research (LaMa)
Justus Liebig University
Heinrich-Buff-Ring 17, 35392, Giessen, Germany

[d] *Dr. H. Amenitsch, Dr. B. Sartori*
Institute of Inorganic Chemistry,
Graz University of Technology,
Stremayrgasse 9, 8010, Graz, Austria

[e] *Z. Liu*
Nanochemistry Department,
Istituto Italiano di Tecnologia,
16163 Genova, Italy

[f] *Dr. F. Lamberti*
Dipartimento di Scienze Chimiche
Università degli Studi di Padova
Via Marzolo, 1, 35131, Padova, Italy
E-mail: francesco.lamberti@unipd.it

[g] *Dr. F. Lamberti*
Dipartimento di Ingegneria dell'Informazione
Università degli Studi di Padova
Via Gradenigo, 6b, 35131, Padova, Italy

[h] *Dr. F. Lamberti*
Zhejiang Beisheng Photovoltaic Co., Ltd.
No.800 Zhenbei Road, Zhili Town, Wuxing District Huzhou, Zhejiang 313000, China

Supporting information for this article is available on the WWW under https://doi.org/10.1002/cctc.202400282

ChemCatChem
Research Article
doi.org/10.1002/cctc.202400282
Chemistry Europe
European Chemical Societies Publishing

potential for facile scaled-up production make BiOBr worthy to optimize as a photoelectrocatalyst.[12]

In most cases, however, the pure BiOBr is used as a photoanode suitable for oxidation reactions, due to its band structure.[13–15] *Operando* chemical stability is a critical factor in the practical application of BiOBr as a photoelectrocatalyst for HER. Since BiOBr has demonstrated reasonable stability only under specific conditions, research efforts are usually directed toward improving its resistance to photocorrosion, a process where the material degrades over prolonged exposure to light.[16] Meanwhile, the negative bias can cause the reduction of BiOBr as well, since the standard potential of Bi^{3-}/Bi^{0} is 46 mV vs. Ag/AgCl.[17] In principle, the Bi- and BiO-terminations found in single-layer BiOBr demonstrate highly active sites for the HER, whereas the inert basal planes of monolayer BiOBr can be activated for the HER by introducing halogen vacancies.[18,19] Similarly, other BiOX compounds like BiOCl and BiOI may offer similar characteristics, but BiOBr remains the most extensively studied for the HER due to its optimal band-gap (2.42 eV).[20] Moreover, incorporating BiOBr with other materials could enhance its structural stability during PEC analysis. For instance, Shi et al. managed to reduce Cr(VI) to Cr(III) with MoS_2/BiOBr.[21] Han et al. fabricated core-shell structured Bi/BiOBr photoelectrode for PEC HER getting a photocurrent of 6 mA/cm^2 at −0.5 V vs. RHE.[22] A 2D MoS_2/BiOBr heterojunction (HJ) is a successful example to suppress self-reduction of the oxybromide during the PEC HER. In our previous work, it was found that within a few- layers MoS_2/BiOBr HJ, the BiOBr structure remains intact during the PEC HER only when the ratio of MoS_2 is 1%.[23] On the other hand, with 50% of MoS_2 inside the HJ, the BiOBr component is reduced to Bi in a short time.[23] However, the HJ with 1% of MoS_2 can only partially hinder the reduction process instead of completely avoiding it, and still a portion of BiOBr is reduced to Bi during PEC. Therefore, the methodology based on the selective modification of layered BiOBr for realizing HJs with cathodic properties is still at its infant stage and deeper mechanistic studies are required for its successful application in HER, at maximized stability.

Based on the above state-of-the-art situation, we present here a more detailed study on the PEC HER process with 2D MoS_2/BiOBr HJ catalysts. To dig more into the mechanism behind such system, we performed density functional theory (DFT) simulations to atomistically describe the HER process on the MoS_2/BiOBr HJ. Our calculations demonstrate that in the HJ with 50% MoS_2, active electrons are more likely to interact with BiOBr instead of reducing absorbed protons on sulfur atoms, leading to the production of metallic Bi. Conversely, in the 1%-MoS_2/BiOBr configuration, the interface between BiOBr and MoS_2 tends to transfer active electrons to the sulfur atoms, thereby promoting HER. Furthermore, we monitored the reduction process of BiOBr to metallic Bi in the HJs by synchrotron wide-angle X-ray diffraction (WAXD) during the PEC reaction. By comparing the HJs with 1% and 50% of MoS_2, the phase transfer in 50%- MoS_2/BiOBr results faster and more complete than that in 1%-MoS_2/BiOBr. More interestingly, under illumination conditions, there is less amount of BiOBr reduced compared to the same situation in dark. This happens most likely because photogenerated holes can neutralize the extra electrons and protect BiOBr from reduction to Bi.

Results and Discussion

The HJ samples are synthesized by a combination of microwave synthesis and liquid phase exfoliation (LPE) methods, as reported before and described briefly here in the experimental section.[20] By tuning the weight ratio of bulk BiOBr and MoS_2 precursors to 100:1 and 1:1, MoS_2/BiOBr van der Waals (vdW) HJs with few and large amount of MoS_2 are prepared. The sample with 1% of MoS_2 precursor is labelled as 1%-MoS_2/BiOBr, while the sample with 50% of MoS_2 is labelled as 50%-MoS_2/BiOBr. The powder X-ray diffraction (P-XRD) patterns of 50%-MoS_2/BiOBr are indexed as the combination of a tetragonal BiOBr phase (ICSD number: 61225) and hexagonal MoS_2 phase (ICSD number: 95569) without the presence of any impurities (Figure S1). Only the BiOBr phase is instead detected in the 1%-MoS_2/BiOBr, because of the small content in MoS_2. Their morphologies were checked with transmission electron microscopy (TEM). As shown in Figure S2, pure exfoliated BiOBr and MoS_2 both provide nanosheets with irregular shape. 2D BiOBr shows a rough size range between 50 and 150 nm, while 2D MoS_2 is more than 300 nm in width. In Figure 1a and 1b, both 1%-MoS_2/BiOBr and 50%-MoS_2/BiOBr show the combination of large MoS_2 and small BiOBr nanosheets. The high-angle annular dark field scanning transmission electron microscopy (HAADF-STEM) and the corresponding STEM-EDX mapping of 1%-MoS_2/BiOBr displayed the existence of Mo and Bi elements, further confirming the existence of MoS_2 in 1%-MoS_2/BiOBr. The distribution of these two elements proved an overlapping of the two structures.

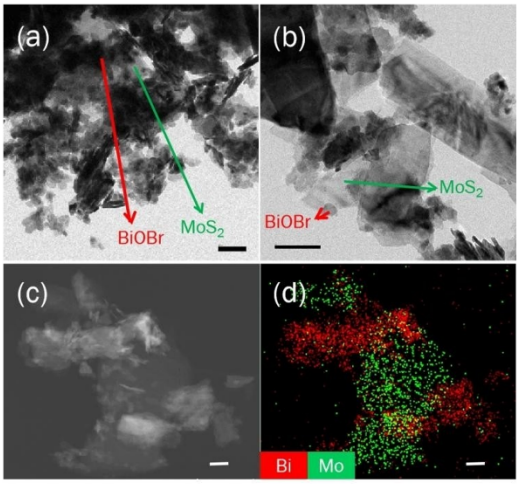

Figure 1. TEM images of (a) 1%-MoS_2/BiOBr and (b) 50%-MoS_2/BiOBr. (c) HAADF-STEM image and (d) EDX elemental mapping of 1%-MoS_2/BiOBr. Scale bars are 100 nm in all images.

ChemCatChem
Research Article
doi.org/10.1002/cctc.202400282
Chemistry Europe
European Chemical Societies Publishing

Raman analysis was further performed to identify vdW interactions between BiOBr and MoS_2. Figure 2a depicts the Raman spectra for 2D layered BiOBr, 2D layered MoS_2, and 1%-MoS_2/BiOBr HJ excited by a 532 nm laser. The Raman spectrum of BiOBr presents a typical Raman peak of A_{1g} mode located at 125 cm^{-1} and a peak of E_{1g} mode located at 161 cm^{-1}.[24] The A_{1g} and E_{1g} phonon modes come from the internal Bi–Br stretching vibration. These Raman peaks for pure BiOBr are consistent with those of the oxyhalide in the 1%-MoS_2/BiOBr HJ. On the other hand, in 50%-MoS_2/BiOBr, the characteristic peaks of BiOBr are weak and this is likely due to the large amount of MoS_2 covering the surface of the sample and fading signals from the pnictogen-containing species. The A_{1g} peak and E_{1g} peak of 1%-MoS_2/BiOBr demonstrate obvious red shift from 125 cm^{-1} and 161 cm^{-1} to 111 cm^{-1} and 156 cm^{-1} compared with that of the pure BiOBr. The red shift reveals that the MoS_2/BiOBr vdW HJ is potentially associated with the interlayer coupling interaction of BiOBr and MoS_2 layers.[25–27] This might result from the Bi–S interaction, which has a lower frequency than Bi–Br.[28,29] The characteristic Raman peaks of MoS_2 are related to an in-plane phonon mode E_{2g} (382 cm^{-1}) of Mo–S and an out-of-plane phonon mode A_{1g} (406 cm^{-1}) of S–S bonds.[30] The difference between these two peaks are 24.3 cm^{-1}, which means the MoS_2 is exfoliated to few-layered materials, in a quasi 2D fashion.[31] As to the HJs, the position of E_{2g} is not changed apparently, while the position of A_{1g}, related to S–S bond, shows a blue shift to 409 and 408 cm^{-1} for 1%-MoS_2/BiOBr and 50%-MoS_2/BiOBr, respectively. This finding represents the initial evidence of surface sulfurs from MoS_2 forming an electrostatic van der Waals (vdW) interaction with BiOBr. Furthermore, the selected area in Figure 2b was analyzed through Raman mapping on a highly resolved nano-Raman set-up.[32] It is clear form this further analysis that the BiOBr layered component is fully dispersed in this area. Figure 2c shows the integrated peak of BiOBr centered at 125 cm^{-1} with a peak width of 20 cm^{-1}, and Figure 2d displays the integrated peak from MoS_2 centered at 409 cm^{-1} with a peak width of 1 cm^{-1}, confirming the existence and distribution of BiOBr and MoS2 inside the area. Figure 2e shows the integration of the peak at 111 cm^{-1} (peak width of 5 cm^{-1}), which is from the HJ. Compared to Figure 2c, it is apparent that the peak at 111 cm^{-1} only appears at the overlapping area of BiOBr and MoS_2 nanosheets, meaning that the interaction between the two components is among the whole overlapping area of BiOBr and MoS_2 nanosheets. Moreover, the deconvolution of the Mo 3d peaks in the X-ray photoelectron spectroscopy (XPS) spectra of the HJs revealed two peaks at 232.2 eV and 229.1 eV, corresponding to $Mo^{4+}3d_{3/2}$ and $3d_{5/2}$ in the 2H phase (Figure S3).[33] This demonstrates that only the 2H MoS_2 is present in the HJs and no traces of the metallic 1T-phase can be detected.

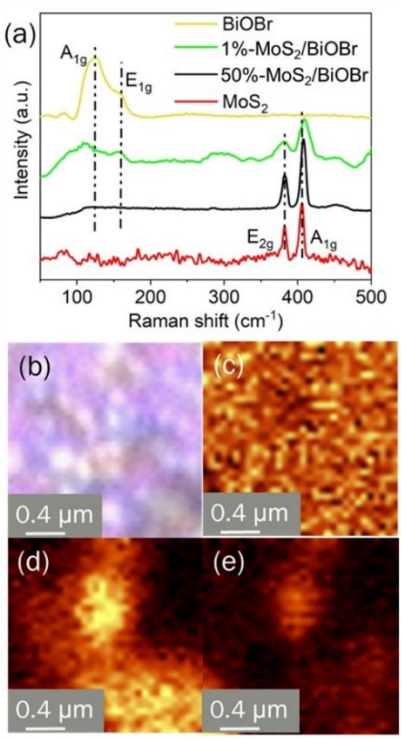

Figure 2. (a) Raman spectra of 2D BiOBr, 2D MoS_2 and 2D MoS_2/BiOBr HJs. At the selected area (b), Raman mapping of the peaks at (c) 125 cm^{-1}, (d) 409 cm^{-1}, and (e) 111 cm^{-1}.

PEC HER has been conducted on photocathodes made of drop-casted MoS_2/BiOBr HJs and pure BiOBr on transparent conductive fluorine-doped tin oxide (FTO) substrates. As shown in Figure 3a and 3b, 50%-MoS_2/BiOBr and 1%-MoS_2/BiOBr yield −16.5 mA/cm^2 and −10 mA/cm^2 at −0.6 V vs. RHE in the first cycle, respectively. This significant enhancement in PEC activity, compared to pristine BiOBr (−3 mA/cm^2) in Figure 3c, suggests that the HJs exhibit more effective catalytic activity than pure BiOBr. However, the HER performance of 50%-MoS_2/BiOBr dropped dramatically from the second cycle, likely due to the reduction of BiOBr since the broad irreversible redox peak of $Bi^{3+} \rightarrow Bi^0$ appears before HER. Meanwhile, BiOBr has shown the redox peak of $Bi^{3+} \rightarrow Bi^0$ as well starting from the 2nd cycle, which is displayed in Figure 3c. Regarding 1%-MoS_2/BiOBr in Figure 3b, the redox peak appears from the 3rd cycle, and the current density for HER remains higher than −7 mA/cm^2 at −0.6 V vs. RHE after 5 cycles. In contrast, 50%-MoS_2/BiOBr shows almost no current after 3 cycles and BiOBr has sustain the low current density of ~-3 mA/cm^2. These results reveal that the HER activity and durability are highly related to the composition inside the HJ, which will be discussed in detail later.

DFT simulations were performed on the 50%-MoS_2/BiOBr to elucidate the HER mechanism, assuming the Mo-edge of MoS_2 as the reaction center. Since it has been reported in literature that the activity for HER linearly corelates with the amount of exposed edges in crystalline MoS_2, we consider here the same

ChemCatChem
Research Article
doi.org/10.1002/cctc.202400282
Chemistry Europe
European Chemical Societies Publishing

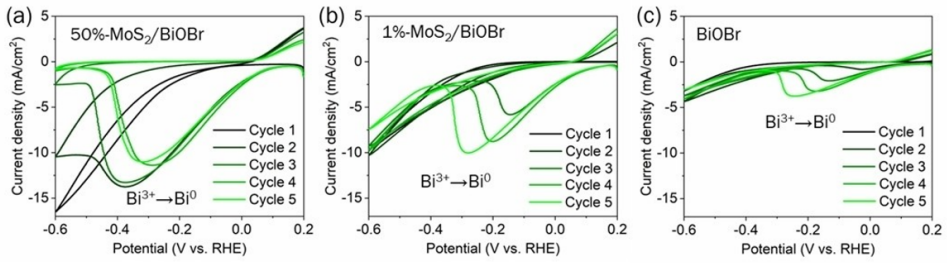

Figure 3. Cyclic voltammetries (CVs) of (a) 50%-MoS_2/BiOBr, (b) 1%-MoS_2/BiOBr and (c) pristine BiOBr.

edges as active catalytic sites also at the interface.[34] As first step of the reaction, we consider the reduction of the interface while adding an electron ($[MoS_2]^-$), to mimic the experimental setup with applied potential at −0.5 V. The first hydrogen prefers to bind at the edge sulfur atom, rather than the molybdenum atom, resulting in strongly bonding interaction, with a calculated adsorption energy of −0.89 eV. Interestingly, no stable structures have been found for the Mo–H interaction. However, after considering solvent effects, entropy and vibrational corrections, the free energy for adding a hydrogen atom to the S edge is more stabilized, with value of −1.47 eV ($[MoS_2]H_S$). The first protonation occurs with the Volmer step, which is the potential-dependent step (PDS) of the reaction, with a maximum reaction free energy of 1.48 eV at −0.5 V vs standard hydrogen electrode (SHE). The PDS is the step leading to an intermediate which requires the highest energy to be obtained, being the limiting step of the whole reaction and possibly being the cause for a reaction pathway to be unfavorable; in the present case, this is correlated to a limiting potential $U_L = -1.48$ eV ($U_L = \Delta G_{PDS}/e$), meaning that to fully overcome this barrier, a potential of −1.5 V should be applied. The activation energy required to obtain the Volmer step is 1.73 eV at −0.5 V, making this first protonation also the rate determining step of the HER reaction. Adding a second proton to the Mo atom did not result in a stable structure, suggesting that the second H prefers to interact with a second S atom close to the first one. This second proton addition can occur either via Tafel or Heyrovsky mechanism. In the Tafel mechanism, a second proton is added to a S atom which neighbors the first one; in the Heyrovsky mechanism the second proton is added directly on top of the first proton (Figure 4a).[35–39] While both pathways are thermodynamically favorable, the Tafel one is the most active one, with a strong energy stabilization at −1.91 eV ($[MoS_2]H_SH_S$), while the Heyrovsky pathway only slightly stabilizes the system up to 1.24 eV ($[MoS_2]H_{S2}$). Interestingly, the Tafel step is virtually barrierless, while to obtain the Heyrovsky step a small activation barrier of 0.02 eV has to be overcome. Eventually, the hydrogen molecule is formed, with a Gibbs free energy stabilization of −2.14 eV ($[MoS_2]2H_S$, Figure 4a). As a result, the $[MoS_2] \rightarrow [MoS_2]^- \rightarrow [MoS_2]H_S \rightarrow [MoS_2]H_SH_S \rightarrow [MoS_2]2H_S$ pathway can proceed with the first endergonic Volmer step, followed by a strongly exergonic Tafel step.

To assess the nature of the reduction pathways for the second proton transfer, we resort here to the analysis of the density of states and d-band center (Figure 4b and 4c). The strong thermodynamic stabilization of the Tafel intermediate is a result of upshift in the d-band center for the pristine surface compared to the Heyrovsky step. In fact, the d-band energy center has been found at −0.79 eV for the Heyrovsky step and is shifted up to −0.63 eV for the Tafel one. The main idea of this analysis is that the closer to the Fermi energy the metal d-band center is, the stronger the adsorbate-metal interaction is, due to a lower occupation of antibonding states. This is also confirmed by the density of states analysis, in which we observe that the antibonding states for the hydrogen atoms involved in the reaction are shifted up in energy, from 0.32 to 0.42 eV for the Heyrovsky and Tafel step, respectively. We believe that the high activation energy barrier observed from the 50%-MoS_2/BiOBr explains the observed experimental behavior; at such elevated concentration of BiOBr, it might be easier for the Bi to become metallic than for the reaction to proceed, in all the potential range observed. Hence, after a few cycles the HER production comes to a stop. On the other hand, when the percentage of MoS_2 is decreased to 1% at the interface, the smaller presence of Bi allows for the HER to continue for more cycles. Changing the potential to more negative values lead to overall stabilization of the Volmer intermediate and the related transition state. However, while the energy of the $[MoS_2]H_S$ intermediate strongly decreases, going from 1.73 eV at U = −0.25 V to 0.48 eV at U = −1.5 V, the decrease in the energy barrier for this step is rather small, from 1.86 at U = −0.25 V to 1.23 eV at U = −1.5 V (Figure 4d). The lower energy predicted at −1.6 V confirms that this key intermediate can be strongly stabilized, ensuring the PEC of the interface even for the 50%-MoS_2/BiOBr for more cycles. Now, it becomes crucial to consider the stability of the entire interface. As the applied potential becomes more negative, the interface may become more susceptible to deterioration, possibly resulting in additional reduction of Bi to its metallic form.

To comprehensively understand the impact of the composition of the HJs on the PEC HER activity, *in-situ* WAXD was

ChemCatChem
Research Article
doi.org/10.1002/cctc.202400282
Chemistry Europe
European Chemical Societies Publishing

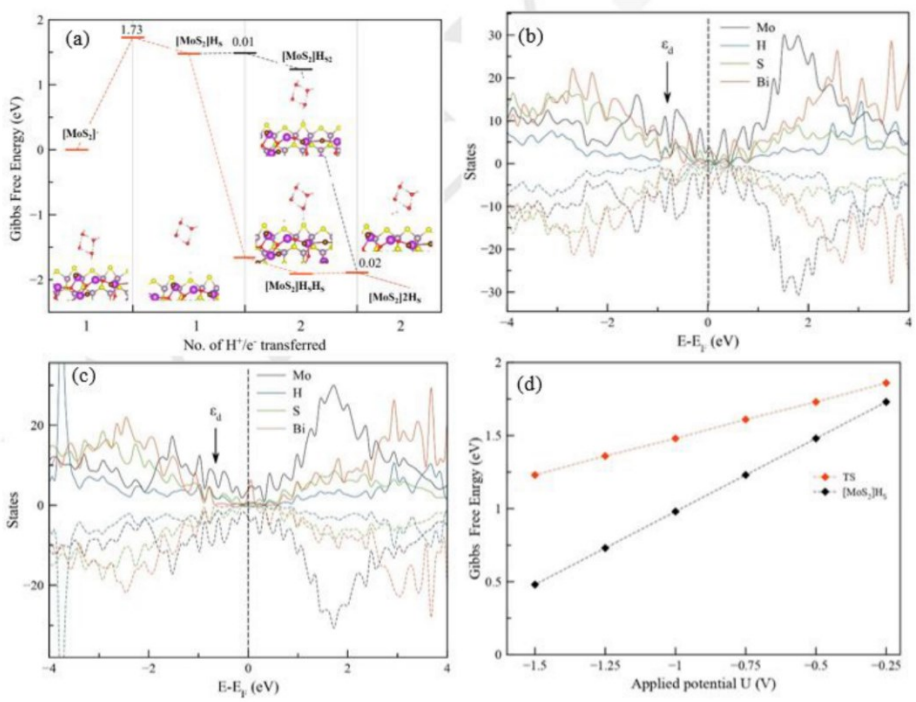

Figure 4. (a) Gibbs free energy reaction pathway for the HER formation at the MoS_2/BiOBr interface, at an applied potential of −0.5 V. Transition states are also reported, as well as the activation energy. Density of states (DOS) on the 3d orbitals for Mo and Bi metal centres, 2p orbitals of S and s orbitals for H for (b) Heyrovsky and (c) Tafel step. (d) Relative Gibbs free energy of the Volmer step and the associated transition state at various applied potentials.

conducted during the PEC HER. Figure 5a–c record a clear phase change of BiOBr from *in-situ* XRD diffractograms of 1%-MoS_2/BiOBr, 50%-MoS_2/BiOBr and pristine BiOBr after each cycle of HER and the patterns with selected ranges of 18.5–25 nm^{-1} of q vectors. Before the catalytic reaction, all the samples display two broad diffraction peaks centered at 22.9 and 23.3 nm^{-1}, which are attributed to the BiOBr phase. Further performing the CVs under PEC environment made gradual formation of Bi from BiOBr, as the intensity of the characteristic peak of metallic Bi at 19.7 nm^{-1} increased continuously, while the intensity of the peaks belonging to BiOBr decreased. When comparing these three samples, it is evident that the phase change inside 50%-MoS_2/BiOBr is much faster than that in 1%-MoS_2/BiOBr and BiOBr. The reduction of BiOBr in 50%-MoS_2/BiOBr and pristine BiOBr is complete after 1 cycle and 3 cycles of PEC reaction, respectively, while 1%-MoS_2/BiOBr can reserve the original BiOBr phase after 5 cycles of reactions. Moreover, the peak intensity ratio of the peaks at 22.9 and 19.7 nm^{-1} is calculated in Figure 6 to compare the phase change of the samples. For 50%-MoS_2/BiOBr, the peak ratio is close to 0 after the first cycle, while the value of 1%-MoS_2/BiOBr remains more than 0.5 after 5 cycles. Given that the peak ratio of pristine BiOBr diminishes to 0 after 3 cycles, it becomes evident that the HJ with just 1% of MoS_2 plays a crucial role in mitigating the reduction of the BiOBr component.

To correlate these findings with the CVs presented in Figure 3, it can be inferred that MoS_2/BiOBr serves as an efficient photoelectrocatalyst, whereas MoS_2/Bi exhibits minimal activity in PEC HER. Therefore, it is important to maintain BiOBr from reducing to Bi. According to the previous DFT calculations, in such a type-I HJ, the small amount of MoS_2 (in 1%-MoS_2/BiOBr) not only attracts photogenerated electrons and provides active sites for HER, but also contains a suitable valence band position which can prevent the transfer of photogenerated holes from BiOBr.[23] In this case, the remaining photogenerated holes on BiOBr can neutralize part of the electrons from UV light or negative bias and protect BiOBr from being reduced. However, these photogenerated holes are not enough to neutralize all the extra electrons inside BiOBr, thus there is a part of BiOBr reduced to Bi after each CV. Conversely, an increasing ratio of MoS_2 inside the HJ changes the band structure and photogenerated holes start to migrate to MoS_2. Without the photogenerated holes staying on BiOBr, BiOBr is rapidly reduced to Bi by electrons from electric field or photo

ChemCatChem
Research Article
doi.org/10.1002/cctc.202400282
Chemistry Europe
European Chemical Societies Publishing

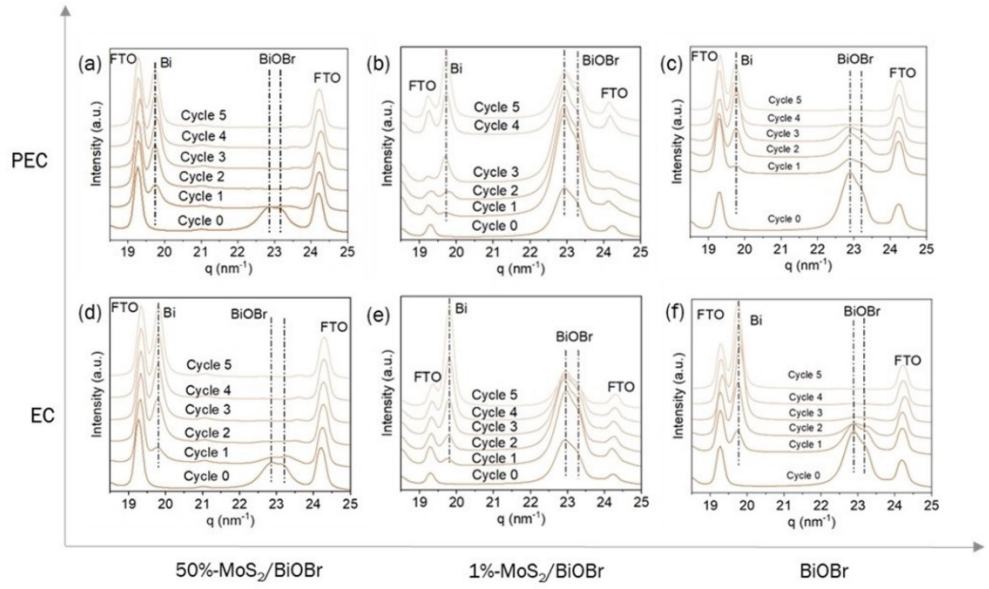

Figure 5. *In situ* WAXD of (a) 50%-MoS_2/BiOBr, (b) 1%-MoS_2/BiOBr and (c) pristine BiOBr during PEC HER, and (d) 50%-MoS_2/BiOBr, (e) 1%-MoS_2/BiOBr and (f) pristine BiOBr during EC HER.

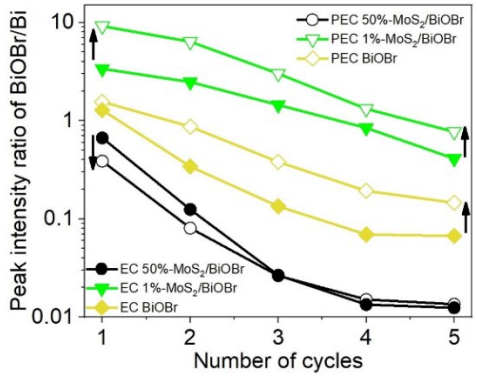

Figure 6. Peak intensity ratios of the peaks at 22.9 (belonging to BiOBr) and 19.7 nm^{-1} (belong to Bi).

energy.[23] When considering influence of the outside electric field, the DFT calculations demonstrate that before the HER happens, the negative potential can destroy the stability of the interface inside the 50%-MoS_2/BiOBr and form a large amount of Bi on the interface firstly (Figure 4). This combination of MoS_2 and Bi is not favorable for HER, unfortunately.

In order to prove the function of the photogenerated holes in stabilizing the structure of BiOBr, we measured the phase change of the samples under purely electrocatalytic (EC) conditions (in dark). As compared in Figure 5b and 5e, within the 1%-MoS_2/BiOBr HJ, it is surprising to observe that the formation of Bi is always less under PEC condition than under EC condition, as the BiOBr/Bi peak ratio under illumination is much higher than in dark after each cycle (Figure 6). A similar trend is found for pristine BiOBr as well (Figure 5c, 5f and 6). On the other side, for 50%-MoS_2/BiOBr, there is no apparent difference since BiOBr is reduced rapidly both under PEC and EC conditions (Figure 5a and 5d), and the peak intensity ratio of BiOBr/Bi is below 1 after the 1st cycle (Figure 6). The phase change of 1%-MoS_2/BiOBr and BiOBr reveals that the UV light does not accelerate the reduction of BiOBr under PEC condition, because the photogenerated holes protect BiOBr from reduction in the PEC environment, while the photogenerated electrons are transferred on the surface of MoS_2 for HER or charge recombination.

Conclusions

In this work, we show the PEC HER performance of layered MoS_2/BiOBr vdW HJs containing different ratios of the two components and analyze their catalytic mechanism, through a joint experimental-theoretical approach. From the measurement of PEC HER activity, emerges a counterintuitive better durability behaviour of the 1%-MoS_2/BiOBr HJ with respect to the 50%-MoS_2/BiOBr. DFT calculations point out, in fact, that the vdW interface in 50%-MoS_2/BiOBr is easier to collapse, and

ChemCatChem
Research Article
doi.org/10.1002/cctc.202400282
Chemistry Europe
European Chemical Societies Publishing

electrons prefer to react with BiOBr instead of the absorbed protons on the edged S sites. In addition, *in situ* WAXD shows a phase change of BiOBr to Bi during the HER. By comparing phase change between 1%-MoS_2/BiOBr and 50%-MoS_2/BiOBr, it is clear that BiOBr is reduced to Bi more rapidly in 50%-MoS_2/BiOBr than in 1%-MoS_2/BiOBr. On one side, in 1%-MoS_2/BiOBr the band structure is more suitable for distributing active electrons for HER; on the other side, under bias, BiOBr in the 50%-MoS_2/BiOBr reduces fastly to Bi and hinders the HER. More importantly, by comparing the phase change under EC and PEC conditions, it is proved that under UV light, the reduction of BiOBr slows down because the photogenerated holes can partially protect the BiOBr phase. The insights here presented on the PEC HER mechanism in this specific layered HJs may be applicable to other analogous systems and thereby enable the future design and development of novel nano-sized heterogeneous catalysts with high efficiency and stability.

Experimental Details

Materials

Bismuth(III) nitrate pentahydrate ($Bi(NO_3)_3 \cdot 5H_2O$), potassium bromide (KBr), ethylene glycol (EG), molybdenum(IV) sulfide (MoS_2), N-methyl-2-pyrrolidone (NMP), ethanol and FTO glass substrates were purchased from Sigma-Aldrich. Milli-Q water was sourced using the Milli-Q ultrapure system for all experiments.

Preparation of Photoelectrocatalysts

To synthesize BiOBr microspheres, a solvothermal method, adapted from Shi et al. was employed using $Bi(NO_3)_3 \cdot 5H_2O$ and KBr as precursors.[40] Initially, 83.3 mg of KBr were dissolved in 10 mL of EG, followed by the addition of 339.5 mg of $Bi(NO_3)_3 \cdot 5H_2O$ to the solution. The mixture was stirred for 30 minutes at room temperature, then transferred to a 40 mL Teflon autoclave for solvothermal treatment at 120 °C for 12 hours. After cooling naturally, the white sample was collected, washed with ethanol and H_2O to remove any unreacted chemicals and impurities.

To create HJs, multilayer MoS_2 was first obtained through liquid phase exfoliation (LPE) using a tip-sonicator for 9 hours with 500 mL of H_2O and 5 g of MoS_2 powder. The resulting mixture was centrifuged at 2000 rpm for 20 minutes, and the suspension was collected. Afterward, the suspension was centrifuged at 8000 rpm for 5 minutes to precipitate the multilayer MoS_2, which served as a precursor for the subsequent steps. Next, the BiOBr microspheres and multilayer MoS_2 were added to 50 mL of NMP for further LPE, with 9 hours of tip-sonication to achieve heterojunction formation. For the 1%-MoS_2/BiOBr configuration, 2 mg of MoS_2 and 200 mg of BiOBr were added, while for the 50%-MoS_2/BiOBr setup, 100 mg of MoS_2 and 100 mg of BiOBr were added. After centrifuging the mixture at 2000 rpm for 20 minutes, stable colloidal suspensions were obtained. Finally, ethanol and water were added to precipitate the products.

Characterization

Brightfield TEM (BF-TEM) imaging was conducted using a JEOL JEM-1011 instrument with an acceleration voltage of 100 kV. To prepare the samples, dilute suspensions of the nanomaterials in ethanol were dropped onto carbon film-coated 200 mesh copper grids. For HRTEM HAADF-STEM imaging and STEM-EDX analyses, an image-Cs-corrected JEOL JEM-2200FS TEM equipped with a Bruker X-Flash 5060 SDD was operated at 200 kV. Holey-amorphous carbon films on Cu grids served as support for these analyses. We characterized samples using a WITec confocal Raman system (α300-Raman WITec GmbH, Ulm, Germany), equipped with a 100X Zeiss objective, NA = 0.9 and a dispersive grating of 600 gr/mm that images a 100 μm core fiber, used to couple microscope to the f = 320 mm spectrometer, as the input slit aperture on a 1×2048 pixels CCD (Newtown CCD, Andor, −80 °C thermoelectric cooled). A solid-state laser, 532 nm, power of 14 mW, was used as the excitation line. The samples were dropped on n-type Si wafer. For the Raman spectra, each measure was obtained accumulating 80 spectra, each with an integration time of 25 s. Raman spectroscopy maps of 4×4 μm and 48×48 points were acquired at 2 seconds integration time per point. XPS spectra were acquired using a spectrometer manufactured by Physical Electronics GmbH (PHI 5000 VersaProbe II).

(Photo)electrochemical Measurements

EC and PEC HER tests were conducted using a three-electrode photoelectrochemical reaction cell immersed in a 0.5 M Na_2SO_4 electrolyte solution. The reference electrode utilized was Ag/AgCl (saturated KCl electrolyte), while the counter electrode consisted of a platinum wire. For the PEC HER experiments, the samples were air-dried and subsequently dispersed in ethanol at a concentration of 5 mg mL^{-1}. Ink solutions of 0.12 mL were drop-cast onto conductive FTO glass substrates. A mercury lamp with a light intensity of 16 mW cm^{-2} served as the light source. Potentiostatic tests were carried out using an Autolab instrument, while CVs were performed at a scan rate of 50 mV s^{-1} within the range of 0.2 to −0.6 V vs. RHE.

In Situ WAXD Characterizations

In situ wide WAXD measurements were performed at the Austrian SAXS beamline of the Elettra Sincrotrone in Trieste.[41] The beamline has been adjusted to a q-resolution ($q = 4\pi/\lambda * \sin(20/2)$) between 18 and 47 nm^{-1} using an X-ray energy of 8 keV. For each sample, the WAXD data was collected after each CV.

Computational Details

Details on the construction of the interface have been reported in our previous study. Briefly, all calculations were performed using spin-polarized density functional theory (DFT) as implemented in the Vienna ab initio simulation package (VASP).[42–44] The Perdew-Burke-Emzerhof (PBE) functional with a plane-wave cutoff energy of 500 eV was used. The structural optimizations were centered at Gamma. A vacuum space of 3 nm in the *y* direction (along interface edges) and of 1.5 nm along the *z* direction (perpendicular to the basal plane) were used to avoid interactions between periodic images. The convergence criteria for the force on each atom was set to 0.02 eV/Å, while the electronic structure energy convergence criteria was 10^{-5} eV. The Grimme D3 method with Becke-Johnson parameters[45] were employed to account for Van der Waals interactions.[46] The vibrational modes were calculated at 298.15 K to obtain the zero-point energy, entropy, and temperature corrections to enthalpy.

To accurately describe proton transfer from water solvent to the reactant, we considered the solvent as follows: a four-water molecule cage was added to the system close to the reaction center, to enable the proton transfer process. Moreover, the whole

ChemCatChem
Research Article
doi.org/10.1002/cctc.202400282
Chemistry Europe
European Chemical Societies Publishing

system was also surrounded by implicit water solvent, giving an additional layer of solvation which can affect the catalysis. The implicit solvent was considered within the VASPsol method.

The coupled proton-electron transfer (CPET) reactions were modelled using the computational hydrogen electrode (CHE) of Norskov.[47] In this approach, the voltage of reference (zero) is defined as for the reversible hydrogen electrode (RHE), where gas-phase hydrogen is converted into protons and electrons (reversibly) at zero volts ($H^+ + e^- \rightarrow {}^1/_2\ H_2$). Because this reaction is in equilibrium, one can make the approximation that the chemical potential of the proton-electron pair, $\mu(H^-) + \mu(e^-)$, equals half of the chemical potential of gas-phase H_2, 1/2 $\mu(H_2)$. As a result, the chemical potential of the proton-electron pair can be adjusted based on the applied potential (U) with the equation (1):

$$\mu(H^+) + \mu(e^-) \rightarrow 1/2\ \mu(H_2) - eU \quad (1)$$

where *e* is the elementary positive charge. It is assumed that both proton and electron transfer occur in concert during an electrochemical step. For all of the electrochemical steps along the reaction path, the free energy change between intermediates was computed to indicate the feasibility of the electrochemical process, *i.e.*, no energy barriers were calculated. Based on the computational hydrogen electrode (CHE) model, the Gibbs free energy change (ΔG) was calculated using Equation (2):

$$\Delta G = \Delta E_{DFT} + \Delta E_{ZPE} - T\Delta S + kTln10\ x\ pH - eU \quad (2)$$

where ΔE_{DFT} is the total energy from DFT simulations, ΔE_{ZPE} is the zero-point energy calculated from vibrational frequencies, T is the temperature (298.15 K), S is the entropy obtained from vibrational frequencies, k is the Boltzmann constant, pH = 7 and U is the electrode potential (−0.5 V). Zero point energy and entropic contribution were directly obtained from frequency calculations using VASPKIT.[48] Activation energies were computed using the Brønsted–Evans–Polanyi (BEP) relationship,[30,31] which relates the kinetic barrier to the corresponding reaction energy for a class of materials.

The d band center (ε_d) for the metal atom involved in the catalysis around the adsorption sites is given by

$$\varepsilon_d = \frac{\int_{-\infty}^{+\infty} \rho(E)(E - E_F)\ dE}{\int_{-\infty}^{+\infty} (E - E_F)\ dE} \quad (3)$$

where ρ(E) is the density of state (DOS) projected on the d-states of the metal atoms and E_F is the Fermi energy of the system.

Acknowledgements

M.W. and T.G. thank Fondazione Compagnia di San Paolo for financial support through the "Bando TRAPEZIO – Paving the way to research excellence and talent attraction" and through the program "Attrazione e retention di docenti di qualità". T.G. would like to acknowledge the support of the European Research Council for the project JANUS BI (grant agreement no. [101041229]). M.C. and T.G. thank the European Commission for the project LIGHT CAP (grant agreement no. [101017821]). R.A. thanks the DFG for project no. 460609161. S.O. thanks the National Science Centre, Poland (grant no. UMO/2020/39/I/ST4/01446) and the "Excellence Initiative – Research University" (IDUB) Program, Action I.3.3 – "Establishment of the Institute for Advanced Studies (IAS)" for funding (grant no. UW/IDUB/2020/25). The computation was carried out with the support of the Interdisciplinary Center for Mathematical and Computational Modeling at the University of Warsaw (ICM UW) under grants no. G83-28 and GB80-24. We acknowledge Elettra – Sincrotrone Trieste for provision of synchrotron radiation facilities (proposal no. 20222129). Sigrid Bernstorff is acknowledged for help during the WAXD measurements.

Conflict of Interests

The authors declare no conflict of interest.

Data Availability Statement

The data that support the findings of this study are available from the corresponding author upon reasonable request.

Keywords: Photoelectrochemistry · hydrogen evolution reaction · van der Walls heterojuction · transition metal dichalcogenide · bismuth oxyhalide

[1] S. Kumaravel, E. Kim, B. B. Kale, A. Adhikari, R. Patel, S. Kundu, *ChemElectroChem* **2022**, *9*, e202200724.
[2] E. Kemppainen, A. Bodin, B. Sebok, T. Pedersen, B. Seger, B. Mei, D. Bae, P. C. K. Vesborg, J. Halme, O. Hansen, P. D. Lund, I. Chorkendorff, *Energy Environ. Sci.* **2015**, *8*, 2991.
[3] C. Ding, J. Shi, Z. Wang, C. Li, *ACS Catal.* **2017**, *7*, 675.
[4] S. Lin, Y. Chen, J. Fu, L. Sun, Q. Jiang, J. F. Li, J. Cheng, C. Lin, Z. Q. Tian, *Int. J. Hydrogen Energy* **2022**, *47*, 41553.
[5] S. S. Imam, R. Adnan, N. H. Mohd Kaus, *J. Environ. Chem. Eng.* **2021**, *9*, 105404.
[6] W. Li, X. Wang, Y. Zhang, S. Zhu, M. Zhao, H. Zhang, Y. Wang, D. Zhang, W. Ran, L. Zhang, N. Li, T. Yan, W. Li, X. Wang, Y. Zhang, S. Zhu, M. Zhao, H. Zhang, Y. Wang, D. Zhang, W. Ran, L. Zhang, N. Li, T. Yan, *Adv. Mater. Interfaces* **2022**, *9*, 2200260.
[7] B. Q. L. Low, W. Jiang, J. Yang, M. Zhang, X. Wu, H. Zhu, H. Zhu, J. Z. X. Heng, K. Y. Tang, W. Y. Wu, X. Cao, X. Q. Koh, C. H. T. Chai, C. Y. Chan, Q. Zhu, M. Bosman, Y. W. Zhang, M. Zhao, Z. Li, X. J. Loh, Y. Xiong, E. Ye, *Small Methods* **2024**, *8*, 2301368.
[8] Y. Ling, Y. Dai, J. Zhou, *J. Colloid Interface Sci.* **2020**, *578*, 326.
[9] Z. Q. Wang, H. Wang, X. F. Wu, T. L. Chang, *J. Alloys Compd.* **2020**, *834*, 155025.
[10] J. Hu, C. Zhai, C. Yu, L. Zeng, Z. Q. Liu, M. Zhu, *J. Colloid Interface Sci.* **2018**, *524*, 195.
[11] K. Li, H. Zhang, Y. Tang, D. Ying, Y. Xu, Y. Wang, J. Jia, *Appl. Catal. B* **2015**, *164*, 82.
[12] K. Dai, D. Li, J. Lv, L. Lu, C. Liang, G. Zhu, *Mater. Lett.* **2014**, *136*, 438.
[13] L. W. Duresa, D. H. Kuo, F. T. Bekena, W. L. Kebede, *J. Phys. Chem. Solids* **2021**, *156*, 110132.
[14] S. S. Liu, Q. J. Xing, Y. Chen, M. Zhu, X. H. Jiang, S. H. Wu, W. Dai, J. P. Zou, *ACS Sustainable Chem. Eng.* **2019**, *7*, 1250.
[15] S. Vinoth, A. Pandikumar, *Renewable Energy* **2021**, *173*, 507.
[16] X. Tu, X. Zhou, S. Ke, Z. Zeng, *Mater. Technol.* **2022**, *37*, 1298.
[17] M. Malys, G. Fafilek, C. Pirovano, R. N. Vannier, *Solid State Ionics* **2005**, *176*, 1769.
[18] H. X. Pan, L. P. Feng, W. Zeng, Q. C. Zhang, X. D. Zhang, Z. T. Liu, *Inorg. Chem.* **2019**, *58*, 13195.
[19] H. Pan, L. Feng, S. Liu, Z. Li, H. Guo, P. Liu, X. Zheng, X. Zhang, J. Liu, *Int. J. Hydrogen Energy* **2022**, *47*, 1683.
[20] X. Wang, Z. Chen, J. Zheng, Y. Li, X. Peng, X. Zhang, H. Yin, X. Xiong, J. Duan, X. Li, Z. Wang, Z. Chen, J. Han, W. Xiao, Y. Yao, *ACS Appl. Energ. Mater.* **2020**, *3*, 11848.

ChemCatChem

Research Article
doi.org/10.1002/cctc.202400282

Chemistry Europe
European Chemical Societies Publishing

[21] Z. Shi, Y. Zhang, G. Duoerkun, W. Cao, T. Liu, L. Zhang, J. Liu, M. Li, Z. Chen, *Environ. Sci.-Nano* **2020**, *7*, 2708.
[22] J. Han, Y. Gao, Y. Li, Z. Chen, X. Liu, X. Xiong, X. Zhang, Y. Jiang, Q. Luo, Y. Song, Z. Wang, X. Li, Z. Chen, W. Xiao, *J. Phys. Chem. C* **2020**, *124*, 24164.
[23] M. Wang, S. Osella, R. Brescia, Z. Liu, J. Gallego, M. Cattelan, M. Crisci, S. Agnoli, T. Gatti, *Nanoscale* **2023**, *15*, 522.
[24] M. M. Ferrer, J. E. F. S. Rodrigues, M. A. P. Almeida, F. Moura, E. Longo, P. S. Pizani, J. R. Sambrano, *J. Raman Spectrosc.* **2018**, *49*, 1356.
[25] J. H. Yu, H. R. Lee, S. S. Hong, D. Kong, H. W. Lee, H. Wang, F. Xiong, S. Wang, Y. Cui, *Nano Lett.* **2015**, *15*, 1031.
[26] F. Neubrech, D. Weber, J. Katzmann, C. Huck, A. Toma, E. Di Fabrizio, A. Pucci, T. Härtling, *ACS Nano* **2012**, *6*, 7326.
[27] M. Cottat, C. D'andrea, R. Yasukuni, N. Malashikhina, R. Grinyte, N. Lidgi-Guigui, B. Fazio, A. Sutton, O. Oudar, N. Charnaux, V. Pavlov, A. Toma, E. Di Fabrizio, P. G. Gucciardi, M. Lamy De La Chapelle, *J. Phys. Chem. C* **2015**, *119*, 15532.
[28] S. R. Zhu, Q. Qi, W. N. Zhao, Y. Fang, L. Han, *J. Phys. Chem. Solids* **2018**, *121*, 163.
[29] X. Guo, Y. T. Huang, H. Lohan, J. Ye, Y. Lin, J. Lim, N. Gauriot, S. J. Zelewski, D. Darvill, H. Zhu, A. Rao, I. McCulloch, R. L. Z. Hoye, *J. Mater. Chem. A* **2023**, *11*, 22775.
[30] M. Thripuranthaka, R. V. Kashid, C. Sekhar Rout, D. J. Late, *Appl. Phys. Lett.* **2014**, *104*, 081911.
[31] H. Li, Q. Zhang, C. C. R. Yap, B. K. Tay, T. H. T. Edwin, A. Olivier, D. Baillargeat, *Adv. Funct. Mater.* **2012**, *22*, 1385.
[32] A. Giugni, B. Torre, M. Allione, G. Das, Z. Wang, X. He, H. N. Alshareef, E. Di Fabrizio, A. Giugni, B. Torre, M. Allione, G. Das, E. Di Fabrizio, Z. Wang, X. He, H. N. Alshareef, *Adv. Opt. Mater.* **2017**, *5*, 1700195.
[33] W. Wei, K. Sun, Y. H. Hu, *J. Mater. Chem. A* **2016**, *4*, 12398.
[34] T. F. Jaramillo, K. P. Jørgensen, J. Bonde, J. H. Nielsen, S. Horch, I. Chorkendorff, *Science* **2007**, *317*, 100.
[35] J. Durst, A. Siebel, C. Simon, F. Hasché, J. Herranz, H. A. Gasteiger, *Energy Environ. Sci.* **2014**, *7*, 2255.
[36] D. Strmcnik, P. P. Lopes, B. Genorio, V. R. Stamenkovic, N. M. Markovic, *Nano Energy* **2016**, *29*, 29.
[37] X. Tian, P. Zhao, W. Sheng, X. Tian, P. Zhao, W. Sheng, *Adv. Mater.* **2019**, *31*, 1808066.
[38] Y. Zheng, Y. Jiao, M. Jaroniec, S. Z. Qiao, *Angew. Chem. Int. Ed.* **2015**, *54*, 52.
[39] N. Krstajić, M. Popović, B. Grgur, M. Vojnović, D. Šepa, *J. Electroanal. Chem.* **2001**, *512*, 16.
[40] X. Shi, X. Chen, X. Chen, S. Zhou, S. Lou, Y. Wang, L. Yuan, *Chem. Eng. J.* **2013**, *222*, 120.
[41] H. Amenitsch, M. Rappolt, M. Kriechbaum, H. Mio, P. Laggner, S. Bernstorff, *J. Synchrotron. Rad.* **1998**, *5*, 506.
[42] G. Kresse, J. Furthmüller, *Phys. Rev. B* **1996**, *54*, 11169.
[43] G. Kresse, J. Hafner, *Phys. Rev. B* **1994**, *49*, 14251.
[44] G. Kresse, J. Furthmüller, *Comput. Mater. Sci.* **1996**, *6*, 15.
[45] S. Grimme, S. Ehrlich, L. Goerigk, *J. Comput. Chem.* **2011**, *32*, 1456.
[46] S. Grimme, J. Antony, S. Ehrlich, H. Krieg, *J. Chem. Phys.* **2010**, *132*.
[47] J. K. Nørskov, J. Rossmeisl, A. Logadottir, L. Lindqvist, J. R. Kitchin, T. Bligaard, H. Jónsson, *J. Phys. Chem. B* **2004**, *108*, 17886.
[48] V. Wang, N. Xu, J. C. Liu, G. Tang, W. T. Geng, *Comput. Phys. Commun.* **2021**, *267*, 108033.

Manuscript received: February 8, 2024
Revised manuscript received: April 10, 2024
Accepted manuscript online: May 6, 2024
Version of record online: ■■, ■■

RESEARCH ARTICLE

In MoS_2/BiOBr photocathode, the active electrons from both UV light and electric field can either reduce the adsorbed H* on the edge of MoS_2 to H_2 or reduce BiOBr to Bi. Varying the MoS_2 content in the HJ impacts the stability of BiOBr in PEC HER. HJs with 1% MoS_2 enhance BiOBr stability, while those with 50% accelerate BiOBr reduction.

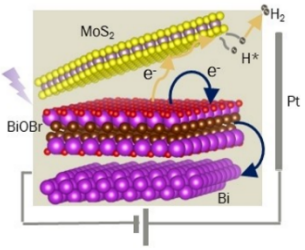

Dr. M. Wang, Prof. S. Osella, Dr. B. Torre, M. Crisci, F. Schmitz, R. Altieri, Prof. E. Di Fabrizio, Dr. H. Amenitsch, Dr. B. Sartori, Z. Liu, Prof. T. Gatti, Dr. F. Lamberti**

1 – 10

Stabilizing Layered BiOBr Photoelectrocatalyst by Van Der Waals Heterojunction Strategy

ChemCatChem

Supporting Information

Stabilizing Layered BiOBr Photoelectrocatalyst by Van Der Waals Heterojunction Strategy

Mengjiao Wang,* Silvio Osella, Bruno Torre, Matteo Crisci, Fabian Schmitz, Roberto Altieri, Enzo Di Fabrizio, Heinz Amenitsch, Barbara Sartori, Zheming Liu, Teresa Gatti, and Francesco Lamberti*

Supporting information

Stabilizing Layered BiOBr Photoelectrocatalyst by Van Der Waals Heterojunction Strategy

Mengjiao Wang*[a], Silvio Osella[b], Bruno Torre[a], Matteo Crisci[c], Fabian Schmitz[c], Roberto Altieri[c], Enzo Di Fabrizio[a], Heinz Amenitsch[d], Barbara Sartori[d], Zheming Liu[e], Teresa Gatti[a], Francesco Lamberti*[f,g,h]

[a] Dr. M. Wang, Dr. B. Torre, Prof. E. Di Fabrizio, Prof. T. Gatti
Dipartimento Scienza Applicata e Tecnologia (DISAT)
Politecnico di Torino
Corso Duca degli Abruzzi 24, 10129, Torino, Italy
E-mail: mengjiao.wang@polito.it

[b] Prof. S. Osella
Chemical and Biological Systems Simulation Lab, Centre of New Technologies
University of Warsaw,
Ochota campus, Banacha 2C, 02097 Warszawa, Poland

[c] M. Crisci, F. Schmitz, R. Altieri.
Institute of Physical Chemistry and Center for Materials Research (LaMa)
Justus Liebig University
Heinrich-Buff-Ring 17, 35392, Giessen, Germany

[d] Dr. H. Amenitsch, Dr. B. Sartori
Institute of Inorganic Chemistry,
Graz University of Technology,
Stremayrgasse 9, 8010, Graz, Austria

[e] Z. Liu
Nanochemistry Department,
Istituto Italiano di Tecnologia,
16163 Genova, Italy

[f] Dr. F. Lamberti
Dipartimento di Scienze Chimiche
Università degli Studi di Padova
Via Marzolo, 1, 35131, Padova, Italy
E-mail: francesco.lamberti@unipd.it

[g] Dr. F. Lamberti
Dipartimento di Ingegneria dell'Informazione
Università degli Studi di Padova
Via Gradenigo, 6b, 35131, Padova, Italy

[h] Dr. F. Lamberti
Zhejiang Beisheng Photovoltaic Co., Ltd.
No.800 Zhenbei Road, Zhili Town, Wuxing District Huzhou, Zhejiang 313000, China

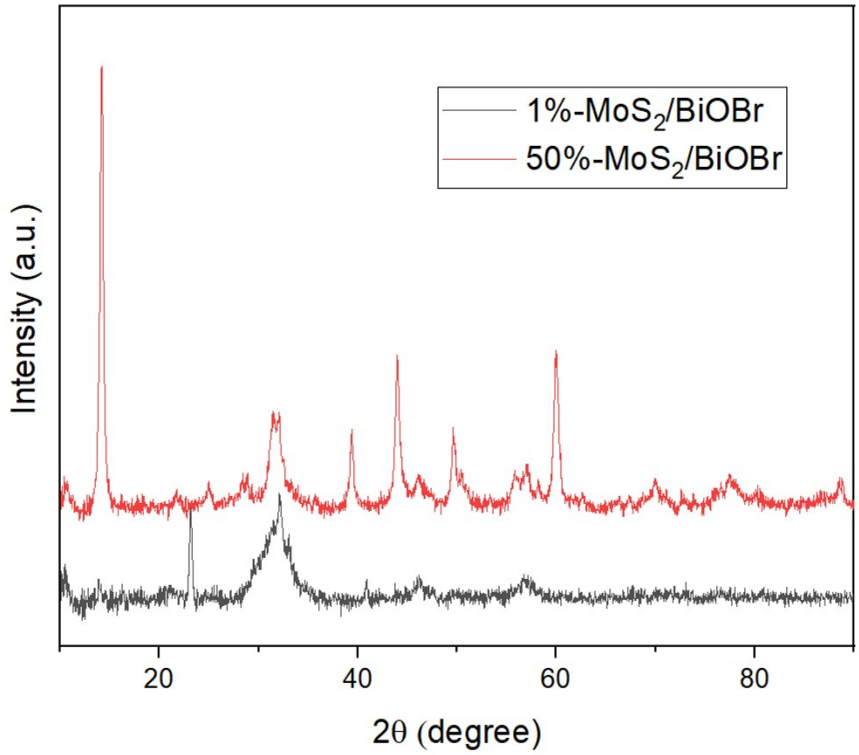

Figure S1. XRD patterns of MoS2/BiOBr HJs.

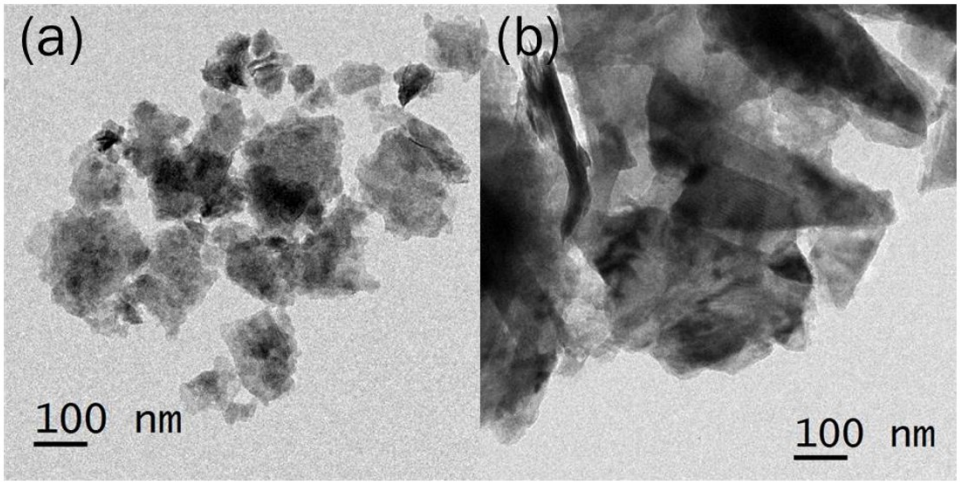

Figure S2. TEM images of (a) 2D BiOBr and (b) 2D MoS2.

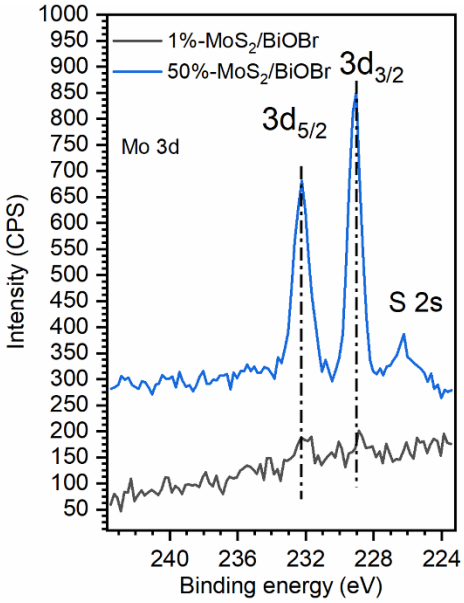

Figure S3. Mo 3d XPS spectrum of 1%-MoS_2/BiOBr and 50%-MoS_2/BiOBr .

Chapter 4: Conclusions & Outlooks

In summary, the dissertation can be split into two major sections and macro topics. The first one is especially focused on the exfoliation and production of 2D materials, with focus on bi-dimensional MoS_2, WS_2 and MoO_3 production, establishing methodologies and processes that will be further used in the second part of this work. In fact, in the second section, the topic was focused on the application of the synthesized materials in energy storage and conversion applications. Here, we report the use of 2D materials as support and active materials in composites with conductive polymer using different synthesis parameters and modification to further enhance the properties of the final material.

Among the work reported here, the paper focused on exfoliation of MoO_3, as in **publication 1**, and on the exfoliation of TMDC, as in **publication 2**, studied extensively and more abstractly the effect of several conditions on the final material obtained. MoO_3 was showed to be preferably exfoliated in a mixture of water and organic solvents, obtaining both a more stable suspension and a higher concentration. DFT calculation and XAS measurements provided, as well, insight on the structural change of the material after the processes and proved to be useful methodology to perform advanced characterization on 2D material. TMDC, instead, were studied in a more general and straightforward manner, but keeping a systematic approach, in **publication 2.** Ultimately, both MoS_2 and WS_2 showed different behaviors, where different surfactants at different concentrations proved to exfoliate and provide a stable suspension for the different materials. In another publication, the production methodology for 1T-MoS_2 was also optimized and characterized in a similar way to the other 2D materials. An already known procedure in literature was used, but it was optimized for our set up and need, obtaining high degree of phase conversion and yields up to 50% the initial amount of MoS_2 used for the exfoliation. Further works, in this section, would need to

focus on the use of different solvents and surfactant and also the optimization of the parameters for such processes, for example to reach higher nanomaterial concentration in 2H and oxides material, while the production of 1T-MoS_2, should be addressed and be improved, especially using safer and more eco-friendly option, instead of n-butyl lithium.

In the other publications, the use of TMDC as storage material was reported and **publication 3** and **4** are proof of it. In the first one a new synthesis procedure using brine (saturated NaCl solution) was tested and showed promising result on the TDMC/PANI hybrids and it was further expanded in the following publication. The procedures are similar, but the insertion of surface functionalization proved to improve the cyclic properties, while maintaining a high specific capacitance for the binary blend. These works, however, want to be a base for further scientific research, since we proved that a functionalized binary blend hybrid performs well and has a very high stability, whilst in literature mainly physical mixtures between different components, often times more than two, are reported and surely present high specific capacitance, but their retention is not often on par, while the interactions and the effect of such degradation are often neglected or not studied at all. Therefore, the use of functionalization first, and of this kind of functionalized material, allows for a clear understanding of the processes underlying the performance degradation and, simultaneously, poses as the base for further components additions. Moreover, the ratio used in the material heavily favored the carbonaceous part, therefore, further studies focusing on the ratio between inorganic and organic part is a promising topic to explore the super-capacitive behavior and the type of energy storage mechanisms in such hybrids.

Furthermore, application in photo-electrocatalytic hydrogen evolution was studied in **publication 5**, where an hybrid heterojunction with both MoS_2 and another 2D material, BiOBr, was prepared in different ratios between the two, showing how a small quantity of TMDC can sharply increase the catalytic performances and the reason behind this improvement was studied using DFT methodologies, showing how the simple reciprocal orientation of the two

materials, greatly affect their interactions and overall properties of the heterojunction.

Chapter 5: Acknowledgments

First and foremost, I would like to thank Prof. Dr. Teresa Gatti for her constant supervision in the past years, between master thesis, laboratory assistant work and the whole PhD project, without her I would not be where I am right now and I would not be able to discuss the current work. I thank her for all the scientific discussions, pointers, suggestions and all the possibilities she gave, ranging from collaborations with outside partners, meeting with them and the numerous conferences she pushed and allowed me to join, allowing me to grow both as a scientist and as a person. All of these were frantic years and without her support and flexibility I would not have managed half of the things I have done during the working period.

Then, my most sincere thanks goes to Prof. Dr. Bernd Smarsly, not only for allowing me to work in his lab in the past years and making sure I was included in his working group despite the language barrier, but also made sure to provide regular valuable suggestions and food for thoughts throughout the thesis work.

I also want to thank all my coworkers that were already here when I started and the ones that will remain once I will be finished. I thank all of them for the reciprocal support, suggestions, and the camaraderie that we developed among all of us in the years that allowed us to push through the hardest of times. I particularly want to thank Roberto for the bond we shared both at work and outside, helping each other and supporting in the darkest moment, while also cheering each other on the successful moments. I also want to thank my companion, office mate and project partner Felix. We shared not only an office and a project but also many more experiences and ideas, with a continuous bouncing of thoughts that helped us shape our own research into what it currently is right now.

I want to thank all the students with whom I worked through the years and to whom I taught a lot, while also been taught as much. To the gremlin trio, Leonardo,

Matilde, and Sara goes my deepest thanks for their collaboration and the beautiful time we spent together in the lab and note, that also bloomed in profound and, hopefully, lasting, friendship. To Micaela also goes big thanks for being such a big support and collaborator in the laboratory, with new and fresh ideas while also being able to share passions and talks even outside of the work environment. Lastly, my thanks go also to Jonas, an outstanding and brilliant mind, whose work sparked and inspired new solutions in my project.

Lastly, I would like to thank older bonds, but as profound as the new one I have created in the past years. To my friends in my home region, to their moral support despite being so far from each other to the time spent together online and the few offline that was able to make my worries disappear like snow on a sunny day.

To my family, of course, goes the biggest thanks. They are my anchor, my certainty even in the darkest of times, and the unmovable object without whose unwavering support I would even be able to imagine arriving where I am now. Mum, Dad, Vale thank you from the bottom of my heart.

Chapter 6: Literature

(1) Intergovernmental Panel on Climate Change (IPCC). Climate Change 2021 – The Physical Science Basis. *Clim. Chang. 2021 – Phys. Sci. Basis* **2023**. https://doi.org/10.1017/9781009157896.

(2) Ritchie, H.; Rosado, P.; Roser, M. *CO2 and Greenhouse Gas Emission*. Published online at OurWorldinData.org.

(3) Ourahou, M.; Ayrir, W.; EL Hassouni, B.; Haddi, A. Review on Smart Grid Control and Reliability in Presence of Renewable Energies: Challenges and Prospects. *Math. Comput. Simul.* **2020**, *167*, 19–31. https://doi.org/10.1016/J.MATCOM.2018.11.009.

(4) Ellabban, O.; Abu-Rub, H.; Blaabjerg, F. Renewable Energy Resources: Current Status, Future Prospects and Their Enabling Technology. *Renew. Sustain. Energy Rev.* **2014**, *39*, 748–764. https://doi.org/10.1016/J.RSER.2014.07.113.

(5) Yang, Y.; Okonkwo, E. G.; Huang, G.; Xu, S.; Sun, W.; He, Y. On the Sustainability of Lithium Ion Battery Industry – A Review and Perspective. *Energy Storage Mater.* **2021**, *36*, 186–212. https://doi.org/10.1016/J.ENSM.2020.12.019.

(6) Armand, M.; Axmann, P.; Bresser, D.; Copley, M.; Edström, K.; Ekberg, C.; Guyomard, D.; Lestriez, B.; Novák, P.; Petranikova, M.; Porcher, W.; Trabesinger, S.; Wohlfahrt-Mehrens, M.; Zhang, H. Lithium-Ion Batteries – Current State of the Art and Anticipated Developments. *J. Power Sources* **2020**, *479*, 228708. https://doi.org/10.1016/J.JPOWSOUR.2020.228708.

(7) Abu, S. M.; Hannan, M. A.; Hossain Lipu, M. S.; Mannan, M.; Ker, P. J.; Hossain, M. J.; Mahlia, T. M. I. State of the Art of Lithium-Ion Battery Material Potentials: An Analytical Evaluations, Issues and Future Research Directions. *J. Clean. Prod.* **2023**, *394*, 136246. https://doi.org/10.1016/J.JCLEPRO.2023.136246.

(8) Zhu, H.; Xu, R.; Wan, T.; Yuan, W.; Shu, K.; Boonprakob, N.; Zhao, C. Nanocomposites of Conducting Polymers and 2D Materials for Flexible Supercapacitors. *Polym. 2024, Vol. 16, Page 756* **2024**, *16* (6), 756. https://doi.org/10.3390/POLYM16060756.

(9) Chatterjee, D. P.; Nandi, A. K. A Review on the Recent Advances in Hybrid Supercapacitors. *J. Mater. Chem. A* **2021**, *9* (29), 15880–15918. https://doi.org/10.1039/D1TA02505H.

(10) Pershaanaa, M.; Bashir, S.; Ramesh, S.; Ramesh, K. Every Bite of Supercap: A Brief Review on Construction and Enhancement of Supercapacitor. *J. Energy Storage* **2022**, *50*, 104599. https://doi.org/10.1016/J.EST.2022.104599.

(11) Murali, G.; Rawal, J.; Modigunta, J. K. R.; Park, Y. H.; Lee, J. H.; Lee, S. Y.; Park, S. J.; In, I. A Review on MXenes: New-Generation 2D Materials for Supercapacitors. *Sustain. Energy Fuels* **2021**, *5* (22), 5672–5693. https://doi.org/10.1039/D1SE00918D.

(12) Shown, I.; Ganguly, A.; Chen, L. C.; Chen, K. H. Conducting Polymer-Based Flexible

Supercapacitor. *Energy Sci. Eng.* **2015**, *3* (1), 2–26. https://doi.org/10.1002/ESE3.50.

(13) Liu, X.; Xu, W.; Zheng, D.; Li, Z.; Zeng, Y.; Lu, X. Carbon Cloth as an Advanced Electrode Material for Supercapacitors: Progress and Challenges. *J. Mater. Chem. A* **2020**, *8* (35), 17938–17950. https://doi.org/10.1039/D0TA03463K.

(14) Gupta, A.; Sardana, S.; Dalal, J.; Lather, S.; Maan, A. S.; Tripathi, R.; Punia, R.; Singh, K.; Ohlan, A. Nanostructured Polyaniline/Graphene/Fe2O3Composites Hydrogel as a High-Performance Flexible Supercapacitor Electrode Material. *ACS Appl. Energy Mater.* **2020**, *3* (7), 6434–6446. https://doi.org/10.1021/ACSAEM.0C00684/SUPPL_FILE/AE0C00684_SI_001.PDF.

(15) Patra, A.; Rout, C. S. Architecturally Robust MoWS2 and Ti3C2Tx MXene Nanosheets Hybrid for High-Performance Energy Storage and Conversion Applications. *Energy Storage* **2023**, *5* (3), e411. https://doi.org/10.1002/EST2.411.

(16) Öztürk, O.; Gür, E. Layered Transition Metal Sulfides for Supercapacitor Applications. *ChemElectroChem* **2024**, *11* (11), e202300575. https://doi.org/10.1002/CELC.202300575.

(17) Shen, M.; Jiang, W.; Liang, K.; Zhao, S.; Tang, R.; Zhang, L.; Wang, J. Q. One-Pot Green Process to Synthesize MXene with Controllable Surface Terminations Using Molten Salts. *Angew. Chemie Int. Ed.* **2021**, *60* (52), 27013–27018. https://doi.org/10.1002/ANIE.202110640.

(18) de Castro, I. A.; Datta, R. S.; Ou, J. Z.; Castellanos-Gomez, A.; Sriram, S.; Daeneke, T.; Kalantar-zadeh, K. Molybdenum Oxides - From Fundamentals to Functionality. *Adv. Mater.* **2017**, *29* (40), 1701619. https://doi.org/10.1002/adma.201701619.

(19) Meyer, J.; Hamwi, S.; Kröger, M.; Kowalsky, W.; Riedl, T.; Kahn, A. Transition Metal Oxides for Organic Electronics: Energetics, Device Physics and Applications. *Adv. Mater.* **2012**, *24* (40), 5408–5427. https://doi.org/10.1002/ADMA.201201630.

(20) Balendhran, S.; Walia, S.; Nili, H.; Ou, J. Z.; Zhuiykov, S.; Kaner, R. B.; Sriram, S.; Bhaskaran, M.; Kalantar-Zadeh, K. Two-Dimensional Molybdenum Trioxide and Dichalcogenides. *Adv. Funct. Mater.* **2013**, *23* (32), 3952–3970. https://doi.org/10.1002/ADFM.201300125.

(21) Ponomarenko, V. P.; Popov, V. S.; Popov, S. V.; Chepurnov, E. L. Photo- and Nanoelectronics Based on Two-Dimensional Materials. Part I. Two-Dimensional Materials: Properties and Synthesis. *Journal of Communications Technology and Electronics*. Pleiades journals September 1, 2020, pp 1062–1104. https://doi.org/10.1134/S1064226920090090.

(22) Kundu, M.; Mondal, D.; Mondal, I.; Baral, A.; Halder, P.; Biswas, S.; Paul, B. K.; Bose, N.; Basu, R.; Das, S. A Rational Preparation Strategy of Phase Tuned MoO3 Nanostructures for High-Performance All-Solid Asymmetric Supercapacitor. *J. Energy Chem.* **2023**, *87*, 192–206. https://doi.org/10.1016/J.JECHEM.2023.08.014.

(23) Song, Y.; Zhao, Y.; Huang, Z.; Zhao, J. Aqueous Synthesis of Molybdenum Trioxide

(h-MoO3, α-MoO3·H2O and h-/α-MoO3 Composites) and Their Photochromic Properties Study. *J. Alloys Compd.* **2017**, *693*, 1290–1296. https://doi.org/10.1016/J.JALLCOM.2016.10.092.

(24) Jittiarporn, P.; Sikong, L.; Kooptarnond, K.; Taweepreda, W. Effects of Precipitation Temperature on the Photochromic Properties of H-MoO3. *Ceram. Int.* **2014**, *40* (8), 13487–13495. https://doi.org/10.1016/J.CERAMINT.2014.05.076.

(25) Hu, H.; Deng, C.; Xu, J.; Zhang, K.; Sun, M. Metastable H-MoO3 and Stable α-MoO3 Microstructures: Controllable Synthesis, Growth Mechanism and Their Enhanced Photocatalytic Activity. *J. Exp. Nanosci.* **2015**, *10* (17), 1336–1346. https://doi.org/10.1080/17458080.2015.1012654.

(26) Song, J.; Ni, X.; Gao, L.; Zheng, H. Synthesis of Metastable H-MoO3 by Simple Chemical Precipitation. *Mater. Chem. Phys.* **2007**, *102* (2–3), 245–248. https://doi.org/10.1016/j.matchemphys.2006.12.011.

(27) Duwal, S.; Kim, M.; Kawaguchi, S.; Hirao, N.; Ohishi, Y.; Yoo, C. S. Phase Transitions and Resistivity Anomaly of Layered MoO3 at High Pressure. *J. Phys. Chem. C* **2018**, *122* (39), 22632–22641. https://doi.org/10.1021/ACS.JPCC.8B06434/ASSET/IMAGES/LARGE/JP-2018-06434E_0008.JPEG.

(28) Kumar, V.; Sumboja, A.; Wang, J.; Bhavanasi, V.; Nguyen, V. C.; Lee, P. S. Topotactic Phase Transformation of Hexagonal MoO3 to Layered MoO3-II and Its Two-Dimensional (2D) Nanosheets. *Chem. Mater.* **2014**, *26* (19), 5533–5539. https://doi.org/10.1021/CM502558T/SUPPL_FILE/CM502558T_SI_001.PDF.

(29) McCarron, E. M.; Calabrese, J. C. The Growth and Single Crystal Structure of a High Pressure Phase of Molybdenum Trioxide: MoO3-II. *J. Solid State Chem.* **1991**, *91* (1), 121–125. https://doi.org/10.1016/0022-4596(91)90064-O.

(30) Singh, A.; Kumar, S.; Ahmed, B.; Singh, R. K.; Ojha, A. K. Temperature Induced Modifications in Shapes and Crystal Phases of MoO3 for Enhanced Photocatalytic Degradation of Dye Waste Water Pollutants under UV Irradiation. *J. Alloys Compd.* **2019**, *806*, 1368–1376. https://doi.org/10.1016/j.jallcom.2019.07.272.

(31) de Castro, I. A.; Datta, R. S.; Ou, J. Z.; Castellanos-Gomez, A.; Sriram, S.; Daeneke, T.; Kalantar-zadeh, K. Molybdenum Oxides – From Fundamentals to Functionality. *Advanced Materials*. Wiley-VCH Verlag October 25, 2017. https://doi.org/10.1002/adma.201701619.

(32) Wen, P.; Guo, J.; Ren, L.; Wang, C.; Lan, Y.; Jiang, X. One-Step Hydrothermal Preparation of 1D α-MoO3 Nanobelt Electrode Material for Supercapacitor. *Nano* **2019**, *14* (7). https://doi.org/10.1142/S1793292019500851.

(33) Ge, H.; Kuwahara, Y.; Yamashita, H. Development of Defective Molybdenum Oxides for Photocatalysis, Thermal Catalysis, and Photothermal Catalysis. *Chem. Commun.* **2022**, *58* (61), 8466–8479. https://doi.org/10.1039/D2CC02658A.

(34) Wu, D.; Shen, R.; Yang, R.; Ji, W.; Jiang, M.; Ding, W.; Peng, L. Mixed Molybdenum Oxides with Superior Performances as an Advanced Anode Material for Lithium-Ion Batteries. *Sci. Reports 2017 71* **2017**, *7* (1), 1–9.

https://doi.org/10.1038/srep44697.

(35) Xing, Y.; Cai, Y.; Cheng, J.; Xu, X. Applications of Molybdenum Oxide Nanomaterials in the Synergistic Diagnosis and Treatment of Tumor. *Appl. Nanosci.* **2020**, *10* (7), 2069–2083. https://doi.org/10.1007/S13204-020-01389-9/FIGURES/5.

(36) Cai, X.; Sang, X. G.; Song, Y.; Guo, D.; Liu, X. X.; Sun, X. Activating the Highly Reversible Mo4+/Mo5+ Redox Couple in Amorphous Molybdenum Oxide for High-Performance Supercapacitors. *ACS Appl. Mater. Interfaces* **2020**, *12* (43), 48565–48571. https://doi.org/10.1021/ACSAMI.0C13692/ASSET/IMAGES/LARGE/AM0C13692_0005.JPEG.

(37) Gowtham, B.; Ponnuswamy, V.; Pradeesh, G.; Chandrasekaran, J.; Aradhana, D. MoO3 Overview: Hexagonal Plate-like MoO3 Nanoparticles Prepared by Precipitation Method. *J. Mater. Sci. Mater. Electron.* **2018**, *29* (8), 6835–6843. https://doi.org/10.1007/s10854-018-8670-7.

(38) Jittiarporn, P.; Sikong, L.; Kooptarnond, K.; Taweepreda, W. INFLUENCE OF CALCINATION TEMPERATURE ON THE STRUCTURAL AND PHOTOCHROMIC PROPERTIES OF NANOCRYSTALLINE MoO3. *Dig. J. Nanomater. Biostructures 10* (4), 1237–1248.

(39) Silva Lucena de Medeiros, S. A.; Menezes de Oliveira, A. L.; Duarte, T. M.; Kennedy, B. J.; Rostas, A. M.; Negrila, C. C.; Galca, A. C.; da Silva Maia, A.; Sambrano, J. R.; Dantas, M. C.; Felix Farias, A. F.; Garcia dos Santos, I. M. α-MoO3 Micro- and Nanoparticles as Catalysts for Biofuel Production. *ACS Appl. Nano Mater.* **2024**. https://doi.org/10.1021/ACSANM.4C01239/ASSET/IMAGES/LARGE/AN4C01239_0009.JPEG.

(40) Ali, S.; Farrukh, M. A. Effect of Calcination Temperature on the Structural, Thermodynamic, and Optical Properties of MoO_3 Nanoparticles. *J. Chinese Chem. Soc.* **2018**, *65* (2), 276–288. https://doi.org/10.1002/jccs.201700163.

(41) Shaheen, I.; Ahmad, K. S. Modified Sol Gel Synthesis of MoO3 NPs Using Organic Template: Synthesis, Characterization and Electrochemical Investigations. *J. Sol-Gel Sci. Technol.* **2021**, *97* (1), 178–190. https://doi.org/10.1007/s10971-020-05398-6.

(42) Babu Reddy, L. P.; Rajprakash, H. G.; Ravikiran, Y. T. Synthesis of A-MoO3 Nanorods by Sol Gel Synthesis and to Investigate Its Room Temperature Humidity Sensing Properties. In *AIP Conference Proceedings*; American Institute of Physics Inc., 2019; Vol. 2142, p 070022. https://doi.org/10.1063/1.5122414.

(43) Chen, Y.; Lu, C.; Xu, L.; Ma, Y.; Hou, W.; Zhu, J. J. Single-Crystalline Orthorhombic Molybdenum Oxide Nanobelts: Synthesis and Photocatalytic Properties. *CrystEngComm* **2010**, *12* (11), 3740–3747. https://doi.org/10.1039/c000744g.

(44) Farzi-kahkesh, S.; Rahmani, M. B.; Fattah, A. Growth of Novel α-MoO3 Hierarchical Nanostructured Thin Films for Ethanol Sensing. *Mater. Sci. Semicond. Process.* **2020**, *120*. https://doi.org/10.1016/j.mssp.2020.105263.

(45) Huang, L.; Fang, W.; Yang, Y.; Wu, J.; Yu, H.; Dong, X.; Wang, T.; Liu, Z.; Zhao, B. Three-Dimensional MoO3 Nanoflowers Assembled with Nanosheets for Rhodamine B Degradation under Visible Light. *Mater. Res. Bull.* **2018**, *108*, 38–45. https://doi.org/10.1016/j.materresbull.2018.08.036.

(46) Xu, L.; Zhou, W.; Chao, S.; Liang, Y.; Zhao, X.; Liu, C.; Xu, J. Advanced Oxygen-Vacancy Ce-Doped MoO3 Ultrathin Nanoflakes Anode Materials Used as Asymmetric Supercapacitors with Ultrahigh Energy Density. *Adv. Energy Mater.* **2022**, *12* (16), 2200101. https://doi.org/10.1002/AENM.202200101.

(47) Sun, P.; Teng, F.; Yang, Z.; Yang, X.; Zhai, S.; Liang, S.; Gu, W.; Hao, W.; Shi, S. Effect of the Phase Structure on the Catalytic Activity of MoO 3 and Potential Application for Indoor Clearance . *J. Mater. Chem. C* **2020**. https://doi.org/10.1039/c9tc05241k.

(48) Fattakhova, Z. A.; Vovkotrub, E. G.; Zakharova, G. S. Microwave-Assisted Hydrothermal Synthesis of α-MoO3. *Russ. J. Inorg. Chem.* **2021**, *66* (1), 35–41. https://doi.org/10.1134/S0036023621010022.

(49) Wang, L.; Zhang, X.; Ma, Y.; Yang, M.; Qi, Y. Rapid Microwave-Assisted Hydrothermal Synthesis of One-Dimensional MoO3 Nanobelts. *Mater. Lett.* **2016**, *164*, 623–626. https://doi.org/10.1016/j.matlet.2015.11.076.

(50) Lin, Y. C.; Kurniawan, A.; Valinton, J. A. A.; Chen, C. H.; Chuang, S. H. Reduced Graphene Oxide–MoO3 Composites via Microwave-Assisted Synthesis for Dual-Functional Photocatalysis of Organic Dyes and Heavy Metal Cation under Simulated Sunlight Irradiation. *J. Taiwan Inst. Chem. Eng.* **2024**, *154*, 105013. https://doi.org/10.1016/J.JTICE.2023.105013.

(51) Gong, J.; Bai, P.; Zhang, Y.; Wang, Q.; Sun, J.; Liu, Y.; Jiang, H.; Feng, Z.; Hu, T.; Meng, C. Vanadate Ion Promoting the Transformation of α-Phase Molybdenum Trioxide (α-MoO3) to h-Phase MoO3 (h-MoO3) for Boosted Zn-Ion Storage. *J. Colloid Interface Sci.* **2023**, *647*, 115–123. https://doi.org/10.1016/J.JCIS.2023.05.146.

(52) Pan, Y.; Yuan, L.; Liu, L.; Fang, W.; Hou, Y.; Fu, L.; Wu, Y. Critical Advances of Aqueous Rechargeable Ammonium Ion Batteries. *Small Struct.* **2023**, *4* (12), 2300201. https://doi.org/10.1002/SSTR.202300201.

(53) Camacho, R. A. P.; Tian, R.; Liu, J.; Zhou, S.; Wu, A.; Huang, H. Superior Lithium-Ion Storage of V-Doped MoO3 Nanosheets via Plasma Evaporation. *Electrochim. Acta* **2021**, *394*, 139121. https://doi.org/10.1016/J.ELECTACTA.2021.139121.

(54) Zhang, H.; Gao, L.; Gong, Y. Exfoliated MoO3 Nanosheets for High-Capacity Lithium Storage. *Electrochem. commun.* **2015**, *52*, 67–70. https://doi.org/10.1016/j.elecom.2015.01.014.

(55) Wu, Q. L.; Zhao, S. X.; Yu, L.; Zheng, X. X.; Wang, Y. F.; Yu, L. Q.; Nan, C. W.; Cao, G. Oxygen Vacancy-Enriched MoO3-x Nanobelts for Asymmetric Supercapacitors with Excellent Room/Low Temperature Performance. *J. Mater. Chem. A* **2019**, *7* (21), 13205–13214. https://doi.org/10.1039/c9ta03471d.

(56) Thomas, T.; Kumar, Y.; Ramos Ramón, J. A.; Agarwal, V.; Sepúlveda Guzmán, S.; R, R.; Pushpan, S.; Loredo, S. L.; Sanal, K. C. Porous Silicon/α-MoO3 Nanohybrid

Based Fast and Highly Sensitive CO2 Gas Sensors. *Vacuum* **2021**, *184*. https://doi.org/10.1016/j.vacuum.2020.109983.

(57) Shen, S. K.; Cui, X. L.; Guo, C. Y.; Dong, X.; Zhang, X. F.; Cheng, X. L.; Huo, L. H.; Xu, Y. M. Sensing Mechanism of Ag/α-MoO3 Nanobelts for H2S Gas Sensor. *Rare Met.* **2021**. https://doi.org/10.1007/s12598-020-01647-3.

(58) Qin, H.; Cao, Y.; Xie, J.; Xu, H.; Jia, D. Solid-State Chemical Synthesis and Xylene-Sensing Properties of A-MoO3 Arrays Assembled by Nanoplates. *Sensors Actuators, B Chem.* **2017**, *242*, 769–776. https://doi.org/10.1016/j.snb.2016.11.081.

(59) Mo, Y.; Tan, Z.; Sun, L.; Lu, Y.; Liu, X. Ethanol-Sensing Properties of α-MoO3 Nanobelts Synthesized by Hydrothermal Method. *J. Alloys Compd.* **2020**, *812*, 152166. https://doi.org/10.1016/j.jallcom.2019.152166.

(60) Nagyné-Kovács, T.; Studnicka, L.; Lukács, I. E.; László, K.; Pasierb, P.; Szilágyi, I. M.; Pokol, G. Hydrothermal Synthesis and Gas Sensing of Monoclinic MoO3 Nanosheets. *Nanomaterials* **2020**, *10* (5), 891. https://doi.org/10.3390/nano10050891.

(61) Kumar, S.; Singh, A.; Singh, R.; Singh, S.; Kumar, P.; Kumar, R. Facile H-MoO3 Synthesis for NH3 Gas Sensing Application at Moderate Operating Temperature. *Sensors Actuators, B Chem.* **2020**, *325*. https://doi.org/10.1016/j.snb.2020.128974.

(62) Internal Market, I. E. and Sme. *Critical Raw Materials*. https://single-market-economy.ec.europa.eu/sectors/raw-materials/areas-specific-interest/critical-raw-materials_en.

(63) Kolobov, A. V.; Tominaga, J. Bulk TMDCs: Review of Structure and Properties. *Springer Ser. Mater. Sci.* **2016**, *239*, 29–77. https://doi.org/10.1007/978-3-319-31450-1_3/FIGURES/39.

(64) Mohl, M.; Rautio, A.-R.; Alene Asres, G.; Wasala, M.; Dnyaneshwar Patil, P.; Talapatra, S.; Kordas, K.; Mohl, M.; Rautio, A.; Asres, G. A.; Kordas, K.; Wasala, M.; Patil, P. D.; Talapatra, S. 2D Tungsten Chalcogenides: Synthesis, Properties and Applications. **2020**. https://doi.org/10.1002/admi.202000002.

(65) Ali, Z.; Hussain, Q.; Yawer, M. A.; Mehmood, M.; Hussain, R.; Shah, A.; Kanwal, H.; Yawer, A.; Ahmad, S.; Zahid, S. Effect of Sulfur Precursors on Hydrothermal Growth of MoS2 Nanostructures and Its Visible-Light-Driven Photocatalytic Activities. *J. Mol. Struct.* **2023**, *1278*, 134929. https://doi.org/10.1016/J.MOLSTRUC.2023.134929.

(66) Wang, L.; Wang, K.; Huang, R.; Qin, Z.; Su, Y.; Tong, S. Hierarchically Flower-like WS2 Microcrystals for Capture and Recovery of Au (III), Ag (I) and Pd (II). *Chemosphere* **2020**, *252*, 126578. https://doi.org/10.1016/j.chemosphere.2020.126578.

(67) Long, L. N.; Quang, N. T.; Khuong, T. T.; Kien, P. T.; Thang, N. H.; Van Khai, T. Controllable Synthesis by Hydrothermal Method and Optical Properties of 2D MoS2/RGO Nanocomposites. *J. Sol-Gel Sci. Technol. 2023 1063* **2023**, *106* (3), 699–714. https://doi.org/10.1007/S10971-023-06072-3.

(68) Nagaraju, C.; Gopi, C. V. V. M.; Ahn, J. W.; Kim, H. J. Hydrothermal Synthesis of MoS2 and WS2 Nanoparticles for High-Performance Supercapacitor Applications. *New J. Chem.* **2018**, *42* (15), 12357–12360. https://doi.org/10.1039/c8nj02822b.

(69) He, D.; Ooka, H.; Li, Y.; Jin, F.; Nakamura, R. Phase-Selective Hydrothermal Synthesis of Metallic MoS_2 at High Temperature. *Chem. Lett.* **2019**, *48* (8), 828–831. https://doi.org/10.1246/cl.190254.

(70) Li, J.; Qi, W.; Li, Y. Facial Synthesis of 1T Phase MoS 2 Nanoflowers via Anion Exchange Method for Efficient Hydrogen Evolution. *ChemistrySelect* **2019**, *4* (7), 2070–2074. https://doi.org/10.1002/SLCT.201803442.

(71) Buravets, V.; Hosek, F.; Burtsev, V.; Miliutina, E.; Maixner, J.; Lapcak, L.; Bajtosova, L.; Cieslar, M.; Procházka, M.; Minar, J.; Kolska, Z.; Svorcik, V.; Lyutakov, O. Rapid and Universal Synthesis of 2D Transition Metal (Ti, Zr, Hf, V, Nb, Ta, Cr, Mo, and W) Sulfides through Oxide Sulfurization in CS2 Vapor. *Inorg. Chem.* **2024**, *63* (18), 8215–8221. https://doi.org/10.1021/ACS.INORGCHEM.4C00475/ASSET/IMAGES/LARGE/IC4C00475_0004.JPEG.

(72) Li, H.; Li, H.; Wu, Z.; Zhu, L.; Li, C.; Lin, S.; Zhu, X.; Sun, Y. Realization of High-Purity 1T-MoS2 by Hydrothermal Synthesis through Synergistic Effect of Nitric Acid and Ethanol for Supercapacitors. *J. Mater. Sci. Technol.* **2022**, *123*, 34–40. https://doi.org/10.1016/J.JMST.2022.01.018.

(73) Tang, D.; Li, J.; Yang, Z.; Jiang, X.; Huang, L.; Guo, X.; Li, Y.; Zhu, J.; Sun, X. Fabrication and Mechanism Exploration of Oxygen-Incorporated 1T-MoS2 with High Adsorption Performance on Methylene Blue. *Chem. Eng. J.* **2022**, *428*, 130954. https://doi.org/10.1016/J.CEJ.2021.130954.

(74) Tian, Y.; He, Y.; Zhu, Y. Low Temperature Synthesis and Characterization of Molybdenum Disulfide Nanotubes and Nanorods. *Mater. Chem. Phys.* **2004**, *87* (1), 87–90. https://doi.org/10.1016/j.matchemphys.2004.05.010.

(75) Lei, Y.; Huo, D.; Liu, H.; Cheng, S.; Ding, M.; Jiang, B.; Zhang, F.; Zhang, Y.; Gao, G. An Investigation of PPy@1T/2H MoS2 Composites with Durable Photothermal-Promoted Effect in Photo-Fenton Degradation of Methylene Blue and in Water Evaporation. *Polymers (Basel).* **2023**, *15* (19), 3900. https://doi.org/10.3390/POLYM15193900/S1.

(76) Liu, Y.; Li, Q.; Zhu, Y.; Chen, X.; Xue, F.; Lyu, M.; Li, Q.; Chen, X.; Deng, J.; Miao, J.; Cao, Y.; Lin, K.; Xing, X. One-Step Synthesis of MoS 2 /NiS Heterostructures with a Stable 1T Phase for an Efficient Hydrogen Evolution Reaction. *Dalt. Trans.* **2023**, *52* (25), 8530–8535. https://doi.org/10.1039/D3DT00838J.

(77) Nie, C.; Zhang, B.; Gao, Y.; Yin, M.; Yi, X.; Zhao, C.; Zhang, Y.; Luo, L.; Wang, S. Thickness-Dependent Enhancement of Electronic Mobility of MoS2Transistors via Surface Functionalization. *J. Phys. Chem. C* **2020**, *124* (31), 16943–16950. https://doi.org/10.1021/ACS.JPCC.0C02657/SUPPL_FILE/JP0C02657_SI_001.PDF.

(78) Fu, Q.; Dai, J. Q.; Huang, X. Y.; Dai, Y. Y.; Pan, Y. H.; Yang, L. L.; Sun, Z. Y.; Miao, T. M.; Zhou, M. F.; Zhao, L.; Zhao, W. J.; Han, X.; Lu, J. P.; Gao, H. J.; Zhou, X. J.; Wang, Y. L.; Ni, Z. H.; Ji, W.; Huang, Y. One-Step Exfoliation Method for Plasmonic Activation of Large-Area 2D Crystals. *Adv. Sci.* **2022**, *9* (32), 2204247.

https://doi.org/10.1002/ADVS.202204247.

(79) Li, H.; Yuan, X.; Wei, Z.; Shi, J.; Jia, Q.; Ma, D.; Li, Y.; Zhang, Y.; Zhu, X. Phase Engineering of High-Purity 1T-MoS2 Synthesis with Organic Chemical Groups for Enhanced Supercapacitors. *Mater. Today Chem.* **2024**, *37*, 102002. https://doi.org/10.1016/J.MTCHEM.2024.102002.

(80) Khamrui, S.; Bharti, K.; Banerjee, D. Study of Spin Localization and Charge Transport in Hydrothermally Synthesized 2H-MoS2. *J. Phys. Chem. C* **2023**, *127* (29), 14486–14494. https://doi.org/10.1021/ACS.JPCC.3C02855/ASSET/IMAGES/LARGE/JP3C02855_0008.JPEG.

(81) Rahaman, M.; Islam, M. J.; Ul-Hamid, A.; Islam, M. R. Role of Defects on the Electrochemical Performance of MnS Nanoparticles Decorated 2H-MoS2 Nanoflower: Experimental and Theoretical Investigation. *Surfaces and Interfaces* **2024**, *45*, 103886. https://doi.org/10.1016/J.SURFIN.2024.103886.

(82) Obaida, M.; Hassan, S. A.; Swelam, M. N.; Moussa, I.; Teleb, N. H.; Afify, H. H. Phase Manipulation of Two-Dimensional MoS2 Nanostructures. *Bull. Mater. Sci.* **2023**, *46* (1), 1–11. https://doi.org/10.1007/S12034-023-02891-W/TABLES/3.

(83) Ma, H.; Wang, Y.; Wang, B.; Ding, J.; Xu, K.; Xia, X.; Wei, S. Synthetic 3D Flower-like 1T/2H MoS2@CoFe2O4 Composites with Enhanced Microwave Absorption Performances. *J. Mater. Sci.* **2023**, *58* (3), 1183–1199. https://doi.org/10.1007/S10853-022-08051-5/TABLES/3.

(84) Hedayati, M. A.; Ahangar, A. M.; Maleki, M.; Ghanbari, H. Low-Temperature Hydrothermal Growth of MoS2 Nanostructures on Carbon Foam for Hydrogen Evolution Reaction. *Diam. Relat. Mater.* **2023**, *139*, 110342. https://doi.org/10.1016/J.DIAMOND.2023.110342.

(85) Venkateshwaran, S.; Devi, P.; Murugan, P.; Senthil Kumar, S. M. Simple Immersion in Polar Solvents Induces Targeted 1T Phase Conversion of MoS2 for HER: A Greener Approach. *ACS Appl. Energy Mater.* **2024**, *7* (3), 1037–1050. https://doi.org/10.1021/ACSAEM.3C02487/ASSET/IMAGES/LARGE/AE3C02487_0011.JPEG.

(86) López-Posadas, C. B.; Wei, Y.; Shen, W.; Kahr, D.; Hohage, M.; Sun, L. Direct Observation of the CVD Growth of Monolayer MoS2 Using in Situ Optical Spectroscopy. *Beilstein J. Nanotechnol. 1057* **2019**, *10* (1), 557–564. https://doi.org/10.3762/BJNANO.10.57.

(87) Xie, Y.; Ma, X.; Wang, Z.; Nan, T.; Wu, R.; Zhang, P.; Wang, H.; Wang, Y.; Zhan, Y.; Hao, Y. NaCl-Assisted CVD Synthesis, Transfer and Persistent Photoconductivity Properties of Two-Dimensional Transition Metal Dichalcogenides. *MRS Adv.* **2018**, *3* (6–7), 365–371. https://doi.org/10.1557/ADV.2018.156.

(88) Xu, Z.; Lv, Y.; Li, J.; Wei, G.; Zhao, S. Pattern Stimulated CVD Growth of 2D MoS2. *ChemistrySelect* **2020**, *5* (22), 6709–6714. https://doi.org/10.1002/SLCT.202001683.

(89) Bay, M.; Çelik, Y.; Ay, F.; Perkgöz, N. K. Catalytic Strategies for Uniform Monolayer MoSe2 Growth in CVD Processes. *Mater. Sci. Semicond. Process.* **2024**, *180*,

108551. https://doi.org/10.1016/J.MSSP.2024.108551.

(90) Kumar, R.; Goel, N.; Jarwal, D. K.; Hu, Y.; Zhang, J.; Kumar, M. Strategic Review on Chemical Vapor Deposition Technology-Derived 2D Material Nanostructures for Room-Temperature Gas Sensors. *J. Mater. Chem. C* **2023**, *11* (3), 774–801. https://doi.org/10.1039/D2TC04188J.

(91) An, Q.; Zhang, T.; Chen, F.; Su, W. Recent Progress in the Synthesis and Physical Properties of 2D Ternary TMDC-Based Vertical Heterostructures. *CrystEngComm* **2023**, *25* (30), 4256–4271. https://doi.org/10.1039/D3CE00562C.

(92) Hu, J.; Zhou, F.; Wang, J.; Cui, F.; Quan, W.; Zhang, Y. Chemical Vapor Deposition Syntheses of Wafer-Scale 2D Transition Metal Dichalcogenide Films toward Next-Generation Integrated Circuits Related Applications. *Adv. Funct. Mater.* **2023**, *33* (40), 2303520. https://doi.org/10.1002/ADFM.202303520.

(93) Buchkov, K.; Rafailov, P.; Minev, N.; Videva, V.; Strijkova, V.; Lukanov, T.; Dimitrov, D.; Marinova, V. Metatungstate Chemical Vapor Deposition of WSe2: Substrate Effects, Shapes, and Morphologies. *Cryst. 2024, Vol. 14, Page 184* **2024**, *14* (2), 184. https://doi.org/10.3390/CRYST14020184.

(94) Budania, P.; Baine, P. T.; Montgomery, J. H.; McNeill, D. W.; Mitchell, S. J. N.; Modreanu, M.; Hurley, P. K. Comparison between Scotch Tape and Gel-Assisted Mechanical Exfoliation Techniques for Preparation of 2D Transition Metal Dichalcogenide Flakes. *Micro Nano Lett.* **2017**, *12* (12), 970–973. https://doi.org/10.1049/MNL.2017.0280.

(95) Liu, H.; Cai, Y.; Han, M.; Guo, S.; Lin, M.; Zhao, M.; Zhang, Y.; Chi, D. Aqueous and Mechanical Exfoliation, Unique Properties, and Theoretical Understanding of MoO3 Nanosheets Made from Free-Standing α-MoO3 Crystals: Raman Mode Softening and Absorption Edge Blue Shift. *Nano Res.* **2018**, *11* (3), 1193–1203. https://doi.org/10.1007/s12274-017-1733-x.

(96) Ooi, S. I.; Ahmad, H. Thermal Release Tape Assisted Mechanical Exfoliation of Pristine TMD and the Performance of the Exfoliated TMD Saturable Absorbers for Q-Switched Laser Generation. *Opt. Mater. (Amst).* **2022**, *128*, 112363. https://doi.org/10.1016/J.OPTMAT.2022.112363.

(97) Guan, L.; Xing, B.; Niu, X.; Wang, D.; Yu, Y.; Zhang, S.; Yan, X.; Wang, Y.; Sha, J. Metal-Assisted Exfoliation of Few-Layer Black Phosphorus with High Yield. *Chem. Commun.* **2018**, *54* (6), 595–598. https://doi.org/10.1039/C7CC08488A.

(98) Liu, F. Mechanical Exfoliation of Large Area 2D Materials from VdW Crystals. *Prog. Surf. Sci.* **2021**, *96* (2), 100626. https://doi.org/10.1016/J.PROGSURF.2021.100626.

(99) Novoselov, K. S.; Geim, A. K.; Morozov, S. V.; Jiang, D.; Zhang, Y.; Dubonos, S. V.; Grigorieva, I. V.; Firsov, A. A. Electric Field in Atomically Thin Carbon Films. *Science (80-.).* **2004**, *306* (5696), 666–669. https://doi.org/10.1126/science.1102896.

(100) Heyl, M.; Burmeister, D.; Schultz, T.; Pallasch, S.; Ligorio, G.; Koch, N.; W List-Kratochvil, E. J.; Heyl, M.; Burmeister, D.; Pallasch, S.; Ligorio, G.; W List-Kratochvil, E. J.; Schultz, T.; Koch, N. Thermally Activated Gold-Mediated

Transition Metal Dichalcogenide Exfoliation and a Unique Gold-Mediated Transfer. *Phys. status solidi – Rapid Res. Lett.* **2020**, *14* (11), 2000408. https://doi.org/10.1002/PSSR.202000408.

(101) Heyl, M.; Grützmacher, S.; Rühl, S.; Ligorio, G.; Koch, N.; List-Kratochvil, E. J. W.; Heyl, M.; Grützmacher, S.; Rühl, S.; Ligorio, G.; List-Kratochvil, E. J. W.; Koch, N. Low Temperature Heating of Silver-Mediated Exfoliation of MoS2. *Adv. Mater. Interfaces* **2022**, *9* (18), 2200362. https://doi.org/10.1002/ADMI.202200362.

(102) Haws, C.; Guha, B.; Perez, E.; Davanco, M.; Song, J. D.; Srinivasan, K.; Sapienza, L. Thermal Release Tape-Assisted Semiconductor Membrane Transfer Process for Hybrid Photonic Devices Embedding Quantum Emitters. *Mater. Quantum Technol.* **2022**, *2* (2), 025003. https://doi.org/10.1088/2633-4356/AC603E.

(103) Liu, G.; Komatsu, N. Readily Available "Stock Solid" of MoS_2 and WS_2 Nanosheets through Solid-Phase Exfoliation for Highly Concentrated Dispersions in Water. *ChemNanoMat* **2016**, *2* (6), 500–503. https://doi.org/10.1002/cnma.201600116.

(104) Huang, J.; Songfeng, E.; Li, J.; Jia, F.; Ma, Q.; Hua, L.; Lu, Z. Ball-Milling Exfoliation of Hexagonal Boron Nitride in Viscous Hydroxyethyl Cellulose for Producing Nanosheet Films as Thermal Interface Materials. *ACS Appl. Nano Mater.* **2021**, *4* (12), 13167–13175. https://doi.org/10.1021/ACSANM.1C02696/ASSET/IMAGES/LARGE/AN1C02696_0005.JPEG.

(105) Tayyebi, A.; Ogino, N.; Hayashi, T.; Komatsu, N. Size-Controlled MoS2 Nanosheet through Ball Milling Exfoliation: Parameter Optimization, Structural Characterization and Electrocatalytic Application. *Nanotechnology* **2019**, *31* (7), 075704. https://doi.org/10.1088/1361-6528/AB5077.

(106) Zhang, Q.; Xu, F.; Lu, P.; Zhu, D.; Yuwen, L.; Wang, L. Efficient Preparation of Small-Sized Transition Metal Dichalcogenide Nanosheets by Polymer-Assisted Ball Milling. *Molecules* **2022**, *27* (22), 7810. https://doi.org/10.3390/MOLECULES27227810/S1.

(107) Grayfer, E. D.; Kozlova, M. N.; Fedorov, V. E. Colloidal 2D Nanosheets of MoS2 and Other Transition Metal Dichalcogenides through Liquid-Phase Exfoliation. *Advances in Colloid and Interface Science*. Elsevier B.V. July 1, 2017, pp 40–61. https://doi.org/10.1016/j.cis.2017.04.014.

(108) Goni, F.; Chemelli, A.; Uhlig, F. High-Yield Production of Selected 2D Materials by Understanding Their Sonication-Assisted Liquid-Phase Exfoliation. *Nanomater. 2021, Vol. 11, Page 3253* **2021**, *11* (12), 3253. https://doi.org/10.3390/NANO11123253.

(109) Gilliam, M. S.; Yousaf, A.; Guo, Y.; Li, D. O.; Momenah, A. A.; Wang, Q. H.; Green, A. A. Evaluating the Exfoliation Efficiency of Quasi-2D Metal Diboride Nanosheets Using Hansen Solubility Parameters. *Langmuir* **2021**, *37* (3), 1194–1205. https://doi.org/10.1021/ACS.LANGMUIR.0C03138/ASSET/IMAGES/LARGE/LA0C03138_0007.JPEG.

(110) Bodík, M.; Annušová, A.; Hagara, J.; Mičušík, M.; Omastová, M.; Kotlár, M.; Chlpík, J.; Cirák, J.; Švajdlenková, H.; Anguš, M.; Roldán, A. M.; Veis, P.; Jergel, M.; Majkova, E.; Šiffalovič, P. An Elevated Concentration of MoS2 Lowers the Efficacy

of Liquid-Phase Exfoliation and Triggers the Production of MoO: X Nanoparticles. *Phys. Chem. Chem. Phys.* **2019**, *21* (23), 12396–12405. https://doi.org/10.1039/c9cp01951k.

(111) Ramalingam, G.; Kathirgamanathan, P.; Ravi, G.; Elangovan, T.; Arjun kumar, B.; Manivannan, N.; Kasinathan, K. Quantum Confinement Effect of 2D Nanomaterials. In *Quantum Dots - Fundamental and Applications*; IntechOpen, 2020. https://doi.org/10.5772/intechopen.90140.

(112) Gan, Z. X.; Liu, L. Z.; Wu, H. Y.; Hao, Y. L.; Shan, Y.; Wu, X. L.; Chu, P. K. Quantum Confinement Effects across Two-Dimensional Planes in MoS2 Quantum Dots. *Appl. Phys. Lett.* **2015**, *106* (23), 233113. https://doi.org/10.1063/1.4922551/27922.

(113) Takagahara, T.; Takeda, K. Theory of the Quantum Confinement Effect on Excitons in Quantum Dots of Indirect-Gap Materials. *Phys. Rev. B* **1992**, *46* (23), 15578. https://doi.org/10.1103/PhysRevB.46.15578.

(114) Mekuye, B.; Abera, B. Nanomaterials: An Overview of Synthesis, Classification, Characterization, and Applications. *Nano Sel.* **2023**, *4* (8), 486–501. https://doi.org/10.1002/NANO.202300038.

(115) Baig, N.; Kammakakam, I.; Falath, W.; Kammakakam, I. Nanomaterials: A Review of Synthesis Methods, Properties, Recent Progress, and Challenges. *Mater. Adv.* **2021**, *2* (6), 1821–1871. https://doi.org/10.1039/D0MA00807A.

(116) Wang, M.; Langer, M.; Altieri, R.; Crisci, M.; Osella, S.; Gatti, T. Two-Dimensional Layered Heterojunctions for Photoelectrocatalysis. *ACS Nano* **2024**, *18* (13), 9245–9284. https://doi.org/10.1021/ACSNANO.3C12274/ASSET/IMAGES/LARGE/NN3C12274_0018.JPEG.

(117) Sen, S. K.; Manir, M. S.; Nur, S.; Hossain, M. N.; Islam, M. J.; Alam, A. K. M. M.; Hakim, M. A. Estimation of Hydrothermally Synthesized Iron Incorporated 2D-Sheet-like α-MoO3 Microstructural and Optical Parameters Treated by Annealing Temperature. *Mater. Res. Express* **2020**, *7* (9), 095005. https://doi.org/10.1088/2053-1591/ABB4F9.

(118) Ma, M. G.; Zhu, J. F.; Jiang, J. X.; Sun, R. C. Hydrothermal-Polyol Route to Synthesis of β-Ni(OH)2 and NiO in Mixed Solvents of 1,4-Butanediol and Water. *Mater. Lett.* **2009**, *63* (21), 1791–1793. https://doi.org/10.1016/j.matlet.2009.05.037.

(119) Sen, S. K.; Paul, T. C.; Manir, M. S.; Dutta, S.; Hossain, M. N.; Podder, J. Effect of Fe-Doping and Post Annealing Temperature on the Structural and Optical Properties of MoO3 Nanosheets. *J. Mater. Sci. Mater. Electron.* **2019**, *30* (15), 14355–14367. https://doi.org/10.1007/S10854-019-01805-Z/FIGURES/9.

(120) Gurusamy, P.; Perumalsamy, S. V.; Gnanasekar, P.; Kulandaivel, J.; Paramasivam, T.; Pandian, T. Synthesis of Ni-Doped 1T/2H MoS2 Nanoparticles as an Efficient and Stable Bifunctional Electrocatalyst for Overall Water-Splitting. *Int. J. Hydrogen Energy* **2024**, *77*, 244–252. https://doi.org/10.1016/J.IJHYDENE.2024.06.214.

(121) Sen, S. K.; Manir, M. S.; Nur, S.; Hossain, M. N.; Islam, M. J.; Alam, A. K. M. M.; Hakim, M. A. Estimation of Hydrothermally Synthesized Iron Incorporated 2D-Sheet-like α -MoO 3 Microstructural and Optical Parameters Treated by Annealing Temperature . *Mater. Res. Express* **2020**, *7* (9), 095005. https://doi.org/10.1088/2053-1591/abb4f9.

(122) Ulrich Schubert; Nicola Hüsing. *Synthesis of Inorganic Materials*; 2019.

(123) Einarsrud, M. A.; Grande, T. 1D Oxide Nanostructures from Chemical Solutions. *Chemical Society Reviews*. Royal Society of Chemistry April 7, 2014, pp 2187–2199. https://doi.org/10.1039/c3cs60219b.

(124) Peterson, A. A.; Vogel, F.; Lachance, R. P.; Fröling, M.; Antal, M. J.; Tester, J. W. Thermochemical Biofuel Production in Hydrothermal Media: A Review of Sub- and Supercritical Water Technologies. *Energy Environ. Sci.* **2008**, *1* (1), 32–65. https://doi.org/10.1039/B810100K.

(125) Dinçer, İ.; Zamfirescu, C. Drying Phenomena: Theory and Applications. *Dry. Phenom. Theory Appl.* **2015**, 1–482. https://doi.org/10.1002/9781118534892.

(126) Schwarz, A.; Bluhm, J.; Schröder, J. Modeling of Freezing Processes of Ice Floes within the Framework of the TPM. *Acta Mech.* **2020**, *231* (8), 3099–3121. https://doi.org/10.1007/S00707-020-02686-8/TABLES/2.

(127) Walton, R. I. Subcritical Solvothermal Synthesis of Condensed Inorganic Materials. *Chem. Soc. Rev.* **2002**, *31* (4), 230–238. https://doi.org/10.1039/B105762F.

(128) Zhu, Z.; Xu, X.; Yao, Y.; Guo, C.; Chen, J.; Zhang, Y.; Wu, K. Liquid Metal-Assisted High-Efficiency Exfoliation of Boron Nitride for Electrically Insulating Heat-Spreader Film. *ACS Appl. Mater. Interfaces* **2022**, *14* (48), 54256–54265. https://doi.org/10.1021/ACSAMI.2C17237/ASSET/IMAGES/LARGE/AM2C17237_0005.JPEG.

(129) Tkachev, S.; Monteiro, M.; Santos, J.; Placidi, E.; Hassine, M. Ben; Marques, P.; Ferreira, P.; Alpuim, P.; Capasso, A. Environmentally Friendly Graphene Inks for Touch Screen Sensors. *Adv. Funct. Mater.* **2021**, *31* (33), 2103287. https://doi.org/10.1002/ADFM.202103287.

(130) Yang, Y.; Hou, H.; Zou, G.; Shi, W.; Shuai, H.; Li, J.; Ji, X. Electrochemical Exfoliation of Graphene-like Two-Dimensional Nanomaterials. *Nanoscale*. Royal Society of Chemistry January 7, 2019, pp 16–33. https://doi.org/10.1039/c8nr08227h.

(131) Shuck, C. E.; Sarycheva, A.; Anayee, M.; Levitt, A.; Zhu, Y.; Uzun, S.; Balitskiy, V.; Zahorodna, V.; Gogotsi, O.; Gogotsi, Y. Scalable Synthesis of Ti3C2Tx MXene. *Adv. Eng. Mater.* **2020**, *22* (3). https://doi.org/10.1002/ADEM.201901241.

(132) Huang, W. X.; Li, Z. P.; Li, D. D.; Hu, Z. H.; Wu, C.; Lv, K. Le; Li, Q. Ti3C2 MXene: Recent Progress in Its Fundamentals, Synthesis, and Applications. *Rare Met. 2022 4110* **2022**, *41* (10), 3268–3300. https://doi.org/10.1007/S12598-022-02058-2.

(133) Brent, J. R.; Savjani, N.; O'Brien, P. Synthetic Approaches to Two-Dimensional Transition Metal Dichalcogenide Nanosheets. *Progress in Materials Science*. Elsevier Ltd August 1, 2017, pp 411–478.

https://doi.org/10.1016/j.pmatsci.2017.06.002.

(134) Timmerman, M. A.; Xia, R.; Le, P. T. P.; Wang, Y.; Elshof, J. E. ten. Metal Oxide Nanosheets as 2D Building Blocks for the Design of Novel Materials. *Chem. – A Eur. J.* **2020**, *26* (42), 9084–9098. https://doi.org/10.1002/CHEM.201905735.

(135) Coleman, J. N. Liquid-Phase Exfoliation of Nanotubes and Graphene. *Adv. Funct. Mater.* **2009**, *19* (23), 3680–3695. https://doi.org/10.1002/ADFM.200901640.

(136) Pinilla, S.; Coelho, J.; Li, K.; Liu, J.; Nicolosi, V.; Liu, J. ✉. Two-Dimensional Material Inks. *Nat. Rev. Mater. 2022* **2022**, *0123456789*, 1–19. https://doi.org/10.1038/s41578-022-00448-7.

(137) Narayan, R.; Kim, S. O. Surfactant Mediated Liquid Phase Exfoliation of Graphene. *Nano Convergence*. Korea Nano Technology Research Society December 1, 2015. https://doi.org/10.1186/s40580-015-0050-x.

(138) Fernandes, J.; Nemala, S. S.; De Bellis, G.; Capasso, A. Green Solvents for the Liquid Phase Exfoliation Production of Graphene: The Promising Case of Cyrene. *Front. Chem.* **2022**, *10*, 311. https://doi.org/10.3389/FCHEM.2022.878799/BIBTEX.

(139) Artur Ciesielski; Paolo Samorì. Graphene via Sonication Assisted Liquid-Phase Exfoliation. *Chem. Soc. Rev.* **2013**, *43* (1), 381–398. https://doi.org/10.1039/C3CS60217F.

(140) Goni, F.; Chemelli, A.; Uhlig, F. High-Yield Production of Selected 2D Materials by Understanding Their Sonication-Assisted Liquid-Phase Exfoliation. *Nanomater. 2021, Vol. 11, Page 3253* **2021**, *11* (12), 3253. https://doi.org/10.3390/NANO11123253.

(141) Charles Hansen. *HANSEN SOLUBILITY PARAMETERS A User's Handbook Second Edition*; 2007.

(142) Jha, R.; Guha, P. K. An Effective Liquid-Phase Exfoliation Approach to Fabricate Tungsten Disulfide into Ultrathin Two-Dimensional Semiconducting Nanosheets. *J. Mater. Sci.* **2017**, *52* (12), 7256–7268. https://doi.org/10.1007/S10853-017-0962-4/TABLES/3.

(143) Gilliam, M. S.; Yousaf, A.; Guo, Y.; Li, D. O.; Momenah, A. A.; Wang, Q. H.; Green, A. A. Evaluating the Exfoliation Efficiency of Quasi-2D Metal Diboride Nanosheets Using Hansen Solubility Parameters. *Langmuir* **2021**, *37* (3), 1194–1205. https://doi.org/10.1021/ACS.LANGMUIR.0C03138/SUPPL_FILE/LA0C03138_SI_001.PDF.

(144) Vebber, G. C.; Pranke, P.; Pereira, C. N. Calculating Hansen Solubility Parameters of Polymers with Genetic Algorithms. *J. Appl. Polym. Sci.* **2014**, *131* (1), 39696. https://doi.org/10.1002/APP.39696.

(145) Venkatram, S.; Kim, C.; Chandrasekaran, A.; Ramprasad, R. Critical Assessment of the Hildebrand and Hansen Solubility Parameters for Polymers. *J. Chem. Inf. Model.* **2019**. https://doi.org/10.1021/ACS.JCIM.9B00656/SUPPL_FILE/CI9B00656_SI_002.PDF.

(146) Hanlon, D.; Backes, C.; Higgins, T. M.; Hughes, M.; O'Neill, A.; King, P.; McEvoy,

N.; Duesberg, G. S.; Mendoza Sanchez, B.; Pettersson, H.; Nicolosi, V.; Coleman, J. N. Production of Molybdenum Trioxide Nanosheets by Liquid Exfoliation and Their Application in High-Performance Supercapacitors. *Chem. Mater.* **2014**, *26* (4), 1751–1763. https://doi.org/10.1021/cm500271u.

(147) Hernandez, Y.; Lotya, M.; Rickard, D.; Bergin, S. D.; Coleman, J. N. Measurement of Multicomponent Solubility Parameters for Graphene Facilitates Solvent Discovery. *Langmuir* **2010**, *26* (5), 3208–3213. https://doi.org/10.1021/la903188a.

(148) Telkhozhayeva, M.; Teblum, E.; Konar, R.; Girshevitz, O.; Perelshtein, I.; Aviv, H.; Tischler, Y. R.; Nessim, G. D. Higher Ultrasonic Frequency Liquid Phase Exfoliation Leads to Larger and Monolayer to Few-Layer Flakes of 2D Layered Materials. *Langmuir* **2021**, *37* (15), 4504–4514. https://doi.org/10.1021/ACS.LANGMUIR.0C03668/ASSET/IMAGES/LARGE/LA0C03668_0007.JPEG.

(149) Jha, R.; Guha, P. K. An Effective Liquid-Phase Exfoliation Approach to Fabricate Tungsten Disulfide into Ultrathin Two-Dimensional Semiconducting Nanosheets. *J. Mater. Sci.* **2017**, *52* (12), 7256–7268. https://doi.org/10.1007/s10853-017-0962-4.

(150) Dutta, S.; Pal, S.; De, S. Mixed Solvent Exfoliated Transition Metal Oxides Nanosheets Based Flexible Solid State Supercapacitor Devices Endowed with High Energy Density. *New J. Chem.* **2019**, *43* (31), 12385–12395. https://doi.org/10.1039/c9nj03233a.

(151) Berardino, C. Di; Bélteky, P.; Schmitz, F.; Lamberti, F.; Menna, E.; Kukovecz, Á.; Gatti, T. Controlled Size Reduction of Liquid Exfoliated Graphene Micro-Sheets via Tip Sonication. *Cryst. 2020, Vol. 10, Page 1049* **2020**, *10* (11), 1049. https://doi.org/10.3390/CRYST10111049.

(152) Biccai, S.; Barwich, S.; Boland, D.; Harvey, A.; Hanlon, D.; McEvoy, N.; Coleman, J. N. Exfoliation of 2D Materials by High Shear Mixing. *2D Mater.* **2019**, *6* (1), 015008. https://doi.org/10.1088/2053-1583/aae7e3.

(153) Johansen, A.; Schafer, T. Effects of Interactions between Powder Particle Size and Binder Viscosity on Agglomerate Growth Mechanisms in a High Shear Mixer. *Eur. J. Pharm. Sci.* **2001**, *12* (3), 297–309. https://doi.org/10.1016/S0928-0987(00)00182-2.

(154) Kaur, A.; Morton, J. A.; Tyurnina, A. V.; Priyadarshi, A.; Holland, A.; Mi, J.; Porfyrakis, K.; Eskin, D. G.; Tzanakis, I. Temperature as a Key Parameter for Graphene Sono-Exfoliation in Water. *Ultrason. Sonochem.* **2022**, *90*, 106187. https://doi.org/10.1016/J.ULTSONCH.2022.106187.

(155) Sesis, A.; Hodnett, M.; Memoli, G.; Wain, A. J.; Jurewicz, I.; Dalton, A. B.; Carey, J. D.; Hinds, G. Influence of Acoustic Cavitation on the Controlled Ultrasonic Dispersion of Carbon Nanotubes. *J. Phys. Chem. B* **2013**, *117* (48), 15141–15150. https://doi.org/10.1021/JP410041Y/SUPPL_FILE/JP410041Y_SI_001.PDF.

(156) Backes, C.; Higgins, T. M.; Kelly, A.; Boland, C.; Harvey, A.; Hanlon, D.; Coleman, J. N. Guidelines for Exfoliation, Characterization and Processing of Layered Materials Produced by Liquid Exfoliation. *Chemistry of Materials*. American

Chemical Society 2017, pp 243–255. https://doi.org/10.1021/acs.chemmater.6b03335.

(157) Jayabal, S.; Wu, J.; Chen, J.; Geng, D.; Meng, X. Metallic 1T-MoS2 Nanosheets and Their Composite Materials: Preparation, Properties and Emerging Applications. *Mater. Today Energy* **2018**, *10*, 264–279. https://doi.org/10.1016/J.MTENER.2018.10.009.

(158) Yang, R.; Mei, L.; Zhang, Q.; Fan, Y.; Shin, H. S.; Voiry, D.; Zeng, Z. High-Yield Production of Mono- or Few-Layer Transition Metal Dichalcogenide Nanosheets by an Electrochemical Lithium Ion Intercalation-Based Exfoliation Method. *Nat. Protoc. 2022 172* **2022**, *17* (2), 358–377. https://doi.org/10.1038/s41596-021-00643-w.

(159) Li, T.; Yao, L.; Liu, Q.; Gu, J.; Luo, R.; Li, J.; Yan, X.; Wang, W.; Liu, P.; Chen, B.; Zhang, W.; Abbas, W.; Naz, R.; Zhang, D. Fluorine-Free Synthesis of High-Purity Ti3C2Tx (T=OH, O) via Alkali Treatment. *Angew. Chemie Int. Ed.* **2018**, *57* (21), 6115–6119. https://doi.org/10.1002/ANIE.201800887.

(160) Firestein, K. L.; Fernando, J. F. S.; Zhang, C.; Lewis, C. E. M.; Golberg, D. V. Delaminated V2C MXene Nanostructures Prepared via LiF Salt Etching for Electrochemical Applications. *ACS Appl. Nano Mater.* **2022**, *12*, 49. https://doi.org/10.1021/ACSANM.2C01838/ASSET/IMAGES/LARGE/AN2C01838_0006.JPEG.

(161) Thakur, A.; Chandran B.S., N.; Davidson, K.; Bedford, A.; Fang, H.; Im, Y.; Kanduri, V.; Wyatt, B. C.; Nemani, S. K.; Poliukhova, V.; Kumar, R.; Fakhraai, Z.; Anasori, B. Step-by-Step Guide for Synthesis and Delamination of Ti3C2Tx MXene. *Small Methods* **2023**, *7* (8), 2300030. https://doi.org/10.1002/SMTD.202300030.

(162) Zhang, T.; Shuck, C. E.; Shevchuk, K.; Anayee, M.; Gogotsi, Y. Synthesis of Three Families of Titanium Carbonitride MXenes. *J. Am. Chem. Soc.* **2023**, *145* (41), 22374–22383. https://doi.org/10.1021/JACS.3C04712/ASSET/IMAGES/LARGE/JA3C04712_0006.JPEG.

(163) Artur Ciesielski; Paolo Samorì. Graphene via Sonication Assisted Liquid-Phase Exfoliation. *Chem. Soc. Rev.* **2013**, *43* (1), 381–398. https://doi.org/10.1039/C3CS60217F.

(164) Hu, C. X.; Shin, Y.; Read, O.; Casiraghi, C. Dispersant-Assisted Liquid-Phase Exfoliation of 2D Materials beyond Graphene. *Nanoscale* **2021**, *13* (2), 460–484. https://doi.org/10.1039/D0NR05514J.

(165) Parvez, K.; Worsley, R.; Alieva, A.; Felten, A.; Casiraghi, C. Water-Based and Inkjet Printable Inks Made by Electrochemically Exfoliated Graphene. *Carbon N. Y.* **2019**, *149*, 213–221. https://doi.org/10.1016/J.CARBON.2019.04.047.

(166) Guan, Z.; Wang, C.; Li, W.; Luo, S.; Yao, Y.; Yu, S.; Sun, R.; Wong, C.-P. A Facile and Clean Process for Exfoliating MoS2 Nanosheets Assisted by a Surface Active Agent in Aqueous Solution. *Nanotechnology* **2018**, *29* (42), 425702. https://doi.org/10.1088/1361-6528/AAD676.

(167) Smith, E.; Dent, G. *Modern Raman Spectroscopy-A Practical Approach*; Jonh Wiley

& Sons: Chichester, 2005.

(168) Morais, A.; Alves, J. P. C.; Lima, F. A. S.; Lira-Cantu, M.; Nogueira, A. F. Enhanced Photovoltaic Performance of Inverted Hybrid Bulk-Heterojunction Solar Cells Using TiO 2 /Reduced Graphene Oxide Films as Electron Transport Layers. *J. Photonics Energy* **2015**, *5* (1), 057408. https://doi.org/10.1117/1.JPE.5.057408.

(169) Elgrishi, N.; Rountree, K. J.; McCarthy, B. D.; Rountree, E. S.; Eisenhart, T. T.; Dempsey, J. L. A Practical Beginner's Guide to Cyclic Voltammetry. *J. Chem. Educ.* **2018**, *95* (2), 197–206. https://doi.org/10.1021/ACS.JCHEMED.7B00361/SUPPL_FILE/ED7B00361_SI_002.DOCX.

(170) Wijeratne, K. Conducting Polymer Electrodes for Thermogalvanic Cells. **2018**, *1971*. https://doi.org/10.3384/DISS.DIVA-152888.

(171) V.S. Bagotsky. *Fundamentals of Electrochemistry - Second Edition*, 2nd ed.; John Wiley & Sons, Inc.: Hoboken, New Jersey, 2006.

(172) M.A. Brett, C.; Oliveira Brett, A. M. *Electrochemistry - Principles, Methods and Applications*; Oxford University Press: New York, 1994.

(173) Mathis, T. S.; Kurra, N.; Wang, X.; Pinto, D.; Simon, P.; Gogotsi, Y. Energy Storage Data Reporting in Perspective—Guidelines for Interpreting the Performance of Electrochemical Energy Storage Systems. *Adv. Energy Mater.* **2019**, *9* (39), 1902007. https://doi.org/10.1002/AENM.201902007.

(174) Yoo, H. D.; Markevich, E.; Salitra, G.; Sharon, D.; Aurbach, D. On the Challenge of Developing Advanced Technologies for Electrochemical Energy Storage and Conversion. *Mater. Today* **2014**, *17* (3), 110–121. https://doi.org/10.1016/J.MATTOD.2014.02.014.

(175) Zhang, X.; Jia, F.; Song, S. Recent Advances in Structural Engineering of Molybdenum Disulfide for Electrocatalytic Hydrogen Evolution Reaction. *Chem. Eng. J.* **2021**, *405*. https://doi.org/10.1016/J.CEJ.2020.127013.

(176) Li, H. A Review of EDLC and Pseudocapacitance with Synergistic Integration of Carbon-Based and Metal Oxide Materials for Enhanced Electrochemical Energy Storage. *Appl. Comput. Eng.* **2024**, *61* (1), 231–244. https://doi.org/10.54254/2755-2721/61/20240968.

(177) Su, Y.-H.; Teng, H.; Jalal, N. I.; Ibrahim, R. I.; Oudah, M. K. A Review on Supercapacitors: Types and Components You May Also like A Novel Poly(Acrylonitrile)-Based Quasi-Solid-State Electrolyte for Dye-Sensitized Solar Cells A Review on Supercapacitors: Types and Components. *J. Phys. Conf. Ser.* **1973**, 12015. https://doi.org/10.1088/1742-6596/1973/1/012015.

(178) Ye, S.-F.; Zhu, K.-H.; Ma, W.; Dou, L.-Y.; Cui, P.-X.; Sha, H.; Han, X.; Wei, X.; Tao, X.-Y. Conducting Polymer Hydrogel Driven By Sodium Chloride as High Performance Flexible Supercapacitor Electrode. *J. Electrochem. Soc.* **2022**, *169* (7), 073501. https://doi.org/10.1149/1945-7111/AC7ADE.

(179) Banerjee, J.; Dutta, K.; Kader, M. A.; Nayak, S. K. An Overview on the Recent Developments in Polyaniline-Based Supercapacitors. *Polym. Adv. Technol.* **2019**,

30 (8), 1902–1921. https://doi.org/10.1002/PAT.4624.

(180) Schoetz, T.; Gordon, L. W.; Ivanov, S.; Bund, A.; Mandler, D.; Messinger, R. J. Disentangling Faradaic, Pseudocapacitive, and Capacitive Charge Storage: A Tutorial for the Characterization of Batteries, Supercapacitors, and Hybrid Systems. *Electrochim. Acta* **2022**, *412*, 140072. https://doi.org/10.1016/J.ELECTACTA.2022.140072.

(181) Helseth, L. E. Comparison of Methods for Finding the Capacitance of a Supercapacitor. *J. Energy Storage* **2021**, *35*, 102304. https://doi.org/10.1016/J.EST.2021.102304.

(182) Eliad, L.; Salitra, G.; Soffer, A.; Aurbach, D. On the Mechanism of Selective Electroadsorption of Protons in the Pores of Carbon Molecular Sieves. *Langmuir* **2005**, *21* (7), 3198–3202. https://doi.org/10.1021/LA049238H/ASSET/IMAGES/LARGE/LA049238HN00001.JPEG.

(183) Eliad, L.; Salitra, G.; Soffer, A.; Aurbach, D. Ion Sieving Effects in the Electrical Double Layer of Porous Carbon Electrodes: Estimating Effective Ion Size in Electrolytic Solutions. *J. Phys. Chem. B* **2001**, *105* (29), 6880–6887. https://doi.org/10.1021/JP010086Y.

(184) Allagui, A.; Benaoum, H.; Olendski, O. On the Gouy–Chapman–Stern Model of the Electrical Double-Layer Structure with a Generalized Boltzmann Factor. *Phys. A Stat. Mech. its Appl.* **2021**, *582*, 126252. https://doi.org/10.1016/J.PHYSA.2021.126252.

(185) Bolt, G. H. Analysis of the Validity of the Gouy-Chapman Theory of the Electric Double Layer. *J. Colloid Sci.* **1955**, *10* (2), 206–218. https://doi.org/10.1016/0095-8522(55)90027-1.

(186) Brown, M. A.; Bossa, G. V.; May, S. Emergence of a Stern Layer from the Incorporation of Hydration Interactions into the Gouy-Chapman Model of the Electrical Double Layer. *Langmuir* **2015**, *31* (42), 11477–11483. https://doi.org/10.1021/ACS.LANGMUIR.5B02389/ASSET/IMAGES/LARGE/LA-2015-02389F_0005.JPEG.

(187) Kant, R.; Singh, M. B. Generalization of the Gouy-Chapman-Stern Model of an Electric Double Layer for a Morphologically Complex Electrode: Deterministic and Stochastic Morphologies. *Phys. Rev. E - Stat. Nonlinear, Soft Matter Phys.* **2013**, *88* (5), 052303. https://doi.org/10.1103/PHYSREVE.88.052303/FIGURES/9/MEDIUM.

(188) Nakamura, M.; Sato, N.; Hoshi, N.; Sakata, O. Outer Helmholtz Plane of the Electrical Double Layer Formed at the Solid Electrode-Liquid Interface. *ChemPhysChem* **2011**, *12* (8), 1430–1434. https://doi.org/10.1002/CPHC.201100011.

(189) Usui, S. Interaction between Dissimilar Double Layers with like Signs under Charge Regulation on the Basis of the Gouy–Chapman–Stern–Grahame Model. *J. Colloid Interface Sci.* **2004**, *280* (1), 113–119. https://doi.org/10.1016/J.JCIS.2004.07.014.

(190) Levine, S.; Matijević, E. A Comparison of Models for the Electric Double Layer. *J. Colloid Interface Sci.* **1967**, *23* (2), 188–199. https://doi.org/10.1016/0021-9797(67)90102-6.

(191) Ross Macdonald, J.; Barlow, C. A. Theory of Double-Layer Differential Capacitance in Electrolytes. *J. Chem. Phys.* **1962**, *36* (11), 3062–3080. https://doi.org/10.1063/1.1732426.

(192) Shao, Y.; El-Kady, M. F.; Sun, J.; Li, Y.; Zhang, Q.; Zhu, M.; Wang, H.; Dunn, B.; Kaner, R. B. Design and Mechanisms of Asymmetric Supercapacitors. *Chem. Rev.* **2018**, *118* (18), 9233–9280. https://doi.org/10.1021/ACS.CHEMREV.8B00252/ASSET/IMAGES/MEDIUM/CR-2018-00252Z_0028.GIF.

(193) Gupta, H.; Kumar, M.; Sarkar, D.; Menezes, P. W. Recent Technological Advances in Designing Electrodes and Electrolytes for Efficient Zinc Ion Hybrid Supercapacitors. *Energy Adv.* **2023**, *2* (9), 1263–1293. https://doi.org/10.1039/D3YA00259D.

(194) Osman, A. I.; Mehta, N.; Elgarahy, A. M.; Hefny, M.; Al-Hinai, A.; Al-Muhtaseb, A. H.; Rooney, D. W. Hydrogen Production, Storage, Utilisation and Environmental Impacts: A Review. *Environ. Chem. Lett. 2021 201* **2021**, *20* (1), 153–188. https://doi.org/10.1007/S10311-021-01322-8.

(195) Vilanova, A.; Dias, P.; Lopes, T.; Mendes, A. The Route for Commercial Photoelectrochemical Water Splitting: A Review of Large-Area Devices and Key Upscaling Challenges. *Chem. Soc. Rev.* **2024**, *53* (5), 2388–2434. https://doi.org/10.1039/D1CS01069G.

(196) Incer-Valverde, J.; Korayem, A.; Tsatsaronis, G.; Morosuk, T. “Colors” of Hydrogen: Definitions and Carbon Intensity. *Energy Convers. Manag.* **2023**, *291*, 117294. https://doi.org/10.1016/J.ENCONMAN.2023.117294.

(197) Liu, F.; Shi, C.; Guo, X.; He, Z.; Pan, L.; Huang, Z. F.; Zhang, X.; Zou, J. J. Rational Design of Better Hydrogen Evolution Electrocatalysts for Water Splitting: A Review. *Adv. Sci.* **2022**, *9* (18), 2200307. https://doi.org/10.1002/ADVS.202200307.

(198) Ferriday, T. B.; Middleton, P. H.; Kolhe, M. L. Review of the Hydrogen Evolution Reaction—A Basic Approach. *Energies 2021, Vol. 14, Page 8535* **2021**, *14* (24), 8535. https://doi.org/10.3390/EN14248535.

(199) Zhu, J.; Hu, L.; Zhao, P.; Lee, L. Y. S.; Wong, K. Y. Recent Advances in Electrocatalytic Hydrogen Evolution Using Nanoparticles. *Chem. Rev.* **2020**, *120* (2), 851–918. https://doi.org/10.1021/ACS.CHEMREV.9B00248/ASSET/IMAGES/MEDIUM/CR9B00248_0041.GIF.

(200) Lasia, A. Mechanism and Kinetics of the Hydrogen Evolution Reaction. *Int. J. Hydrogen Energy* **2019**, *44* (36), 19484–19518. https://doi.org/10.1016/J.IJHYDENE.2019.05.183.

(201) Krstajić, N.; Popović, M.; Grgur, B.; Vojnović, M.; Šepa, D. On the Kinetics of the Hydrogen Evolution Reaction on Nickel in Alkaline Solution: Part I. The

Mechanism. *J. Electroanal. Chem.* **2001**, *512* (1–2), 16–26. https://doi.org/10.1016/S0022-0728(01)00590-3.

(202) Prats, H.; Chan, K. The Determination of the HOR/HER Reaction Mechanism from Experimental Kinetic Data. *Phys. Chem. Chem. Phys.* **2021**, *23* (48), 27150–27158. https://doi.org/10.1039/D1CP04134G.

(203) Bao, F.; Kemppainen, E.; Dorbandt, I.; Bors, R.; Xi, F.; Schlatmann, R.; van de Krol, R.; Calnan, S. Understanding the Hydrogen Evolution Reaction Kinetics of Electrodeposited Nickel-Molybdenum in Acidic, Near-Neutral, and Alkaline Conditions. *ChemElectroChem* **2021**, *8* (1), 195–208. https://doi.org/10.1002/CELC.202001436.

(204) Nørskov, J. K.; Bligaard, T.; Logadottir, A.; Kitchin, J. R.; Chen, J. G.; Pandelov, S.; Stimming, U. Trends in the Exchange Current for Hydrogen Evolution. *J. Electrochem. Soc.* **2005**, *152* (3), J23. https://doi.org/10.1149/1.1856988/XML.

(205) Stratton, S. M.; Zhang, S.; Montemore, M. M. Addressing Complexity in Catalyst Design: From Volcanos and Scaling to More Sophisticated Design Strategies. *Surf. Sci. Rep.* **2023**, *78* (3), 100597. https://doi.org/10.1016/J.SURFREP.2023.100597.

(206) Krishnan, U.; Kaur, M.; Singh, K.; Kumar, M.; Kumar, A. A Synoptic Review of MoS 2 : Synthesis to Applications. *Superlattices and Microstructures*. Academic Press April 1, 2019, pp 274–297. https://doi.org/10.1016/j.spmi.2019.02.005.

(207) Nguyen, T. P.; Kim, S. Y.; Lee, T. H.; Jang, H. W.; Le, Q. Van; Kim, I. T. Facile Synthesis of W2C@WS2 Alloy Nanoflowers and Their Hydrogen Generation Performance. *Appl. Surf. Sci.* **2020**, *504*, 144389. https://doi.org/10.1016/j.apsusc.2019.144389.

(208) Chen, J.; Li, F.; Tang, Y.; Tang, Q. Tuning the Phase Stability and Surface HER Activity of 1T′-MoS 2 by Covalent Chemical Functionalization. *J. Mater. Chem. C* **2020**, *8* (44), 15852–15859. https://doi.org/10.1039/D0TC03943H.

(209) Liu, Z.; Nie, K.; Qu, X.; Li, X.; Li, B.; Yuan, Y.; Chong, S.; Liu, P.; Li, Y.; Yin, Z.; Huang, W. General Bottom-Up Colloidal Synthesis of Nano-Monolayer Transition-Metal Dichalcogenides with High 1T′-Phase Purity. *J. Am. Chem. Soc.* **2022**, *144* (11), 4863–4873. https://doi.org/10.1021/JACS.1C12379/ASSET/IMAGES/LARGE/JA1C12379_0007.JPEG.

(210) Chen, Z.; Duan, X.; Wei, W.; Wang, S.; Ni, B. J. Recent Advances in Transition Metal-Based Electrocatalysts for Alkaline Hydrogen Evolution. *J. Mater. Chem. A* **2019**, *7* (25), 14971–15005. https://doi.org/10.1039/C9TA03220G.

(211) Choi, S.; Kim, C.; Lee, J. Y.; Lee, T. H.; Kwon, K. C.; Kang, S.; Lee, S. A.; Choi, K. S.; Suh, J. M.; Hong, K.; Jun, S. E.; Kim, W. K.; Ahn, S. H.; Han, S.; Kim, S. Y.; Lee, C. H.; Jang, H. W. Vertically Aligned MoS2 Thin Film Catalysts with Fe-Ni Sulfide Nanoparticles by One-Step Sulfurization for Efficient Solar Water Reduction. *Chem. Eng. J.* **2021**, *418*. https://doi.org/10.1016/J.CEJ.2021.129369.

(212) Peng, L.; Liang, Y.; Wu, S.; Li, Z.; Sun, H.; Jiang, H.; Zhu, S.; Cui, Z.; Li, L. Nanoporous Ni/NiO Catalyst for Efficient Hydrogen Evolution Reaction Prepared by Partial Electro-Oxidation after Dealloying. *J. Alloys Compd.* **2022**, *911*, 165061.

https://doi.org/10.1016/J.JALLCOM.2022.165061.

(213) Gong, M.; Zhou, W.; Tsai, M. C.; Zhou, J.; Guan, M.; Lin, M. C.; Zhang, B.; Hu, Y.; Wang, D. Y.; Yang, J.; Pennycook, S. J.; Hwang, B. J.; Dai, H. Nanoscale Nickel Oxide/Nickel Heterostructures for Active Hydrogen Evolution Electrocatalysis. *Nat. Commun. 2014 51* **2014**, *5* (1), 1–6. https://doi.org/10.1038/ncomms5695.

(214) Rana, A. G.; Schwarze, M.; Tasbihi, M.; Sala, X.; García-Antón, J.; Minceva, M. Influence of Cocatalysts (Ni, Co, and Cu) and Synthesis Method on the Photocatalytic Activity of Exfoliated Graphitic Carbon Nitride for Hydrogen Production. *Nanomaterials* **2022**, *12* (22). https://doi.org/10.3390/NANO12224006/S1.

(215) Kalasapurayil Kunhiraman, A.; Ramasamy, M. Nickel-Doped Nanobelt Structured Molybdenum Oxides as Electrocatalysts for Electrochemical Hydrogen Evolution Reaction. *J. Nanoparticle Res.* **2017**, *19* (6), 1–10. https://doi.org/10.1007/s11051-017-3890-y.

(216) Batugedara, T. N.; Brock, S. L. A Little Nickel Goes a Long Way: Ni Incorporation into Rh2P for Stable Bifunctional Electrocatalytic Water Splitting in Acidic Media. *ACS Mater. Au* **2023**, *3* (4), 299–309. https://doi.org/10.1021/ACSMATERIALSAU.2C00080/ASSET/IMAGES/LARGE/MG2C00080_0008.JPEG.

(217) Mannix, A. J.; Kiraly, B.; Hersam, M. C.; Guisinger, N. P. Synthesis and Chemistry of Elemental 2D Materials. *Nature Reviews Chemistry*. Nature Publishing Group January 11, 2017, pp 1–14. https://doi.org/10.1038/s41570-016-0014.

(218) Hirsch, A.; Hauke, F. Post-Graphene 2D Chemistry: The Emerging Field of Molybdenum Disulfide and Black Phosphorus Functionalization. *Angew. Chemie Int. Ed.* **2018**, *57* (16), 4338–4354. https://doi.org/10.1002/anie.201708211.

(219) Huang, Y.; Pan, Y. H.; Yang, R.; Bao, L. H.; Meng, L.; Luo, H. L.; Cai, Y. Q.; Liu, G. D.; Zhao, W. J.; Zhou, Z.; Wu, L. M.; Zhu, Z. L.; Huang, M.; Liu, L. W.; Liu, L.; Cheng, P.; Wu, K. H.; Tian, S. B.; Gu, C. Z.; Shi, Y. G.; Guo, Y. F.; Cheng, Z. G.; Hu, J. P.; Zhao, L.; Yang, G. H.; Sutter, E.; Sutter, P.; Wang, Y. L.; Ji, W.; Zhou, X. J.; Gao, H. J. Universal Mechanical Exfoliation of Large-Area 2D Crystals. *Nat. Commun.* **2020**, *11* (1), 1–9. https://doi.org/10.1038/s41467-020-16266-w.

(220) Ji, F.; Ren, X.; Zheng, X.; Liu, Y.; Pang, L.; Jiang, J.; Frank, S. (; Liu,). 2D-MoO 3 Nanosheets for Superior Gas Sensors †. **2016**, *8*, 8696. https://doi.org/10.1039/c6nr00880a.

(221) Datta, R. S.; Haque, F.; Mohiuddin, M.; Carey, B. J.; Syed, N.; Zavabeti, A.; Zhang, B.; Khan, H.; Berean, K. J.; Ou, J. Z.; Mahmood, N.; Daeneke, T.; Kalantar-Zadeh, K. Highly Active Two Dimensional α-MoO3-: X for the Electrocatalytic Hydrogen Evolution Reaction. *J. Mater. Chem. A* **2017**, *5* (46), 24223–24231. https://doi.org/10.1039/c7ta07705j.

(222) Etman, A. S.; Abdelhamid, H. N.; Yuan, Y.; Wang, L.; Zou, X.; Sun, J. Facile Water-Based Strategy for Synthesizing MoO3-x Nanosheets: Efficient Visible Light Photocatalysts for Dye Degradation. *ACS Omega* **2018**, *3* (2), 2201–2209. https://doi.org/10.1021/acsomega.8b00012.

(223) Sricharan, M.; Gupta, B.; Moolayadukkam, S.; Ramakrishna Matte, H. S. S. Exfoliation in a Low Boiling Point Solvent and Electrochemical Applications of MoO 3. *Beilstein J. Nanotechnol* **2020**, *2020*, 662–670. https://doi.org/10.3762/bjnano.11.52.

(224) Dalle Feste, P.; Crisci, M.; Barbon, F.; Tajoli, F.; Salerno, M.; Drago, F.; Prato, M.; Gross, S.; Gatti, T.; Lamberti, F. Work Function Tuning in Hydrothermally Synthesized Vanadium-Doped MoO3 and Co3O4 Mesostructures for Energy Conversion Devices. *Appl. Sci.* **2021**, *11* (5), 2016. https://doi.org/10.3390/app11052016.

(225) Schiettecatte, P.; Rousaki, A.; Vandenabeele, P.; Geiregat, P.; Hens, Z. Liquid-Phase Exfoliation of Rhenium Disulfide by Solubility Parameter Matching. *Langmuir* **2020**, *36* (51), 15493–15500. https://doi.org/10.1021/ACS.LANGMUIR.0C02517/SUPPL_FILE/LA0C02517_SI_001.PDF.

(226) Zhou, Y.; Xu, L.; Liu, M.; Qi, Z.; Wang, W.; Zhu, J.; Chen, S.; Yu, K.; Su, Y.; Ding, B.; Qiu, L.; Cheng, H. M. Viscous Solvent-Assisted Planetary Ball Milling for the Scalable Production of Large Ultrathin Two-Dimensional Materials. *ACS Nano* **2022**, *16* (7), 10179–10187. https://doi.org/10.1021/ACSNANO.1C11097/ASSET/IMAGES/LARGE/NN1C11097_0005.JPEG.

(227) Wu, Y. L.; Hong, J. Bin; Zhong, W. X.; Wang, C. X.; Li, Z. F.; Dmytro, S. Auxiliary Ball Milling to Prepare WS2/Graphene Nanosheets Composite for Lithium-Ion Battery Anode Materials. *Tungsten* **2024**, *6* (1), 124–133. https://doi.org/10.1007/S42864-023-00216-2/FIGURES/8.

(228) Li, L.; Shinde, S. L.; Fujita, T.; Kondo, T. Ball-Milled MoS2 with Graphene Shows Enhanced Catalytic Activity for Hydrogen Evolution Reaction. *Sci. Technol. Adv. Mater.* **2024**, *25* (1). https://doi.org/10.1080/14686996.2024.2359360.

(229) Zhang, C.; Tan, J.; Pan, Y.; Cai, X.; Zou, X.; Cheng, H. M.; Liu, B. Mass Production of 2D Materials by Intermediate-Assisted Grinding Exfoliation. *Natl. Sci. Rev.* **2020**, *7* (2), 324–332. https://doi.org/10.1093/NSR/NWZ156.

(230) Li, Z.; Li, K.; Li, Y.; Yu, Y.; Lv, J.; Liu, X.; Guan, K.; Lei, W.; Zhang, S.; Zhang, H. Modified Molten Salt Assisted Exfoliation of Large-Size 2D Materials. *Adv. Funct. Mater.* **2024**, *34* (10), 2310371. https://doi.org/10.1002/ADFM.202310371.

(231) Bai, Y.; Liu, C.; Chen, T.; Li, W.; Zheng, S.; Pi, Y.; Luo, Y.; Pang, H.; Bai, Y.; Liu, C.; Chen, T.; Li, W.; Zheng, S.; Pi, Y.; Pang, H.; Luo, Y. MXene-Copper/Cobalt Hybrids via Lewis Acidic Molten Salts Etching for High Performance Symmetric Supercapacitors. *Angew. Chemie Int. Ed.* **2021**, *60* (48), 25318–25322. https://doi.org/10.1002/ANIE.202112381.

(232) Paolucci, V.; D'Olimpio, G.; Lozzi, L.; Mio, A. M.; Ottaviano, L.; Nardone, M.; Nicotra, G.; Le-Cornec, P.; Cantalini, C.; Politano, A. Sustainable Liquid-Phase Exfoliation of Layered Materials with Nontoxic Polarclean Solvent. *ACS Sustain. Chem. Eng.* **2020**, *8* (51), 18830–18840. https://doi.org/10.1021/ACSSUSCHEMENG.0C04191/ASSET/IMAGES/LARGE/SC0C04191_0007.JPEG.

(233) Occhiuzzi, J.; Politano, G. G.; D'Olimpio, G.; Politano, A. The Quest for Green Solvents for the Sustainable Production of Nanosheets of Two-Dimensional (2D) Materials, a Key Issue in the Roadmap for the Ecology Transition in the Flatland. *Mol. 2023, Vol. 28, Page 1484* **2023**, *28* (3), 1484. https://doi.org/10.3390/MOLECULES28031484.

(234) D'Olimpio, G.; Occhiuzzi, J.; Lozzi, L.; Ottaviano, L.; Politano, A. Dimethyl 2-Methylglutarate (Iris): A Green Platform for Efficient Liquid-Phase Exfoliation of 2D Materials. *Adv. Sustain. Syst.* **2022**, *6* (11), 2200277. https://doi.org/10.1002/ADSU.202200277.

(235) Hu, C.-X.; Shin, Y.; Read, O.; Casiraghi, C. Dispersant-Assisted Liquid-Phase Exfoliation of 2D Materials beyond Graphene. *Nanoscale* **2021**, *13* (2), 460–484. https://doi.org/10.1039/D0NR05514J.

(236) Griffin, A.; Nisi, K.; Pepper, J.; Harvey, A.; Szydłowska, B. M.; Coleman, J. N.; Backes, C. Effect of Surfactant Choice and Concentration on the Dimensions and Yield of Liquid-Phase-Exfoliated Nanosheets. *Chem. Mater.* **2020**, *32* (7), 2852–2862. https://doi.org/10.1021/acs.chemmater.9b04684.

(237) Palsaniya, S.; Nemade, H. B.; Dasmahapatra, A. K. Mixed Surfactant-Mediated Synthesis of Hierarchical PANI Nanorods for an Enzymatic Glucose Biosensor. *ACS Appl. Polym. Mater.* **2019**, *1* (4), 647–656. https://doi.org/10.1021/ACSAPM.8B00103/ASSET/IMAGES/LARGE/AP-2018-00103N_0007.JPEG.

(238) Gupta, S.; Singh, P.; Moghadas, B.; Grim, B. J.; Kodibagkar, V. D.; Green, M. D. Synthesis of PEG and Quaternary Ammonium Grafted Silicone Copolymers as Nanoemulsifiers. *ACS Appl. Polym. Mater.* **2020**, *2* (5), 1856–1864. https://doi.org/10.1021/ACSAPM.0C00103/SUPPL_FILE/AP0C00103_SI_001.PDF.

(239) Read, O.; Shin, Y.; Hu, C. xia; Zarattini, M.; Boyes, M.; Just-Baringo, X.; Panigrahi, A.; Larrosa, I.; Casiraghi, C. Insights into the Exfoliation Mechanism of Pyrene-Assisted Liquid Phase Exfoliation of Graphene from Lateral Size-Thickness Characterisation. *Carbon N. Y.* **2022**, *186*, 550–559. https://doi.org/10.1016/J.CARBON.2021.09.075.

(240) Wang, M.; Crisci, M.; Pavan, M.; Liu, Z.; Gallego, J.; Gatti, T. New Insights into the Surfactant-Assisted Liquid-Phase Exfoliation of Bi2S3 for Electrocatalytic Applications. *Catalysts* **2023**, *13* (3), 551. https://doi.org/10.3390/CATAL13030551/S1.

(241) Li, H.; Zhang, Q.; Yap, C. C. R.; Tay, B. K.; Edwin, T. H. T.; Olivier, A.; Baillargeat, D. From Bulk to Monolayer MoS2: Evolution of Raman Scattering. *Adv. Funct. Mater.* **2012**, *22* (7), 1385–1390. https://doi.org/10.1002/adfm.201102111.

(242) Chakraborty, B.; Matte, H. S. S. R.; Sood, A. K.; Rao, C. N. R. Layer-Dependent Resonant Raman Scattering of a Few Layer MoS2. *J. Raman Spectrosc.* **2013**, *44* (1), 92–96. https://doi.org/10.1002/JRS.4147.

(243) Berkdemir, A.; Gutiérrez, H. R.; Botello-Méndez, A. R.; Perea-López, N.; Elías, A. L.; Chia, C. I.; Wang, B.; Crespi, V. H.; López-Urías, F.; Charlier, J. C.; Terrones, H.; Terrones, M. Identification of Individual and Few Layers of WS2 Using Raman Spectroscopy. *Sci. Rep.* **2013**, *3*. https://doi.org/10.1038/srep01755.

(244) Krishnan, S. G.; Arunachalam, A.; Jagadish, P.; Khalid, M. 2D Materials for Supercapacitor and Supercapattery Applications. *ACS Symp. Ser.* **2020**, *1353*, 33–47. https://doi.org/10.1021/BK-2020-1353.CH002.

(245) Han, Y.; Ge, Y.; Chao, Y.; Wang, C.; Wallace, G. G. Recent Progress in 2D Materials for Flexible Supercapacitors. *J. Energy Chem.* **2018**, *27* (1), 57–72. https://doi.org/10.1016/J.JECHEM.2017.10.033.

(246) Palaniselvam, T.; Baek, J. B. Graphene Based 2D-Materials for Supercapacitors. *2D Mater.* **2015**, *2* (3), 032002. https://doi.org/10.1088/2053-1583/2/3/032002.

(247) Ali, M.; Afzal, A. M.; Iqbal, M. W.; Mumtaz, S.; Imran, M.; Ashraf, F.; Ur Rehman, A.; Muhammad, F. 2D-TMDs Based Electrode Material for Supercapacitor Applications. *Int. J. Energy Res.* **2022**, *46* (15), 22336–22364. https://doi.org/10.1002/ER.8698.

(248) Mohan, V. V.; Manuraj, M.; Anjana, P. M.; Rakhi, R. B. WS2 Nanoflowers as Efficient Electrode Materials for Supercapacitors. *Energy Technol.* **2022**, *10* (3), 2100976. https://doi.org/10.1002/ENTE.202100976.

(249) Song, Z.; Wang, Z.; Yu, R. Strategies for Advanced Supercapacitors Based on 2D Transition Metal Dichalcogenides: From Material Design to Device Setup. *Small Methods* **2023**, 2300808. https://doi.org/10.1002/SMTD.202300808.

(250) Mishra, A.; Shetti, N. P.; Basu, S.; Raghava Reddy, K.; Aminabhavi, T. M. Carbon Cloth-Based Hybrid Materials as Flexible Electrochemical Supercapacitors. *ChemElectroChem* **2019**, *6* (23), 5771–5786. https://doi.org/10.1002/CELC.201901122.

(251) Yao, Z.; Sun, H.; Sui, H.; Liu, X. 2D/2D Heterojunction of R-Scheme Ti3C2 MXene/MoS2 Nanosheets for Enhanced Photocatalytic Performance. *Nanoscale Res. Lett.* **2020**, *15* (1), 1–12. https://doi.org/10.1186/S11671-020-03314-Z/FIGURES/9.

(252) Wang, X.; Li, H.; Li, H.; Lin, S.; Ding, W.; Zhu, X.; Sheng, Z.; Wang, H.; Zhu, X.; Sun, Y. 2D/2D 1T-MoS 2 /Ti 3 C 2 MXene Heterostructure with Excellent Supercapacitor Performance. https://doi.org/10.1002/adfm.201910302.

(253) Yang, G.; Takei, T.; Yanagida, S.; Kumada, N. Hexagonal Tungsten Oxide-Polyaniline Hybrid Electrodes for High-Performance Energy Storage. *Appl. Surf. Sci.* **2019**, *498*, 143872. https://doi.org/10.1016/j.apsusc.2019.143872.

(254) Gan, X.; Zhang, J.; Liu, J.; Bai, Y.; Su, X.; Wang, W.; Cao, Z.; Zhao, H.; Ao, Y.; Wang, P. Polyaniline Functionalization of Defective 1T-MoS2 Nanosheets for Improved Electron and Mass Transfer: Implications for Electrochemical Sensors. *ACS Appl. Nano Mater.* **2023**, *6* (13), 11725–11736. https://doi.org/10.1021/ACSANM.3C01679/ASSET/IMAGES/LARGE/AN3C01679_0009.JPEG.

(255) Joo, H.; Han, H.; Cho, S. Fabrication of Poly(Vinyl Alcohol)-Polyaniline Nanofiber/Graphene Hydrogel for High-Performance Coin Cell Supercapacitor. *Polym. 2020, Vol. 12, Page 928* **2020**, *12* (4), 928. https://doi.org/10.3390/POLYM12040928.

(256) Chao, Y.; Ge, Y.; Chen, Z.; Cui, X.; Zhao, C.; Wang, C.; Wallace, G. G. One-Pot Hydrothermal Synthesis of Solution-Processable MoS 2 / PEDOT:PSS Composites for High-Performance Supercapacitors. *Cite This ACS Appl. Mater. Interfaces* **2021**, *13*, 7285–7296. https://doi.org/10.1021/acsami.0c21439.

(257) Aftab, J.; Ali, A.; Mehmood, S.; Aftab, A.; Ahmad, I.; Bhopal, M. F.; Hussain, M.; Shah, Z. U.; Shah, A. U.; Padhiar, M. A.; Wang, M.; Bhatti, A. S. Facile Synthesis of Synergetic MoO2/MoS2@GO Nanohybrid as Energy-Efficient Electrode Material for High-Performance Asymmetric Supercapacitor Applications. *J. Energy Storage* **2023**, *74*, 109324. https://doi.org/10.1016/J.EST.2023.109324.

(258) Boll, F.; Fadda, M.; Happel, M.; Crisci, M.; Athanassiou, A.; Smarsly, B.; Bella, F.; Lamberti, F.; Perotto, G.; Gatti, T. Multicomponent Synergistic Contribution in Nanoengineered Nanofibers for Flexible Energy Storage. *ACS Appl. Energy Mater.* **2024**, *7*, 4733–4744. https://doi.org/10.1021/ACSAEM.4C00417/ASSET/IMAGES/LARGE/AE4C00417_0004.JPEG.

(259) Zhao, W.; Pan, J.; Fang, Y.; Che, X.; Wang, D.; Bu, K.; Huang, F. Metastable MoS_2: Crystal Structure, Electronic Band Structure, Synthetic Approach and Intriguing Physical Properties. *Chem. - A Eur. J.* **2018**, *24* (60), 15942–15954. https://doi.org/10.1002/chem.201801018.

(260) Balendhran, S.; Walia, S.; Nili, H.; Ou, J. Z.; Zhuiykov, S.; Kaner, R. B.; Sriram, S.; Bhaskaran, M.; Kalantar-Zadeh, K. Two-Dimensional Molybdenum Trioxide and Dichalcogenides. *Adv. Funct. Mater.* **2013**, *23* (32), 3952–3970. https://doi.org/10.1002/adfm.201300125.

(261) Jana, M. K.; Rao, C. N. R. Two-Dimensional Inorganic Analogues of Graphene: Transition Metal Dichalcogenides. *Philosophical Transactions of the Royal Society A: Mathematical, Physical and Engineering Sciences*. Royal Society of London September 13, 2016. https://doi.org/10.1098/rsta.2015.0318.

(262) Kulkarni, B.; Alsaiari, M.; M S, J.; J, K.; Jalalah, M.; Harraz, F. A.; Balakrishna, R. G. Performance of Functionalized 1T-MoS2 as Composite Counter Electrode Material for QDSSCs and Its Analogy with 2H-MoS2. *Mater. Res. Bull.* **2021**, *134*. https://doi.org/10.1016/J.MATERRESBULL.2020.111096.

(263) Tang, Q.; Jiang, D. E. Stabilization and Band-Gap Tuning of the 1T-MoS2 Monolayer by Covalent Functionalization. *Chem. Mater.* **2015**, *27* (10), 3743–3748. https://doi.org/10.1021/ACS.CHEMMATER.5B00986/ASSET/IMAGES/LARGE/CM-2015-00986X_0007.JPEG.

(264) Zhang, H.; Koledin, T. D.; Xiang, W.; Hao, J.; Nanayakkara, S. U.; Attanayake, N. H.; Li, Z.; Mirkin, M. V.; Miller, E. M. Stabilizing the Heavily-Doped and Metallic Phase of MoS2 Monolayers with Surface Functionalization. *2D Mater.* **2021**, *9* (1), 015033. https://doi.org/10.1088/2053-1583/AC3F44.

(265) Presolski, S.; Pumera, M. Covalent Functionalization of MoS2. *Materials Today*. Elsevier B.V. April 1, 2016, pp 140–145. https://doi.org/10.1016/j.mattod.2015.08.019.

(266) Im, H.; Bala, A.; So, B.; Kim, Y. J.; Kim, S. Customization of MoS2 Phototransistors

via Thiol-Based Functionalization. *Adv. Electron. Mater.* **2021**, *7* (11), 2100644. https://doi.org/10.1002/AELM.202100644.

(267) Zhou, L.; He, B.; Yang, Y.; He, Y. Facile Approach to Surface Functionalized MoS 2 Nanosheets. *RSC Adv.* **2014**, *4* (61), 32570–32578. https://doi.org/10.1039/C4RA04682J.

(268) Jaiswal, M. K.; Carrow, J. K.; Gentry, J. L.; Gupta, J.; Altangerel, N.; Scully, M.; Gaharwar, A. K.; K Jaiswal, H. M.; Carrow, J. K.; Gentry, J. L.; Gaharwar, A. K.; Gupta, J.; Altangerel, N.; Scully, M. Vacancy-Driven Gelation Using Defect-Rich Nanoassemblies of 2D Transition Metal Dichalcogenides and Polymeric Binder for Biomedical Applications. *Adv. Mater.* **2017**, *29* (36), 1702037. https://doi.org/10.1002/ADMA.201702037.

(269) Vishnoi, P.; Sampath, A.; Waghmare, U. V.; Rao, C. N. R. Covalent Functionalization of Nanosheets of MoS2 and MoSe2 by Substituted Benzenes and Other Organic Molecules. *Chem. – A Eur. J.* **2017**, *23* (4), 886–895. https://doi.org/10.1002/CHEM.201604176.

(270) Naz, R.; Abbas, W.; Liu, Q.; Shafi, S.; Gull, S.; Khan, S.; Rasheed, T.; Song, G.; Gu, J. Covalent Functionalization of Electrochemically Exfoliated 1T-MoS2 Nanosheets for High-Performance Supercapacitor Electrode. *J. Alloys Compd.* **2023**, *951*, 169944. https://doi.org/10.1016/J.JALLCOM.2023.169944.

(271) Stergiou, A.; Tagmatarchis, N. Molecular Functionalization of Two-Dimensional MoS2 Nanosheets. *Chem. – A Eur. J.* **2018**, *24* (69), 18246–18257. https://doi.org/10.1002/CHEM.201803066.

(272) García-Dalí, S.; Paredes, J. I.; Villar-Rodil, S.; Martínez-Jódar, A.; Martínez-Alonso, A.; Tascón, J. M. D. Molecular Functionalization of 2H-Phase MoS2Nanosheets via an Electrolytic Route for Enhanced Catalytic Performance. *ACS Appl. Mater. Interfaces* **2021**, *13* (28), 33157–33171. https://doi.org/10.1021/ACSAMI.1C08850/ASSET/IMAGES/LARGE/AM1C08850_0004.JPEG.

(273) Zhao, Y.; Zhang, Y.; Yang, Z.; Yan, Y.; Sun, K. Synthesis of MoS_2 and MoO_2 for Their Applications in H_2 Generation and Lithium Ion Batteries: A Review. *Sci. Technol. Adv. Mater.* **2013**, *14* (4), 043501. https://doi.org/10.1088/1468-6996/14/4/043501.

(274) Cai, L.; Cheng, W.; Yao, T.; Huang, Y.; Tang, F.; Liu, Q.; Liu, W.; Sun, Z.; Hu, F.; Jiang, Y.; Yan, W.; Wei, S. High-Content Metallic 1T Phase in MoS2-Based Electrocatalyst for Efficient Hydrogen Evolution. *J. Phys. Chem. C* **2017**, *121* (28), 15071–15077. https://doi.org/10.1021/ACS.JPCC.7B03103/ASSET/IMAGES/LARGE/JP-2017-03103N_0004.JPEG.

(275) Li, H.; Han, X.; Jiang, S.; Zhang, L.; Ma, W.; Ma, R.; Zhou, Z. Controllable Fabrication and Structure Evolution of Hierarchical 1T-MoS2 Nanospheres for Efficient Hydrogen Evolution. *Green Energy Environ.* **2022**, *7* (2), 314–323. https://doi.org/10.1016/J.GEE.2020.09.003.

(276) Chang, L.; Sun, Z.; Hu, Y. H. 1T Phase Transition Metal Dichalcogenides for Hydrogen Evolution Reaction. *Electrochem. Energy Rev. 2021 42* **2021**, *4* (2), 194–

218. https://doi.org/10.1007/S41918-020-00087-Y.

(277) Rong, J.; Ye, Y.; Cao, J.; Liu, X.; Fan, H.; Yang, S.; Wei, M.; Yang, L.; Yang, J.; Chen, Y. Restructuring Electronic Structure via W Doped 1T MoS2 for Enhancing Hydrogen Evolution Reaction. *Appl. Surf. Sci.* **2022**, *579*, 152216. https://doi.org/10.1016/J.APSUSC.2021.152216.

(278) Zhang, Y.; Kuwahara, Y.; Mori, K.; Louis, C.; Yamashita, H. Hybrid Phase 1T/2H-MoS 2 with Controllable 1T Concentration and Its Promoted Hydrogen Evolution Reaction. *Nanoscale* **2020**, *12* (22), 11908–11915. https://doi.org/10.1039/D0NR02525A.